Structural Integrity Monitoring in a Hot Geothermal Well Using Fibre Optic Distributed Temperature Sensing

Doctoral Thesis
(Dissertation)

to be awarded the degree
Doctor of Engineering (Dr.-Ing.)

submitted by
Thomas Reinsch
from Werl, NRW, Germany

approved by the Faculty of Energy and Management Science,
Clausthal University of Technology,

Date of Oral Examination
July 24, 2012

Chairperson of the Board of Examiners
Prof. Dr.-Ing. N. Meyer

Chief Reviewer
Prof. Dr. K. M. Reinicke

Reviewer
PD Dr. Dr.-Ing. habil. C. Teodoriu

Reviewer
Prof. Dr. rer. nat. E. Huenges

Eidesstattliche Erklärungen

Hiermit erkläre ich an Eides statt, dass ich die bei der Fakultät für Energie- und Wirtschaftswissenschaften der Technischen Universität Clausthal eingereichte Dissertation selbständig und ohne unerlaubte Hilfe angefertigt habe.
Die benutzten Hilfsmittel sind vollständig angegeben.

Potsdam, 13. April 2012

_____

Thomas Reinsch

Hiermit erkläre ich an Eides statt, dass ich bisher noch keinen Promotionsversuch unternommen habe.

Potsdam, 13. April 2012

_____

Thomas Reinsch

Abstract

The structural integrity of a wellbore is essential for a safe and sustainable utilisation of a subsurface reservoir. It affects the isolation of different reservoir and aquifer layers as well as the safety of the personnel drilling, completing and operating the well. This study was performed in order to investigate the structural wellbore integrity of a hot geothermal well in Iceland using the Raman based fibre optic distributed temperature sensing (DTS) technology.

Prior to the on-site measurements, a proper fibre for the application of the DTS system has been selected. The optical fibres have been tested at elevated temperatures in ambient and inert atmosphere to set an operating temperature limit for these fibres. SEM micrographs, together with coating colour changes have been used to characterize the high temperature performance of the fibres. After selection of a proper fibre for deployment, a novel wellbore cable has been designed, manufactured and tested prior to a permanent installation behind the anchor casing in well HE-53, Hellisheiði geothermal field, SW Iceland. DTS temperature data have been acquired together with optical time domain reflectometry (OTDR) data during three different field campaigns. Data have been acquired during the installation in spring 2009, during the onset of a production test in summer 2009 and after a 8.5 month shut-in period in summer 2010. Maximum temperatures, measured within the annulus were 230 °C after two weeks of hot fluid production. Data have been used to evaluate the DTS accuracy as well as the degradation of the optical fibre.

Using the DTS temperature data, information about the structural integrity of the wellbore could be acquired. The measured temperature data from the cementation of the anchor casing have been compared to temperature data modelled with a theoretical cement hydration model. In order to match measured and calculated temperature traces for each depth, the slurry density has been varied in the model. For a large depth interval, pumped and modelled slurry densities correspond to each other with an error of less than 50 kg/m^3. Little match between measured and modelled temperatures, on the contrary, has been observed in depth intervals with large calliper variations or previously known loss zones.

For the temperature data acquired during the flow testing time, a novel way to estimate in-situ thermal parameters of the formation surrounding a wellbore has been developed. Together with wellhead fluid data, acquired during the flow test, as well as a wellbore temperature simulator to calculate wellbore temperatures in different depths, the conductive heat transfer to the formation could be determined. For basaltic rocks, a relation between porosity, thermal conductivity, specific heat

capacity, as well as density exists. From the heat transfer, the porosity and hence all thermal parameters could be estimated.

Combining the information about the cementation and the thermal parameters of the formation, a temperature anomaly, observed during the production of hot geothermal fluid has been analysed. As the well temperature was constantly increasing during the first two weeks of flow testing, the annular temperature decreased locally and subsequently in adjacent depth intervals. The effect of decreasing temperatures can be explained by drying and fracturing effects within the cemented annulus and hence a loss of zonal isolation within this intervals. An annular temperature simulation has been used to test and validate this hypothesis.

Zusammenfassung

Die strukturelle Integrität einer Bohrung ist für eine sichere und nachhaltige Nutzung einer untertägigen Lagerstätte von wesentlicher Bedeutung. Sie ist essentiell für die Isolation verschiedener Reservoirschichten und Aquifere, als auch für die Sicherheit des Personals welches die Bohrung abteuft und betreibt. Diese Studie wurde durchgeführt, um die strukturelle Integrität einer heißen Geothermiebohrung in Island mit Hilfe von ortsverteilten faseroptischen Temperaturmessungen (DTS) zu untersuchen.

Vor den Messungen in Island wurde eine geeignete Faser für den Einsatz der DTS-Technologie unter den gegebenen Bedingungen in einer heißen Geothermiebohrung ausgewählt. Verschiedene optischen Fasern wurden bei erhöhten Temperaturen in Umgebungsluft und Inertatmosphäre getestet, um eine maximal mögliche Betriebstemperatur für einen permanenten Einsatz dieser Fasern zu ermitteln. Rasterelektronenmikroskopische Aufnahmen wurden zusammen mit Farbveränderungen der Faserbeschichtung verwendet, um die Temperaturbeständigkeit der Fasern zu bewerten.

Nach Auswahl einer geeigneten Faser wurde ein neuartiges Bohrlochkabel entworfen, hergestellt und vor einer dauerhaften Installation im Ringraum hinter der Ankerrohrfahrt in der Bohrung HE-53, Hellisheiði Geothermie-Feld, SW Island getestet. DTS-Temperaturdaten wurden zusammen mit optischen Zeitbereichsreflektometriedaten (OTDR) während drei verschiedener Messkampagnen gesammelt. Messungen wurden während der Installation im Frühjahr 2009, während dem Beginn eines Produktionstests im Sommer 2009 und nach einem 8,5 monatigen Abschluss der Bohrung im Sommer 2010 durchgeführt. Während des Produktionstests wurden hierbei maximale Ringraumtemperaturen von 230 °C ermittelt. Die OTDR-Daten wurden zur Bewertung der Veränderung der optischen Dämpfungseigenschaften und einer damit einhergehenden Alterung der Faser verwendet.

Aus den DTS Temperaturdaten konnten Informationen über die strukturelle Integrität der Bohrung ermittelt werden. Die während der Zementation der Ankerrohrfahrt gemessene Temperaturentwicklung wurde mit einem simulierten Temperaturverlauf aus einem theoretischen Zementhydratationsmodell verglichen. Um gemessene und simulierte Temperaturentwicklungen für jede Teufe in Übereinstimmung zu bringen, wurde die Dichte der Zementsuspension im theoretischen Modell variiert. Für ein großes Teufenintervall stimmen verpresste und simulierte Zementdichte bis auf einen Fehler von weniger als 50 kg/m^3 überein. Eine geringere Übereinstimmung zwischen gemessenen und simulierten Temperaturen wurde für Teufenintervalle mit

großen Bohrlochausbrüchen oder Intervallen mit massiven Spülungsverlusten während des Bohrprozesses beobachtet.

Für die während der Produktion gemessenen Temperaturdaten, wurde eine neuartige Methode zur in-Situ Bestimmung thermischer Formationseigenschaften entwickelt. Zusammen mit Informationen über das geförderte Fluid am Bohrlochkopf, sowie einem thermischen Bohrlochsimulator, mit dessen Hilfe ein Temperaturprofil in der produzierenden Bohrung berechnet werden kann, konnte die Wärmeübertragung zwischen Bohrlochfluid und Formation bestimmt werden. Für basaltische Gesteine besteht ein Zusammenhang zwischen Porosität, Wärmeleitfähigkeit, spezifischer Wärmekapazität und Dichte. Mit Hilfe der gemessenen Wärmeübertragung konnte die Porosität abgeschätzt und damit alle thermischen Eigenschaften der Formation ermittelt werden.

Durch die Kombination der Informationen über die Befestigung und der thermischen Formationseigenschaften konnte eine Temperaturanomalie, die während der Produktion beobachtet wurde, analysiert werden. Während sich die Fluidtemperatur in der Bohrung in den ersten zwei Wochen der Produktion kontinuierlich erhöhte, wurden im Ringraum lokal und fortschreitend in einander angrenzenden Teufenintervallen, sinkende Temperaturen gemessen. Sinkende Temperaturen können durch ein Aufbrechen von Rissen und Austrocknungserscheinungen innerhalb des zementierten Ringraums hervorgerufen werden. Dadurch kann es zu einem Verlust der Isolation zwischen verschiedenen geologischen Schichten und damit zu einem Verlust der strukturellen Integrität der Bohrung kommen. Mit Hilfe einer thermischen Simulation konnte diese Hypothese getestet und validiert werden.

Contents

List of Figures xvii
List of Tables xx

Nomenclature **xxi**

1. Introduction **1**
1.1. High Temperature Logging Instrumentation 2
1.1.1. Electrical Circuitry 2
1.1.2. Optical Fibres 2
1.2. Site Conditions - HE-53 4
1.3. Structural Wellbore Integrity Monitoring 7

2. Fibre Optic Laboratory Experiments **9**
2.1. Fibre Tests - Fibre Selection 9
2.1.1. Experimental Set-Up 9
2.1.2. Results 10
2.1.2.1. Colour Changes 12
2.1.3. Discussions 12
2.1.3.1. Heating in inert atmosphere and air 12
2.1.3.2. Colour Changes 13
2.1.4. Conclusions 14
2.2. Cable Tests 15
2.2.1. Experimental Set-Up 16
2.2.2. Results 16
2.2.3. Discussions 18
2.2.4. Conclusions 19

3. Fibre Optic Field Experiments **21**
3.1. Installation of DTS Sensor cable 21
3.1.1. Concept 21
3.1.2. Field Work 22
3.1.3. Discussions 24
3.2. Fibre Optic Measurements 25
3.2.1. First DTS Logging Campaign: Well Cementation 27
3.2.1.1. Experimental Set-Up and Measurement Schedule . 27
3.2.1.2. Results 27

3.2.1.3. Discussions 29
3.2.2. Second DTS Logging Campaign: Flow Test 31
3.2.2.1. Experimental Set-Up and Measurement Schedule . 31
3.2.2.2. Results 31
3.2.2.3. Discussions 37
3.2.3. Third DTS Logging Campaign: Shut-In 40
3.2.3.1. Experimental Set-Up and Measurement Schedule . 40
3.2.3.2. Results 42
3.2.3.3. Discussions 43

4. Wellbore Temperature Simulator **47**
4.1. Theoretical Concept 47
4.1.1. Wellhead Conditions 47
4.1.2. Well Temperature Profile 50
4.1.2.1. Momentum Transport 50
4.1.2.2. Energy Transport 51
4.2. Model Formulation 52
4.3. Model Validation 54

5. Heat Transfer in Wellbores **57**
5.1. Theoretical Concept 57
5.1.1. Conductive Heat Transfer 57
5.1.1.1. Infinite Media 58
5.1.1.2. Finite Media 59
5.1.1.3. Conductive Heat Transfer in a Wellbore 61
5.1.1.4. Thermal Properties of Components in HE-53 . . . 62
5.1.2. Convective Heat Transfer 65
5.1.2.1. Heat Transfer to the Wellbore Fluid in Shut-in Periods 65
5.2. Experiments 66
5.2.1. Conductive Heat Transfer to the Formation 66
5.2.1.1. Results 68
5.2.1.2. Discussions 72
5.2.2. Thermal Properties of the Formation 74
5.2.2.1. Results 76
5.2.2.2. Discussions 77
5.2.3. Heat Transfer to the Wellbore Fluid in Shut-in Periods . . . 81
5.2.3.1. Results 81
5.2.3.2. Discussions 82
5.3. Conclusions 84

6. Annular Temperature Simulator **85**
6.1. Model Formulation . . . 85
6.1.1. Geometry and Discretisation . . . 85
6.1.2. Finite-Difference Model . . . 85
6.1.2.1. Inner Node . . . 87
6.1.2.2. Contact Node . . . 87
6.1.2.3. Boundary Node . . . 87
6.1.3. Initial Conditions . . . 88
6.2. Model Validation . . . 88

7. Cement Hydration **91**
7.1. Cement Properties . . . 91
7.1.1. Thermal Conductivity . . . 91
7.1.2. Specific Heat Capacity . . . 93
7.1.3. Acoustic Properties . . . 94
7.1.4. Compressive and Tensile Strength . . . 97
7.1.5. Hydration Kinetics . . . 98
7.1.5.1. Influence of Chemical Composition . . . 98
7.1.5.2. Influence of Water/Cement Ratio . . . 99
7.1.5.3. Influence of Cement Fineness . . . 100
7.1.5.4. Influence of Curing Temperature . . . 100
7.1.5.5. Influence of Applied Pressure . . . 101
7.1.5.6. Mechanisms and Thermo-Chemical Concept of Cement Hydration . . . 101
7.1.5.7. Effect of Additives . . . 102
7.2. Hydration Model . . . 102
7.2.1. Model Formulation . . . 102
7.2.2. Model Implementation . . . 104
7.3. Annular Temperature Model . . . 105
7.3.1. Model Formulation . . . 105
7.3.2. Model Implementation . . . 110
7.3.3. Model Validation . . . 112
7.4. Discussions . . . 115

8. Structural Wellbore Integrity Monitoring **117**
8.1. Cement Job Evaluation - Volumetric Balance . . . 117
8.1.1. Observation . . . 117
8.1.2. Discussions . . . 122
8.2. Cement Job Evaluation - Density Profile . . . 123
8.2.1. Observation . . . 123
8.2.2. Discussions . . . 124

8.3. Structural Integrity Evaluation -Fracture Evolution Within Annulus 127
8.3.1. Observation . . . 127
8.3.2. Hypothesis . . . 131
8.3.3. Simulation . . . 133
8.3.3.1. Geometry . . . 134
8.3.3.2. Initial Conditions . . . 134
8.3.3.3. Boundary Conditions . . . 134
8.3.3.4. Inner Sources . . . 135
8.3.4. Results . . . 137
8.3.4.1. Simulated Temperature Anomaly . . . 137
8.3.4.2. Simulated vs. Measured Temperature Anomaly . . . 138
8.3.5. Discussions . . . 139

9. Summary **145**

10. Conclusions **147**
10.1. Fibre Degradation . . . 147
10.2. Installation . . . 147
10.3. Thermal Properties of the Formation . . . 147
10.4. Cementation . . . 148
10.5. Structural Wellbore Integrity Monitoring . . . 148

A. Drilling Progress HE-53 **151**

B. Lithology HE-53 **153**

C. Installation **155**

D. DTS Data Points **159**

E. Wavetek Measurements **165**

F. Input Parameters for Hydration Calculation **169**

G. Moody Diagram **173**

H. Flow Charts **175**
H.1. Wellbore Simulator . . . 177
H.2. Cement Hydration . . . 179

I. DTS Calibration **183**
I.1. Theory . . . 183
I.2. Calibration Procedure . . . 183
I.3. Calibration of Wellbore Cable for HE-53 . . . 184

J. Publication in Measurement Science and Technology **187**

References **217**

Acknowledgements **219**

List of Figures

1.1. Active Volcanic Zones in Iceland. 5

2.1. Experimental set up for heating fibres in ambient air and inert atmosphere. 10
2.2. SEM micrographs of optical fibres. 11
2.3. Coating colour change of heated fibres. 13
2.4. Design of optical cable. 15
2.5. Experimental set up for the cable tests. 17
2.6. Attenuation after heating of the cable. 18

3.1. Installation of the fibre optic cable. 23
3.2. Attenuation during cement job. 24
3.3. Schematic experimental set-up for DTS and OTDR measurements. 26
3.4. Experimental set-up during cementation of the anchor casing. . . . 27
3.5. DTS temperature evolution during cementation. 28
3.6. Accuracy of DTS measurements during cementation. 29
3.7. DTS temperature evolution during the onset of flow test. 33
3.8. Wellhead temperature evolution during a flow test in HE-53 in 2009. 34
3.9. Temperature versus cable-casing distance during the flow test. . . . 34
3.10. Evolution of attenuation along optical fibre during the flow test. . . 36
3.11. Offest correction of DTS temperature measurements during flow test. 37
3.12. Flow test data from HE-53. 41
3.13. Degradation of optical fibre after flow test - temperature measurements. 43
3.14. Degradation of optical fibre after flow test - attenuation measurements. 44

4.1. Typical set-up to measure flow rate and enthalpy. 49
4.2. One dimensional well model. 52
4.3. Comparison between measured and modelled pressure and temperature profiles in HE-53. 56

5.1. Steady state conductive heat transfer in a multilayer cylinder. . . . 60
5.2. Sketch of a decentralized multilayer cylinder. 60
5.3. Thermal conductivities of Hawaiian basalt. 64
5.4. Heat loss for both cable branches at 350 h_{DTS} after beginning of logging. 70

5.5. Error propagation for the measured heat loss. 71
5.6. Decentralized Anchor Casing in HE-53. 71
5.7. Formation thermal parameters calculated based on temperature measurements at 350 h_{DTS}. 78
5.8. Error in calculating the thermal conductivity. 79
5.9. Comparison of thermal conductivity and Bond Index calculated at 37 h after cementation. 79
5.10. Comparison of Logs from Cement Job. 83

6.1. Geometry and discretisation of the one-dimensional radial symmetric wellbore model. 86
6.2. Compare steady state of modelled and calculated annular temperatures. 89
6.3. Compare modelled temperatures with results of OpenGeoSys. . . . 90

7.1. Comparison of thermal conductivities. 94
7.2. CBL attenuation vs. acoustic impedance. 96
7.3. Compressional wave velocity vs. compressive strength for cements. . 98
7.4. DTS temperature log shortly after casing installation. 106
7.5. Onset of cement hydration. 107
7.6. Initial temperature conditions for hydration model. 108
7.7. Temperature of injected water during hydration. 110
7.8. Comparison between measured and simulated temperature evolutions during hydration. 113
7.9. Comparison of measured and simulated wellbore temperature. . . . 114

8.1. Temperature evolution during beginning of cementation. 118
8.2. Comparison of measured and simulated temperature evolution for different thermal properties of the formation. 124
8.3. Simulated cement density profile of cement behind the anchor casing. 125
8.4. DTS temperature data for individual depth intervals during the flow test. 128
8.5. Analysis of the observed temperature anomaly. 129
8.6. Temperature versus distance cable-casing. 130
8.7. Rate of temperature change versus distance cable-casing. 130
8.8. Comparison of depth intervals with and without the temperature anomaly. 131
8.9. Concept of fracture evolution 134
8.10. Enthalpy of water at different temperatures. 136
8.11. Simulated temperature evolution within annulus with temperature anomaly. 138
8.12. Comparison of measured and simulated anomaly. 139
8.13. Comparison between measured and simulated anomaly properties. . 140

A.1. Drilling progress. 152

B.1. Lithology. 154

C.1. Installation of the DTS sensor cable. 158

G.1. Moody diagram. 174

H.1. Flowchart symbols. 176
H.2. Simplified flowchart of the wellbore simulator. 178
H.3. Flowchart for cement hydration model 180
H.4. Flowchart for the annular temperature increase during cement hydration. 181
H.5. Flowchart to iterate best fit for slurry density. 182

I.1. Experimental Set-up for the calibration of the fibre optic cable. . . 185
I.2. Polynomial correction of DTS temperature measurements. 186

List of Tables

1.1. Location of aquifers in well HE-53 for the uppermost 300 m (MD). . 6

3.1. Diameter of drill bit and casing as well as depth information for well HE-53. 22
3.2. Chronicle of different activities at HE-53. 25
3.3. Cementing report for well HE-53. 30
3.4. Chronicle of different activities at HE-53 in summer 2009. 32

4.1. Comparison of modelled pressure profiles with literature data. . . . 55

5.1. List of thermal properties. 62
5.2. Fitted thermal conductivities for Hawaiian basalt with zero and 100 % porosity. 63
5.3. Thermal conductivities and geometry information used for calculation. 68
5.4. Error for quantities used in Equation 5.29. 69

7.1. Mix design of cement slurry used for cementing well HE-53. 92
7.2. Technical data for the Portland cement used for cementing well HE-53. 92
7.3. Compressional-wave speed for slurry components. 95
7.4. Acoustic properties of well cement. 96
7.5. Clinker phases forming during the hydration of cement. 99

8.1. List of cement jobs for the anchor casing of HE-53. 119
8.2. List of activities and cement quantities lost during different well operations. 121
8.3. List of different materials to simulate temperature anomaly. 135

C.1. List of different activities in well HE-53 prior and during the cementation of the anchor casing. 156
C.2. Depth correlation of different well logs. 156
C.3. Depth of installation interpreted from three different Casing Collar Locator logs. 157

D.1. Depth to DTS data points together with the distance between cable and casing. 164

E.1. List of OTDR measurements. 167

F.1. Input parameters for annular temperature simulation. 170
F.2. Input parameters for hydration calculation. 171

I.1. Calibration temperatures. 184
I.2. Parameters for polynomial fitting of DTS temperature data. 185

Nomenclature

Abbreviations

API	American Petroleum Institute
CAL	calliper log
CBL	cement bond log
CCL	casing collar locator log
C_2S	$(CaO)_2 \cdot SiO_2$
C_3A	$(CaO)_3 \cdot Al_2O_3$
C_3S	$(CaO)_3 \cdot SiO_2$
CaAF	$(CaO)_3 \cdot Al_2O_3 \cdot Fe_2O_3$
DTS	distributed temperature sensing
EVZ	east volcanic zone
HPI	polyimide coated fibre with hermetic carbon layer
$L^*a^*b^*$	color space
NG	natural gamma ray log
NN	neutron-neutron log
NR	natural resistivity log
NVZ	north volcanic zone
OGS	OpenGeoSys
$OTDR$	optical time domain reflectometry
PFA	perfluoralkoxylalkan
PI	polyimide coated fibre
SiC	silicon carbide
SLE	surface excess length
SOI	silicon on isolator
SRO	surface readout unit
TT	temperature trace
TW	televiewer log
TZF	three zone tube furnace
WVZ	west volcanic zone

Greek symbols

α_{DOH}	degree of hydration	-
$\dot{\alpha}_{DOH}$	hydration rate	$1/\text{h} = 1/(3600\ \text{s})$
$\tilde{\dot{\alpha}}_{DOH}$	auxiliary variable (dimensionless hydration rate)	-
ζ	surface roughness	mm
η	dynamic viscosity	kg/(m s)

$\widetilde{\eta}_\alpha$	dimensionless permeability	-
λ	thermal conductivity	W/(m K)
ν	kinematic viscosity	m^2/s
σ_s	shear bond strength	MPa
σ_c	compressive strength	MPa
σ_t	tensile strength	MPa
ς	variance	$(°C)^2$
Θ	angle from the horizontal	°
ϕ	volume fraction, porosity	m^3/m^3
φ	angle of decentralisation	°
χ	ratio of hydration products to reacted cement	m^3/m^3
ψ	heat transfer coefficient	$W/(m^2\ K)$
Ω	function of chemical composition	-
Roman symbols		
$\widetilde{A}_\alpha$	dimensionless chemical affinity	-
a^*	color axis red/green	-
A_{ID}	area of pipe	cm^2
BI	bond index	-
$\widetilde{B}$	auxiliary variable (dimensionless Blaine fineness)	-
B	Blaine fineness	m^2/kg
b^*	color axis blue/yellow	-
c_p	specific heat capacity	J/(kg K)
$c_{hyd,0}$	material constant for hydration calculation	-
c_{hyd}	constant for hydration calculation	-
c_{RJ}	constant to calculate the fluid enthalpy	$kg/(cm^2\ s)$
d	thickness of a layer	m
ΔE^*_{ab}	colour difference	-
E_a	apparent acivation energy	J
$f(t)$	transient heat conduction function	-
$f_{R,2Ph}$	two-phase friction coefficient	-
Gr	Grashof number	-
$\widetilde{h}_t$	auxiliary variable (dimensionless total enthalpy)	-
h	enthalpy	J/kg
H_w	water height in the weir box	m
h_{DTS}	time after beginning of DTS logging	h
ID	inner diameter	m
I	intensity of backscattered photonse	counts
J	total number of time steps	-
L^*	color axis black/white	-
L_c	characteristic length	m
$\dot{m}$	mass flow rate	kg/s
m	mass	kg

Nu	Nusselt number	-
Nu^*	pseudo Nusselt number	-
OD	outer diameter	m
Pr	Prandtl number	-
$\widetilde{p}_c$	auxiliary variable (dimensionless critical pressure)	-
p_0	wellhead pressure	Pa
p_c	critical pressure	Pa
$\dot{Q}$	heat transfer	W
$\dot{Q}_L$	heat loss per unit length	W/m
Ra	Rayleigh number	-
R	conduction resistance	K/W
R^2	coefficient of determination	-
Re_{2Ph}	two-phase Reynolds number	-
s	pressure dependence of hydration	-
S_{DTS}	slope value for DTS temperature calculation	K
$\widetilde{T}$	auxiliary variable (dimensionless temperature)	-
T	temperature	K
t	time	s
U	over-all heat transfer coefficient	W/(m^2 K)
u_m	mixture velocity in well	m/s
u_p	compressional wave velocity	m/s
u_v	vapour velocity in well	m/s
$\dot{V}$	volumetric flow rate	m^3/s
V	volume	m^3
w	mass fraction, quality	kg/kg
w/c	water/cement ratio	kg/kg
Z	acoustic impedance	kg/(m^2 s)
z_h	depth interval/segment	m

Subscript

α	degree of hydration
a	anchor
ast	Anti-Stokes
aux	auxiliary constant
c	constant
cem	cement
$cond$	conductive
$conv$	convective
csg	casing
err	error
$evap$	evaporation
f	fluid
for	formation

hce	hydrated part of the cement	
HS	Hashin-Shtrikman	
hyd	hydration	
in	inner side	
ini	initial	
k	control variable	-
L	unit length	
l	liquid	
m	two-phase mixture	
max	maximum	
meas	measured	
min	minimum	
n	number of node	
out	outer side	
p	production	
pa	cement paste	
por	anhydrous cement	
ref	reference	
r	radius	
rc	reference coil	
RJ	Russel James	
s	solid	
sim	simulated	
sl	slurry	
st	Stokes	
t	total	
th	thermal	
u	ultimate	
V	volumetric	
v	vapour	
w	water	
Superscripts		
a	atmospheric conditions	
corr	corrected	
ID	inner diameter	
j	number of iteration/number of time steps	
l	control variable	-
OD	outer diameter	
p	specific pressure condition	

1. Introduction

Within mitigation strategies for the climate change, geothermal energy plays an important role for the future energy supply (Sims et al., 2007). In order to characterize a geothermal reservoir and to design a strategy for a sustainable production of energy, measuring transient well-bore temperatures is important. Not only can transient temperature measurements after the drilling process be used to determine static formation temperatures (e.g. Dowdle and Cobb, 1975) but they can also be used to identify relevant feed zones to a well (e.g. Nowak, 1953; Stefánsson and Steingrímsson, 1980). Formation temperatures as well as temperature changes during the production or injection of geothermal fluid are necessary information to design the infrastructure at a geothermal site (Saadat et al., 2010).

Over the last two decades, fibre optic distributed temperature sensing (DTS) based on Raman backscattering has been increasingly used for wellbore applications, e.g. in the petroleum industry (Williams et al., 2000; Johnson et al., 2004; Pimenov et al., 2005) as well as for geothermal (Hurtig et al., 1994; Förster et al., 1997; Günzel and Wilhelm, 2000; Henninges, 2005) and climate studies (Freifeld et al., 2008). DTS-technology is a means to acquire quasi continuous temperature measurements along the entire length of an optical fibre. Integrating an optical fibre in an appropriate wellbore cable, a temperature profile over the entire length of the cable can be determined. Permanently installed behind casing, temperature information can be acquired without well intervention. DTS is especially well suited for the application under harsh wellbore conditions. The passive fibre optic cable can be remotely controlled and no electronics have to be lowered into the well. To acquire a continuous temperature profile, a laser pulse is coupled into the fibre and backscattered photons of the Stokes and Anti-Stokes wavelengths are recorded. The ratio of both wavelengths can be calibrated to ambient temperatures and is therefore sensitive to differential attenuation changes within these frequency bands along the fibre. From the travel time of the signal, the location of the temperature information along the fibre can be determined (e.g. Hartog, 1983).

Conventional high temperature geothermal wells, like in high enthalpy areas in Iceland, reach temperatures up to $350 - 380$ °C (Arnórsson, 1995). To increase the energy output from individual geothermal wells, accessing unconventional geothermal reservoirs comes into the focus of current research activities (e.g. Fridleifsson and Elders, 2005; Bignall, 2010). Tapping geothermal fluids at supercritical conditions might enhance the energy output from a single well by an order of magnitude (Albertsson et al., 2003). In order to acquire temperature data from such wells,

electronic as well as fibre optic logging devices can be used.

1.1. High Temperature Logging Instrumentation

1.1.1. Electrical Circuitry

At elevated temperatures, like in high temperature geothermal wells, standard electronic circuitry cannot be deployed without a proper heat shield (Sarian and Gibson, 2005). Conventional wellbore logging equipment has a temperature rating of 177 °C(350 °F) (Sarian and Gibson, 2005). For long term applications at high temperatures (> 200 °C), Silicon on Isolator (SOI) and Silicon Carbide (SiC) devices can be used (e.g. Dreike et al., 1994; Flandre et al., 2001) to manufacture downhole point sensors.

Data can be acquired with wireline logging as well as memory tools. Wireline logging devices need a specially designed wellbore cable, capable of transmitting energy and data at high temperatures. Most commercially available high temperature logging cables have a maximum operating temperature of 316 °C(600 °F). Due to the high cost of such cables, however, these devices are currently not widely used in wellbore applications. Having a memory tool, an additional temperature resistant power supply has to be provided. Memory tools are widely used in high temperature applications, as a simple metal wire can be used to lower a non-communicating device down into a well at temperature conditions exceeding commercial wellbore cable limitations.

1.1.2. Optical Fibres

Optical fibres are well suited for the application at elevated temperatures, although special fibres have to be selected for different applications. An optical fibre is commonly composed of an optical core and an optical clad with a lower refractive index than the core, to guide light within the core (Thyagarajan and Ghatak, 2007). Core and clad are made of silica with some doping molecules to adjust the refractive index (Thyagarajan and Ghatak, 2007). Silica itself can withstand a temperature well above 1000 °C before it melts, but is very brittle. To increase the strength of the fibre, an appropriate coating material has to be chosen for the desired application. Among these, polymer and metal materials can be used at elevated temperatures. Polyimide coatings, for example, can commonly be operated at temperatures up to 300 °C. For higher temperatures, metal coatings can be employed at temperatures up to 700 °C (Jaaskelainen, 2010). High attenuation values of metal coated fibres, however, limit the deployment of greater lengths of these kind of fibres (Bogatyrev and Semjonov, 2007; Reinsch and Henninges, 2010).

Ingression of hydrogen is another important aspect that has to be considered using optical fibres in harsh environments. Within the geothermal fluid of high

temperature geothermal wells in Iceland, hydrogen is often present (Arnórsson and Gunnlaugsson, 1985; Arnórsson, 1995). In hydrogen rich environments, optical properties of fibres degrade rapidly due to hydrogen ingression and hydroxyl formation (Smithpeter et al., 1999; Williams et al., 2000; Normann et al., 2001). Hydrogen ingression and subsequent hydroxyl formation causes strong absorption peaks at relevant wavelengths (Stone and Walrafen, 1982; Humbach et al., 1996; Williams et al., 2000). Increasing differential attenuation between the Stokes and Anti-Stokes band skews temperature measurements over time (Normann et al., 2001). To reduce the ingression of hydrogen and the subsequent formation of hydroxyl within the interstices of the silica, hermetic carbon coatings have been used as a hydrogen diffusion barrier. Hydrogen diffusion through carbon coatings, however, can be detected at temperatures above 100 °C (Lemaire and Lindholm, 2007). Recently, pure silica core fibres have been shown to be well suited for application in hydrogen rich environments (Kaura and Sierra, 2008).

Mechanical stress onto the fibre can lead to micro- and macrobending loss, influencing the wavelength dependent attenuation characteristics. Changing temperatures, a different coefficient of thermal expansion (CTE) between coating and silica material as well as degradation and stiffening of coating material can cause *microbending* loss, which is defined as the loss induced by „small random bends and stress in the fiber axis“ (Lingle, Jr. et al., 2007). Large deflections of the fibre axis leads to *macrobending* loss. The term “large” is defined relative to the fibre core diameter (Lingle, Jr. et al., 2007).

In order to monitor wavelength dependent transmission changes along the fiber, attenuation measurements at standard telecommunication (850 and 1300 nm) wavelengths can be used to qualitatively monitor the optical properties (Smithpeter et al., 1999). Hydrogen ingression causes strong absorption peaks which can be detected using the attenuation ratio $\Gamma = \frac{a^{1300}}{a^{850}}$ (Humbach et al., 1996; Smithpeter et al., 1999). Due to the proximity of the 1300 nm testing wavelength to the hydroxyl absorption peaks at 1270 and 1380 nm, the ratio increases with increasing hydrogen load of the optical fibre. Using the ratio of attenuation values, different degradation processes and resulting influences on the measured temperatures can be assigned to different regions along the fibre.

Using conventional DTS units, the influence of hydrogen on the measured temperatures can be reduced using an experimental set-up where both ends of the fibre can be accessed. Averaging measurements from both ends alleviates the problem of skewed temperature measurements. Another means to mitigate the effect of hydrogen onto measured temperatures is the dual laser principle where measurements from two different incident wavelengths are used (Lee, 2007; Suh and Lee, 2008). If only one end of the fibre can be accessed, the dual laser principle can be used to account for wavelength dependent changes along the attenuation profile.

Within this study an optical fibre for the installation within a hot geothermal well was selected, a novel fibre optic cable was developed together with the industry

and tested under in-situ temperature conditions (Chapter 2). The fibre was selected on the basis of heating experiments under laboratory conditions. Heating tests were also conducted to test the performance of the fibre optic cable at elevated temperatures. In order to test the technique of a permanent installation of the fibre optic cable behind casing in a hot geothermal well in Iceland, this cable has been installed behind the anchor casing of well HE-53 in the Hellisheiði geothermal field in SE Iceland. Temperature measurements were performed during the cementation (May 2009) of the anchor casing and the onset of a flow test (July/August 2009) as well as after the termination of this flow test when wellbore temperatures reached static formation temperatures, again (August 2010) (Chapter 3). Data from the different field campaigns were used to investigate the performance of the optical fibre as well as different aspects of the structural wellbore integrity (Chapters 7 and 8).

1.2. Site Conditions - HE-53

For a permanent installation behind casing, well HE-53 in the Hellisheiði geothermal field, SW Iceland, was available (Figure 1.1). HE-53 was planned to be a exploration well, drilled in a new area of the geothermal field.

Geology - Hellisheiði Geothermal Field Iceland is located on the mid-oceanic ridge in the North Atlantic Ocean. High eruption rates due to the active upwelling of a plume with a lateral dimension of 2400 km Breddam et al. (2000), led to the build up of the Icelandic landmass. The plate boundary between the American and European continent runs through Iceland as a zone of active volcanism, seismicity and graben structures Björnsson et al. (1977). It can be subdivided into the North Volcanic Zone (NVZ) and in the south into the West and East Volcanic Zone (WVZ and EVZ, respectively, Figure 1.1), each composed of several volcanic systems containing a central volcano, fissure swarms or both (Thordarson and Larsen, 2007, and references herein).

The Hellisheiði geothermal field is situated within the Western Volcanic Zone (WVZ) close to the Hengill central volcano. The Hengill volcanic system is associated with two presently exploited geothermal systems. To the North, the Nesjavellir geothermal field produces electrical energy and hot water for space heating since several decades. Recently, the Hellisheiði geothermal field in the south of the volcano was started to be exploited. Due to the meteoric origin of the geothermal fluid in the Hengill area (Arnórsson, 1995), its salinity is very low with a concentration of total dissolved solids of approx. 1500 ppm (Franzson et al., 2005).

Within the Hellisheiði area, HE-53 is situated in the Hverahlið geothermal field. The geology in the vicinity of well HE-53 is dominated by lava successions with

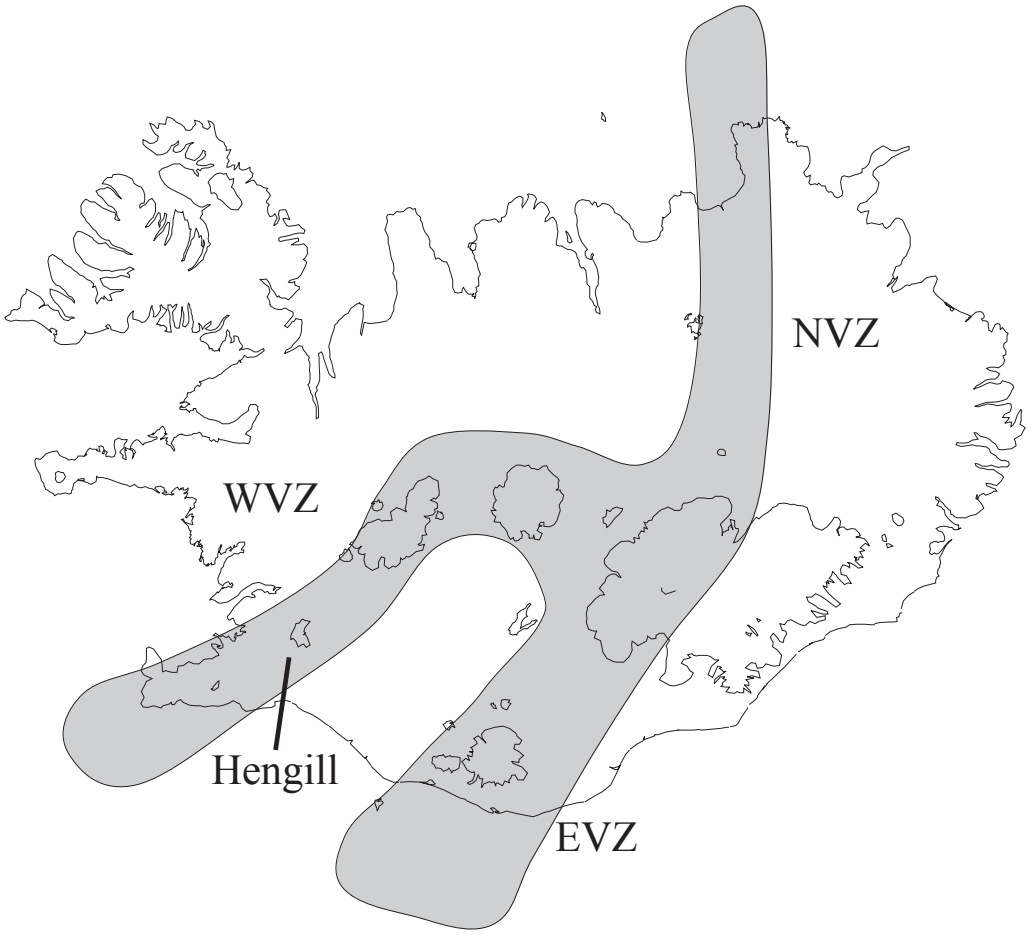

Figure 1.1.: Iceland. The shaded area indicates the active volcanic zones (Eastern, Western and Northern Volcanic Zone). The location of the Hengill central volcano is indicated in the South-West.

Table 1.1.: Location of aquifers in well HE-53 for the uppermost 300 m (MD). The amount of circulation loss during drilling is listed together with the means to identify the aquifer as well as lithological information (pers. comm. Steinþór Níelsson, ISOR - Iceland GeoSurvey).

Depth (m)	Circulation Loss	Detection	Lithology
130	>35 l/s	Total loss of circulation.	Pillow-basalt
140	>35 l/s	Total loss of circulation.	Pillow-basalt
154	>35 l/s	Total loss of circulation.	Pillow-basalt
160	>35 l/s	Total loss of circulation.	Pillow-basalt
300?	10 l/s	Temperature logs.	Basalt-breccia

intercalated hyaloclastite formations. Alterations range from fresh rocks which are in contact to the shallow groundwater aquifers through zeolith assemblages to high temperature assemblages. Chlorite, epidote, wollastonite and actinolite minerals have been found. The lava formations are mainly formed during interglacial periods, whereas the hyaloclastites formed in subglacial eruptions. Generally, they are of high porosity but low permeability. Hydrothermal alteration leads to a further reduction of permeability. In between the volcanic succession, intrusive rocks can be found. They are mostly identified by their compact nature and relatively low indications of alteration (Níelsson and Franzson, 2010).

From deep wells (2000-2800 m) it is known that a high temperature system of $200 - 320$ °C is situated below $600 - 1000$ m depth (Níelsson and Franzson, 2010). Geothermal fluid within the Hellisheiði geothermal field is currently produced from 30 wells which are operated at wellhead pressures from $15 - 25$ bar (Sigfusson and Gunnarsson, 2011). As the produced fluid is at the boiling point, temperatures can be derived from steam tables. $15 - 25$ bar correspond to production temperatures of $200 - 225$ °C (Lemmon et al., 2007). The wells have an average discharge of 37 kg/s and an enthalpy of 1675 J/kg (Sigfusson and Gunnarsson, 2011).

Aquifers Different parameters have been used to locate aquifers within geothermal fields. The depth of different aquifers in the vicinity of well HE-53 has been determined using circulation losses, temperature logs, hydrothermal alteration as well as other relevant drilling data (Helgadóttir et al., 2010; Níelsson and Franzson, 2010). Several aquifers have been located in well HE-53. For the uppermost 300 m, which are of importance for the installed temperature cable, the location of the aquifers is listed in Table 1.1.

1.3. Structural Wellbore Integrity Monitoring

During flow testing, HE-53 turned out to be an exceptionally powerful well. Flow rates of 54 kg/s and enthalpies of 2650 J/kg were measured in September 2009. During the first two weeks of flow testing, wellhead temperatures rose up to 260 °C. High pressure conditions and temperature changes during well testing, production or injection activities in a geothermal well are known to cause a high risk of well failure (e.g. Goodwin and Crook, 1992; Thiercelin et al., 1998; Southon, 2005).

Information about the structural integrity of a well can be gathered from standard well logs, although special tools are needed for a detailed investigation. In Iceland, standard logs for each well are (Stefánsson and Steingrímsson, 1980; Danielsen, 2010):

1. Temperature (T)
2. Pressure (p)
3. Calliper Log (CAL)
4. Cement Bond Log (CBL)
5. Casing Collar Locator Log (CCL)
6. Natural Gamma Ray Log (NG)
7. Natural Resistivity Log (NR)
8. Neutron-Neutron Log (NN)
9. Directional Survey (Gyro)
10. Additional Logs:

    Televiewer Log (sonic and video) (TW)

whereas temperature and pressure are monitored at regular intervals throughout the lifetime of the well. All other logs are commonly measured during the drilling process or work-over activities. At elevated temperatures, however, the selection of tools to monitor the structural integrity of a well is limited due to the limitations of electrical circuitry, as mentioned above. Pressure and temperature gauges, as well as calliper tools are available for high temperature environments (Danielsen, 2010). An acoustic televiewer for temperatures up to 300 °C has recently been developed and deployed in Iceland (Massiot et al., 2010). The application of available logging tools is therefore dependent on the downhole conditions and commonly restricted to drilling and work-over activities, when the well is actively cooled.

Cement bond logs are used to evaluate the quality of the casing cementation. The bonding between cement and casing is measured by an acoustic signal and

its propagation between transmitter and receiver along the casing (Smolen, 1996). Information can be used to estimate the zonal isolation between different lithologies as well as the strength of the cement. An exact measure of the amount of cement in place, however, cannot be provided (Smolen, 1996). In addition to CBL and calliper data, which is used to calculate the amount of cement needed for cementing a casing, temperature data can be used to describe the location of cement during the cementation process (Guyod, 1946; Suman, Jr. and Ellis, 1977; Jutten and Morriss, 1990). When cement is mixed with water, it starts to hydrate, releasing latent heat of hydration. The released heat can be used to monitor the top of cement within the annulus as well as intervals of high or low temperature increase, related to large and small amounts of cement in place, respectively (Guyod, 1946; Jutten and Morriss, 1990).

In order to increase the knowledge about the cement quality, two dimensional information can be acquired using sonic tools (Smolen, 1996). Information about the integrity of completions with multiple casings, however, is only available for the innermost casing.

Different geophysical logs can be used to acquire a snap-shot of time dependent processes like the evolution of a mikroannulus. In order to monitor the entire cementation process, several logs have to be acquired in specific time intervals. To overcome this limitation, DTS measurements have recently been made to monitor the cementation process continuously (e.g. Fujii et al., 2008; Henninges et al., 2008). Using a combination of different logs, together with DTS temperature data, the cement head as well as problems during cementing could be identified (Henninges et al., 2008).

During the different fibre optic logging campaigns, several thermal effects have been observed that can be related to processes influencing the structural integrity of geothermal wells. For the cementation of the anchor casing, the temperature increase due to the hydration of cement has been observed. Measured (Chapter 3) and modelled (Chapter 6 and 7) temperature evolutions are compared in order to estimate the quality of the cement in different depth intervals together with other available well logs (Chapter 8). Data acquired about the integrity of the cementation will be used to interpret a temperature anomaly measured during the flow test in summer 2009 (Chapter 8).

In order to increase the accuracy of the modelled temperature evolution (Chapter 6), observed conduction and convection phenomena within the well are studied in detail (Chapter 5). The amount of convective heat transfer between casing and wellbore fluid during shut-in periods like the cementation is calculated. Furthermore, the conductive heat transfer to the formation could be determined calculating the temperature difference between a simulated wellbore temperature profile (Chapter 4) and measured DTS temperatures. The heat transfer has been used to estimate relevant thermal properties of the formation.

2. Fibre Optic Laboratory Experiments

Prior to the installation in Iceland, a fibre has been selected and a cable has been manufactured and tested. This chapter describes the fibre tests which are the basis for the selection of a fibre for deployment (published as: Reinsch and Henninges, 2010, see Appendix J). After the fibre had been selected and a cable had been manufactured, tests have been performed to evaluate the high temperature performance of the cable.

2.1. Fibre Tests - Fibre Selection

For the deployment under the harsh conditions of a typical hot geothermal well (see Section 1.2), the selection of a proper fibre for deployment is important. Only a very limited range of fibres with special coating materials can be used at temperatures up to or even higher than 300 °C. Different commercially available high temperature fibres have been tested in a preliminary study (Reinsch, 2008). Among these were fibers with polyimide coatings as well as metal coatings. Despite their limited temperature range in comparison to metal coatings, polyimide coatings have shown to possess the most favourable properties at temperature conditions expected during the production of hot fluid within a conventional geothermal well in Iceland ($\approx$ 200 °C, see Section 1.2).

2.1.1. Experimental Set-Up

Polyimide fibres were selected for deployment on the basis temperature cycling experiments (Reinsch, 2008). To test the performance of a fibre with an additional hermetic carbon layer beneath the polyimide coating (HPI), and to compare it to a fibre with an ordinary polyimide coating (PI), two samples have been selected for further testing. In order to characterise the different fibres, samples have been heated in ambient air and inert atmosphere within a Carbolite® three-zone tube furnace (TZF, Figure 2.1). Samples of 1 m length were treated at constant temperatures of 250 °C for 190 h, 300 °C for 269 h and 350 °C for 216 h, to investigate an operating limit for these fibres. A sample of each fibre was heated in ambient air and a second one in an argon atmosphere (Figure 2.1). Each sample was placed in a

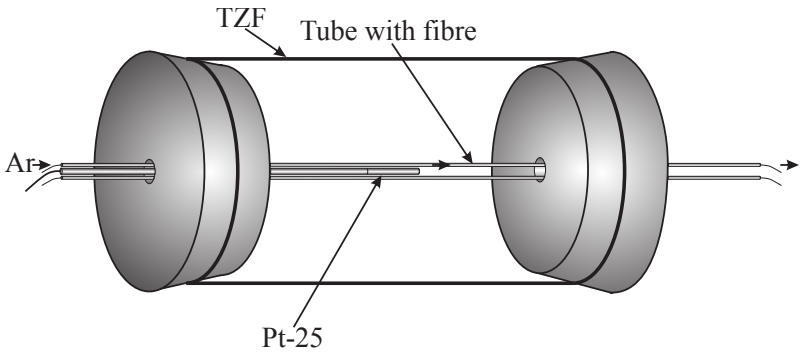

Figure 2.1.: Experimental set up for heating fibres in ambient air and inert atmosphere. Small tubes were heated within the three zone tub furnace (TZF) and argon was flushed continuously through one of the tubes during heating. A Pt-25 was used as reference temperature sensor.

stainless steel tube with an outer diameter of 2 mm and a wall thickness of 0.2 mm. For each fibre type, two tubes were placed in the centre of the TZF and one of the tubes was continuously flushed with ≈ 50 ml/min Argon 5.0.

The effect of argon flow on the measured DTS temperature is negligible. In order to test this, a 20 m section of a several hundred meter long fibre optic cable was placed in an oven. The temperature difference between inside and outside the oven was 100 °C. Flushing the cable with ≈ 50 ml/min argon did not change measured DTS temperatures along the fibre.

SEM micrographs and coating colour changes have been analysed to estimate the state of degradation. In order to quantify colour changes, high resolution digital photographs have been taken using a Nikon D3 camera. The samples have been illuminated using an Osram Dulux L 18W/12 Lumilux Deluxe Daylight lamp (5400 K).

2.1.2. Results

Figure 2.2 shows SEM micrographs of the PI and HPI fibres, heated at different temperatures in ambient air and argon atmosphere. SEM micrographs of the fibres clearly show an increase in size and frequency of surface depressions with temperature. Furthermore, depressions increase both in size and frequency in ambient air, compared to fibres heated in argon atmosphere. The surface depressions were not evenly distributed along the fibre. The HPI sample developed fewer and smaller depressions compared to the PI sample.

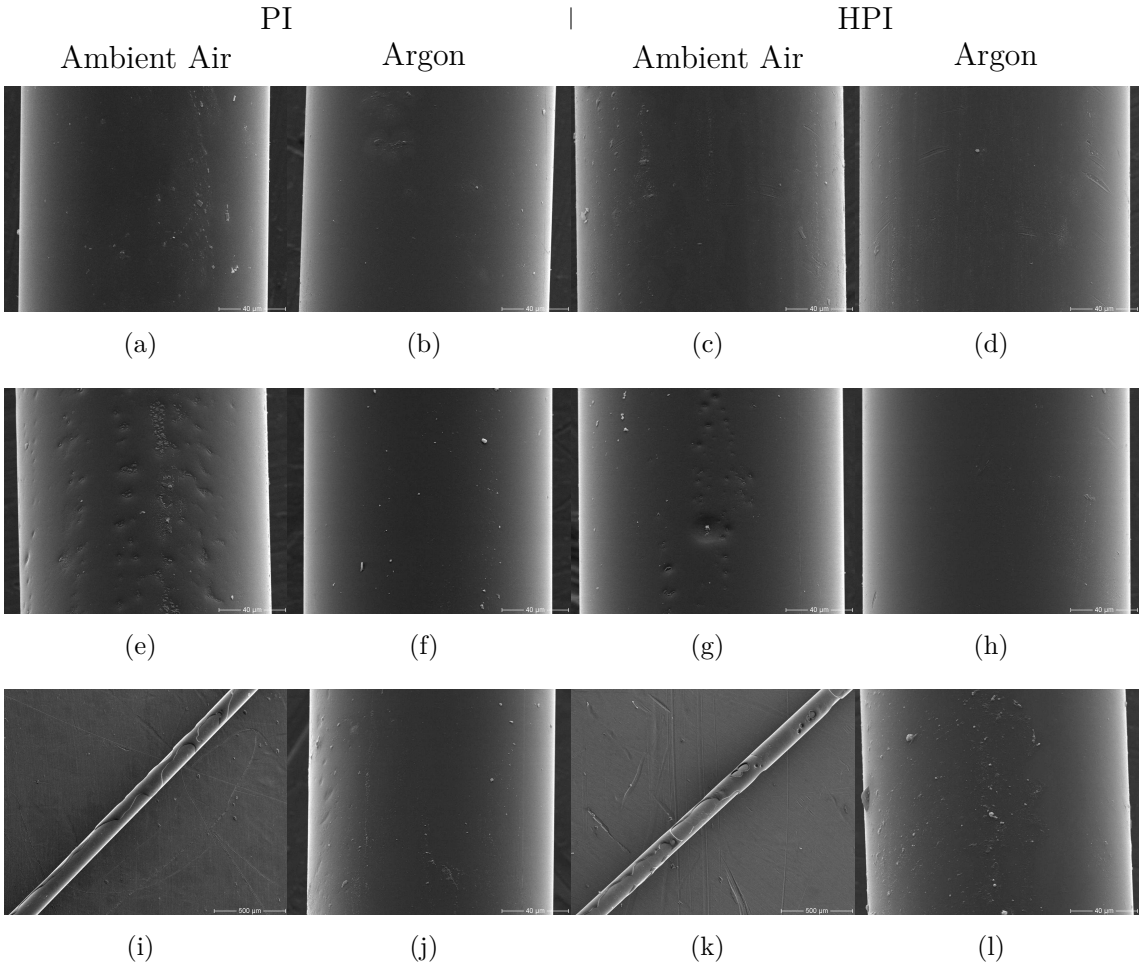

Figure 2.2.: SEM micrographs from PI and HPI fibres. Samples were heated at constant temperature. The scale bar in the lower right corner indicates 40 μm for all pictures except (i) and (k) where it is 500 μm. (a)-(d): 250 °C, 190 h; (e)-(h): 300 °C, 269 h; (i)-(l): 350 °C, 216 h.

2.1.2.1. Colour Changes

Due to degradation, the cladding was partly exposed for samples heated at 350 °C. For each fibre, three representative areas where the coating was still covering the cladding have been used to determine a sRGB value for the coating colour. These values have been converted to the CIE 1976 L*a*b* colour space (Carter et al., 2004) using a CIE 1931 - 2° standard colorimetric observer. The L* axis represents colours from black to white, a* represents green to red and b* blue to yellow. Averages and standard deviations of the colours has been calculated for each fibre from the recorded digital photographs. The colour difference along a single axis has been calculated as the norm $\Delta L^* = |L^* - L^*_R|$, $\Delta a^* = |a^* - a^*_R|$ and $\Delta b^* = |b^* - b^*_R|$, respectively. The subscript R denotes the reference sample. Total colour differences ΔE^*_{ab} have been calculated as the Euclidean distance within the L*a*b* space according to Equation 2.1.

$$\Delta E^*_{ab} = \sqrt{(\Delta L^*)^2 + (\Delta a^*)^2 + (\Delta b^*)^2} \tag{2.1}$$

The calculations are based on colorimetry and the results are therefore illuminant-dependent. In order to compare absolute values of colour differences, measurement conditions have to be identical.

Colour changes were observed for all fibres that have been heated (Figure 2.3). Different fibres show different colour changes with temperature and atmosphere. The colour remains similar, however, for the samples heated at 250 °C and 300 °C. ΔE^*_{ab} values stay below 10 compared to the reference fibre. At 350 °C colour changes considerably for all fibres and ΔE^*_{ab} increases to more than 10.

Initially, polyimide fibres have a light yellow colour. The additional carbon layer beneath the polyimide coating of the HPI fibre causes a dark, greenish appearance of this fibre. After heating, the colour appearance did not change for the HPI fibre as much as for the light yellow PI fibre without the carbon layer. The difference at 350 °C in comparison to the colour changes at 300 °C is large for the PI fibre, whereas it appears to be small for the HPI fibre.

2.1.3. Discussions

2.1.3.1. Heating in inert atmosphere and air

Polyimide coatings suffer from curing, thermal, thermo-oxidative and moisture-induced degradation at elevated temperatures and degradation rates increase with increasing temperature (Cella, 1996; Stolov et al., 2008). The SEM micrographs show large differences for fibres heated in ambient air and argon atmosphere (Figure 2.2). Fibres heated in argon atmosphere show less signs of degradation as the fibre samples heated in ambient air. Thermooxidative and moisture induced degradation are unlikely to occur due to the low oxygen and moisture content within the flushed

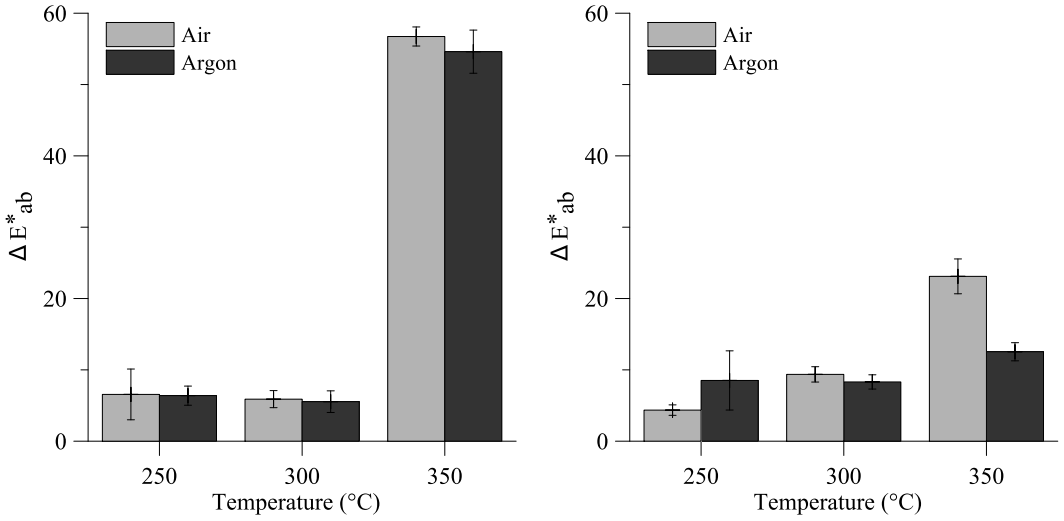

(a) PI. (b) HPI.

Figure 2.3.: Coating colour change ΔE^*_{ab} for the PI and HPI fibre. Non heated fibre samples have been used as reference.

tubes. Therefore, thermal degradation and curing reactions remain as the most relevant degradation mechanisms.

Morphological and colour changes were observed to increase with temperature for all samples. This is in good agreement with increasing degradation rates at elevated temperatures (Cella, 1996; Stolov et al., 2008).

Heated in argon atmosphere, the HPI fibre shows fewer and smaller depressions on the surface after the 350 °C period. Differences in the chemical composition and thickness of the polyimide material might cause this phenomenon. Depressions, however, were not evenly distributed. Either a larger volume would need to be analyzed or thermogravimetric measurements would need to be done in order to quantify differences in the volume change and differences in weight due to heating.

2.1.3.2. Colour Changes

Observing colour changes is a quick and inexpensive means to approximate the state of degradation of the polyimide coating material. For fibres heated at temperatures up to 300 °C, an irreversible increase in attenuation levels has not been observed (Reinsch, 2008) and colour changes remain below $\Delta E^*_{ab} \approx 10$ (Figure 2.3). For fibre samples heated at temperatures up to 350 °C, colour changes of $\Delta E^*_{ab} > 10$ have been observed. Attenuation measurements for PI fibres heated up to 375°C for a much shorter period of time, show an irreversible increase in loss characteristics (Reinsch, 2008). The increase of ΔE^*_{ab} seems to correlate with the transition of reversible to irreversible attenuation changes. A more detailed analysis including

simultaneous measurements of additional loss and colour changes would need to be done to define appropriate threshold values for every fibre.

The additional carbon layer of the HPI fibre adds difficulty to this simple approach. For the PI fibre, the colour of the fibre is only determined by the colour of the polyimide material. For the HPI fibre, the colour appears darker due to the underlying black carbon layer. As stated earlier, the polyimide layer degrades at elevated temperature. Eventually, it exposes the underlying cladding in the case of the PI fibre or the underlying carbon coating for the HPI fibre. If it comes into contact with air at elevated temperatures, the carbon coating degrades as well. Loss of the black carbon coating significantly increases calculated colour changes for the HPI fibre. Since only areas of the samples, where the polyimide coating covers the fibre, have been considered, this effect should be negligible.

2.1.4. Conclusions

For high temperature applications, the selection of a proper fibre is essential for a successful and long-lasting installation of the sensing cable. Therefore, different fibres have been tested in order to select a suitable fibre for the deployment in the harsh environment of a geothermal well.

One of the limitations for measuring temperatures over distances of several kilometres is the optical budget of the surface readout unit. For most units available today, this budget is about $20 - 25$ dB. For fibres having high attenuation values, the optical budget limits the deployable length. Attenuation values higher than a few dB/km are not tolerated for wellbore applications with sensor lengths of several kilometres. Due to the high attenuation values at low temperatures, the tested metal coated fibres cannot be used for DTS in wellbore applications. Thus, polyimide fibres have been chosen despite their limited operating temperature range in comparison with metal coated fibres. To test the performance of a carbon coated fibre that reduces the hydrogen ingression within the hostile environment of a geothermal well, tests with a HPI and a reference PI fibre have been conducted. To keep attenuation at moderate levels, degradation of the coating material has to be minimised.

Further testing has been done in order to select an operating limit for the selected polyimide fibres. If a polyimide fibre is heated in an inert atmosphere, degradation of the coating material, especially thermooxidative and moisture induced degradation, can be greatly reduced. Although 350 °C is close to the glass transition temperature of polyimide, utilisation at these temperatures might be possible for an extended period of time. The HPI fibre, in particular, might be suitable for a deployment at temperatures close to 350 °C.

The results for ΔE^*_{ab} show that colour changes might be used to indicate irreversible attenuation changes at temperatures above 300 °C. An appropriate threshold value, however, would need to be determined for every fibre.

Based on these results, a wellbore cable has been designed, the HPI fibre has

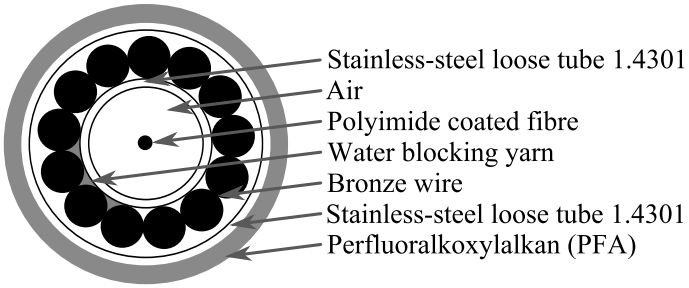

Figure 2.4.: Design of optical cable (courtesy of nkt cables GmbH, Cologne).

been incorporated and laboratory as well as measurements under in-situ conditions within a geothermal well in Iceland have been performed. Results of long term monitoring will be analysed with regard to reversible and irreversible attenuation changes. If the optical properties degrade such that loss characteristic do not allow for DTS measurements but the additional loss is reversible, DTS measurements will be possible as soon as the temperature rises, again. If the loss is irreversible, the fibre is lost for further DTS measurements.

2.2. Cable Tests

In order to meet the requirements for a permanent installation in Iceland, a novel fibre optic cable (Figure 2.4) has been engineered, manufactured and tested prior to the installation.

The wellbore cable was developed in collaboration with nkt cables GmbH. The outer diameter (OD) of the cable is 5.0 $\pm$ 0.2 mm. The sensing fibre is embedded in a stainless steel (material 1.4301) loose tube with an outer diameter of 1.8 mm. The armour is made of bronze wire. Water blocking yarn is used to reduce fluid migration along the cable. A second stainless steel loose tube (OD 3.5 mm) protects the armour. The cable is jacketed with a 0.75 mm layer of Perfluoralkoxylalkan (PFA).

During the production of hot fluid, subsurface installations within the well expand thermally. Thermal expansion of the casing and therefore an increase of the OD has the same effect as pressurising the casing and can lead to tensile and radial cracks in the cement (e.g. Goodwin and Crook, 1992; Thiercelin et al., 1998). Beside the expansion of the casing, the pore pressure within the cement increases as well. Following experiments made with Class G cement paste, the pore pressure increase due to the increase in temperature can be as high as 0.6 MPa/°C (Ghabezloo et al., 2009). Thus, for a temperature increase experienced under flow testing conditions, pore pressures can exceed several 10s of MPa. Therefore, the mechanical stress onto the cable is considerable, especially at locations where cracks evolve. In order

to reduce the mechanical coupling between the cement and the metal tubes and thus to increase the probability of a successful installation, a layer of PFA has been extruded onto the cable. Furthermore, increased corrosion of the cable at elevated temperatures should be reduced as the PFA acts as a sealing component.

2.2.1. Experimental Set-Up

Prior to a field test, the cable has been tested under laboratory conditions at the Helmholtz Centre Potsdam GFZ German Research Centre for Geosciences. In order to test the feasibility of flushing the cable continuously with argon during a field trial in Iceland, several heating experiments have been performed (Figure 2.5). The cable has been coiled on a drum made of cast iron. This drum has been placed within an oven with forced air circulation (UFE 600, Memmert), capable of operating at temperatures up to 300 °C. In order to monitor the temperature within the cable drum and at different points around the cable, four platinum resistance thermometers have been used. Three PT-100 and one PT-25 reference temperature gauges have been deployed.

In order to measure the temperature along the cable, a DTS-800 from Sensa has been connected to the sensing fibre in a double ended configuration. The inner tube of the cable has been connected to an argon gas cylinder for flushing the cable. A pressure tight in- and outlet for the optical fibres has been used for simultaneous flushing and temperature logging.

The cable has been heated in different steps until a maximum temperature of 280 °C. During the test, the cable has been flushed periodically with 50 ml/min Argon 5.0. The flushing has been turned off at times of increasing temperature. After a few hours at elevated temperature, the flushing has been turned on again. The flushed gas has been sampled at the beginning and at different times during the flushing period. The samples have been analysed using gas chromatography mass spectroscopy (GCMS) for H_2 and carbohydrates. From time to time, data has been acquired using a handheld Draeger MiniWarnB gas meter to detect H_2.

2.2.2. Results

Figure 2.6(a) shows the evolution of hydrogen generation within the cable at different times and temperatures. H_2 concentrations increased roughly exponentially with increasing temperature, but could be reduced by flushing the cable with argon. Carbohydrates were not detected within the samples.

An optical spectrum was measured before and after the temperature test (Figure 2.6(b)). The absorption measured within the cable has been compared to values published for hydrogen absorption in fused silica by Humbach et al. (1996). An increase in attenuation can be clearly detected around 1270 and 1370 nm. Another

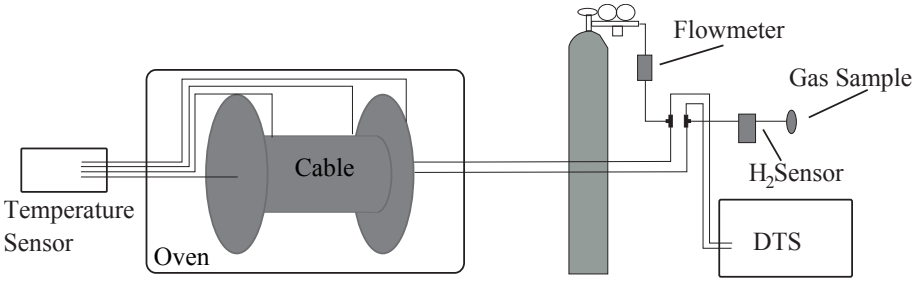

(a) Set Up.

(b) Picture showing the cable within the oven (Picture: Harald Frater/GFZ).

Figure 2.5.: Experimental set up for the cable tests.

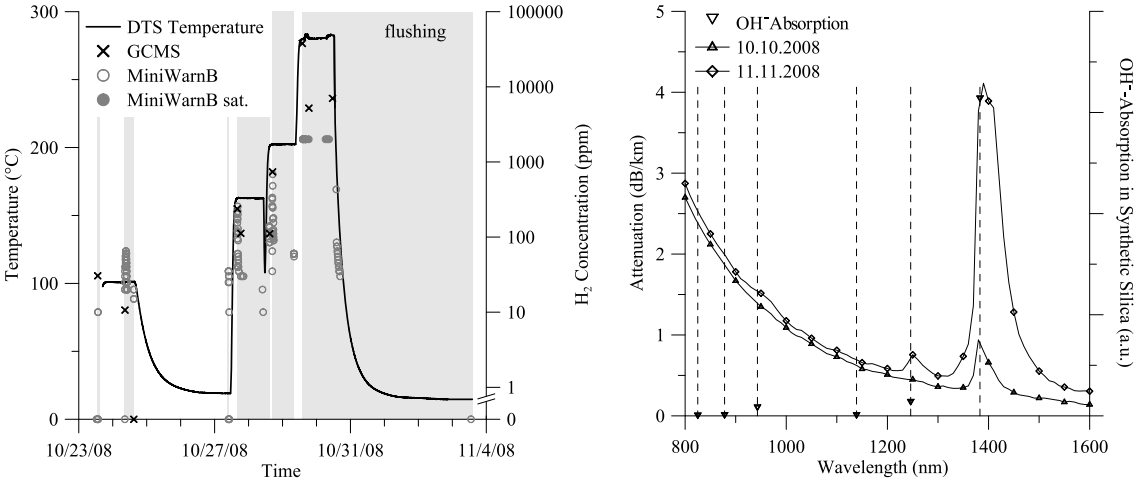

(a) Results from flushing experiment. (b) Optical spectrum.

Figure 2.6.: (a) Results from flushing experiments. Measured DTS temperature is displayed by the solid line, whereas times of flushing are indicated by the grey shaded area. Gas concentrations measured by the GCMS at different times are shown with crosses. Concentration measured using the hand-held gas meter are indicated by open circles. Note that the max. detectable concentration for the hand-held gas meter is 2000 ppm. Values above this limit are indicated by solid circles (MiniWarnB sat.). (b) Optical spectrum from before and after the laboratory tests (courtesy of nkt cables GmbH). Absorption peaks from Humbach et al. (1996)

peak evolved around 950 nm.

At the termination of the cable, between the two stainless steel loose tubes, a blueish oil was visible at the end of the high temperature period.

2.2.3. Discussions

It is known that oil from the manufacturing process can lead to an increased hydrogen load of optical fibres deployed in wellbore applications (Williams et al., 2000). Within the novel wellbore cable, oil from the manufacturing process was left and probably migrated along the bronze wires. The flash point for the oil used in the manufacturing process of this cable is at 175 °C (personal communication: Olaf Geckeis, nkt cables GmbH). At high temperatures ($\geq$ 200 °C), oil has been cracked and hydrogen was produced, increasing the attenuation at 1270 and 1370 nm. The hydrogen could penetrate the inner stainless steel loose tube and diffuse into the silica core. Flushing the cable with argon could significantly reduce the hydrogen concentration within the cable. Although the cable has been identified as a source of hydrogen at high temperatures, it has been approved for installation in Iceland.

Temperatures were expected to be ≤ 200 °C during the flow test in HE-53. Flushing the cable with argon was supposed to prevent the optical degradation of the fibre.

2.2.4. Conclusions

The novel fibre optic cable has been tested under high temperature conditions within the laboratory. Although a significant hydrogen production was detected at temperatures even below 200 °C, flushing the cable with argon could reduce the hydrogen concentration (patented technology Geckeis et al., 2011). Expected temperatures within the well selected for deployment were around 200 °C. Therefore, flushing the cable was assumed to ensure a long lifetime of the fibre optic cable.

For future cables, however, it is recommended to clean the cable from remaining oil. Another means to reduce the hydrogen production within the fibre optic cable would be the substitution of the used oil with an oil rated for higher temperatures.

3. Fibre Optic Field Experiments

3.1. Installation of DTS Sensor cable

After selecting a fibre for deployment and testing the novel manufactured fibre optic cable, it has been installed behind casing within the geothermal well HE-53 in the Hellisheiði geothermal field, SW Iceland. This chapter describes the installation as well as the results from the three logging campaigns during cementation, flow testing and shut-in of the well.

3.1.1. Concept

In Iceland, the casing profile of high-temperature geothermal wells is standardized following the standard American Petroleum Institute (API) oilfield tubular diameters (Thorhallsson, 2008). A typical casing profile for high-temperature wells, which is used in the Hellisheiði geothermal field as well, is shown in Figure 3.1(a). For well HE-53, a slim hole casing diameter has been chosen (Table 3.1). Here, the surface casing runs down to 61.3 m, the anchor/safety casing goes down to 299 m, a production casing down to 959 m and a perforated liner down to a depth of about 2463.3 m[1,2]. The kick-off for the deviation is in about 443 m depth.

For the installation of the anchor casing, conventional rigid blade centralizers are used (Econ-o-glider™, Downhole Products Ltd., *OD* 17"). A centralizer is installed underneath every joint below the surface casing and underneath every second joint within the surface casing. A table showing the exact depth of the joints and centralizers together with pictures of the installation can be found in Appendix C.

In order to increase the lifetime of the cable and the accuracy of the measurements, an installation in a loop configuration with a 180° separation between both cable branches around the perimeter of the casing was chosen. The loop configuration was designed to allow for a continuous flushing of the cable with argon as well as performing DTS temperature measurements from both ends of the fibre. DTS measurements in a double ended configuration can reduce the detrimental effects of fibre alteration like the ingression of hydrogen or the degradation of the coating material on the measured temperatures. From Chapter 2 it is known that heating the fibre in inert atmosphere instead of air is capable of reducing the degradation

[1] All depth are given in meter below surface.

[2] According to the Icelandic nomenclature, the first two casing strings are referred to as *surface* and *anchor/safety* casing, respectively.

Table 3.1.: Diameter of drill bit and casing as well as depth information for well HE-53 (Icelandic nomenclature and drillers depth; courtesy of Reykjavik Energy).

Casing	Slim Diameter Bit Size (in)	Casing *OD* (in)	HE-53 Depth m	Drilling Depth m
Surface Casing	21	18 5/8	61.3	62.8
Anchor Casing	17 1/2	13 3/8	299	302.8
Production Casing	12 1/4	9 5/8	959	959.1
Perforated Liner	8 1/2	7	2463.3	2500.6

of the coating. Furthermore, it has been observed that flushing the cable could significantly contribute to a reduction of harmful chemical species (e.g. hydrogen) along the cable and therefore increase the lifetime of the installation.

The separation of the cable was meant to increase the probability for a successful measurement of a temperature profile down to the total depth of installation. Damaging one branch of the cable, the possibility for an undamaged second branch is still given. DTS temperature measurements in single ended configuration would still be possible.

For the turnaround at the very bottom of the cable installation, two of the centralizers' rigid blades have been carved and additional aluminium profiles were attached to fix the cable (Figure 3.1(b)). In order to protect the cable during installation of the casing, a second centralizer was mounted to the casing below the modified one with an offset of 30°.

The cable is attached to the centralizers, using button head ties. In between the joints, tape and ties are used to attach the cable close to the casing. On the joints, the cable is attached with tape, again. Thus, the distance between anchor casing and cable varies along the well between zero and approx. three centimetres (Figure 3.1(c)). The depth of the different data points, together with the distance between casing and cable, averaged over a section of one meter is listed in Appendix D.

3.1.2. Field Work

During the installation, the cable was cut two times, leaving one end accessible down to 179.5 m (western side of the well) and the second down to the turnaround at 261.3 m (eastern side of the well). Furthermore, a damage of the fibre at the eastern side was detected in a depth of about 235 m (Figure 3.2). For the accessible parts of the cable, similar attenuation values were measured before and after the installation.

Having the cable cut, flushing it with argon could not be performed. Potential harmful chemical species could not be removed from the cable. With only one end of

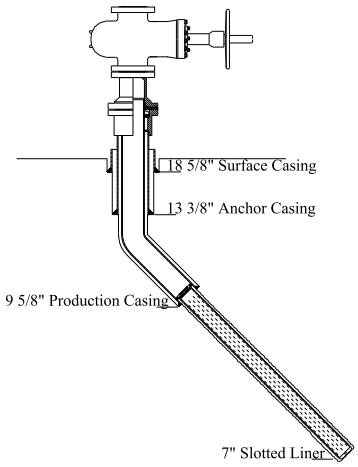

(a) Casing Profile.

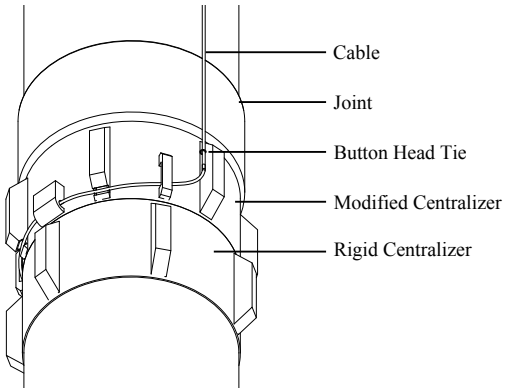

(b) Cable Turnaround.

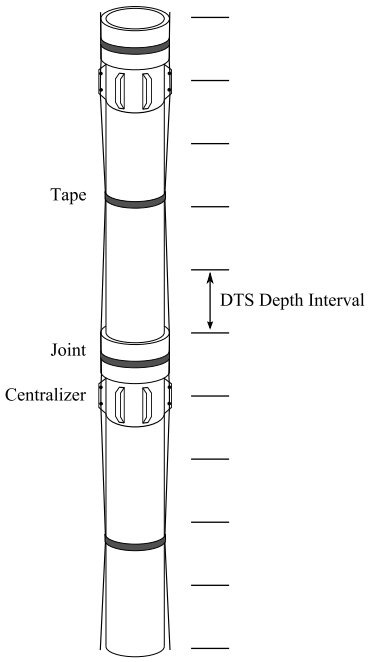

(c) Cable Installation.

Figure 3.1.: (a) Casing profile for Icelandic high temperature wells (modified after Thorhallsson, 2003, Icelandic nomenclature) and (b) schematic sketch of the turnaround below the first casing joint above the float collar. (c) Sketch showing the position of the cable behind casing. DTS temperatures are averaged over a 1 m interval, which is indicated as well (not to scale).

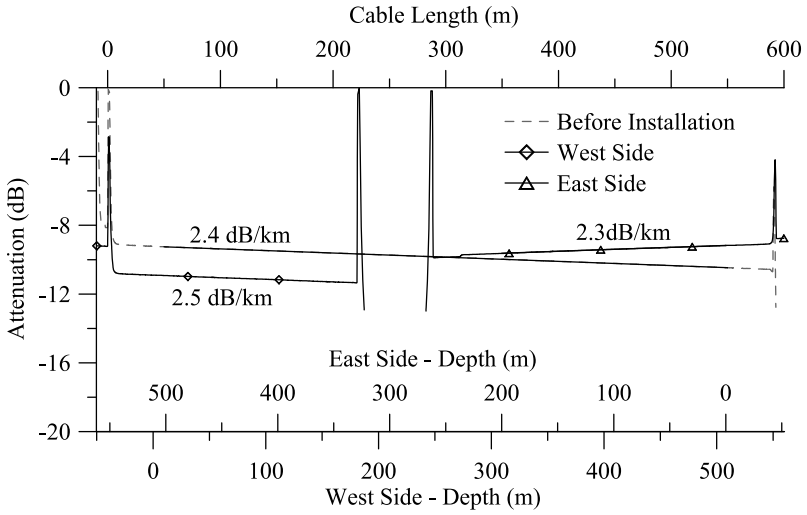

Figure 3.2.: Attenuation measurements at 850 nm from before the installation and after the cementation of the casing. The length scale corresponds to the cable length. Attenuation values are given for the cable.

the fibre at the surface, the state of the cable for each branch can only be monitored using optical reflectometry techniques.

3.1.3. Discussions

During installation the cable was damaged at several positions limiting its utilization. The following points were identified as possible reasons for the damaging of the cable during installation:

1. **Lithology:** The well is drilled in very young, brittle and unconsolidated rock formations. Rock fragments might have been carried along with the casing during installation which could have damaged the cable in narrow borehole sections.

2. **Borehole breakouts:** Large borehole breakouts occurred within the penetrated rock formations. The cable might have been damaged due to a possible loss of centralization of the casing within these breakout sections.

3. **Movement of centralizers:** After the bottom of the borehole had been touched, the casing was lifted about 5 m to reach its final position. This might have led to a differential movement between casing and centralizers to which the cable is attached to.

Table 3.2.: Chronicle of different activities at HE-53. The duration of DTS measurements is listed as well.

Activity	Date	Duration (h)
Begin Drilling	April 2009	
Installation Anchor Casing	May 2009	43
Installation Production Casing	May 2009	
Installation Perforated Liner	June 2009	
Finish Drilling	June 2009	
Begin Flow Test	July 2009	356
Begin Cooling the Wellhead	November 2009	
Detect Casing Damage	November 2009	
Emergency Cementation	November 2009	
Workover Activities	August 2010	24

In order to better protect the turnaround of the cable during the installation, a more protective modification of the bottom centralizer has to be developed. Furthermore, pulling back of the casing should be avoided if the casing is carrying instrumentation. Increasing the number of wiper trips prior to the installation of an instrumented casing might be a further possible measure to reduce the number of rock fragments in unconsolidated and brittle formations similar to those occurring in Iceland.

Similar permanent installations of fibre optic cables behind casing have been successfully performed at other sites, e.g. in sedimentary successions at Mallik, Canada (Henninges et al., 2005) and Ketzin, Germany (Prevedel et al., 2008), or in oils wells in China (Zhou et al., 2010). Although the length of the installation exceeded the one in Iceland by a factor of 3-4 and the clearance between casing and formation was even smaller at these sites, the cables have been installed without any or only minor damages. Compared to these installations, the brittle nature of the rock formations seems to be a reasonable explanation for the damages encountered during the installation described herein.

During flow testing and hence warming of the well, further damages were detected. These are attributed to the thermal expansion of the casing.

3.2. Fibre Optic Measurements

Three successive field campaigns have been performed. First, data has been acquired directly after the installation of the sensor cable during the cementation of the anchor casing in May 2009. A second field campaign has been performed during the onset of a flow test in July/August 2009. In order to evaluate the performance of the fibre optic cable after the flow test, a third campaign has been performed in August 2010 after a 8.5 month shut-in period (Table 3.2).

For the three field campaigns, a similar experimental set-up was used (Figure

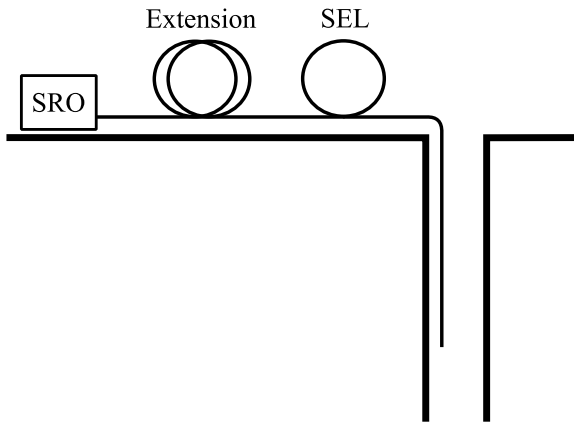

Figure 3.3.: Schematic experimental set-up for DTS and optical time domain reflectometry (OTDR) measurements.

3.3). A 100 m fibre optic extension was used to connect the surface readout unit (SRO) with the wellbore cable. At the surface, an excess length (SLE) of approx. 15 m of the wellbore cable was accessible to gather reference temperature information. For the distributed temperature measurements, a DTS 800 from Sensa has been used. Beside temperature measurements, optical time domain reflectometry (OTDR) measurements were performed to measure the optical attenuation at 850 and 1300 nm using a MTS5100 from Wavetek. The evolution of attenuation over time is used to evaluate the degradation of the optical fibre.

As mentioned previously, measured DTS temperature is strongly dependent on the attenuation ratio between the Stokes and the Anti-Stokes band. Wavelength dependent attenuation changes, skew measured temperatures. Attenuation measurements at standard telecommunication wavelengths (850 and 1300 nm) can be used to qualitatively monitor the optical properties of the fibre (Smithpeter et al., 1999) and help to identify different degradation processes and their resulting influence on measured temperatures in different sections along the fibre.

The reason for wavelength dependent attenuation changes are basically twofold. Either the fibre is stressed mechanically or chemically. Mechanical stress can lead to micro and macrobending loss. The dependency of attenuation on the wavelength, however, is dependent on the type of fibre as well as the stress applied to the fibre. Detailed discussions on bending loss characteristics can be found elsewhere (e.g. Marcuse, 1976; Walker, 1986; Buck, 2004; Lingle, Jr. et al., 2007). Chemical stress, like the ingression of chemical agents, e.g. hydrogen, into the fibre and eventual chemical reactions can lead to absorption losses at specific wavelengths. For hydrogen, the attenuation ratio Γ increases with increasing ingression into the fibre.

Figure 3.4.: Experimental Set-up during cementation of the anchor casing. The cable is feed through the BOP stack and the surface excess length is placed on the rig. The fibre optic extension is wrapped in a yellow plastic bag to keep it dry during the measurements.

3.2.1. First DTS Logging Campaign: Well Cementation

3.2.1.1. Experimental Set-Up and Measurement Schedule

In order to evaluate the performance of the cementation and to test the measurement equipment after the installation, first attenuation and temperature measurements have been performed during the cementation of the anchor casing for a duration of approximately 46 h. The integration time for the DTS measurements was 27 s.
Here, an approximately 20 m long SLE (western and eastern cable branch) was placed on the rig and exposed to ambient weather conditions (Figure 3.4). Reference temperature information was gathered from a nearby weather station to evaluate the absolute accuracy of the measurements. The distance to the weather station "Hellisheiði" is approx. 1.5 km to the north east. The elevation above the sea level is similar to the elevation of the well. In between weather station and well, a flat topography predominates.

3.2.1.2. Results

Temperature Measurements

Two plots showing the temperature evolution within the annulus during the cementation of the anchor casing are shown in Figure 3.5. Temperature within the annulus increases during the measurement. Periodic temperature variations can be seen with depth. The wavelength is approximately $5 - 6$ m. For the first 8 h_{DTS}[3],

[3]For the different logging campaigns, the beginning of the DTS logging is used as reference time; h_{DTS} indicates hours after beginning of DTS logging.

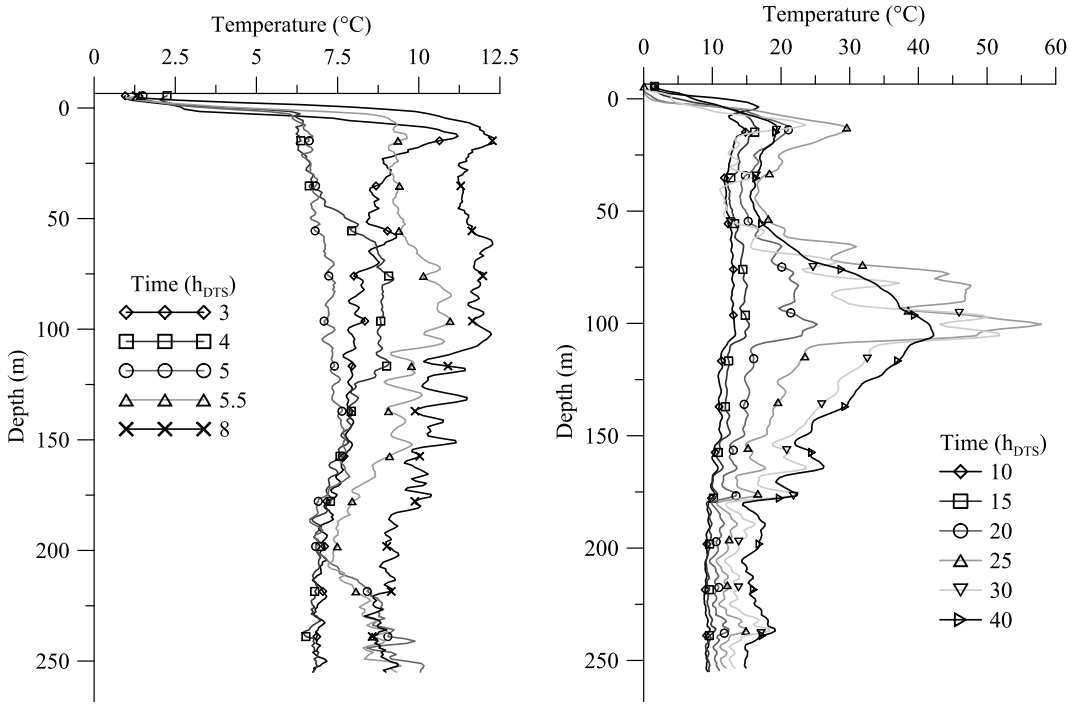

(a) Temperature profile during cement jobs. (b) Temperature profile during hydration.

Figure 3.5.: (a) Temperature profile during different cement jobs (3 m moving average) and (b) temperature profile during hydration of cement (3 m moving average).

the temperature varies by a few degrees Celsius. After 8 h_{DTS}, temperature increases rapidly by more than 40 °C. A strong temperature decrease and a smoothing of the temperature profile was observed between 30 and 40 h_{DTS} for the uppermost 107 m.

Attenuation Measurements

Attenuation measurements from before the installation and after cementation are shown in Figure 3.2. Before the installation, the attenuation profile was smooth, showing no signs of damages along the cable. During the installation, the cable was cut two times. A further damage could be detected on the longer branch on the eastern side (Section 3.1.2). Changes of the attenuation during the cementation itself were not detected.

Accuracy

In order to quantify the absolute accuracy of the DTS measurements during the cementation process, the DTS temperatures along the SLE of the eastern cable branch were measured and compared to ambient weather conditions (Figure 3.6).

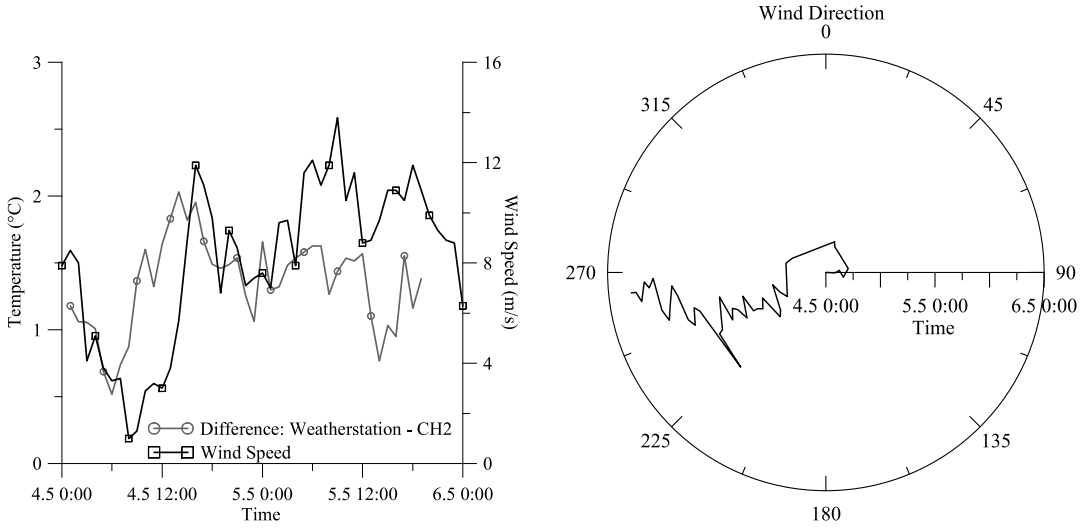

(a) Influence of wind speed.

(b) Wind direction.

Figure 3.6.: DTS temperature measurements in comparison to data measured by a nearby weather station. Wind blew from the weather station directly towards the well. Weather data courtesy of the Icelandic Meteorological Office, Station Hellisheiði (64°01.127', 21°20.543' (64.0188, 21.3424)).

On average, temperatures logged by the DTS were 1.3 °C lower than temperatures from the weather station with a standard deviation of 0.3 °C. Depending on the speed of the wind, which blew constantly roughly from the station in direction to the well, absolute differences range from 0.5 to 2.0 °C.

3.2.1.3. Discussions

Temperature Measurements

The annular temperature changes due to the exothermic hydration of the cement paste (see as well Chapter 7). The period of the observed temperature variations with depth resembles the length of individual casing pipes. The temperature variations along the profile, therefore, correspond to the location of the cable within the annulus. Higher temperatures correspond to locations where the cable is fully surrounded by cement, lower temperatures correspond to depth sections, where the cable is either attached to the colder casing or little cement is in place.

During the first eight hours, temperature variations are caused by the pumping of cement. Table 3.3 lists the different steps of cementing the anchor casing in HE-53. The slurry temperature was slightly higher than the well temperature after the drilling process. After pumping, the heat of hydration led to the rapid increase of temperatures along the well axis. The water table within the well was at 107 m

Table 3.3.: Cementing Report for well HE-53. First the casing was cemented through the string. Then, cement was pumped through the kill line. Mica and polypropylene fibres were used as additives. The time refers to hours after beginning of continuous temperature logging.

Cement Job	Volume m^3	Density kg/m^3	Time h_{DTS}	Remarks	Additives
1	12.7	1670	4.68	string	250 kg mica
2	16.9	1690	5.03	kill line	250 kg mica, 13.6 kg pp-fibres
3	11.1	1720	6.92	kill line	200 kg mica
4	4.0	1730	7.25	kill line	
5	1.0	1730	7.65	kill line	
6	1.0	1730	8.07	kill line	
7	0.8	1730	8.58	kill line	
8	0.6	1730	8.92	kill line	
9	0.9	1740	9.87	kill line	
10	0.5	1740	10.42	kill line	
11	0.3	1740	11.58	kill line	

after the cement string was removed. Temperatures above, increased to much higher values than below due to the difference in density and specific heat capacity between fluid and air filling the well. Before cement bond logging (CBL) at about 29.5 h_{DTS}, the well was filled with cold water leading to a decrease in temperature in the upper part of the well.

Attenuation

During the installation, the cable was cut. A mechanical damage was observed on the eastern cable branch. As only single ended measurements could be performed, absolute temperature readings from below the damage are skewed, as bending loss can be wavelength dependent. Therefore, reliable temperature information was recovered down to 179.6 m on the western branch and 235 m on the eastern branch. The damage appears to be quite small. An influence on the measured DTS temperature has not been observed during the first hours of logging (before cementing, Figure 3.5(a)), when the temperature profile was almost isothermal at low temperature. For large temperature changes, the effect of differential attenuation becomes more important (see Section 3.2.2). The temperature decrease in Figure 3.5(b) at around 235 m can be either caused by the damage on the cable and or it can be a real temperature step. The damage becomes more important for the large temperature differences during the production of hot fluid.

Accuracy

Although, relative temperature readings are quite accurate, the absolute accuracy is difficult to determine due to the absence of a reference temperature point along the cable. For double ended measurements, the absolute accuracy has been determined

during the calibration procedure to be about 0.5 °C (Appendix I). For single ended measurements, however, this value decreases, as differential attenuation changes between the Stokes and Anti-Stokes signal cannot be compensated for. To validate the absolute temperature accuracy, temperature data from the SLE has been compared to temperature data from the "Hellisheiði" weather station. Absolute temperature differences can mainly be influenced by different factors:

1. Erroneous temperature readings of the DTS system.
2. Erroneous temperature readings of the weather station.
3. Microclimatic temperature differences caused by the rig itself or the topography between the weather station and the well.

The first aspect seems to be the most important factor for the constant temperature offset, as only single ended measurements could be performed. Small variations are caused by microclimatic temperature changes due to the heat produced by the rig itself. Smaller temperature differences at lower wind speeds, i.e. higher temperatures measured at the SLE, correspond to a longer residence time of the wind above the rig, before it reached the SLE.

The relative accuracy of the DTS 800 expected for this measurement has been determined to be about $\Delta T_{relative} = 0.1$ °C for an integration time of 10 min in double ended configuration (Henninges, 2005) for a fibre of 2908 m length.

3.2.2. Second DTS Logging Campaign: Flow Test

3.2.2.1. Experimental Set-Up and Measurement Schedule

During the second field campaign, temperature measurements were performed for a period of approx. 356 h. Prior to the start of the flow test, baseline temperature data were acquired for a duration of 20 h. The surface excess length of the cable (SLE) was placed within an ice bath and a constant offset correction was applied to the measured temperatures using the data acquired within this bath. For the western branch, the SLE had a length of 16 m, for the eastern cable branch of 15 m. The integration time was initially 18 s per temperature profile, but has been changed to 104 s at the 2.8.2009. Two times a day, additional OTDR measurements were performed to evaluate the degradation of the optical fibre at high temperature conditions during the flow test.

3.2.2.2. Results

Temperature Measurements

For the flow testing period, temperature plots for different times are shown in Figure 3.7. A detailed list of different activities prior, during and after the flow test can be

Table 3.4.: Chronicle of different activities at HE-53 in summer 2009. The time of different activites with reference to the DTS logging time is listed.

Activity	Date	Time (GMT)	Time (CET)	Time (h_{DTS})
Begin DTS measurement	28.07.09	14:52	16:52	0.00
Pressure release for logging	29.07.09	10:37	12:37	19.75
Pressure release for logging ended	29.07.09	11:08	13:08	20.27
Begin bleeding	29.07.09	16:52	18:52	26.00
Open valve to silencer (⌀25 mm nozzle)	30.07.09	13:43	15:43	46.85
Close valve to silencer (⌀25 mm nozzle)	30.07.09	13:50	15:50	46.97
Change nozzle (⌀100 mm nozzle)	30.07.09	13:52	15:52	47.00
Open valve to silencer (⌀100 mm nozzle)	30.07.09	15:04	17:04	48.20
End DTS measurement	12.08.09	11:15	13:15	356.38

found in Table 3.4.

Prior to production testing well HE-53, baseline temperature measurements were performed ($0 - 20$ h_{DTS}). The temperature was homogeneous at about 10 °C along the cable, except for two variations in $0 - 37$ m and $39 - 78$ m, where measured temperatures were considerably higher by $10 - 15$ °C (Figure 3.7(a)). After 20 h of logging, the well was opened for bleeding; i.e. gas at top of the well column was released. During the first 6 h of bleeding, temperatures below approx. 235 m rose by about 10 °C. The temperature profile above did not change. After 26 h_{DTS}, a subsequent temperature increase was observed in adjacent depth intervals. Starting at the bottom of the installation, the temperature increase continued to migrate upwards. Temperatures below 40 m increased whereas they decreased above. Initially high temperatures of 25 °C in 15 m depth, for example, decreased by 8 °C. The temperature increase below 40 m slowed down after $30 - 32$ h_{DTS} and the temperature profile stabilized. Measured temperature within the annulus decreased slightly, before a rapid increase after 46 h_{DTS}, when the well was opened for production (Figure 3.7(b)). A temperature increase was observed for the entire time DTS measurements were performed. Shortly after the rapid temperature increase, the DTS signal was lost below 235 m.

The overall temperature signal exhibits similar periodic temperature changes with depth (Figure 3.9) as observed during the cementation (Section 3.2.1). Furthermore, strong negative temperature excursions were measured in about 175 m and 235 m. Maximum temperatures measured within the annulus at the end of the measurement campaign reached 229.98 °C at 162.87 m (Figure 3.8).

During the flow testing time, OTDR attenuation measurements were performed two times a day. Plugging and unplugging of the connectors between the different surface readout units had an influence on the measured DTS temperatures (Figure

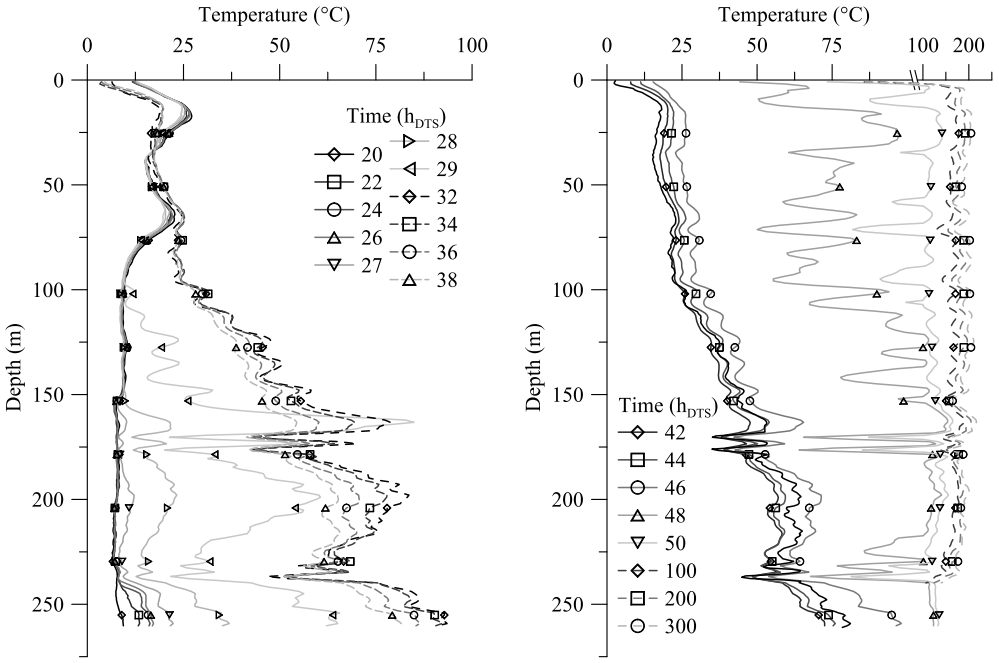

(a) Temperature profile during bleeding. (b) Temperature profile during flow test.

Figure 3.7.: (a) Temperature profile during bleeding (3 m moving average). The static formation temperature profile is displayed at 20 h_{DTS} of measurement. (b) Temperature profile during the onset of the flow test (3 m moving average).

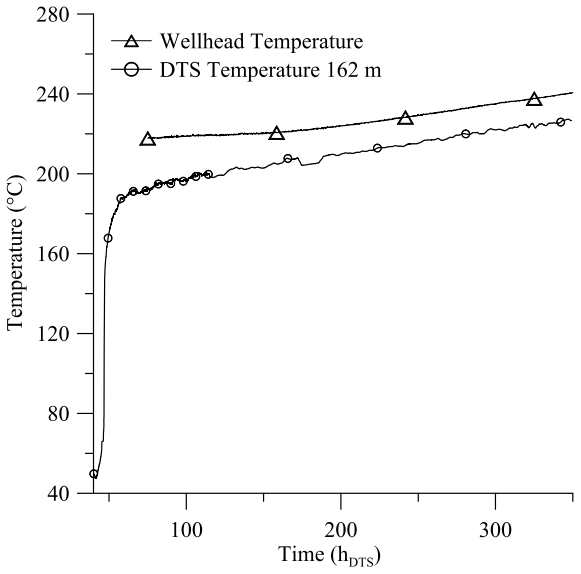

Figure 3.8.: Comparison of wellhead temperature evolution and DTS temperature readings during a flow test in HE-53 in 2009. Temperatures at the wellhead are calculated according to the boiling point pressure for pure water. DTS temperature readings from a depth of 162.87 m below ground surface are displayed. Wellhead pressure courtesy of Reykjavik Energy.

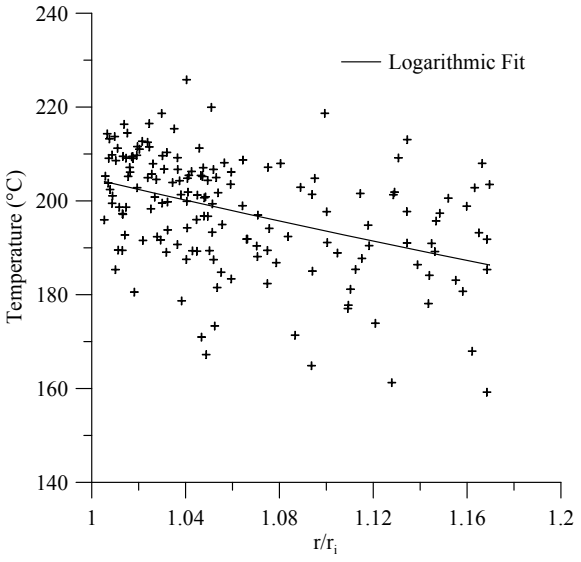

Figure 3.9.: Temperature versus cable-casing distance during the flow test at 350 h_{DTS}. The distance is plotted as ratio between radius to the cable and inner radius of the cement, i.e. the anchor casing-cement interface.

3.8, e.g. at time 173.5 h_{DTS}). A list of all OTDR measurements can be found in Appendix E.

After the well was opened for production (⌀25 mm nozzle), temperature rose quickly due to the massive production of hot water. Local temperature variations correspond to the varying casing-cable distance. After 300 h of production, the temperature could be fitted with using a logarithmic function to the ratio $r_{DTS}/r_{csg,a}^{OD}$:

$$T(r_{DTS}) = -117.63 \ \ln \frac{r_{DTS}}{r_{csg,a}^{OD}} + 204.76 \tag{3.1}$$

where $T(r_{DTS})$ is the DTS temperature at the cable position r_{DTS} and $r_{csg,a}^{OD}$ is the radius to the anchor casing-cement interface. The coefficient of determination for the logarithmic fit is $R^2 = 0.18$. The measurements were stopped after two weeks of continuous logging.

After the end of the fibre optic logging campaign, flow testing continued until end of November 2009. Figure 3.8 shows the calculated evolution of the wellhead temperature in comparison to the measured DTS temperature. Wellhead pressure was continuously measured during the production period. As a two phase fluid is produced from the well, the wellhead temperature has been calculated according to the boiling point curve of pure water (Lemmon et al., 2007). The wellbore fluid salinity in the Hellisheiði geothermal field is below 1500 ppm Franzson et al. (2005). Calculated temperatures are therefore slightly lower than actual values (after Driesner and Heinrich, 2007). The difference, however, is small and is neglected in the following.

Attenuation Measurements

During the heating of the well, changing attenuation ratio values were detected in different sections along the fibre.

1. **Region 1** $(0 - 170$ m): The attenuation ratio has been averaged over 80 m with a central depth of 100 m. No changes of the attenuation ratio could be detected. The absolute attenuation at 850 nm remained similar from 2.3 dB/km (0-150 m) after the installation to 2.4 dB/km (0-150 m) at the beginning of the flow test but increased to 2.8 dB/km (0-150 m) at the end of the second logging campaign.

2. **Region 2** $(170 - 180$ m): The attenuation ratio has been averaged over 15 m with a central depth of 176 m. The attenuation ratio changes significantly in the course of the experiment. It increases with increasing temperature.

3. **Region 3** $(180 - 230$ m): The attenuation ratio has been averaged over 25 m with a central depth of 200 m. A small linear increase of the attenuation ratio was detected over time. The attenuation at 850 nm increased up to 4.2 dB/km (190-220 m) for this region.

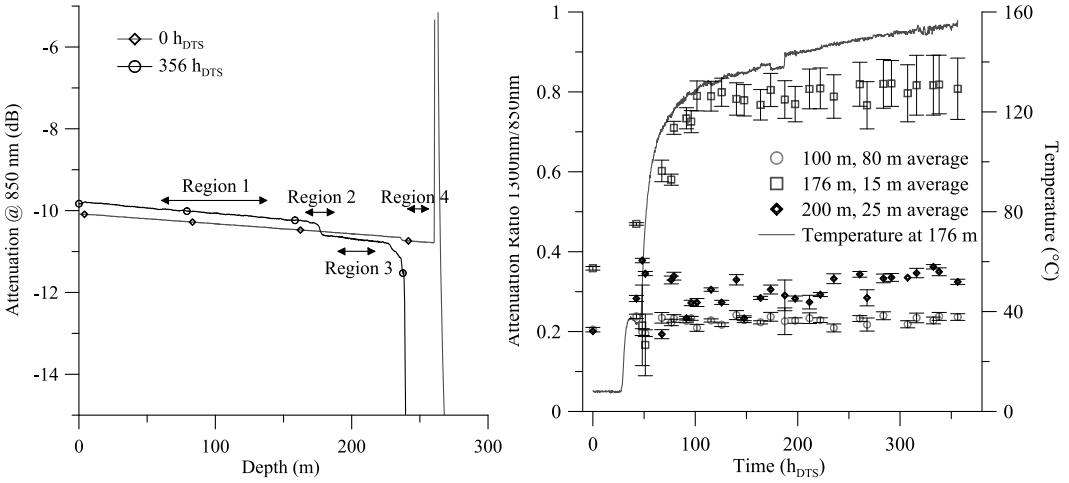

(a) Attenuation profiles. (b) Attenuation ratios.

Figure 3.10.: Attenuation profiles (a) at 850 nm for the beginning and the end of the second measurement campaign. Different regions along the fibre are indicated (see text for details). (b) Attenuation ratios calculated for different depths over time. The temperature trace was measured in 176 m depth.

4. **Region 4** (230 − 270 m): After heating of the well, no data could be collected below approx. 230 m.

Accuracy

In order to correct for any effects which might alter the DTS temperature measurements, like bad connectors or small bendings of the fibre, 15 m of the fibre optic cable have been placed within an ice bath outside the well. All temperature data have been corrected for an offset measured in the ice bath with a constant temperature of 0 °C (Figure 3.11).

A possibility to access information about the accuracy is the temperature evolution at the wellhead compared to the temperature evolution in a hot section of the cable (Figure 3.8). For the later period of logging ($200 - 340$ h_{DTS}), the wellhead temperature as well as the cable temperature have been linearly fitted. The temperature increase for the wellhead temperature was 0.1120 ± 0.0001 K/h, whereas for the cable it was slightly different 0.1179 ± 0.0004 K/h. For a flow testing period of 300 h, this results in a temperature difference of ΔT_{slope} =1.77 K.

At high temperatures, bad connectors have a significant influence on the measured temperature due to an increase in differential attenuation of the backscattered signal. After correcting for the temperature loss in the ice bath, an influence on the temperature of up to $\Delta T_{connector}$ =4.6 K has been detected in Figure 3.8 at 173.3 h_{DTS}

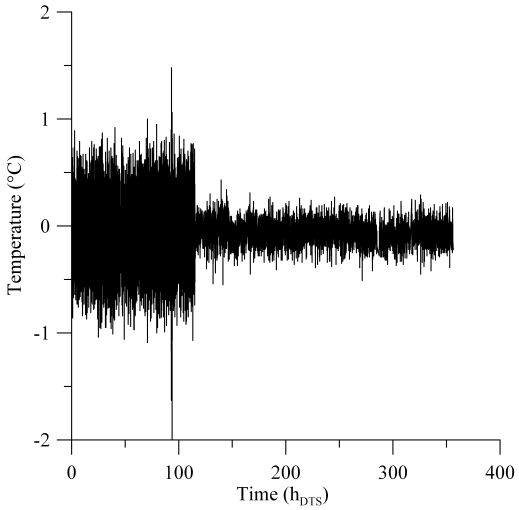

Figure 3.11.: DTS point 170 within ice bath after offset correction. Note with increasing the integration time from 17 s to 1 : 43 min at the 2.8.2009, the temperature scattering was reduced.

for a bad SLE. Changing the SLE could significantly reduce the error at 187 h_{DTS}. At other times (e.g. 163 h_{DTS} or 198 h_{DTS}) the error introduced by plugging and unplugging resulted in a temperature change lower than $\Delta T_{connector}$ =2.0 K.

3.2.2.3. Discussions

Temperature Measurements
The measured annular temperature depends on the wellbore conditions, i.e. static temperature, bleeding or flow testing conditions. Furthermore, the measured temperature is dependent on the cable-casing distance as well as the cement quality behind the different casings. From the CBL of the production casing it is known (see Chapter 5), that the cement bonding is homogeneous over the entire depth interval of DTS measurements. Therefore, effects of different cement qualities behind the production casing on the measured DTS temperatures is assumed to be negligible.

Static Temperature Conditions During static temperature conditions, temperatures within the annulus were constant except for the uppermost 78 m, where two separate temperature maxima could be observed. The upper positive temperature excursion has been observed between 0 and 37 m depth, and the lower between 39 and 78 m (Figure 3.7(a)). Here, the relatively high formation temperature of 28 °C might be related to the geothermal surface activity found in a distance of approx. 250 m to the SE (Saemundsson, 1995). Vapour might migrate along perme-

able layers, i.e. aquifers, within this depth ranges. Furthermore, these layers might have been previously heated during flow testing of the neighbouring well HE-36 and seeping of hot geothermal fluid into the ground.

Bleeding During bleeding of the well ($20 - 46\ \mathrm{h}_{DTS}$), gas pressure was released at the wellhead and the water table could rise to the surface. The ascent of fluid from below the cable led to an increase in measured temperatures within the first 10 h of bleeding. When the fluid table reached the wellhead ($32\ \mathrm{h}_{DTS}$), the rapid ascent of warmer fluid from deeper parts of the well was stopped as the released volume of fluid per unit time is smaller than the volume of gas released per unit time. The temperature slowly cooled down until the well was opened for flow testing after about $46\ \mathrm{h}_{DTS}$.

Flow Testing Due to the rapid ascent of hot fluid, the temperature within the well increased. The measured temperature within the annulus was strongly influenced by the distance between cable and casing (see Section 3.2.1). Little casing-cable distance resulted in higher temperatures, greater distance, lower temperatures. Overall, the temperature measured within the annulus is strongly influenced by the thermal properties of the cement in different depth intervals as well as the calliper of the well. Small calliper diameters and dilute cement within the annulus led to a lower DTS temperature, as heat could be transmitted to the formation more effectively.

Attenuation Measurements

From the attenuation measurements, different mechanisms of degradation could be assigned to different regions (Figure 3.10). Whereas only little changes were observed in Region 1, significant changes were observed for the other regions. The strong increase of the attenuation ratio with temperature during the onset of the flow test indicates mechanical stress onto the fibre (Region 2). Due to the thermal expansion of the subsurface installations, the cable and thus the fibre became either squeezed in a certain depth range or bending occurred in this depth. Due to a further increase in temperature during the flow test, the attenuation ratio continues to increase as well. Beside mechanical stress, an increased hydrogen load of the fibre might partly attribute to the change in the attenuation ratio Γ. Only chemical stress alone cannot account for the strong attenuation increase. If the temperature increase lead to an increase in the hydrogen load alone, this should have been observed in other depth intervals as well.

During the flow test, temperature rose quickly over the entire length of the cable. With increasing temperature, the intensity of elastically backscattered photons (Rayleigh scattering) increases, increasing the overall attenuation along the cable. The absolute attenuation at 850 nm remained at a similar value in Region 1 between the end of the first logging campaign (2.3 dB/km) and the beginning of the flow test (2.4 db/km). The increase with increasing temperatures at the end of

the second logging campaign (2.8 dB/km) can be partly attributed to an increased Rayleigh scattering intensity with increasing temperature. The relative temperature sensitivity of the Rayleigh signal is approximately $0.005 - 0.008$ %/°C (Grattan and Meggitt, 1995; Ikushima et al., 2000). For a temperature increase along the fibre of 200 °C, the relative increase in attenuation is $1 - 1.6$ %, whereas 16 % have been observed. On the one hand, this difference might be explained by the fact that the relative attenuation increase with temperature is just an approximate value. No reference measurements with this fibre type have been performed. On the other hand, the increased attenuation might be attributed to an increased degradation of the fibre. The latter explanation is more probable, as the difference between calculated and observed changes is in the order of one magnitude.

Region 3 shows a small, but gradual increase of the attenuation ratio. This indicates chemical changes of the transmission properties. Most probable, chemical changes occurred within the fibre. Although the exact mechanism of the degradation process cannot be determined with the available data alone, hydrogen ingression and the subsequent formation of hydroxyl within the fibre is a probable scenario. The increased degradation can be observed by the strong increase of the attenuation at 850 nm, as well.

Below Region 3, attenuation increases with depth until the cable was cut in 235 m. What led to the increased attenuation slightly above this depth cannot be determined from the available data.

Accuracy

During the flow test, only single ended DTS measurements could be performed. Temperatures were compensated for a constant offset, using the information from the SLE.

A gradual degradation of the temperature accuracy caused by a wavelength dependent attenuation change and an increased attenuation ratio $\Gamma = \frac{a^{1300}}{a^{850}}$ has not been observed (Figure 3.10), although the attenuation at 850 nm slightly changed in Region 1. Therefore, a degradation of the temperature accuracy based on a wavelength dependent attenuation change could not be detected ($\Delta T_{degradation}$ =0 K). The comparison between the slopes of the wellhead temperature and the cable temperature did not show a significant difference at the end of the logging period. For an increase in degradation, the slope of the DTS temperature should be changing to lower values over time, compared to the slope of the wellhead temperature, as an increased degradation results in a decrease in DTS temperatures.

The different slopes indicate a non-constant temperature difference between both measurements, which was expected as heat is constantly transferred to the formation (see as well Chapter 5). The absolute difference of 1.77 K over a period of 300 h is very small compared with the range of measured temperatures and the different location of the measurements. Neither an increase in degradation with temperature, nor an increased slope difference with increasing temperature could be determined,

due to the small difference in slope values. A degradation due to changes within the fibre itself is therefore not very likely for Region 1 during this measurement campaign. It has to be noted, that the wellhead temperature is not in the same depth as the DTS temperature used for this comparison. Temperature trends within the well might be slightly different than at the wellhead.

Bad connectors increase the differential attenuation and have an influence on the calculated temperatures. The error of a DTS temperature measurement, introduced by a bad connector, has been determined to be up to 2.0 K. For a bad SLE, the increased differential attenuation resulted in an error of 4.6 K.

Accounting for the different contributions (calibration, connector, relative accuracy, degradation) and neglecting the error introduced by a bad SLE, the absolute error within Region 1 has been determined to be $\Delta T_{DTS} = 2.6$ K according to:

$$\Delta T_{DTS} = \Delta T_{connector} + \Delta T_{calibration} + \Delta T_{relative} + \Delta T_{degradation} \tag{3.2}$$

In the low temperature range, measured temperatures are more accurate, as the influence of bad connectors is lower. The absolute deviation for the uppermost part of the fibre (i.e. close to the wellhead) is probably better than 1 °C, which can be validated with ice bath measurements (see Section 3.2.3)

3.2.3. Third DTS Logging Campaign: Shut-In

3.2.3.1. Experimental Set-Up and Measurement Schedule

During the flow test, a casing damage has been detected for the production casing in a depth of 310 m. In order to close this leakage zone, the well was shut-in and filled with cement in the end of November 2009. The top of cement within the well was measured to be in a depth of approx. 130 m. The complete flow test history is displayed in Figure 3.12.

Before the work-over activities in August 2010, another fibre optic logging campaign has been performed. This third field campaign took place after the well was flow tested for three months and a subsequent 8.5 months shut-in and thermal recovery period. Temperature measurements were performed for a few hours in order to assess the state of degradation of the fibre. The surface excess length of the cable (west and east: 16 m) was placed within an ice bath, again, and measured temperature data were corrected for a constant offset. The integration time was 103 s for each temperature profile.

Temperature measurements have been performed and compared to undisturbed temperature profiles from shortly before the flow test and to a conventional temperature log which was measured simultaneously in the neighbouring well HE-36 (horizontal distance approx. 10 m).

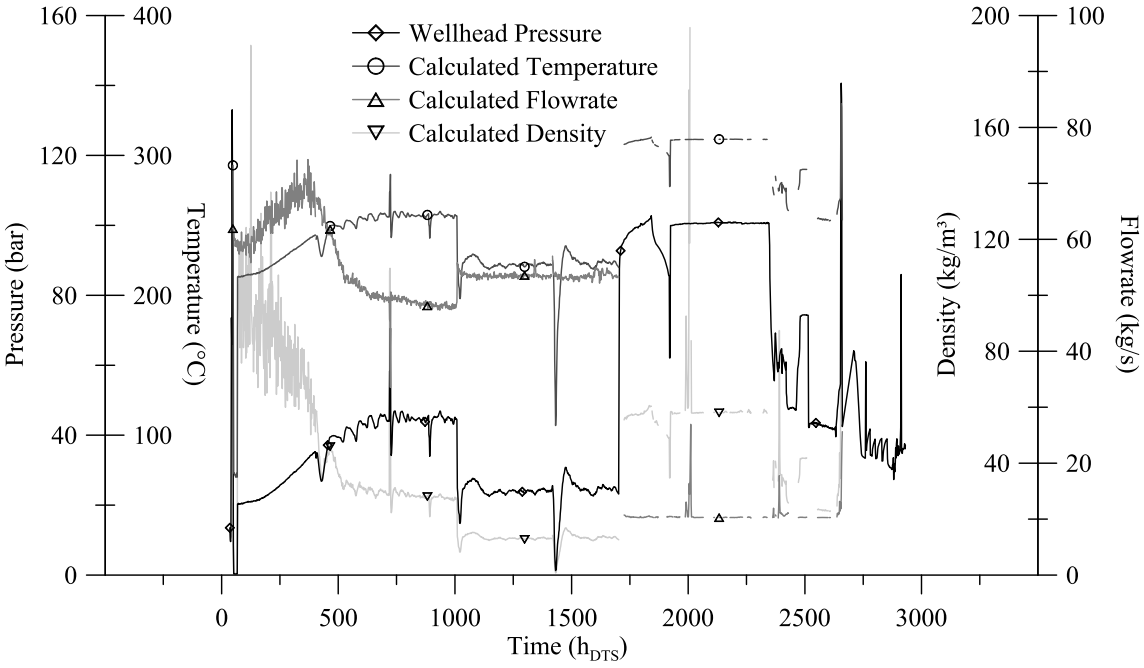

Figure 3.12.: Flow test data from HE-53. Wellhead pressure has been measured and according temperatures have been calculated for water at the boiling point curve. The flow rate and the density at the wellhead are calculated as well. For details on available wellhead data and the calculations, please refer to Chapter 4. Wellhead data courtesy of Reykjavik Energy.

3.2.3.2. Results

Temperature Measurements

The measured DTS temperature is shown in Figure 3.13(a). The profile from before the flow test is assumed to resemble static formation temperatures. In order to see if the temperature profile is static, it has been compared to a profile from the neighbouring well HE-36. Formation temperatures are similar at about $80 - 155$ m. Temperatures below the water table in HE-36 are similar to those, measured in HE-53 in the depth interval $120 - 155$ m. Below 155 m, a temperature increase in HE-36 has been observed. The increase can be attributed to a subsurface blowout in HE-53 at the end of the flow test in November 2009. Measured temperatures in HE-36, therefore, are different to DTS temperature readings from before the flow test below 155 m.

The comparison of different temperature profiles shows that measured DTS temperatures from before and after the flow test differ by more than 10 °C in specific depth intervals. The temperature profile within the uppermost 80 m resembles the profile measured before the flow test. Although DTS temperature from after the flow test is about 10 °C higher than before in the depth interval $40 - 120$ m, the overall appearance with two maximum temperatures and a minimum in between in a depth of about 40 m is similar (Figure 3.13(a)). Below this depth, measured DTS temperatures decrease with a minimum of approx. −4 °C in a depth of 155 m. Further down, temperatures increased slightly, but remained below 5 °C whereas actual temperatures measured in HE-36 are up to 10 °C higher. The strong variations in DTS temperature after the flow test below 155 m does neither resemble measured temperatures from before the flow test in HE-53, nor temperatures measured in HE-36.

Attenuation Measurements

After the flow test, a strong degradation of the optical properties was detected (Figure 3.14(a)). The fibre was cut in about 175 m, where the damage was observed during the onset of the flow test. The attenuation at 850 nm increased from 2.4 dB/km (0-150 m) at the beginning of the flow test to 18.6 dB/km ($0 - 150$ m) at the time of the third logging campaign. Differential attenuation Γ along the fibre increased by approx 100 % (Figure 3.13(b)).

In Figure 3.14(b), the attenuation has been plotted without the trend shown in Figure 3.14(a). The attenuation change strongly corresponds to the temperature profile which was measured during the flow test. High attenuation values correspond to sections of high temperature along the fibre.

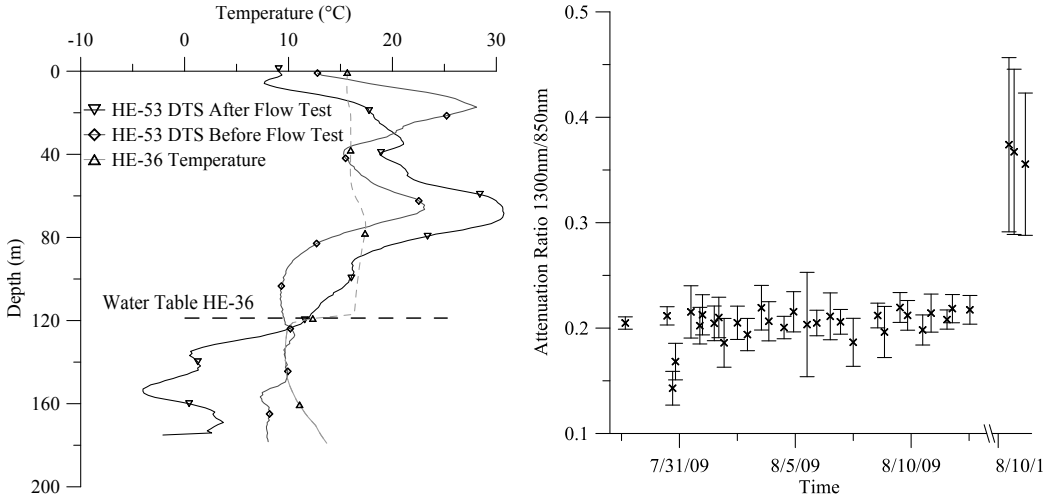

(a) Temperature Comparison. (b) Attenuation Ratio.

Figure 3.13.: (a) Comparison of different temperature profiles measured before and after the flow testing operation. A conventional log from a neighbouring well (HE-36) has been used to evaluate the performance of the DTS measurements after the flow test. The water table in HE-36 well is indicated. (b) Attenuation ratio 1300 nm/850 nm for different times during the three field campaigns.

Accuracy

From the comparison of different temperature profiles in Figure 3.13(a), it can be seen that DTS temperature readings after the flow test differ by ± 10 °C from ambient temperatures. Above 40 m, DTS temperatures are lower, within the intervall $40 - 120$ m, temperatures are higher and below, they are lower, again.

3.2.3.3. Discussions

The heavy degradation of the optical fibre observed during the third field campaign can be attributed to the following processes:

1. Mechanical stress onto the cable due to differences in thermal expansion of the subsurface installations during the flow test.

2. Degradation of the coating material due to the exposure to high temperatures.

3. Chemical degradation of the light guiding silica structure due to the cracking of oil within the cable and an increased diffusion rate of molecules within the silica at high temperatures.

The first two issues would result in an overall increase in attenuation at all wavelengths. Loss increase caused by microbending is commonly not wavelength dependent (Buck, 2004), a strong increase in the attenuation ratio Γ, however, can be

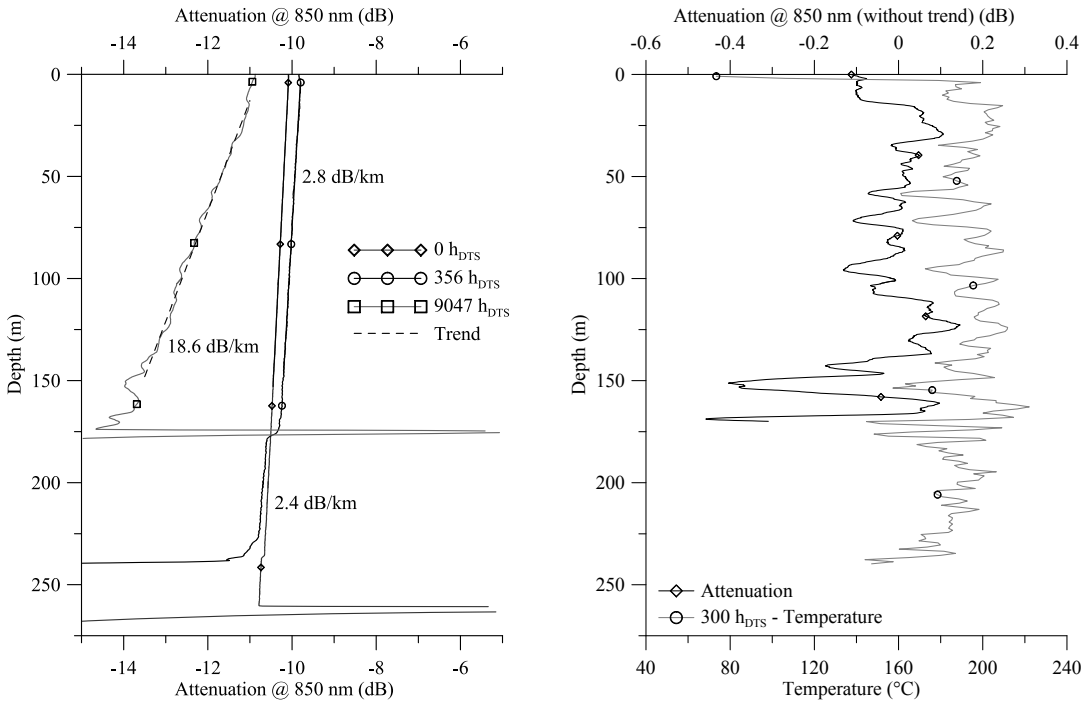

(a) Attenuation. (b) Attenuation without trend.

Figure 3.14.: (a) Comparison of different attenuation profiles from before, during and after the flow test for the eastern branch. (b) Attenuation without trend related to a temperature measurement from during the flow test.

observed. A distinction between the first two can be obtained based on the fact that stress onto the cable would result in a local variation in signal levels, whereas the degradation of the coating material would result in a smooth but steeper attenuation profile. Chemical degradation is most probably caused by the ingression of hydrogen, released from the cable itself (see Chapter 2).

A mechanical damage of the cable occurred at the very end of the fibre in approx 180 m depth. The steep overall attenuation profile at wavelengths distant to the typical hydroxyl absorption bands, might be caused by a thermal degradation of the coating material. As the attenuation is strongly correlated to the temperatures experienced during the flow test, the fibre coating experienced a different degree of degradation and thus a different increase in microbending loss.

The increase in the attenuation ratio 1300 nm/850 nm indicates an increase in the hydrogen load of the fibre. As the fibre could not be flushed with inert gas, the ingression of hydrogen from the cable itself could not be reduced. Due to the ingression of hydrogen, the attenuation ratio between the Stokes and the Anti-Stokes band changed in the course of the flow test. This, most likely led to the skewed temperature profile which was measured in August 2010.

DTS temperatures of -4 °C can be attributed to the degradation of the fibre and do not resemble actual temperature formation temperatures after the shut-in period. Furthermore, temperature variations along the profile, e.g. in about 150 m depth can be correlated with large changes in the attenuation profile (Figure 3.14). During the second logging campaign, however, a severe degradation of the temperature signal could not be determined.

For the depth interval $40 - 120$ m higher DTS temperatures were measured after the flow test, although the degradation due to hydrogen ingression should lead to lower DTS temperature readings. Here, the DTS temperature profile from before the flow test might not resemble static formation temperatures. During drilling activities, the well was actively cooled down. Possibly, the static temperature of the permeable layers at top (above and below 40 m), identified in section 3.2.2, did not fully recover during the 1 month shut-in period between well completion and beginning of the flow test. Furthermore, changing geothermal activity within the aquifers or an influence of the subsurface blowout in HE-53 might be possible explanations.

4. Wellbore Temperature Simulator

After collecting field data, described in the previous chapter, the data is analysed with regards to wellbore heat transfer and wellbore integrity. The fluid temperature within a flowing well determines the temperature evolution within the annulus. In order to compare measured DTS temperatures with wellbore fluid temperatures (Chapter 5), a temperature profile has to be determined on the basis of available wellhead data. The development, implementation and testing of a wellbore temperature simulator is described within this chapter.

In order to simulate the temperature conditions within the flowing well producing a two-phase fluid, a wellbore simulator has been implemented in Python (van Rossum, 1995). Wellhead data provided by Reykjavik Energy is used to calculate fluid enthalpy and mass flow rate at wellhead pressure conditions using an empirical formula proposed by James (1962, 1970) for a fluid at two-phase conditions. Based on the models presented in Rist (1996) and Hasan and Kabir (2010), temperature, pressure and enthalpy profiles can be calculated.

4.1. Theoretical Concept

4.1.1. Wellhead Conditions

From the measurement of wellhead pressure p_0, critical pressure p_c and the water height in the weir box H_w, i.e. the liquid flow rate at ambient pressure, the condition of a two-phase fluid at the wellhead can be determined (Figure 4.1). The calculation scheme follows the discussion in Grant et al. (1982); Mendieta (1991).

James (1962, 1970) proposed an empirical relationship between the pressure at the end of a horizontal pipe, discharging to the atmosphere, the total enthalpy h_t (J/kg) and the mass flow rate $\dot{m}_t$(kg/s) per unit area A_{ID}(cm^2) within the pipe for a two-phase flow of pure water. The pressure measured at the end of the pipe is called lip or critical pressure p_c (MPa) and the relation is valid if the flow at the end of the pipe is at sonic velocity (James, 1962; Grant et al., 1982):

$$\frac{\dot{m}_t \widetilde{h}_t^{1.102}}{A_{ID} \widetilde{p}_c^{0.96}} = c_{RJ} \tag{4.1}$$

where $\widetilde{h}_t = h_t/h_{aux}$ with the auxiliary constant h_{aux} =1 J/kg and $\widetilde{p}_c = p_c/p_{aux}$ with the auxiliary constant p_{aux} =1 MPa were introduced to correct for the units and c_{RJ} =1680 kg/cm^{2}s being the constant proposed by Russel James.

After the fluid is flashed to the atmosphere, the liquid phase is separated and the liquid mass flow rate at atmospheric conditions $\dot{m}_l^a$ at 100 °C is measured in a weir box (Figure 4.1). The superscript a denotes atmospheric conditions. For a two-phase flow, the total mass flow rate $\dot{m}_t$ is the sum of the liquid $\dot{m}_l$ and the vapour flow rate $\dot{m}_v$:

$$\dot{m}_t = \dot{m}_l + \dot{m}_v = \dot{m}_l^a + \dot{m}_v^a \tag{4.2}$$

The liquid flow rate at atmospheric conditions $\dot{m}_l^a$ can be measured using the water height in the weir box (Kulin and Compton, 1975; Mendieta, 1991, and references therein):

$$\dot{m}_l^a = \dot{V}_c \rho (\widetilde{H}_w + 0.00085)^{2.5} \tag{4.3}$$

where H_w is the height of the water within the weir box, $\widetilde{H}_w = H_w/H_{aux}$ with the auxiliary constant H_{aux} =1 m, $\dot{V}_c$ =1.38 m^3/s is a constant volumetric flow rate and ρ is the density of water at 100 °C.

From energy conservation, the total enthalpy h_t can be calculated as the sum of the enthalpies of the liquid phase h_l and vapour phase h_v, weighted by the mass fraction of the steam w_v (quality):

$$h_t = (1 - w_v)h_l + w_v h_v = (1 - w_v^a)h_l^a + w_v^a h_v^a \tag{4.4}$$

From Equation 4.2 and 4.4, the quality of the steam at atmospheric conditions can be calculated:

$$w_v^a = \frac{\dot{m}_v^a}{\dot{m}_t} = \frac{\dot{m}_t - \dot{m}_l^a}{\dot{m}_t} = \frac{h_t - h_l^a}{h_v^a - h_l^a} \tag{4.5}$$

Combining Equation 4.1, 4.4 and $\dot{m}_t = \dot{m}_l^a/(1 - w_v^a)$ gives (Grant et al., 1982):

$$\dot{m}_l^a = \frac{c_{RJ}(h_v^a - h_t)}{\widetilde{h}_t^{1.102}(h_v^a - h_l^a)} A_{ID} \widetilde{p}_c^{0.96} \tag{4.6}$$

The total enthalpy h_t remains the only unknown in Equation 4.6. Linearising this equation ($\widetilde{h}_t^{1.102} \approx h_t$), an accuracy of 1.5 % can be achieved for the enthalpy calculation (Grant et al., 1982). Ramey Jr. (1978) proposed a hand calculator program to solve this equation with an accuracy of ±2 % at most and ±0.6 % for an enthalpy below 1630 kJ/kg. Within this study, it is solved for h_t using Newton iteration following Mendieta (1991):

$$f(h_t) = \dot{m}_l^a - \frac{c_{RJ}(h_v^a - h_t)}{\widetilde{h}_t^{1.102}(h_v^a - h_l^a)} A_{ID} \widetilde{p}_c^{0.96} = 0 \tag{4.7}$$

With an initial guess for the enthalpy h_i, a better solution h_{i+1} is:

$$h_{i+1} = h_i - \frac{f(h_i)}{\frac{\partial f(h_i)}{\partial h}} \approx h_i - \frac{f(h_i)\Delta h}{f(h_i + \Delta h) - f(h_i)} \tag{4.8}$$

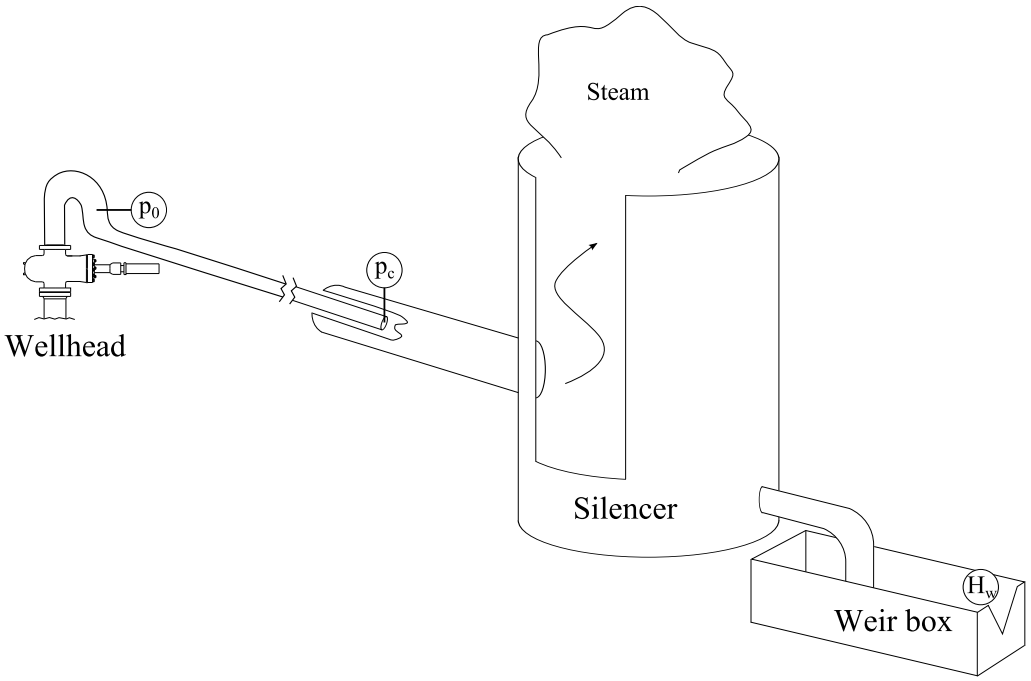

Figure 4.1.: Typical set-up to measure flow rate and enthalpy by the Russell James method. Measured values are indicated by schematic gauges.

As a stop criterion for the algorithm, $f(h_t)$ <1 g/s has been defined (Mendieta, 1991).

Having calculated the enthalpy h_t, the total flow rate $\dot{m}_t$ can be calculated:

$$\dot{m}_t = \frac{\dot{m}_l^a}{1 - w_v^a} = \frac{\dot{m}_l^a (h_v^a - h_l^a)}{(h_v^a - h_t)} \tag{4.9}$$

Grant et al. (1982) gives values for the absolute accuracy in determining the fluid enthalpy using the lip pressure method. From several flow tests in New Zealand, he determined the accuracy to be $\Delta h_t = 20$ kJ/kg and $\Delta \dot{m}_t = 4\%$ for a careful controlled data collection system and $\Delta h_t = 50$ kJ/kg and $\Delta \dot{m}_t = 8\%$ for a "normal" system, respectively.

Knowing the total mass flow and the enthalpy of the fluid, the total thermal capacity of the well can be calculated according to (Grant et al., 1982):

$$\dot{Q}_{th} = \dot{m}_t h_t \tag{4.10}$$

The enthalpy has been calculated with reference to 0 °C. Hence, the thermal capacity is given with reference to 0 °C as well.

In order to calculate the density of the fluid at the wellhead, the quality of the steam at wellhead pressure conditions $w_v^{p_0}$ has to be calculated:

$$w_v^{p_0} = \frac{h_t - h_l^{p_0}}{h_v^{p_0} - h_l^{p_0}} \tag{4.11}$$

where the liquid and steam enthalpy at different pressures can be derived from literature (Lemmon et al., 2007). With the steam mass fraction $w_v^{p_0}$ and the liquid mass fraction $w_l^{p_0} = 1 - w_v^{p_0}$, the density of the two-phase fluid can be calculated (Rist, 1996):

$$\rho_m^{p_0} = \frac{\rho_v(p_0)}{1 - w_l^{p_0}(1 - \rho_v(p_0)/\rho_l(p_0))} \tag{4.12}$$

where the liquid and steam density $\rho_l(p_0)$ and $\rho_v(p_0)$ can be derived from literature data, as well.

4.1.2. Well Temperature Profile

From the wellhead conditions, a temperature profile can be simulated for the flowing well. The changing momentum of the fluid, the change in pressure with increasing depth as well as the change in energy of the fluid has to be considered for the calculation.

4.1.2.1. Momentum Transport

In order to determine the temperature profile of a flowing well, the pressure increase with increasing depth can be calculated as the sum of static head, friction and kinetic gradient (Hasan and Kabir, 2010; Rist, 1996):

$$\begin{aligned} -\frac{dp}{dz} &= \left(\frac{dp}{dz}\right)_{static} + \left(\frac{dp}{dz}\right)_{friction} + \left(\frac{dp}{dz}\right)_{kinetic} \\ &= g\rho_m \sin\theta + f_{R,2Ph}\frac{1}{2}\left(\frac{\dot{m}_t}{A_{ID,csg,p}}\right)^2 \frac{1}{\rho_m ID_{csg,p}} + \rho_m u_v \frac{du_m}{dz} \end{aligned} \tag{4.13}$$

where g is the gravity acceleration, ρ_m is the density of the mixture (Equation 4.12), θ is the deviation of the well from the horizontal and z is the distance in vertical direction. The frictional increase in pressure is calculated following the ansatz of Hagedorn and Brown (1965) in Rist (1996), where the differences between flow regimes are neglected but slip is considered. $f_{R,2Ph}$ is the two-phase friction coefficient calculated from the two-phase Reynolds number Re_{2Ph} in the Moody diagram (Moody, 1944) (Appendix G). $\dot{m}_t$ is again the total mass flow, $A_{ID,csg,p}$ the cross sectional area of the production casing and $ID_{csg,p}$ is its inner diameter. u_v and u_m are the gas and mixture velocity within the well, respectively.

From the mass fraction, the volumetric liquid fraction ϕ_l can be derived:

$$\phi_l = w_l \frac{\rho}{\rho_l} \tag{4.14}$$

Using the information about pressure p and volumetric liquid fraction ϕ_l, the dynamic viscosity of the two-phase mixture η_m can be calculated from the liquid and

steam dynamic viscosity (Rist, 1996):

$$\eta_m = \eta_l^{\phi_l} \eta_v^{1-\phi_l} \tag{4.15}$$

where the dynamic viscosities $\eta_l(p)$ and $\eta_v s(p)$ of the liquid and steam phase can be derived from literature (e.g. in Lemmon et al., 2007). For Equation 4.15, the viscosities are given in cP = 10^{-3}kg/(s m). The two-phase Reynolds number Re_{2Ph} can now be calculated as (Rist, 1996):

$$Re_{2Ph} = \frac{4}{\pi} \frac{\dot{m}_t}{ID_{csg,p}\eta_m} \tag{4.16}$$

where η_m has to be converted to kg/(m s). The friction factor $f_{R,2Ph}$ can now be calculated using the approximation of Haaland (1983):

$$\frac{1}{\sqrt{f_{R,2Ph}}} = -1.8 \log_{10} \left[\left(\frac{\zeta / ID_{csg,p}}{3.7} \right)^{1.11} + \frac{6.9}{Re_{2Ph}} \right] \tag{4.17}$$

where ζ (mm) is the roughness of the pipe.

4.1.2.2. Energy Transport

Beside the pressure increase, changes in the enthalpy of the fluid have to be considered. The change in enthalpy with increasing depth can be calculated as the sum of change due to pressure change because of ascent of the fluid column, acceleration and wellbore heat transfer (Hasan and Kabir, 2010):

$$\begin{aligned} \frac{dh}{dz} &= \left(\frac{dh}{dz} \right)_{asc} - \left(\frac{dh}{dz} \right)_{acc} - \left(\frac{dh}{dz} \right)_{transfer} \\ &= g \sin\theta - u_m \frac{du_m}{dz} - \frac{\dot{Q}_L}{\dot{m}_t} \end{aligned} \tag{4.18}$$

where u_m is the velocity of the mixture and $\dot{Q}_L$ is the amount of energy lost to the formation per unit length Δz. The energy loss can be expressed as condensation and change in the quality of the fluid. The amount of heat transferred to the formation is dependent on the thermal properties of the well completion and of the formation as well as on the temperature difference between fluid and formation (Chapter 5). For a fluid at pressure p, the latent heat of condensation is defined as the difference between liquid and steam enthalpy:

$$\Delta h^p = h_v^p - h_l^p \tag{4.19}$$

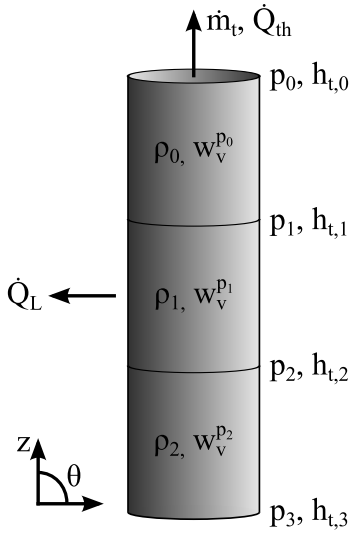

Figure 4.2.: One dimensional model of a well. Parameters modelled at each step are indicated.

4.2. Model Formulation

From data recorded by ISOR, the wellhead conditions have been calculated. The total mass flow $\dot{m}_t$ as well as total enthalpy h_t and density $\rho_m^{p_0}$ of the two-phase fluid at wellhead pressure conditions p_0 was determined.

For the comparison of simulated temperatures and measured DTS temperatures, only the uppermost 300 m are of interest. In order to calculate a well temperature profile for this shallow depth interval, a simple one-dimensional computer model has been implemented to simulate a two-phase flow in a vertical pipe. It can be used, however, to calculate to greater depth as well. Based on the theoretical discussion in Section 4.1.2, the well has been discretised and pressure and enthalpy increase has been calculated for every depth intervall. A schematic model of the discretised wellbore is shown in Figure 4.2.

The following algorithm has been used to calculate a pressure and enthalpy profile with a discretisation step width z_h. A simplified flowchart of this program can be found in Appendix H.:

1. Pressure and enthalpy (p_0 and $h_{t,0}$) is given at the wellhead.
2. Calculate the vapour and liquid mass fraction $w_v^{p_0}$ and $w_l^{p_0} = 1 - w_v^{p_0}$ (Equation 4.11).
3. Calculate the density of the fluid $\rho_m^{p_0}$ (Equation 4.12).
4. Calculate density increase due to wellbore heat transfer.

a) Calculate the latent heat of condensation at pressure p_0: Δh^{p_0} (Equation 4.19).

b) Calculate the mass per segment $m_{z_h} = \rho^{p_0} V_{z_h}$, where V_{z_h} is the volume of the segment.

c) Calculate the ascent velocity $u_m = \dot{m}_t / m_{z_h}$ (segment/s).

d) Calculate the heat loss per segment $Q_{z_h} = z_h Q_L$ (W/segment), where Q_L is the loss per unit length.

e) Calculate the condensate mass per segment $m_{con,z_h} = Q_{z_h} / \Delta h^{p_0} / u_m$.

f) Calculate the new liquid mass fraction $w_{l,con}^{p_0} = (\dot{m}_t w_l^{p_0} + m_{con,z_h}) / \dot{m}_t$.

g) Recalculate the density (Step 3).

5. Calculate the volume fraction of the liquid ϕ_l (Equation 4.14).
6. Calculate the dynamic viscosity η_m (Equation 4.15).
7. Calculate the two-phase Reynolds number Re_{2Ph} (Equation 4.16).
8. Calculate the friction factor $f_{R,2Ph}$ (Equation 4.17).
9. Calculate the pressure increase within each segment (Equation 4.13)
10. Calculate the enthalpy increase due to the ascent of the fluid (Equation 4.18).
11. Calculate new pressure and enthalpy ($p_1 = p_0 + \Delta p$ and $h_{t,1} = h_{t,0} + \Delta h$).
12. For subsequent depth elements, use calculated pressure p_1 and enthalpy h_1 and restart at Step 2.

The pressure increase due to the kinetic gradient has been neglected for this calculation. For typical flow rates in HE-53 $\dot{m}_t$ =45.93 kg/s (27.8.2011: enthalpy h_t =1568 kJ/kg and wellhead pressure p_0 =58.9 bar_g) a density of 114 kg/m^3 has been calculated at the surface. This changes to 140 kg/m^3 in 500 m depth. The mixture velocity in 500 m can be calculated as:

$$u_m^{500\ m} = \dot{m}_t / (\pi r_{csg,p}^{ID\ 2} \rho_m^{500\ m}) = 9\ m/s \tag{4.20}$$

where $r_{csg,p}^{ID}$ is the radius of the production casing. The velocity changes by 2 m/s during its ascent to the surface. The change in pressure due to the acceleration is 2508 Pa and therefore negligible compared to the static head of 559170 Pa for a uniform column of 114 kg/m^3. The same applies for the enthalpy change due to acceleration of the fluid. For the values mentioned above, the change in enthalpy is 22 J/kg for 500 m and therefore negligible compared to the increase due to the ascent (4905 J/kg) or heat transfer (10886 J/kg). Compared to the accuracy in determining the enthalpy (20 kJ/kg), both contributions are small.

For the surface roughness of geothermal well casings, values given in literature range from 0.2 mm to $2 \cdot 10^{-4}$ mm (Ambastha and Gudmundsson, 1986; Hadgu et al., 1994). For the calculations above, a value of 0.2 mm has been used (Ambastha and Gudmundsson, 1986), assuming a rough pipe. Effects of non-condensible gases as well as dissolved gases were not considered.

The calculated density is the density at the top of each segment. As it changes with depth, a more elaborate algorithm has to consider the average density between top and bottom of the segment. This could be done using an iterative procedure:

I. Calculate pressure increase using the density at top (Steps 2 to 9, without Step 4).

II. Calculate the density at the bottom of the segment according to the calculated pressure.

III. Calculate the average density for the segment.

IV. Recalculate the pressure increase using the average density (Step I). This algorithm is used until the change in pressure between successive iterations is below a certain threshold, defined by the user.

V. Calculate the pressure increase using the average density and consider the condensation as well (Steps 2 to 9, including Step 4).

The influence of the averaged density is small if the length of the segments is small. For this experiment, the length of individual segments is defined as 0.5 m and the pressure profile of the uppermost 300 m is of interest. The influence of the averaged density is in the range of 0.01 kg/m^3 per step for the flow data on 27.8.2009. The error per step is therefore $\frac{0.01(kg/m^3)}{114(kg/m^3)} \cdot 100\% = 9 \cdot 10^{-3}\%$ and will be neglected. As the error is small, averaging the density has not been implemented. The wellhead pressure is assumed to be logged at 1.5 m above ground surface.

In order to calculate a temperature profile, a heat transfer to the formation has to be assumed. Within the first 350 h_{DTS}, the average density at the wellhead is 81 kg/m^3. 63 kg/s of two-phase fluid are produced. Due to the high production rate, however, the influence of the assumed heat transfer on the measured temperature is negligible. Changing the heat transfer by an order of magnitude ($1 - 10$ kW/m) for the profile at 350 h_{DTS}, the simulated temperature variation in 500 m depth was below 0.005 °C. The heat transfer per meter has been set to be 1 kW (see as well Chapter 5).

4.3. Model Validation

Table 4.1 shows a comparison between measured and modelled data in Ambastha and Gudmundsson (1986) and data modelled in this study. The overall agreement

Table 4.1.: Comparison between modelled data and modelled and measured data from Ambastha and Gudmundsson (1986). The pressure gradient is an average value for the uppermost 500 m.

Well	Measured (bar/m)	Modelled * (bar/m)	Modelled this study (bar/m)	Remarks
Cerro Prieto 90	0.0275	0.0275	0.0280	
Los Azufres 18	0.0104	0.0088	0.0090	
Ngawha 11	0.0494	0.0770	0.0475	Phase transition
Okoy 7	0.0207	0.0220	0.0145	
Cerro Prieto 91	0.0398	0.0333	0.0280	
Mofete 2	0.0064	0.0071	0.0114	
HGP-A	0.0042	0.0049	0.0071	
East Mesa 6-1	0.0030	0.0060	0.0060	
Krafla 9	0.0274	0.0117	0.0090	
Utah State 14-2	0.0275	0.0192	0.0144	
HE-53	0.0176		0.0182	not included in *

(*) Ambastha and Gudmundsson (1986)

between between logged data and modelled pressure profiles is reasonable, although not good in most cases. For well Ngawha 11, the phase transition from a single- to a two-phase fluid is in about 100 m depth and cannot be handled by this algorithm. Therefore, only the uppermost 90 m have been considered. Although the modelled pressure gradient within this study is not as accurate, compared to measured data, as the results from Ambastha and Gudmundsson (1986), a good agreement between measured and modelled pressure data in HE-53 has been observed.

Figure 4.3 shows the comparison between measured and modelled pressure and temperature data. Logged temperature data from ISOR corresponds well to calculated temperatures from the pressure log for a two-phase fluid at boiling point pressure. Compared to the log, measured wellhead pressure, however, shows an offset of 1.97 bar and is therefore supposed to be wrong. In the following, wellhead pressures will be reduced by this value. After the offset correction, modelled pressure and temperature profiles fit well and the difference in the pressure profile is $\frac{0.0183-0.0176}{0.0176} \cdot 100\% = 3.98\%$. For the uppermost 300 m, the absolute difference between measured and modelled temperatures is below 1 °C.

The performance of the wellbore simulator used in this study is sufficient for the temperature profile determination along the wellbore.

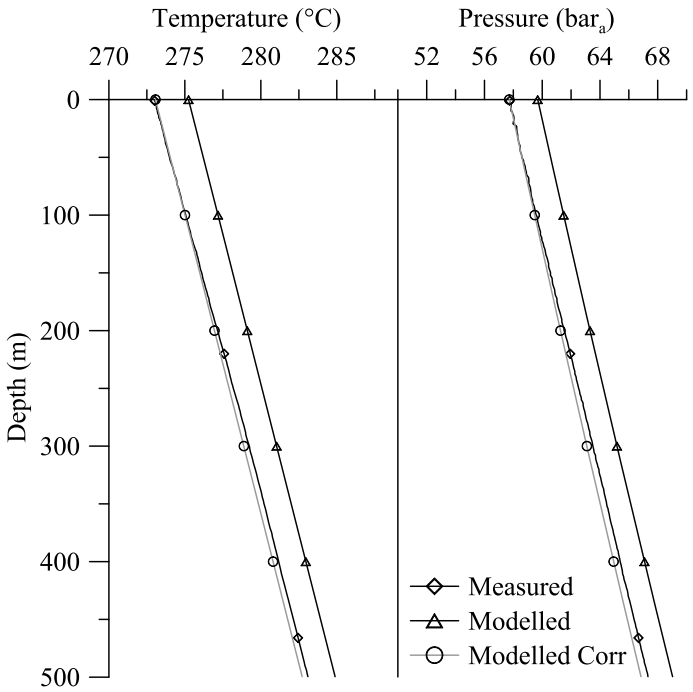

Figure 4.3.: Comparison between measured and modelled pressure and temperature profiles from the 27.8.2009 in HE-53. Wellhead pressure data p_0 has been reduced by 1.97 bar in order to match to measured pressure and temperature data from ISOR.

5. Heat Transfer in Wellbores

When a fluid moves within a wellbore, heat is transferred between the fluid and the surrounding medium due to different temperatures between wellbore fluid and geothermal temperatures (Ramey Jr., 1962). Quantitatively, this heat transfer can be described in terms of conduction, convection and radiation (Cengel, 2002). For wellbore heat transmission, conduction and convection are the most important processes. Although radiation plays a role in e.g. gas filled annuli, the role of radiation will be neglected in the following discussion. In order to understand the temperature evolution within the annulus behind the anchor casing, conductive and convective heat transfer phenomena are discussed within this chapter.

Based on the theoretical discussion, measured DTS data will be used to quantify the influence of conductive and convective heat transfer mechanisms in-situ. DTS temperature data from the cement job will be used in comparison to conventional temperature logging data to evaluate the importance of convection within the wellbore during shut-in periods. Furthermore, temperature measurements within the annulus can be used in combination with a simulated wellbore temperature profile (Chapter 4) to determine the heat transfer in different depths of the well. The calculated heat loss can be used to determine the thermal properties of the formation in-situ.

5.1. Theoretical Concept

The heat transport in a porous medium can be described using the following equation (Diersch, 2009):

$$\frac{\partial}{\partial t}\left[\phi\rho_f c_{p,f} + (1-\phi)\rho_s c_{p,s}\right] + \frac{\partial}{\partial x_i}(\rho_f q_{f,i} c_{p,f}) - \frac{\partial}{\partial x_i}\left(\lambda_{ij}\frac{\partial T_f}{\partial x_j}\right) = \dot{Q}_V, \qquad (5.1)$$

where the subscript f denotes the fluid phase and s the solid phase. ϕ is the porosity of the medium, ρ (kg/m^3) the density, c_p (J/(kg K)) the specific heat capacity and q is the Darcy flux in (m/s). $\dot{Q}_V$ is the volumetric heat supply (W/m^3) and $\lambda_{i,j}$ (W/(m K)) the thermo dispersion tensor (conductive + dispersive heat transfer).

5.1.1. Conductive Heat Transfer

Neglecting fluid flow within a porous medium like the formation, a lot of problems in wellbore heat transfer can be approximated using a conductive one-dimensional

radial symmetric approach (Köckritz, 1979, and references therein). Without convective and dispersive heat transfer, conductive heat transport in radial direction r can be simplified to (Crank, 1975):

$$\frac{\partial T}{\partial t} = \alpha \left(\frac{\partial^2 T}{\partial r^2} + \frac{1}{r} \frac{\partial T}{\partial r} \right) \tag{5.2}$$

with a constant thermal diffusivity $\alpha = \frac{\lambda}{\rho c_p}$ (m^2/s) and λ being the thermal conductivity[1]. Generally, the thermal diffusivity is a function of temperature. For simplicity, however, the thermal properties are assumed to be constant.

In steady state conditions, conductive heat transfer $\dot{Q}_{cond}$ in radial direction through a cylindrical layer can be expressed by Fourier's law (Fourier, 1822):

$$\dot{Q}_{cond} = \lambda A \frac{\partial T}{\partial r} \text{ or } \dot{q}_{cond} = \lambda \frac{\partial T}{\partial r} \tag{5.3}$$

where A is the surface area and $\dot{q}_{cond}$ the heat transfer per unit area.

5.1.1.1. Infinite Media

An analytical solution for the temperature increase of an infinite homogeneous and isotropic medium, initially at zero temperature, heated by a constant line source of unit length $\dot{Q}_L$ is given in Carslaw and Jaeger (1959):

$$T(r,t) = \frac{\dot{Q}_L}{4\pi\lambda} \left[-Ei(-\frac{r^2}{4\alpha t}) \right] \tag{5.4}$$

where a perfect thermal contact is assumed between line source and medium. Hence, the contact resistance is zero. $Ei(x)$ is the exponential integral (Gautsch and Cahill, 1972):

$$Ei(x) = -\int_{-x}^{\infty} \frac{\exp^{-t}}{t} dt, \; x > 0 \tag{5.5}$$

which can be rewritten in series representation (Gautsch and Cahill, 1972; Press et al., 1992; Oldham et al., 2009):

$$-Ei(-x) = E_1(x) = -\gamma - \ln x - \sum_{n-1}^{\infty} \frac{(-1)^n x^n}{n! n}, \tag{5.6}$$

where $E_1(x)$ is a representation of the exponential integral and γ is the Euler-Mascheroni constant (Oldham et al., 2009):

$$\gamma = \lim_{n \to \infty} \left(\sum_{k=1}^{n} \frac{1}{k} - \ln n \right) \approx 0.57721 \tag{5.7}$$

[1] For simplicity, only a scalar thermal conductivity λ is considered.

For short times t, the exponential integral can be approximated according to (Carslaw and Jaeger, 1959):

$$-Ei(-x) = \ln\frac{1}{x} - \gamma + x - \frac{1}{4}x^2 + \mathcal{O}(x^3) \tag{5.8}$$

For large values of t, the following approximation holds true (Carslaw and Jaeger, 1959):

$$-Ei(-x) = \ln\frac{1}{x} - \gamma + \mathcal{O}(x) \tag{5.9}$$

Despite the thermal resistance and the finite radius of a wellbore, a line source approach (Equation 5.4) can often be used to approximate the radial temperature distribution around the well. Given enough time, the solution for a cylindrical source loosing heat at constant flux converges with the solution for a constant line source (Carslaw and Jaeger, 1959; Ramey Jr., 1962). In wellbore literature, the expression representing the time dependence of the heat transfer is often called the transient heat conduction function $f(t)$ (e.g. Ramey Jr., 1962; Willhite, 1967; Köckritz, 1979). For many reservoir problems, $f(t)$ can be approximated by Equation 5.9 for times longer than one week (Ramey Jr., 1962). Köckritz (1979, and references therein) specifies this $\alpha t/r^2 > 12.5$ for the radius to the cement-formation interface.

5.1.1.2. Finite Media

For multilayer hollow cylinder (Figure 5.1), steady temperature conditions can be described introducing the conduction resistance R (Cengel, 2002):

$$R = \frac{T_i - T_o}{\dot{Q}} = \frac{\ln(r_o/r_i)}{2\pi L\lambda}, \tag{5.10}$$

where T is the wall temperature at radius r and the subscripts denote the inner and outer wall of an individual layer. $\dot{Q}$ is the heat transfer through the cylindrical layer of length L. For different layers, individual thermal resistances can be defined. In electrical analogy, these resistances can be combined in series arrangement to form the total thermal resistance R_t of a multilayer cylinder (Cengel, 2002).

$$R_t = R_1 + R_2 + ... = \frac{\ln(r_2/r_1)}{2\pi L\lambda_1} + \frac{\ln(r_3/r_2)}{2\pi L\lambda_2} + ... \tag{5.11}$$

In case the casing is not centralized (Figure 5.2), the conductive heat transfer is not axisymmetric. The overall heat transfer $\dot{Q}$ for two eccentric pipes of length L with homogeneous surface temperatures in steady state conditions can be calculated according to Hahne (2006):

$$\dot{Q} = \frac{2\pi L\lambda(T_i - T_o)}{\cosh^{-1}\frac{r_i^2 + r_o^2 - e^2}{2r_i r_o}} \tag{5.12}$$

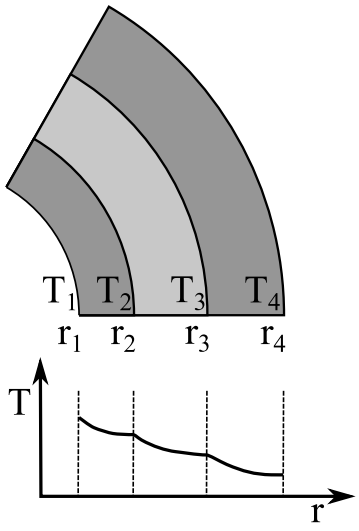

Figure 5.1.: Steady state conductive heat transfer in a multilayer cylinder.

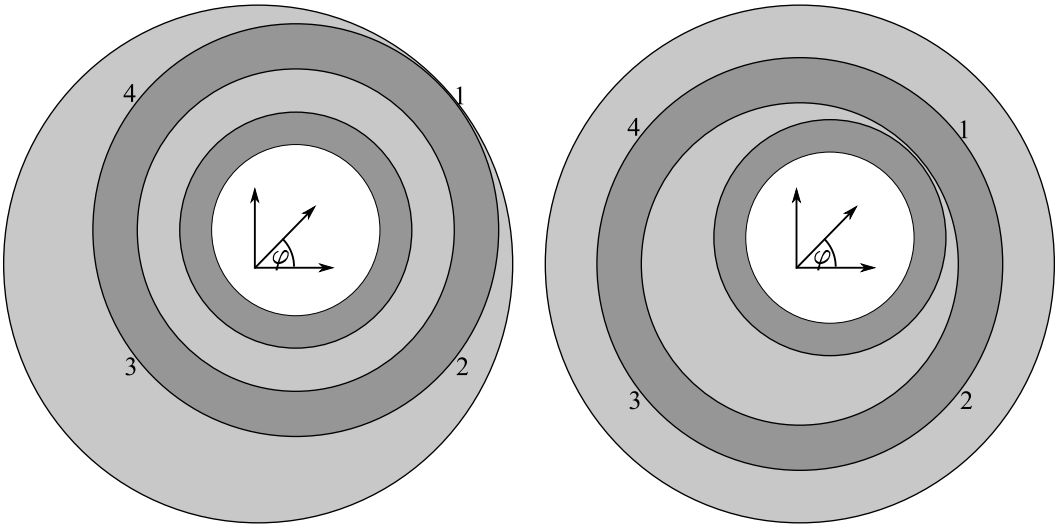

(a) Decentralized Anchor Casing. (b) Decentralized Production Casing.

Figure 5.2.: Sketch of a decentralized multilayer cylinder. The casings are indicated in dark grey, the cemented annulus in light grey. The possible extreme position of the DTS sensor cable within the annulus is indicated by numbers. The direction of decentralisation is described by the angle φ.

where r_i and r_o is the radius of the inner and outer surface, respectively, and e is the eccentricity, i.e. the distance between the centres of the isothermal surfaces. The heat loss is therefore larger for a decentralized casing.

The DTS sensor cable is installed on opposite sides around the perimeter of the anchor casing. Thus, DTS temperature data, measured at locations 1 and 3 (Figure 5.2), is therefore different and the calculated conductive heat transfer should vary between both cable branches. For locations 2 and 4, no temperature difference can be determined if the annulus is homogeneously cemented, except the thermal parameters for the formation are known and the temperature heat loss can be calculated according to Ramey Jr. (1962); Willhite (1967) (see next section). Whether the production or the anchor casing is decentralized, cannot be determined from the temperature data. Furthermore, a decentralisation in opposite directions for the production and the anchor casing, cannot be distinguished.

5.1.1.3. Conductive Heat Transfer in a Wellbore

Similar to the discussion in Section 5.1.1.2, Ramey Jr. (1962, and references therein) introduced the over-all heat transfer coefficient U (W/(m^2 K)) to describe the heat transfer for a layered hollow cylinder, i.e. a wellbore with its different casings and annuli. The heat transfer per unit length $\dot{Q}_L$ between well and formation is proportional to the temperature difference ΔT, where U represents the proportionality factor and accounts for the thermal resistance of different casings and annuli (Willhite, 1967):

$$\dot{Q}_L = 2\pi r U_r \Delta T \tag{5.13}$$

where the over-all heat transfer coefficient U_r is characteristic for the circumference $2\pi r$. The overall heat transfer coefficient can be expressed in terms of the conduction resistance R (Equation 5.11) as:

$$U_r = \frac{1}{2\pi r R_t} \tag{5.14}$$

If a fluid moves through the casing, the characteristic radius r is the inner radius of the innermost casing, in this case the production casing $r^{ID}_{csg,p}$. The characteristic temperature difference is given by the difference between fluid temperature T_f and cement-formation interface temperature T^{ID}_{for} (Willhite, 1967). Therefore, the over-all heat transfer coefficient $U_{r^{ID}_{csg,p}}$, characteristic for the circumference $2\pi r^{ID}_{csg,p}$, can then be calculated according to (Willhite, 1967):

$$U_{r^{ID}_{csg,p}} = \frac{1}{r^{ID}_{csg,p}} \left(\frac{\ln\left(\frac{r^{OD}_{csg,p}}{r^{ID}_{csg,p}}\right)}{\lambda_{csg}} + \frac{\ln\left(\frac{r^{ID}_{csg,a}}{r^{OD}_{csg,p}}\right)}{\lambda_{cem}} + \frac{\ln\left(\frac{r^{OD}_{csg,a}}{r^{ID}_{csg,a}}\right)}{\lambda_{csg}} + \frac{\ln\left(\frac{r^{ID}_{for}}{r^{OD}_{csg,a}}\right)}{\lambda_{cem}} \right)^{-1} \tag{5.15}$$

where λ_i is the thermal conductivity of the different layers (casing and cement) and $r^{ID}_{csg,p}$ and $r^{OD}_{csg,p}$ is the inner and outer radius of the production casing, respectively.

Table 5.1.: List of thermal properties. Materials of wellbore completion are listed together with some abundant rocks types in Iceland (thermal conductivity λ, specific heat capacity c_p and density ρ).

Material	λ W/(m K)	c_p J/(kg K)	ρ kg/m^3	Source
Air (20 °C, 1 *bar*)	0.026	1007	1.19	(1)
Water (20 °C, 1 *bar*)	0.598	4179	998.21	(1)
Water (99.63 °C, 1 *bar*)	0.679	4216	958.61	(1)
Carbon Steel	45-55	465	7850	(1)
Cement	≈1			(3)
Icelandic Rock Types				
Basaltic lava flows	1.5-2.1			(2)
Intrusives	1.5-2.0			(2)
Breccias	1.6-2.9			(2)
Sediments	1.1-2.1			(2)

(1) Baehr and Stephan (2008)
(2) Oxburgh and Agrell (1982), core data from a single well
(3) Nelson (1986)

$r^{ID}_{csg,a}$ and $r^{OD}_{csg,a}$ is the inner and outer radius of the anchor casing and r^{ID}_{for} is the radius to the cement-formation interface. The expression for $U_{r^{ID}_{csg,p}}$ neglects any thermal resistance at the contact of different layers as well as possible convective transport phenomena. The annuli are assumed to be fully cemented.

In case the approximation 5.9 is valid, Equation 5.4 can be simplified and combined with Equation 5.13 to calculate the cement-formation interface temperature T^{ID}_{for} for an overall-heat transfer coefficient $U = U_{r^{ID}_{csg,p}}$ (Willhite, 1967):

$$T^{ID}_{for}(t) = \frac{T_f f(t) + \frac{2T_{for}\lambda_{for}}{U\ r^{ID}_{csg,p}}}{\frac{2\lambda_{for}}{U\ r^{ID}_{csg,p}} + f(t)} \tag{5.16}$$

where $f(t)$ is the transient heat conduction function (Equation 5.9), T_{for} is the initial formation temperature and λ_{for} its thermal conductivity. For a given interface temperature, the heat loss per unit length $\dot{Q}_L$ can be calculated according to Equation 5.13.

5.1.1.4. Thermal Properties of Components in HE-53

To determine the wellbore heat transfer in HE-53 in Iceland, thermal conductivity values have been compiled for typical Icelandic rock types (Table 5.1). The data indicate an increasing thermal conductivity with decreasing porosity ϕ, i.e. increasing depth (Oxburgh and Agrell, 1982; Flóvenz and Saemundsson, 1993). For the

Table 5.2.: Fitted thermal conductivities for Hawaiian basalt with zero and 100 % porosity. Porosity is filled with air or water.

Saturation fluid	Porosity 0 %	100 %
Air	$\lambda(\phi)$ =1.79 W/(m K)	$\lambda(\phi)$ =0.18 W/(m K)
Water	$\lambda(\phi)$ =2.12 W/(m K)	$\lambda(\phi)$ =0.56 W/(m K)

uppermost 300 m, it is therefore in the lower range of measured values and can be estimated using the arithmetic mean (Flóvenz and Saemundsson, 1993):

$$\lambda(\phi) = (1 - \phi)\lambda_s + \phi\lambda_f \tag{5.17}$$

where ϕ is again the porosity and λ_s and λ_f is the thermal conductivity of the solid rock matrix and the thermal conductivity of the fluid phase, filling the pore space, respectively.

There exist several models to calculate the thermal conductivity of a mixture. Generally, the arithmetic mean is seen as the upper limit and the harmonic mean as the lower limit of all different models, whereas the geometric mean is more successful in describing measured conductivity values (Clauser and Huenges, 1995):

$$\lambda(\phi) = \lambda_s^{(1-\phi)}\lambda_f^{\phi} \tag{5.18}$$

Within the Hellisheiði geothermal field, basalts with an olivine tholeiitic composition can be found (Sigvaldason, 1969; Jakobsson, 1972). For mostly tholeiitic basalt samples and samples from olivine tholeiitic lava flows on the island of Hawaii, Robertson and Peck (1974) measured conductivities with an even greater variability than Oxburgh and Agrell (1982). Measured thermal conductivities in Hawaiian basalt samples vary between 0.84 W/(m K) and 2.4 W/(m K) for water saturated rocks and $0.88 - 1.80$ W/(m K) for dry samples, depending on the porosity (ϕ=0.02-0.98) (Robertson and Peck, 1974). A geometrical mean model has been fitted to the data of Robertson and Peck (1974) (see Figure 5.3) and end member conductivities have been determined by this fit. Table 5.2 lists the fitted thermal conductivities at zero and 100 % porosity for air and water saturated pores. Porosity values for mostly basaltic rock samples, listed in a database of rock properties in Icelandic geothermal systems, have been measured in the range $0 - 49$ % (Sigurdsson et al., 2000).

Grain densities for basaltic rocks range from $2200 - 3173$ kg/m^3(Robertson and Peck, 1974; Franzson et al., 2001) with an average value of 2958 kg/m^3 for the data measured by Robertson and Peck (1974).

Based on data from Bartoli (1890); Roberts-Austen and Rücker (1891); Poole (1914), Goranson (1942) determined the specific heat capacity of basalt at different temperatures according to:

$$c_p = c_1 + c_2 T - \frac{c_3}{T^2} \tag{5.19}$$

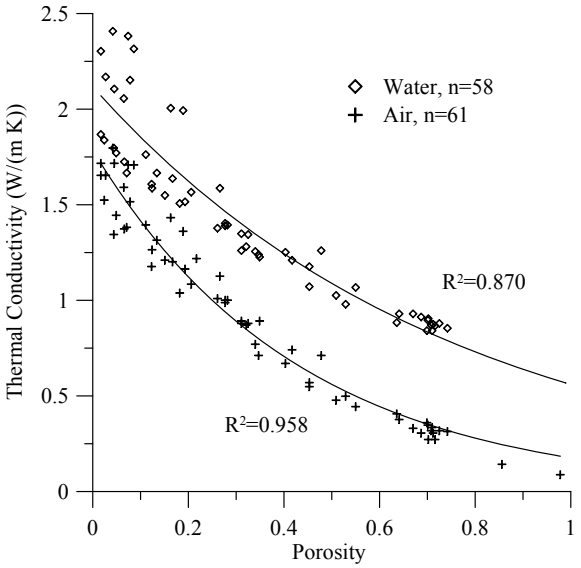

Figure 5.3.: Thermal conductivities vs. porosity of Hawaiian basalt samples measured for water and air saturated pores (Robertson and Peck, 1974). Data has been fitted by a geometrical mean function. The coefficient of determination R^2 is given together with the number of samples used to calculate the fit.

where T is the temperature in K and $c_1 - c_3$ are the constants 902 J/(kg K), 0.402 J/(kg K^2) and $0.122 \cdot 10^8$ (J K)/kg, respectively. Equation 5.19 is valid for the temperature range $0 - 1200$ °C with an error of ± 5 %. At 100 °C, e.g., the specific heat capacity of basalt is 964 ± 48 J/(kg K).

Similar to Equation 5.17, a linear relation for the density $\rho(\phi)$ and specific heat capacity $c_p(\phi)$ as a function of porosity ϕ can be deduced:

$$\rho(\phi) = \phi\rho_f + (1-\phi)\rho_s \tag{5.20}$$

$$c_p(\phi) = \phi\frac{\rho_f}{\rho}c_{p,f} + (1-\phi)\frac{\rho_s}{\rho}c_{p,b} \tag{5.21}$$

where ρ_f and ρ_s is the fluid and average solid density and $c_{p,f}$ and $c_{p,s}$ is the specific heat capacity of the fluid and the solid grains, respectively.

The water table in well HE-53 has been determined on the basis of a p/T log in well HE-36 to be in 118 m (Chapter 3). Above 118 m the porosity is assumed to be air-saturated, below, water-saturated.

5.1.2. Convective Heat Transfer

5.1.2.1. Heat Transfer to the Wellbore Fluid in Shut-in Periods

So far, only the conductive heat transfer phenomenon has been discussed. If the wellbore fluid is at different temperature than the surrounding casing, convective heat transfer between casing and fluid has to be considered. The heat transfer due to convection depends on the fluid properties like dynamic viscosity η, thermal conductivity λ, density ρ, and specific heat c_p, as well as the fluid velocity u. Furthermore, the geometry and roughness of the solid surface as well as the type of fluid flow (laminar or turbulent) influence the heat transfer (Cengel, 2002). Generally, the convection heat transfer can be described by Newton's law of cooling (Cengel, 2002):

$$\dot{Q}_{conv} = \psi_{conv} A (T_s - T_\infty) \tag{5.22}$$

where ψ_{conv} (W/(m^2 K)) is the convective heat transfer coefficient, A is the heat transfer surface area, T_s the surface temperature and T_∞ the temperature in great distance from the surface.

To quantify the increase in heat transfer through a fluid layer due to convection relative to pure conduction, the dimensionless Nusselt number Nu can be defined as (Cengel, 2002):

$$Nu = \frac{\dot{Q}_{conv}}{\dot{Q}_{cond}} = \frac{\psi_{conv} L_c}{\lambda} \tag{5.23}$$

where $\dot{Q}_{conv}$ is the convective heat transfer, involving some fluid movement, and $\dot{Q}_{cond}$ is the conductive heat transfer for a fluid at rest with a thermal conductivity λ. L_c is the characteristic length. The Nusselt number, therefore, describes the increase in heat transfer due to convection relative to pure conduction. A Nusselt number of $Nu = 1$, represents a pure conductive heat transfer across the fluid layer.

For a fluid in an enclosure, the heat transfer due to conduction and convection can be described using the concept of an effective thermal conductivity λ_{eff} (Cengel, 2002):

$$\lambda_{eff} = \lambda Nu \tag{5.24}$$

where λ is the thermal conductivity of the fluid.

There exist several empirical formulas to describe the Nusselt number of different surface geometries and fluids. In order to approximate the case of a fluid at rest in a vertical large diameter casing, the approximation for convection at a vertical plate has been applied within this study. After Cengel (2002), the Nusselt number for convective flow at a vertical plate with a constant surface temperature can be described by:

$$Nu = \left(0.825 + \frac{0.387 Ra^{1/6}}{[1 + (0.492/Pr)^{9/16}]^{8/27}} \right)^2 \tag{5.25}$$

where Ra is the Rayleigh number and Pr is the Prandtl number for the fluid. The Rayleigh number is the product of the Grashof number Gr and the Prandtl number (Cengel, 2002):

$$Ra = GrPr \tag{5.26}$$

where the Grashof number describes the ratio of the buoyancy force and the viscous force acting on the fluid (Cengel, 2002):

$$Gr = \frac{g\beta(T_s - T_f)L_c^3}{\nu^3} \tag{5.27}$$

where g is the gravity acceleration, β is the coefficient of volume expansion for the fluid, T_s and T_f are surface and fluid temperature, respectively. L_c is the characteristic length and ν the kinematic viscosity. Here, the hydraulic diameter, which is the ID of the casing, has been used as characteristic length.

The Prandtl number is a dimensionless quantity describing the relative thickness of the velocity layer to the thermal boundary layer, which forms at the interface between the surface and a convecting fluid (Cengel, 2002):

$$Pr = \frac{\nu}{\alpha} \tag{5.28}$$

where ν is again the kinematic viscosity and α is the thermal diffusivity of the fluid.

5.2. Experiments

Based on the preceding discussion, the DTS temperature measurements (Chapter 3) will be revisited. Using the simulated wellbore temperature profile (Chapter 4) and the measured temperature profile along the DTS cable during the flow testing period, the heat loss along the well can be quantified with a spatial resolution of 1 m[2] for both branches of the cable. In order to determine the heat transfer between the fluid flowing within the well and the surrounding formation, quasi-steady-state temperature conditions, i.e. a timestep-wise constant temperature difference between the wellbore fluid and the outer radius of the well, can be analysed. From the measured heat transfer, thermal parameters of the formation can be calculated. From the temperature during the cementation process, the influence of wellbore convection on the wellbore fluid temperature can be evaluated.

5.2.1. Conductive Heat Transfer to the Formation

In case of a constant temperature difference between the wellbore fluid and the DTS cable, the transfer of heat between the wellbore and the surrounding formation can

[2] 1 m is the spatial resolution of the measured DTS temperature data.

be calculated following Equations 5.10 and 5.11. This is the case for the DTS temperatures measured during the flow test (Chapter 3). Figure 3.8 shows a constant offset between measured DTS temperatures and wellhead temperatures. Using wellhead data, a wellbore temperature for every depth can be modelled according to Chapter 4. From the installation of the DTS sensor cable, the position of the cable within the annulus is known.

The DTS cable is installed behind the anchor casing. A four layer hollow cylinder model can be applied to calculate the heat loss. As a two-phase fluid is produced, the fluid flow within the well is turbulent. For a turbulent flow, the fluid temperature within each depth interval can be assumed to be homogeneous. Therefore, the inner wall of the production casing (first layer) is assumed to be at the wellbore fluid temperature ($T_f = T^{ID}_{csg,p}$). The cemented annulus between anchor casing and production casing forms the second layer, whereas the anchor casing itself is the third layer. Due to the varying distance between DTS cable and casing, the thickness of the forth layer varies. The heat loss can therefore be calculated according to:

$$\begin{aligned}\dot{Q} =& \frac{T^{ID}_{csg,p} - T_{DTS}}{R_t} = \frac{2\pi r^{ID}_{csg,p} U (T^{ID}_{csg,p} - T_{DTS})}{L} \\ =& (T_{csg,p} - T_{DTS}) \left(\frac{\ln\left(\frac{r^{OD}_{csg,p}}{r^{ID}_{csg,p}}\right)}{2\pi L \lambda_{csg}} + \frac{\ln\left(\frac{r^{ID}_{csg,a}}{r^{OD}_{csg,p}}\right)}{2\pi L \lambda_{cem}} + \frac{\ln\left(\frac{r^{OD}_{csg,a}}{r^{ID}_{csg,a}}\right)}{2\pi L \lambda_{csg}} + \frac{\ln\left(\frac{r_{DTS}}{r^{OD}_{csg,a}}\right)}{2\pi L \lambda_{cem}} \right)^{-1}\end{aligned} \tag{5.29}$$

where $T^{ID}_{csg,p} - T_{DTS}$ is the difference between simulated wellbore fluid temperature and the measured DTS temperature, λ_i is the thermal conductivity of the different layers and $r^{ID}_{csg,p}$ and $r^{OD}_{csg,p}$ is the inner and outer radius of the production casing, respectively. $r_{csg,a}$ is the radius of the anchor casing and r_{DTS} is the position of the cable.

Assuming a quasi-steady-state the temperature at the interface cement-formation can be calculated. After calculating $\dot{Q}$ from Equation 5.29, this equation can be used to determine the interface temperature T^{ID}_{for}. Exchanging r_{DTS} with the radius of the interface cement-formation r^{ID}_{for}, T_{DTS} with T^{ID}_{for} and using $\dot{Q}$ as input parameter, the interface T^{ID}_{for} can be calculated. In case of a further casing, the thermal resistance of a further casing and cemented annulus has to be considered.

From Equation 5.4 it is known, that the interface temperature T^{ID}_{for} changes for a constant heat transfer $\dot{Q}$. The heat transfer is generally not constant for a changing interface temperature, as the temperature difference between fluid and cement-formation interface varies. In HE-53, however, the wellhead temperature increased slowly, but constantly. The increase in the measured DTS temperature T_{DTS} is only slightly higher than the increase for the fluid temperature. Over a period of 300 h, the difference between both slopes has been determined to be 1.77 °C. The change in the temperature difference, is therefore small, if only short times are important.

Table 5.3.: Thermal conductivities λ and geometry information together with information on the error estimation used for calculation of formation thermal conductivity. For casing diameters see Table 3.1.

Material	*ID* (m)	*OD* (m)	λ (W/(m K))	Source
production casing	0.108 ± 0.001	0.122 ± 0.001	50 ± 5	(1)
cement	0.122 ± 0.001	0.157 ± 0.001	1.0 ± 0.2	(2)
anchor casing	0.157 ± 0.001	0.173 ± 0.001	50 ± 5	(1)
cement	0.173 ± 0.001	0.222 ± 0.001	1.0 ± 0.2	(2)
surface casing	0.222 ± 0.001	0.237 ± 0.001	50 ± 5	(1)
drill bit/cement	0.237 ± 0.001	0.267 ± 0.001	1.0 ± 0.2	(2)
formation		10000		

(1) Baehr and Stephan (2008)
(2) Nelson (1986)

A timestep-wise constant temperature difference and hence, quasi-steady-state temperature conditions can be assumed.

5.2.1.1. Results

As temperature increased during the flow test, a strong degradation of the optical properties, i.e. an increased attenuation, has been observed for the eastern branch below 175 m (Chapter 3). Therefore, only data for the uppermost 175 m of the well will be described in detail.

According to Equation 5.29, the heat loss has been calculated for every depth section and both cable branches. Geometry information used for the calculation is listed together with thermal conductivities in Table 5.3. Figure 5.4 shows the heat loss calculated from the temperature difference between modelled wellbore temperatures and measured DTS temperatures for both cable branches at 350 h_{DTS} after beginning of the DTS logging (approx. 300 h after beginning of flow test). On average, the overall heat loss within the surface casing ($10 - 60$ m) is 923 W/m for the eastern branch and 1090 W/m for the western branch. Below, ($70 - 150$ m), it is 872 W/m for the eastern branch and 905 W/m for the western branch. The standard deviation is 220 W/m and 176 W/m within, and 188 W/m and 239 W/m below the surface casing for the eastern and western branch, respectively. The corresponds to $16 - 26$ % of the average value.

Overall, the heat loss is similar for both cable branches, except for some specific depth intervals, where the measured difference between both branches is higher than 250 W/m. These are especially the depth intervals of $10 - 40$ m and depths below 142 m. Within the interval $10 - 40$ m, the difference is smallest close to the locations where the cable is attached to the centralizers at the casing joints. The increased difference corresponds to a depth interval of elevated CBL amplitudes from the

Table 5.4.: Error for quantities used in Equation 5.29. For details, see text.

Quantity	Associated error
r_{DTS}	± 0.005 m
T_{well}	± 1 °C
T_{DTS}	± 4.4 °C

production casing.

For the depths below 142 m, increasing differences in heat loss between both branches were observed. The difference increased with increasing depth below a narrow well section in $142 - 155$ m. Very large differences, up to 1000 W/m, have been calculated for depths below 155 m.

The error in heat loss determination $\dot{Q}_{L,err}$ has been determined on the basis of a error propagation procedure after Gauss. Table 5.3 and 5.4 list the errors related to each quantity in Equation 5.29. Δr_{DTS} is the error associated with the assumed position of the DTS cable (casing-cable distance). The error in well temperature ΔT_{well} has been determined in Chapter 4 and the error in DTS temperature measurements during the second logging campaign ΔT_{DTS} =2.6 °C in Chapter 3.

Another error is introduced by the assumption of a constant temperature offset between well and annular temperatures. The error for this assumption has been determined according to the difference in slope values in Chapter 3. After 300 h, the temperature offset changed by 1.77 °C. Furthermore, the heat transfer during the first hours of flow testing is much higher than assumed by the calculated temperature offset at a later time. Neglecting the uncertainties at the beginning and projecting the error introduced by the assumption of a constant temperature offset to the measured DTS temperature T_{DTS}, however, the error for the temperature uncertainty ΔT_{DTS} can be estimated to be $2.6 + 1.77 = 4.4$ °C.

Thermal conductivities for steel vary by ± 5 W/(m K) (Table 5.1) and variations in the thermal conductivity of cement is taken from Nelson (1986) for an assumed slurry density variation of approx. 100 kg/m^3 (see Figure 7.1). Figure 5.5 shows the calculated error for the measured heat loss (Figure 5.4). The error correlates with the location of the cable within the annulus. On average, the error is about 50 % of the measured value. Figure 5.6 shows the decentralized anchor casing within the cellar of HE-53. The decentralization is approximately e =3.5 cm. A significantly different heat loss between both branches, however, cannot be measured for the uppermost few meters of the well (Figure 5.6(b)).

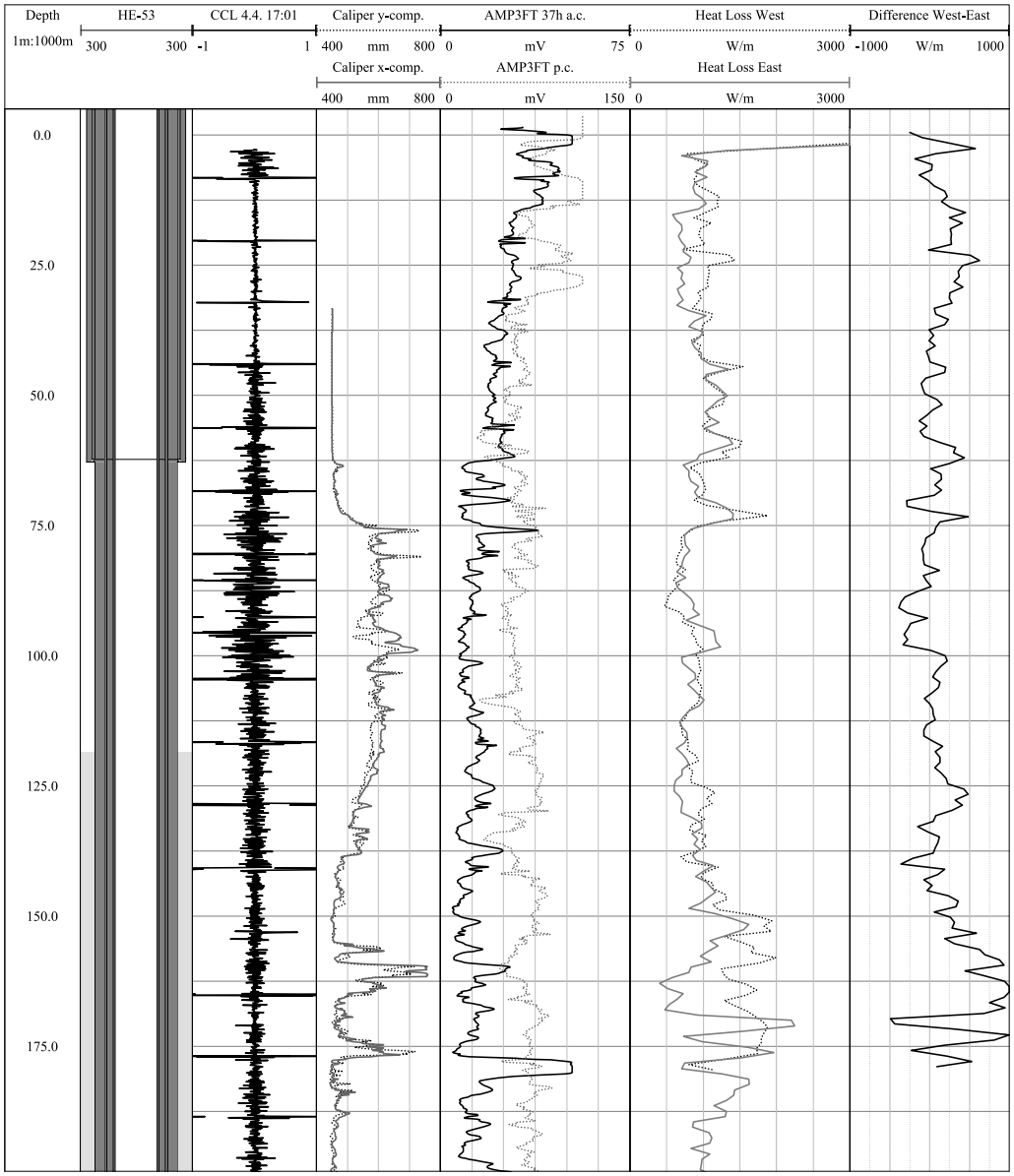

Figure 5.4.: The well design is shown together with a CCL log, calliper data and the CBL amplitude of a 3 ft transmitter receiver spacing (37 h after cementation) from the anchor casing (a.c.). Furthermore, a CBL log acquired for the production casing (p.c.) is shown. The formation water table behind the casing is indicated. Heat loss was calculated for both cable branches at the end of the second logging campaign, i.e. 350 h_{DTS} after beginning of logging.

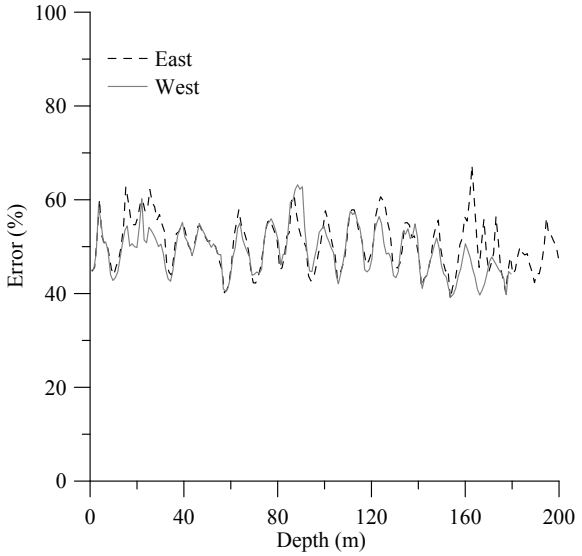

Figure 5.5.: Results for the error propagation for the measured heat loss after Gauss.

(a) Decentralized Anchor Casing in HE-53.

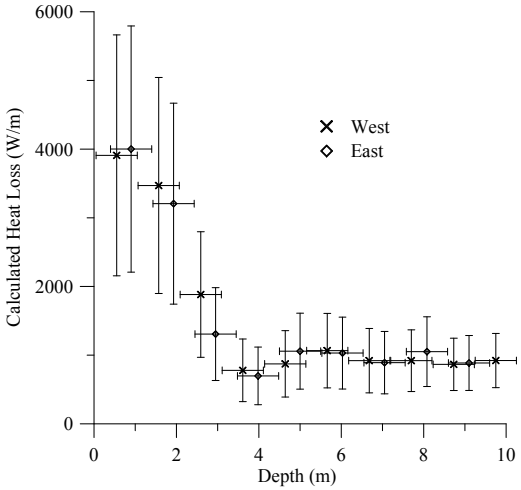

(b) Heat Loss.

Figure 5.6.: (a) Decentralized anchor casing in HE-53. On the lower right side, the eastern branch is visible, leaving the cemented annulus within the cellar of HE-53. On the left side, the western branch of the cable can be seen. (b) Heat loss vs. depth for both cable branches with associated error. Here an error of ± 0.5 m is assumed for the depth determination. For a detailed discussion, see text.

5.2.1.2. Discussions

Several uncertainties influence the result of this calculation. These can be subdivided into four main categories, related to the installation, the measurement technique, the wellbore temperature simulation and the simplified assumptions.

1. **Installation:** The exact position of the cable within the annulus is unknown. Absolute distances between cable and casing may vary by a few millimeters. The depth to the individual depth intervals for the DTS measurement is determined based on CCL data at the bottom of the installation as well as a cold spot at the surface. For the cold spot (25 cm) it is not known whether it is situated at the beginning or the end of a depth interval. The depth of installation adds another uncertainty, as the position of the centralizers after lifting the casing is only assumed to be directly below the casing joints, which have been located by a CCL log with an accuracy of a few centimetres. Furthermore, the cable has been cut at the turnaround. Where exactly it has been cut is unknown. The accuracy in depth is therefore less than 0.5 m. As thermal conductivities of different components of the subsurface installation are unknown, assumed values might increase the error of the calculated heat loss.

2. **Measurement:** The absolute accuracy of the measured temperatures at elevated temperatures is decreased and cannot be determined, as no reference temperature measurement has been performed under static temperature conditions. Therefore, the measured temperature might be skewed by a few degrees. The uncertainty of the measurement, however, is supposed to be less than 4.6 °C (bad connector, see Chapter 3).

3. **Simulation:** A wellbore temperature profile has been simulated from wellhead conditions. The accuracy of the simulation has been proven to be better than 1 °C for the time of the conventional temperature log (Chapter 4). The accuracy at other times, however, is unknown.

4. **Simplification:** Several assumptions and simplifications have been made for this calculation. The thermal properties of the different cylindrical layers have been taken from literature data and set to be constant at different temperatures. A large error is introduced, setting the cement quality to be constant with only little density variation (see Chapter 8). Furthermore, the accuracy of the geometric information, i.e. different radii of the casings, is unknown. The thermal expansion of the steel casings has been neglected, although the expansion of the different casings for a temperature increase of 200 °C is in the order of the error given in Table 5.3.

The error for both cable branches, is similar and depend on the same uncertainties in similar depth intervals. Absolute values of calculated heat loss might be

skewed by some erroneous assumptions on geometry or thermal parameters of the subsurface installations. A comparison between data acquired from opposite sides can nevertheless help to identify regions of interest.

Overall, the calculated heat loss from the measured DTS temperature is close to the theoretical heat loss calculated following the approach of Ramey Jr. (1962); Willhite (1967). For an arbitrary water saturated formation porosity of 30 %, which is in the range of porositiy values reported by Sigurdsson et al. (2000), the thermal parameters for the formation can be calculated according to Equations 5.18, 5.21, 5.20. Using Equation 5.4 the temperature at the interface can be approximated (Equation 5.16). From the temperature difference between fluid and interface, the heat loss can be calculated according to Equation 5.13. For an average fluid temperature of 230 °C and a formation temperature of 10 °C, the heat transfer to the formation after 300 h is 868 W/m, which is close to the value calculated from the measured DTS temperature (Figure 5.4). Within the section of the surface casing, the calculated heat transfer is 806 W/m, which is slightly lower than measured values. Although absolute values for the theoretical heat loss depend on the input parameters, there is a reasonable match between theoretical and measured heat loss values. Therefore, the estimated error for the measured heat transfer is probably lower than the calculated 50 %.

For the eastern cable branch, an average heat loss of 972 W/m has been calculated for the uppermost 175 m of the well at 350 h_{DTS}. Neglecting changes in the wellbore geometry as well as the formation temperature with depth, and assuming a constant heat loss along the entire length of the well (2463 m), a total loss of 2.4 MW can be estimated. At the same time, the thermal capacity of the well at the surface has been calculated to be 96 MW (Equation 4.10). The subsurface heat transfer is therefore in the range of 2.5 % of the thermal capacity of the well.

Based on the results from the calculation for both cable branches on either side of the casing, a decentralization of the casing cannot be detected. Especially at top, where a decentralisation can be observed between the anchor casing and the conductor pipe, a difference between the measured heat loss between both sides of the casing cannot be observed. A reason for this might be a decentralized production casing which compensates for the temperature differences of the decentralized anchor casing. Another possibility might be a different cement quality within the uppermost few meters. In Figure 5.6(a), however, the cement within the annulus behind the anchor casing seems to be homogeneously distributed.

As a centralizer has been installed beneath every joint below the surface casing and below every second joint within the surface casing and a clear trend indicating a decentralisation to a single side over the entire length of the well cannot be observed, the casing is assumed to be properly centralized below surface. Local differences in calculated heat loss might be caused by different cement qualities on different sides of the casing. A lower cement content, for example, can increase the heat transfer by allowing a fluid to convect within the annulus. Therefore the heat transfer is

greater in such depth intervals.

Different thermal properties on different sides of the casing were calculated for the depth interval $10 - 40$ m. A difference in heat loss of more than 250 W/m was calculated at positions which do not correspond to casing joints. At the joints, the difference between both cable branches was lower, indicating similar thermal conditions and a homogeneous heat transfer through the cemented annulus between production casing and anchor casing. In between the joints, where the cable is attached directly to the casing, a different heat loss has been measured. This corresponds to the elevated CBL amplitudes of the production casing. Changing cement properties within the annulus around the perimeter of the well can explain the different heat loss values. Another interval of elevated difference in heat loss was located in a depth below approx. 150 m, where calliper data shows a significant reduction in wellbore diameter. As the well has been cemented through the annulus, cement might have been pumped along preferred channels within the annulus. Therefore, more cement might have been placed on one side than the other.

5.2.2. Thermal Properties of the Formation

The annular temperature evolution is dependent on the thermal properties of the formation. Thermal conductivity, specific heat capacity and density determine the thermal heat transfer to the formation at any time. For an improved understanding of the annular DTS temperature evolution during different activities in HE-53, it is therefore important to constrain the reasonable range of thermal formation properties discussed in Section 5.1.1.4.

The heat transfer to the formation is directly related to the formation thermal properties (Carslaw and Jaeger, 1959; Ramey Jr., 1962). If the thermal heat transfer is known, the thermal properties of the formation can be estimated (e.g. Günzel and Wilhelm, 2000; Eppelbaum and Kutasov, 2006; Freifeld et al., 2008). Günzel and Wilhelm (2000); Freifeld et al. (2008) for example used DTS temperature data of a temperature recovery after applying a known thermal perturbation to the wellbore to estimate the formation thermal conductivity. Eppelbaum and Kutasov (2006) modified the semi-analytical solution of Kutasov and Kagan (2003) to calculate the wall temperature of a constant heat source in order to to obtain the formation thermal conductivity by measuring the wall temperature. A relation between the wall temperature of a variable heat source and the formation thermal conductivity is given in Kutasov (2007).

Within this study, a relation between porosity, thermal conductivity, specific heat capacity and density is used in combination to measured DTS temperature data and wellhead information on the produced fluid in order to characterize the formation surrounding the well. The formation porosity, thermal conductivity, specific heat capacity and density is determined using the measured heat transfer (Section 5.2.1) and applying the line source model proposed by Carslaw and Jaeger (1959).

During heating of the well, the cement-formation interface temperature changes. Therefore, steady state conditions cannot be reached. The difference between wellbore fluid and DTS cable temperatures, however, is apparently almost constant after a few hours of hot fluid production. Therefore, the heat loss is nearly constant over time. Assuming a timestep-wise constant DTS temperature and extrapolating the measured DTS temperature to the cement-formation interface by the means of the previously calculated heat loss, the interface temperature can be determined for every time step.

Applying the line source model from Equation 5.4 to the calculated heat loss $\dot{Q}_L$ (Section 5.2.1) and the temperature T_{for}^{ID} at the cement-formation interface r_{for}^{ID}, the relation between the thermal diffusivity α_{for} and the thermal conductivity of the formation λ_{for} is defined:

$$\lambda_{for} = \frac{\dot{Q}_L}{4\pi T_{for}^{ID}(t)} \left[-Ei(-\frac{r_{for}^{ID\ 2}}{4\alpha_{for} t}) \right] \tag{5.30}$$

where t is the time of the temperature measurement in seconds after beginning of heating. Equation 5.30 cannot easily be solved, as the thermal diffusivity of the formation $\alpha_{for}(\lambda_{for}, c_{p,for}, \rho_{for})$ is a function of λ_{for}, $c_{p,for}$ and ρ_{for}. For a given density and specific heat capacity, however, the thermal conductivity can be calculated according to an iterative procedure:

1. Estimate a reasonable λ_{for}.
2. Calculate the thermal diffusivity $\alpha_{for} = \frac{\lambda_{for}}{\rho_{for} c_{p,for}}$ for a constant ρ_{for} and $c_{p,for}$.
3. Calculate the exponential integral $Ei\left(-\frac{r_{for}^{ID\ 2}}{4\alpha_{for} t}\right)$.
4. Solve Equation 5.30 to calculate a new λ_{for}.
5. Calculate a new thermal diffusivity α_{for}.
6. Restart at Step 3 until the change in λ_{for} between subsequent steps is negligible.

A relation between porosity ϕ and thermal parameters of Icelandic rocks is given by Equations 5.17, 5.20 and 5.21. The thermal parameters of the formation can therefore be described by a single parameter ϕ. For pure conductive heat transfer, Equations 5.17 and 5.30 can be combined to:

$$g(\phi) = \left| \frac{\dot{Q}_L}{4\pi T_{for}^{ID}(t)} \left[-Ei(-\frac{r_{for}^{ID\ 2}}{4\alpha(\phi) t}) \right] - \left(\lambda_{rock}^{(1-\phi)} \lambda_{fluid}^{\phi} \right) \right| \tag{5.31}$$

where $g(\phi)$ represents the absolute difference between calculated and measured thermal conductivity and $\alpha(\phi) = \frac{\lambda(\phi)}{\rho(\phi) c_p(\phi)}$ is the porosity dependent thermal diffusivity.

Equation 5.31 cannot be solved analytically for ϕ. Therefore, $g(\phi)$ has to be minimized by variation of the porosity. In case there is a porosity ϕ so that $g(\phi) = 0$, the thermal behaviour can be described by thermal conduction, alone. In case the measured thermal conductivity exceeds the theoretical value given by a porosity of 0.02 % (lowest value in Robertson and Peck, 1974), a pure conductive process cannot describe the heat transfer to the formation. Fluid convection within the porous formation has to account partly for the heat transfer.

In order to account for the heat transfer via convection, an effective thermal conductivity λ_{eff} can be determined similar to Equation 5.24. For an arbitrary porosity of 50 %, which is the maximum porosity reported in the database of igneous rocks in icelandic geothermal systems (Sigurdsson et al., 2000), the effective thermal conductivity in Equation 5.32 can be varied so that $g(\phi)$ is minimised:

$$g(\phi) = \left| \frac{\dot{Q}_L}{4\pi T_{for}^{ID}(t)} \left[-Ei(-\frac{r_{for}^{ID\ 2}}{4\alpha_{eff}(\phi)t}) \right] - \lambda_{eff} \right| \tag{5.32}$$

where $\alpha_{eff}(\phi) = \frac{\lambda_{eff}}{\rho(\phi)c_p(\phi)}$ is the effective thermal diffusivity for a given porosity. The effective thermal conductivity λ_{eff} can be used to calculate a pseudo Nusselt number Nu^* for every depth according to:

$$Nu^* = \frac{\lambda_{eff}}{\lambda(\phi = 0.5)} \tag{5.33}$$

The Nusselt number is defined as the relation between conduction and convection for a fluid in an enclosure. This concept cannot be applied, as the formation is a two component system of a solid and liquid phase. The concept of relating conductive and convective heat transfer, however, can be applied. Therefore, the dimensionless number relating both phenomena is called the pseudo Nusselt number Nu^*.

The error in determining the formation thermal conductivity has been determined based on the error estimation in the heat loss $\dot{Q}_{L,err}$ (Section 5.2.1). For every depth interval z, a maximum heat loss $\dot{Q}_{L,max}(z) = \dot{Q}_L(z) + \dot{Q}_{L,err}(z)$ and a minimum heat loss $\dot{Q}_{L,max}(z) = \dot{Q}_L(z) - \dot{Q}_{L,err}(z)$ has been calculated. For these values a maximum and minimum cement-formation interface temperature has been calculated, neglecting the uncertainties in the radius and thermal conductivity of the cement between the cable and the cement-formation interface, $T_{for,max}^{ID}$ and $T_{for,min}^{ID}$, respectively. Maximum and minimum values have been used to calculate maximum and minimum thermal parameters of the formation.

5.2.2.1. Results

In Figure 5.7, the calculated heat loss is shown together with the deduced thermal conductivities and thermal diffusivities of the formation. For simplicity, a single specific heat capacity of solid basalt ($c_{p,s}$) has been chosen for the calculation.

1040 J/(kg K) has been calculated for a temperature of 200 °C according to Equation 5.19. In depth intervals, where a solution of Equation 5.31 could be determined based on pure conductive heat transfer, this value λ is displayed. For a pure conductive solution, the Nusselt number is $Nu = 1$. In case a pure conductive solution was not found, the effective thermal conductivity λ_{eff} is shown. The same applies to the thermal diffusivity.

Depths of high heat loss correspond to depths of high thermal conductivities and high thermal diffusivities. In depth intervals of 50 % porosity, a pure conductive result was not obtained. Additional convective heat transfer is needed to account for the measured heat loss. Above 118 m, the porosity is assumed air saturated; below, to be water saturated.

Significantly elevated conductivities can be observed at the surface, in the depth interval $40 - 60$ m as well as in about 73 m and 97 m depth and below 150 m. A clear correlation between thermal parameters and the lithology was not observed, although low conductivity values are concentrated in the depth interval of basaltic breccia ($103 - 141$ m). Here, a purely conductive process can explain the observed heat loss.

The error calculated for the heat loss, $\dot{Q}_{L,err}$, has been used to estimate the error in determining the formation thermal properties. Figure 5.8 shows the error associated with minimum and maximum heat loss values, which can be higher than 10 W/(m K) in some depth intervals.

In order to test whether the calculated thermal parameters correlate with the cement properties within the annulus of the anchor casing, i.e. if the calculated thermal conductivity of the formation is sensitive to the cement quality only, Figure 5.9 shows the Bond Index versus the calculated thermal conductivity. The Bond Index was calculated based on the measured CBL 3 ft amplitude measured for the anchor casing 37 h after beginning of cementation (see Chapter 7). The coefficient of determination R^2 for a linear fit is 0.0008 and 0.0025 for the eastern and western branch, respectively. A correlation between both quantities was therefore not observed.

5.2.2.2. Discussions

For the calculation of the formation porosity and hence the thermal parameters of the formation, the following assumptions have to be made:

1. Steady temperature difference between wellbore and cable for every depth section, i.e. a constant heat loss to the formation.

2. Homogeneous thermal conductivities for every component of the subsurface installation (e.g. homogeneous cement).

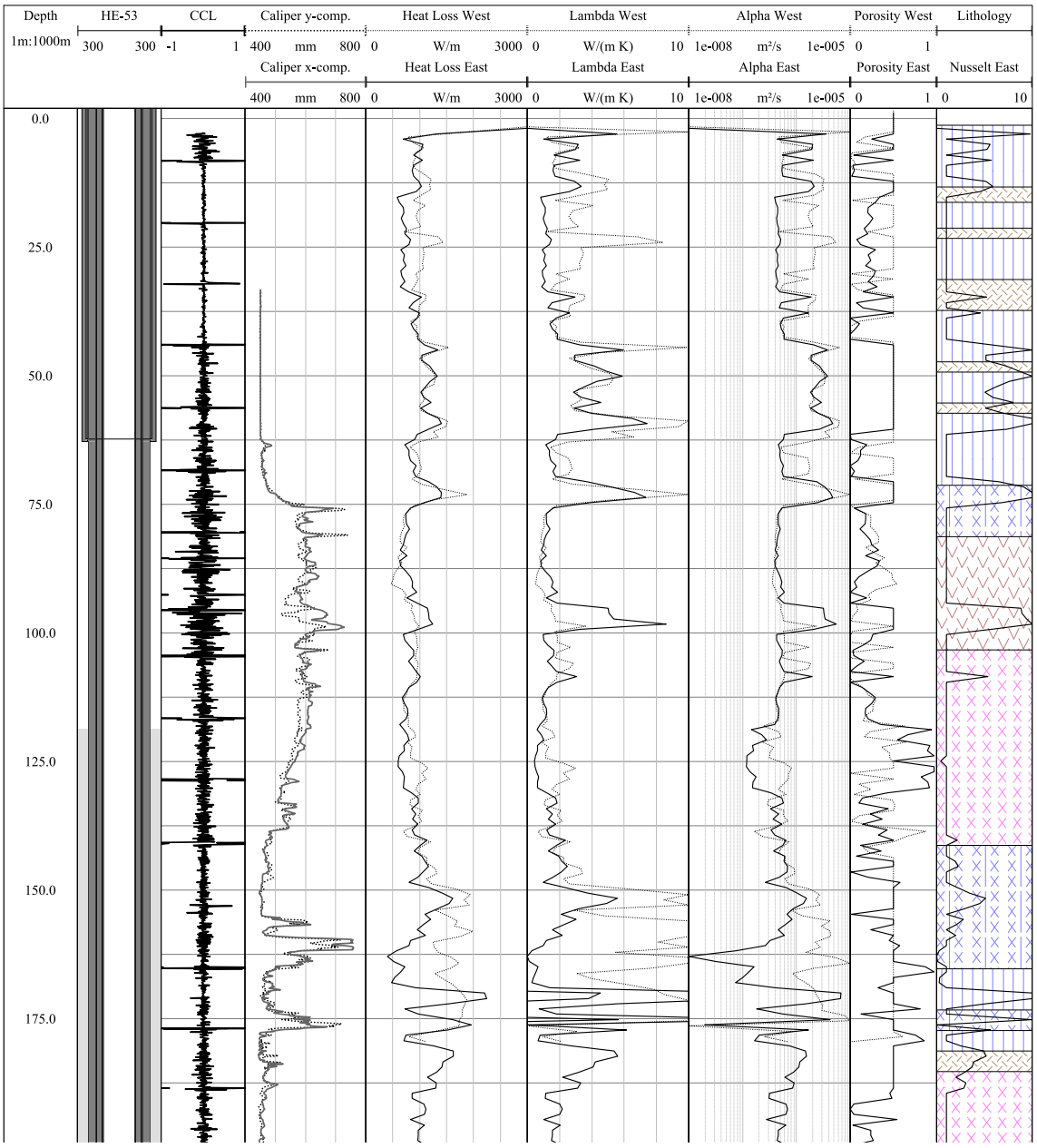

Figure 5.7.: The well design is shown together with a CCL log and calliper data. From the calculated heat loss, the porosity and from this the effective thermal conductivity as well as the thermal diffusivity of the formation were calculated for both cable branches. A porosity of $\phi = 0.5$ has been assumed if a conductive solution was not found. A lithology log is shown in comparison to the pseudo Nusselt number Nu^*. See text for further information. The lithologic units are explained in Appendix B. Well design, CCL, calliper and lithologic data courtesy of Reykjavik Energy.

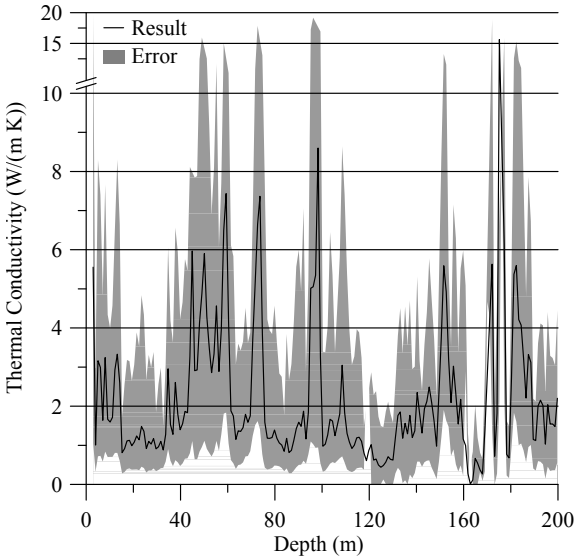

Figure 5.8.: Error in calculating the thermal conductivity for the eastern cable branch.

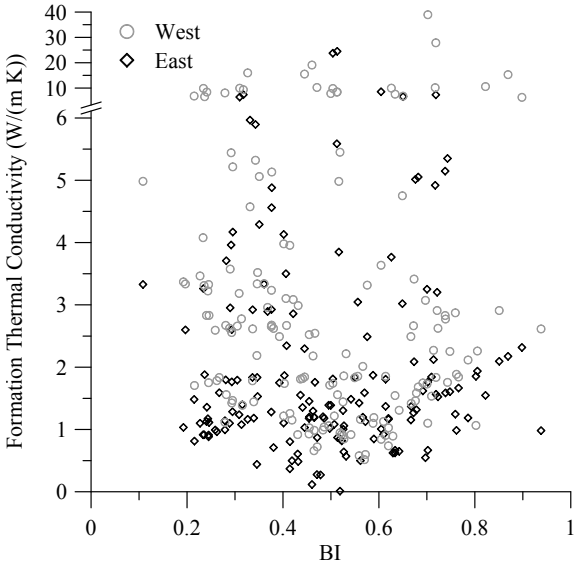

Figure 5.9.: Comparison of thermal conductivity and Bond Index for the anchor casing calculated at 37 h after cementation. A dependency of the calculated thermal conductivities of the formation on the Bond Index was not observed.

3. Centralized Casing.

4. Smooth calliper for every depth section.

5. Smooth differences in thermal conductivities between different depth intervals and therefore a small vertical temperature gradient.

6. Homogeneous thermal properties for the formation in every depth interval.

Using the geometry information and the thermal conductivities listed in Tables 3.1, 5.1 as well as Table 5.3, and having data about the radial distance between anchor casing and cable (Appendix D), the total heat loss from the well can be calculated for every depth interval according to Equations 5.10 and 5.11. Together with the calliper information and the DTS temperature measurement, the heat transfer can be used to calculate the temperature at the interface between cement and formation (Equation 5.10).

Using the interface temperature and the information about the time the well has been heated with the calculated thermal power, the thermal conductivity can be calculated according Equation 5.4, if the density and specific heat capacity of the formation is known. If not, Equation 5.31 has to be minimized. For the calculation, a series expansion has been performed until differences between values calculated for the Ei function were negligible. Although the wellbore diameter is quite large and the production time of 300 h rather short, i.e. the line source approach a strong simplification, the calculated formation properties are reasonable. Measurements at greater times would even reduce the error introduced by the simplified line source approach.

The absolute error calculated for the formation thermal conductivities appears to be quite high. In Section 5.2.1, however, it was stated that the error in heat transfer is probably overestimated, so the resulting error in thermal conductivity might be overestimated in practice.

In order to test the correlation between the cement quality behind the anchor casing and the calculated thermal parameters of the formation, two different quantities, obtained using different physical phenomena, have been compared. The Bond Index, calculated from the CBL data of the anchor casing, recorded during the cementation process has been plotted versus the calculated thermal conductivity. Although the heat loss calculation is sensitive to a change in the cement quality, i.e. the density and thermal conductivity of the cement, and the variation in the cement density is probably larger than the assumed ± 100 kg/m^3 (see Chapter 8), a clear trend cannot be observed between both datasets. The calculated formation thermal properties are therefore not dependent on the cement quality behind the anchor casing, alone.

In case of calculated thermal conductivities higher than 2.12 W/(m K), which is the maximum conductivity for the rock matrix (see Table 5.2), heat transfer to the formation is increased. Beside an increased cement density or a possible convective

fluid movement within the annulus, a convective fluid movement within the formation might cause an elevated heat transfer. As the water table within the formation is below 118 m, convective liquid movement is a reasonable explanation below this depth. Above, convecting air might have caused decreased temperatures, although this effect should be smaller than for water. Furthermore, rocks not represented by relations 5.18 to 5.21 are a reasonable explanation.

During drilling activities, several cement plugs have been placed in the section of the surface casing as well as the anchor casing. Drilling fluid has been injected into the formation in different depth intervals and cement has been lost to the formation during the cementation of the casings. Furthermore, the simple relations between porosity and thermal properties of the formation do not account for a contamination of the pore space with cementious materials. Therefore, although the heat loss is purely conductive, a simple conductive solution for the thermal properties might be obscured. The calculated thermal conductivities, however, lie very well in the expected range. Furthermore, zones of total drilling fluid loss in about $150 - 160$ m (Table 1.1 and Appendix A) can be correlated with elevated thermal conductivity values. The determined formation thermal properties might therefore be regarded as *apparent thermal properties*.

5.2.3. Heat Transfer to the Wellbore Fluid in Shut-in Periods

During the hydration of cement, heat is generated within the annulus. In order to understand the temperature evolution within the annulus, the convective heat transfer to the wellbore fluid has to be analysed. It can be determined from conventional wireline temperature logs acquired during the cementation of the casing. From the change in thermal energy of the wellbore fluid during the cement hydration, i.e. the change in temperature, an average convective heat transfer coefficient $\overline{\psi}_{conv}$ can be determined:

$$\overline{\psi}_{conv} = \frac{(T(t_1) - T(t_2))\rho_f c_p V_f}{A_{ID}\Delta t} \tag{5.34}$$

where V_f is the volume of fluid within the depth interval, A_{ID} is the inner surface area of the pipe within this interval, $T(t_1) - T(t_2)$ is the temperature change of the fluid during the time interval $\Delta t = t_2 - t_1$. ρ_f and $c_{p,f}$ are the fluid density and heat capacity, respectively. The calculated heat transfer coefficient is required to heat the wellbore fluid and can be compared to the theoretical value, determined for a convecting fluid at a planar, vertical surface.

5.2.3.1. Results

During the cementation process, three successive conventional temperature logs have been measured during the hydration of the cement (see Appendix, Table C.1). As can be seen in Figure 5.10, the temperature variation between the fluid temperature

and the DTS temperature within the cement is very small in the lower part of the well, beneath 107 m. The first temperature data have been logged at the beginning of the rapid hydration reaction, whereas the second temperature log has been done a few hours later at the time of most rapid hydration reaction. The last measurement was done after the hydration reaction already slowed down in some depth intervals. Conventionally logged temperatures are slightly higher than DTS measurements except for areas of large borehole breakouts, where the temperature increase is higher due to the larger amount of hydration products. Another feature influencing the DTS temperature is the location of the cable within the annulus (see Chapter 3). The average temperature difference for the depth interval $113 - 260$ m is 0.76 °C, 0.53 °C and 1.66 °C for the first, second and third log, respectively.

5.2.3.2. Discussions

As mentioned in Chapter 3, cold water has been filled into the well prior to the first CBL log. During the first and second temperature log, the water level within the well was at approx. 107 m. Furthermore, DTS temperatures have been determined to be 1.3 °C too low, on average (Chapter 3). Accounting for this inaccuracy and taking into account the large borehole breakouts, temperatures behind casing (DTS) and within the well (conventional log) are similar.

Conventional wireline tools are commonly decentralized, if not properly centralized. Especially in large diameter casings a decentralization is likely to occur. Most probably, the temperature logging tool is touching the casing wall along the entire depth of the well. Therefore, the temperature information was measured close to the casing wall, where temperatures should be higher than in the centre of the casing. As temperature changes between adjacent depths are less pronounced for the conventional temperature log than for the DTS measurement, e.g. at locations of large borehole breakouts, a thermal homogenization of the wellbore fluid temperature between different depth intervals occurred. Such a homogenization mechanism can only be explained by a convective fluid movement, as the thermal conductivity of water is too low to account for a homogenization over several meters.

In order to quantify the heat transfer between anchor casing and wellbore fluid, calculations are done for a single depth, exemplary. For a 1 m interval in 120 m depth, a temperature difference between first and second reference log up to 14 °C has been measured. In order to heat the fluid column within the anchor casing by 14 °C, a constant thermal power of 126 W/m is needed for the time between the two successive measurements. This value can be compared with a pure conductive heat transfer process. The measured temperature difference between casing (from DTS) and wellbore fluid (from conventional log) is $T(120\text{ m}) - T_{DTS}(120\text{ m}) = -0.91$ °C. Adding the average measurement offset for the first logging campaign (1.3 °C, see Chapter 3), the temperature difference between DTS and conventional temperature

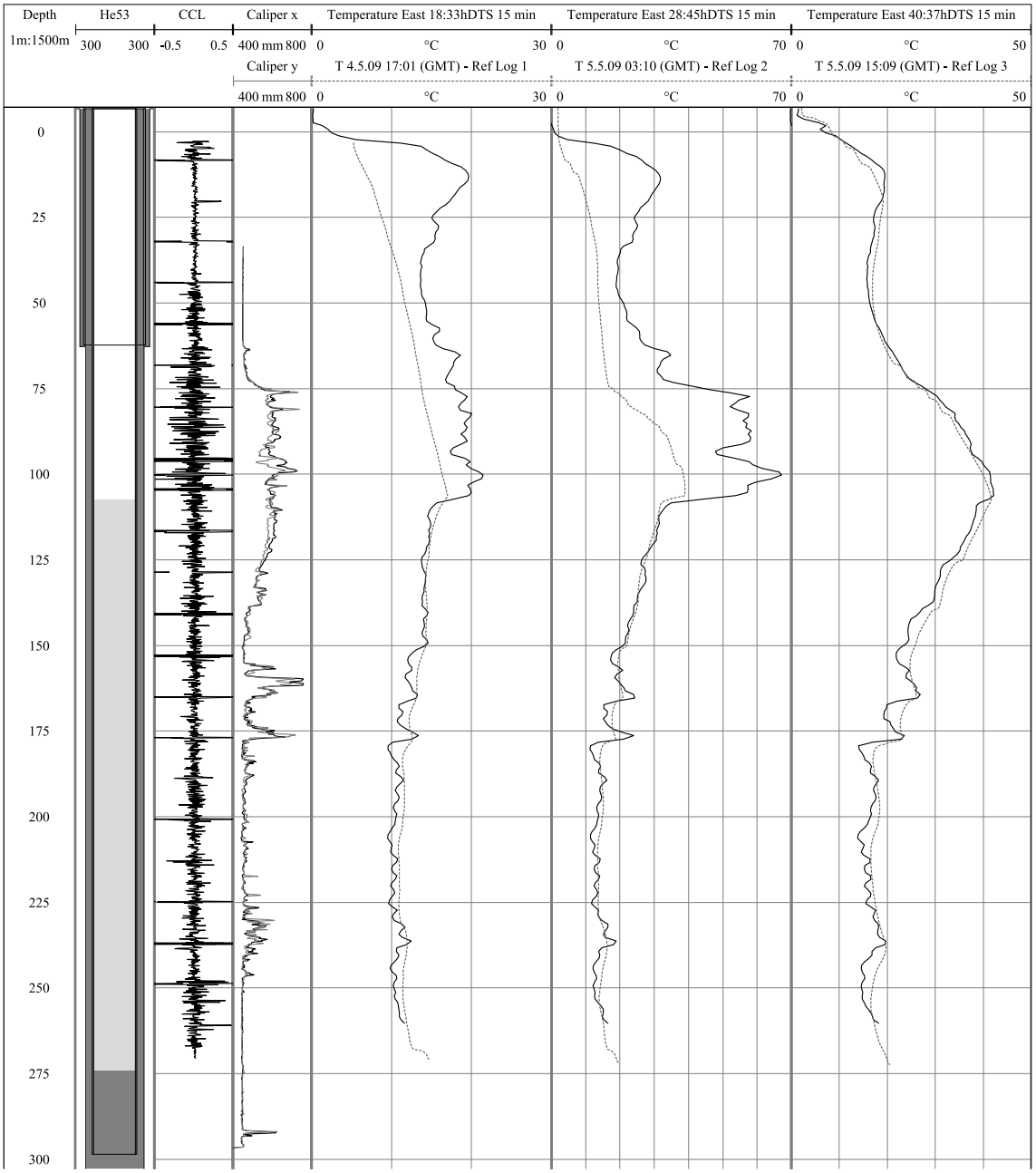

Figure 5.10.: Comparison of logs from the cement job. Casing collar locator log (CCL) and calliper log are displayed together with temperature logs from a conventional wireline temperature gauge in comparison to 25 minute averages of DTS temperature data during hydration of the cement.

data is less than 2.5 °C, for a distance of more than 2 cm between conventional temperature gauge and casing wall. Assuming that the temperature difference has been as low as 2.5 °C, which is reasonable, as the second temperature log has been acquired at a time of most rapid temperature increase in the well, and applying Equation 5.3 for a surface area of 0.87 m^2 (circumferential surface around logging tool), the calculated thermal power is only 65 W/m. This is not sufficient to heat the entire fluid volume within the casing.

Applying Equations 5.24 - 5.28 for a convecting fluid at a vertical plate to calculate the effective thermal conductivity λ_{eff} for liquid water at 20 °C and a temperature difference of 2.5 °C, the thermal conductivity of the wellbore fluid is increased by a factor of four. The heat transfer is therefore enhanced and 254 W/m can be transmitted to the wellbore fluid.

Assuming a homogeneous wellbore fluid temperature, the assumption of a convecting fluid at a vertical plate can be used to sufficiently calculate the low temperature difference between DTS temperature measurements and the wellbore fluid. Furthermore, homogenised temperatures over several depth intervals, as observed at locations of large breakouts, can be sufficiently explained by a convective wellbore fluid flow. From the available data, however, it is not possible to decide whether this approach overestimates the heat transfer between casing and fluid. Only the lower limit can be examined, i.e. the minimum heat transfer necessary to reproduce the observed temperature difference.

5.3. Conclusions

Due to several uncertainties and assumptions for the installation as well as uncertainties in the DTS temperature measurements, the calculated error for the values determined within this chapter is relatively high. Average values, however, lie very well within the expected range. Therefore, heat loss values, thermal properties of the formation as well as the determined heat transfer coefficient will be used for further calculations.

6. Annular Temperature Simulator

Different wellbore activities like cementation or flow testing led to changing temperatures along the DTS cable. The aim of this chapter is to develop and test an annular temperature simulator capable of modelling the temperature evolution within the annulus for variable wellbore conditions.

6.1. Model Formulation

Based on the theoretical discussion in Chapter 5, a one-dimensional radial symmetric finite-difference model has been implemented in Python (van Rossum, 1995) in order to solve the conductive heat transfer equation and to simulate the temperature evolution within the annulus during cementation and flow testing. Different criteria for the boundary conditions apply for the cementation and flow testing period. The general transient temperature model will be described within this chapter. Specific changes to the model, based on the scenario to be modelled, will be discussed in the following chapters.

6.1.1. Geometry and Discretisation

As shown in Figure 6.1, the wellbore has been discretised in radial direction. The step size between individual nodes is equidistant for all cylindrical layers except for the formation, where it increases exponentially. The step size and radius to the contact between two materials has been adjusted such that the position of the contact node coincides with the location of the contact. Three types of nodes have been assigned. Boundary nodes represent the first node at the contact casing - wellbore fluid and the last node of the formation. Inner nodes have adjacent nodes with equal material properties next to them. Material contacts are represented by contact nodes. These nodes have different thermal properties on either side of the node, representing the two materials in contact. A perfect thermal contact is assumed.

6.1.2. Finite-Difference Model

For the discretisation discussed above, a finite-difference model has been implemented. For every layer (casing, cement and formation), four parameters have been

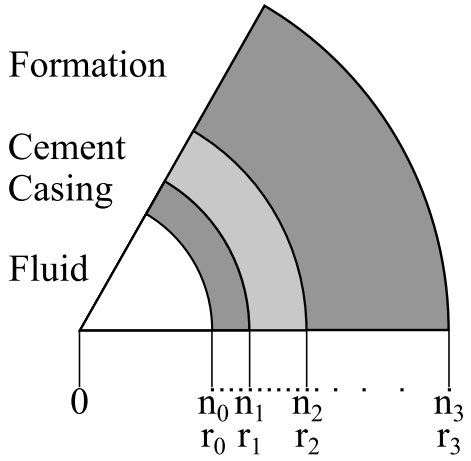

Figure 6.1.: Geometry and discretisation of the one-dimensional radial symmetric wellbore model. Nodes are displayed at the bottom. The radius to different material contact nodes is denoted with r_i, n_i denotes the number of nodes before the material contact.

assigned:

1. thickness d_i
2. thermal conductivity λ_i
3. specific heat capacity $c_{p,i}$
4. density ρ_i

where the subscript i denotes the different materials. Parameters 2 to 4 are used to calculate the thermal diffusivity $\alpha_i = \frac{\lambda_i}{\rho_i c_{p,i}}$ for every material. Equation 5.2 is used to calculated the transient temperature change at every node n. For the calculation, an implicit scheme has been implemented.

In order to calculate the differential Equation 5.2, the derivatives are replaced by central finite-differences. The temperature at every node $T(r_n)$ is influenced by the temperature at neighbouring nodes $T(r_{n-1})$ and $T(r_{n+1})$, and material properties between them. The resulting system of linear equations to be solved for the transient temperature change due to conduction at location r_n and time $j\Delta t$ in implicit expression is therefore:

$$T(r_n)^j = M \begin{pmatrix} T(r_{n-1})^{j+1} \\ T(r_n)^{j+1} \\ T(r_{n+1})^{j+1} \end{pmatrix} \tag{6.1}$$

with the matrix M, representing the coupling between different nodes and j indicates the number of time steps Δt. Numerically, the linear matrix equation is solved using the LAPACK routine *dgesv* (Anderson et al., 1999) implemented in the NumPy package (Ascher et al., 1999).

6.1.2.1. Inner Node

In order to approximate the transient temperature change at an inner node n, finite-differences are calculated for each node. The matrix M becomes (Crank, 1975; Pirow and Buchen, 2004):

$$\left(\; -\frac{\alpha\Delta t}{V_{in}+V_{out}}\left(\frac{A_{in}}{\Delta r_{in}}\right) \quad 1+\frac{\alpha\Delta t}{V_{in}+V_{out}}\left(\frac{A_{in}}{\Delta r_{in}}+\frac{A_{out}}{\Delta r_{out}}\right) \quad -\frac{\alpha\Delta t}{V_{in}+V_{out}}\left(\frac{A_{out}}{\Delta r_{out}}\right) \; \right) \tag{6.2}$$

with $A_{out} = 2\pi(r+0.5\Delta r_{out})h$ and $A_{in} = 2\pi(r-0.5\Delta r_{in})h$ being the surface area to the neighbouring outer and inner node, respectively. Δr_{in} and Δr_{out} is the distance between neighbouring inner and outer nodes and h is the height of an element. $V_{in} = \pi r^2 h - \pi(r-0.5\Delta r_{in})^2 h$ and $V_{out} = \pi(r+0.5\Delta r_{out})^2 h - \pi r^2 h$ are the volumes on the inner side and outer side of the node, belonging to this node. For an equidistant step size, this simplifies to:

$$\left(\; -\tau(\tfrac{1}{\Delta r}-\tfrac{1}{2r}) \quad 1+2\tfrac{\tau}{\Delta r} \quad -\tau(\tfrac{1}{\Delta r}+\tfrac{1}{2r}) \; \right) \tag{6.3}$$

with an auxiliary expression $\tau = \frac{\alpha\Delta t}{\Delta r}$.

6.1.2.2. Contact Node

For contact nodes, the matrix 6.2 is adjusted for the different materials. For simplicity, contact nodes have an equidistant step size on either side:

$$\left(\; -\tau_2\left(\frac{A_{in}\lambda_{in}}{\Delta r}\right) \quad 1+\tau_2\left(\frac{A_{in}\lambda_{in}}{\Delta r}+\frac{A_{out}\lambda_{out}}{\Delta r}\right) \quad -\tau_2\left(\frac{A_{out}\lambda_{out}}{\Delta r}\right) \; \right) \tag{6.4}$$

where $\tau_2 = \frac{\Delta t}{V_{in}\rho_{in}c_{p,in}+V_{out}\rho_{out}c_{p,out}}$ and the subscripts *in* and *out* indicate properties on the inner and outer side, respectively.

6.1.2.3. Boundary Node

A Dirichlet boundary condition has been chosen for the outermost node $n = N$. The temperature is held constant at r_N. Therefore, Equation 6.1 simplifies to:

$$T(r_N)^j = \left(\; 0 \quad 1 \; \right) \left(\begin{array}{c} T(r_{N-1})^{j+1} \\ T(r_N)^{j+1} \end{array} \right) \tag{6.5}$$

Different boundary node criteria apply for the cementation period and for the flow testing period. In order to model the temperature evolution during the cementation process, the concept of a mirror node (Neumann boundary condition, no-flow) has been chosen for the first node $n = 0$ at the interface wellbore fluid - production casing. Equation 6.1 becomes (Cengel, 2002):

$$T(r_0)^j = \left(\; 1+\tau\tfrac{2}{\Delta r^2} \quad -\tau\tfrac{2}{\Delta r^2} \; \right) \left(\begin{array}{c} T(r_0)^{j+1} \\ T(r_1)^{j+1} \end{array} \right) \tag{6.6}$$

with $\tau = \frac{\alpha \Delta t}{\Delta r}$.

During the cementation, heat is transferred between the anchor casing and the wellbore fluid. In order to model the heat transfer between casing and fluid, the concept of convective heat transfer at a vertical plate (Equation 5.25) has been chosen. For each calculation step, the heat transfer has been calculated based on the temperature difference between casing and wellbore fluid. Due to convection, the wellbore fluid is assumed to be isothermal and heat is exchanged with the first two nodes of the casing. Each node contribute with half the energy, which is exchanged with the fluid (see Chapter 7).

For the flow testing period, a Dirichlet boundary condition has been chosen at the interface. The hot wellbore fluid is assumed to keep the first node at constant temperature for a specific depth interval. This assumption is validated as a two phase fluid is produced. The heat transfer between wellbore fluid and casing slightly changes its density. From Section 4.2, however, it is known that the wellbore fluid temperature change due to conductive heat transfer to the formation is negligible. Furthermore, a high fluid production rate of 63 kg/s (Figure 3.12, averaged over the first 300 h of production) and a density of 81 kg/m^3 (at wellhead pressure p_0), i.e. a turbulent fluid ascent with a velocity of 21 m/s, assures a low residence time of the fluid within each depth interval. The boundary node at the interface wellbore fluid - casing therefore changes to:

$$T(r_0)^j = \begin{pmatrix} 1 & 0 \end{pmatrix} \begin{pmatrix} T(r_0)^{j+1} \\ T(r_1)^{j+1} \end{pmatrix} \tag{6.7}$$

6.1.3. Initial Conditions

Different initial conditions apply for the different simulated scenarios. The specific initial conditions used for each simulation will be described when the model is applied in the following chapters.

6.2. Model Validation

In order to validate the finite-difference model, modelled temperatures have been compared to the analytical solution at steady state conditions for a one and a two layer model (Figure 6.2). Initially, all nodes are at constant temperature of 0 °C. Then, the inner wall temperature at a radius of 0.2 m has been increased to 100 °C. The temperature at the outer side was kept constant. After a few hours, the modelled temperature approached steady state conditions. The overall difference between modelled and calculated temperatures is well below the resolution of the DTS system.

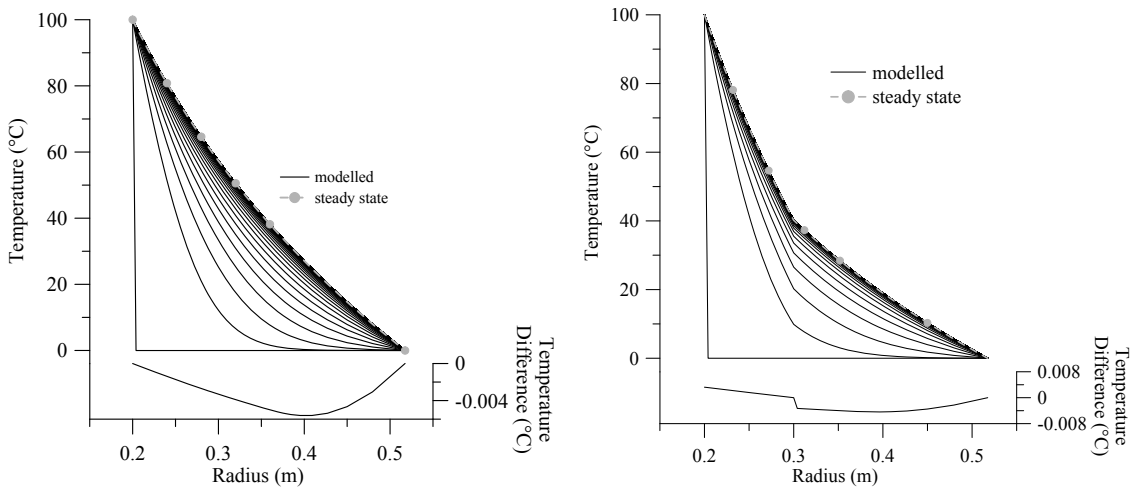

(a) 1 Layer. (b) 2 Layers.

Figure 6.2.: Compare steady state of modelled and calculated annular temperatures. Modelled temperature profiles are displayed for every 1 h and the maximum modelled time was 350 h. For the first layer, the thermal conductivity was 2 W/(m K) and for the second 4 W/(m K).

In order to validate the transient temperature evolution calculated by the finite-difference model, a similar one dimensional radial symmetric model has been set up in the free software package OpenGeoSys (OGS) (Wang et al., 2009; Watanabe et al., 2010). Modelled temperature results are shown in Figure 6.3 (OGS temperature data provided by G. Blöcher, Helmholtz Centre Potsdam). The results show that the absolute deviation between modelled temperatures using OGS and the simple finite-difference code used in this study is below 0.5 °C.

Another means to validate the finite-difference model is the comparison of released energy due to hydration of cement (see Chapter 7) and the energy content within the system at the end of the simulation. For a constant heat capacity and thermal conductivity of the cement during the hydration process, the accuracy of the simulation has been determined to be better than 3 %. For a specfic hydration scenario, 19.39 MJ have been released during the hydration. The energy content of the system at the end of the simulated hydration was 19.92 MJ. If the difference of 0.5 MJ is stored in the hydrating annulus alone, the temperature within the annulus would be changed by approx. 0.3 °C, which is in the range of the detection limit of the DTS system. Considering all uncertainties related with the hydration process, an accuracy of 3 % for the finite-difference simulation is sufficient.

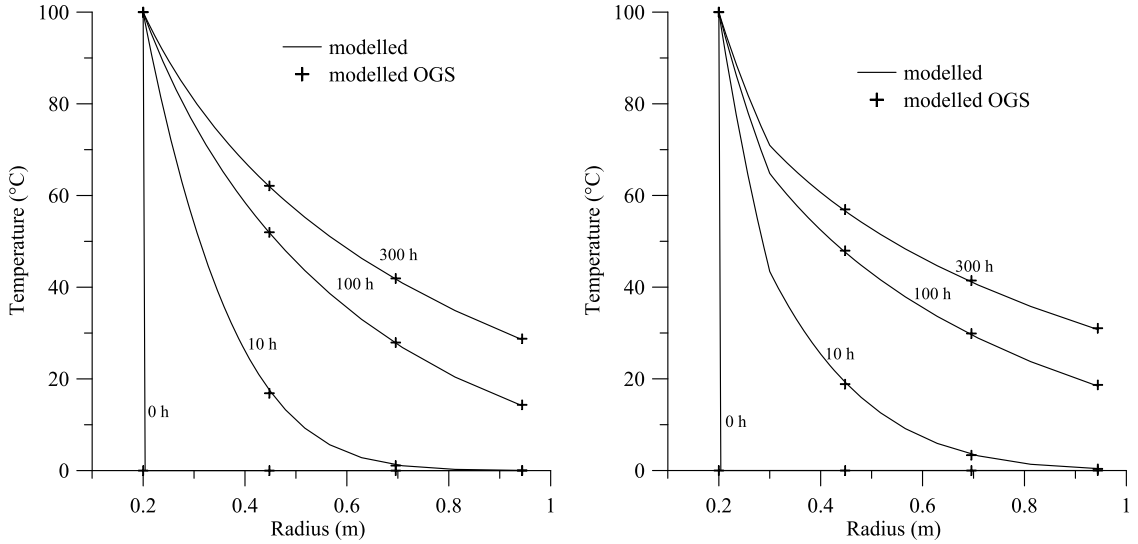

(a) 1 Layer.

(b) 2 Layers.

Figure 6.3.: Compare modelled temperatures with results modelled with OpenGeoSys. Modelled temperature profiles are displayed for 0 h, 10 h, 100 h and 300 h. For the first layer, the thermal conductivity was 2 W/(m K) and 4 W/(m K) for the second layer.

7. Cement Hydration

DTS temperatures have been measured during the cementation of the anchor casing. In order to simulate the temperature evolution within the annulus during the cement hydration using the annular temperature simulator developed in Chapter 6, a theoretical cement hydration model is described in this chapter. The hydration is modelled in order to increase the understanding of the cement properties and evaluate the performance of the cementation.

Different aspects of cement hydration will be discussed. The cement hydration model of Lin and Meyer (2009) will be presented and applied to the cement mix used in Iceland. Furthermore, bulk properties of the Icelandic cement will be calculated. Therefore, a distinction between the terms cement paste - combination of Portland cement and water - and the term slurry - cement, water and additives - will be made.

After Odler (2004),

> hydration is defined as a reaction of an anhydrous compound with water, yielding a new compound, a hydrate. In cement chemistry hydration is understood to be the reaction of a non-hydrated cement or one of its constituents with water, associated with both chemical and physico-mechanical changes of the system, in particular with setting and hardening.

For cementing the anchor casing in well HE-53, a mixture of Portland cement, Silica flour, Perlite, Bentonite, water and some Retarder was used. The exact mass composition is listed in Table 7.1. The presented composition corresponds to a specific gravity of 1666 kg/m^3 and a water/cement ratio (w/c) of 0.8. The Portland cement used is provided by Iceland Cement Ltd.. Technical information on the properties of the Portland cement are listed in Table 7.2.

7.1. Cement Properties

7.1.1. Thermal Conductivity

Bentz (2007) reports that the thermal conductivity for the tested cement pastes did not change significantly with increasing degree of hydration α_{DOH}. Within this

Table 7.1.: Mix design of cement slurry used for cementing well HE-53 with a density 1666 kg/m^3 (cement composition courtesy of Reykjavik Energy). Thermal properties from various sources. The retarder has been treated as water. As information about the thermal properties of Harborlite Perlite, which is used in Iceland, is not available, data from a complementary product has been listed.

Material	Density (kg/m^3)	Mass Frac.	Therm. Cond. (W/(mK))	Sp. Heat Cap. (J/(kgK))	Source
Portland Cement	3050	0.446	1.55	750	(1)
Silica Flour	2650	0.178	7.69	742	(2)
Perlite	350	0.089	0.39	387	at 20 °C (3)
Bentonite	2380	0.089	0.73	1120	(4)
Water	1000	0.357	0.598	4181	at 20 °C (5)
Retarder	1000	0-0.0003			see water

(1) Bentz (2007); van Breugel (1991)
(2) Horai and Simmons (1969); Hemingway (1987)
(3) Europerl (2011)
(4) Wyo-Ben, Inc. (2011)
(5) Baehr and Stephan (2008)

Table 7.2.: Technical data for the Portland cement used for cementing well HE-53 (Iceland Cement Ltd., 2007).

Physical Properties			
Density		3050	kg/m^3
Blaine Fineness		4600	cm^2/g
Compressive Strength	after 2 days	25	MPa
Compressive Strength	after 28 days	54	MPa
Chemical Composition			
SiO_2		25.4	%
Al_2O_3		4.8	%
Fe_2O_3		3.2	%
CaO	incl. free lime	57.0	%
MgO		3.1	%
SO_3		3.3	%
Cl		0.02	%
Na_2O-eq ·		1.5	%
CaO	free lime	1.5	%
Clinker Phases	Iceland Cement Ltd. (2007); Bogue (1929)		
C_3S		52	%
C_2S		20	%
C_3A		7.5	%
C_4AF		11.5	%

study, it is therefore considered to be constant and only dependent on the composition of the cement slurry. To calculate the thermal conductivity of different cement slurries, Bentz (2007) applied the mixture theory of immiscible constituents. Measured thermal conductivity values lie very well within the Hashin-Shtrikman (HS) bounds. To calculate the overall thermal conductivity of the Icelandic slurry, the mixture theory of immiscible constituents has been applied according to Berryman (1995):

$$\lambda_{HS,i} = \left(\sum_{n=1}^{N} \frac{\phi_n}{\lambda_n + 2\lambda_i} \right) 2 * \lambda_i, \tag{7.1}$$

where λ_n and ϕ_n denotes the thermal conductivity and volume fraction of the i-th component in the mixture. $\lambda_{HS,i}$ will be calculated for every component λ_i separately and then ordered in increasing quantity. The lowest value is defined as the Hashin-Shtrikman lower bound $\lambda_{HS,min}$, the upper bound is $\lambda_{HS,max}$ (Hashin and Shtrickman, 1962; Berryman, 1995).

The thermal conductivity of the cement paste depends on the water/cement ratio (w/c) and decreases with increasing water content. For every w/c, the average of the upper and lower Hashin-Shtrikman bounds has been used for further calculation. For the determination of the slurry thermal conductivity, different quantities of additives were considered. Hashin-Shtrikman bounds were calculated for the mixture of paste and additives.

Values calculated for different water cement ratios, i.e. different slurry densities, correspond to values compiled by Nelson (1986) for different cement slurries (Figure 7.1). Absolute differences between calculated thermal conductivities and the data from Nelson (1986) might be explained by different contents of crystalline silica of high thermal conductivity (Table 7.1).

7.1.2. Specific Heat Capacity

During hydration, the specific heat capacity of the cement paste changes (van Breugel, 1991). The specific heat capacity of the slurry will therefore alter throughout the process of hydration. The overall specific heat capacity of the slurry $c_{p,sl}$ can be calculated using a simple law of mixtures (van Breugel, 1991):

$$c_{p,sl} = \sum_{n=1}^{N} w_i c_{p,i} \tag{7.2}$$

where w_i and $c_{p,i}$ is the mass fraction and specific heat capacity of the individual components, respectively. Here the specific heat of water and cement powder has been combined to the specific heat of the paste $c_{p,pa}$ (van Breugel, 1980, 1991):

$$c_{p,pa} = w_{ce}(\alpha_{DOH} c_{p,hce} + (1 - \alpha_{DOH}) c_{p,por}) + w_w c_{p,w} \tag{7.3}$$

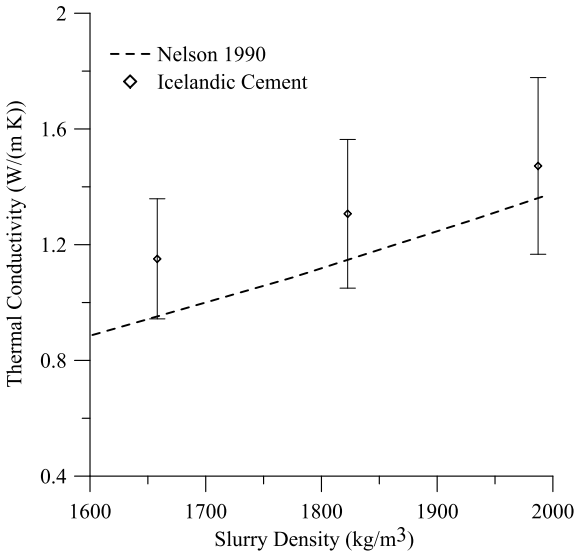

Figure 7.1.: Thermal conductivities calculated from Hashin-Shtrikman bounds for the cement used in HE-53 in comparison to data measured by Nelson (1986). For calculated data, error bars display the upper and lower HS-bounds. Measured data lies within the HS-bounds for the Icelandic slurry composition.

where α_{DOH} is the degree of hydration, w_w and w_{ce} is the mass fraction of water and cement powder in the water/cement subsystem, respectively. $c_{p,por}$ is the specific heat of anhydrous cement powder (Table 7.1), $c_{p,w}$ is the specific heat of water and $c_{p,hce}$ is the fictitious specific heat of the hydrated part of the cement, which can be calculated following van Breugel (1980):

$$c_{p,hce} = 0.0084(T - 273) + 0.339 \tag{7.4}$$

where T (K) is the temperature.

7.1.3. Acoustic Properties

Compressional-Wave Velocity

Based on a simple linear three component model (hydrated cement, water and solid), the compressional-wave velocity u_p can be calculated (personal comm.: Matteo Loizzo):

$$u_p = V_w u_{p,w} + \phi_{ce}\frac{\alpha_{DOH}}{\alpha_{DOH,u}}u_{p,ce} + \phi_{ce}(1 - \frac{\alpha_{DOH}}{\alpha_{DOH,u}})u_{p,s} + \phi_{sol}u_{p,sol} \tag{7.5}$$

where ϕ_w, ϕ_{ce} and ϕ_{sol} are the volume fractions of water, hydrated cement and solids including the unhydrated fraction of the cement. $\alpha_{DOH}/\alpha_{DOH,u}$ is the normalized fraction of cement that is already hydrated and $\alpha_{DOH,u}$ is the ultimate degree of

Table 7.3.: Compressional-wave speed for slurry components. Values are derived on the basis of laboratory data and do not correspond to real velocities for the three components (pers. comm.: Matteo Loizzo)

Component	u_p (m/s)
Hydrated cement	6663.334
Water	804.939
Solids and unhydrated cement	3738.321

hydration. $u_{p,w}$, $u_{p,ce}$ and $u_{p,sol}$ are theoretical compressional-wave velocities for the three component system. Table 7.3 lists the velocities for the individual components.

Acoustic Impedance

Together with the density of the cement slurry ρ, the compressional-wave velocity u_p can be used to calculate the acoustic impedance (Smolen, 1996):

$$Z = \rho u_p \tag{7.6}$$

Acoustic Attenuation

One way to measure the quality of the cementation process within a well, is the acoustic Cement Bond Log (CBL). A CBL measures the attenuation of an acoustic signal on its way through the casing. For a fully bonded casing, i.e. the annulus behind the casing is completely filled with cement and the cement is bonded to the casing, the acoustic impedance can be used to calculate the CBL attenuation in different depths. Based on the dataset from Jutten et al. (1989) (Table 7.4) a simple linear regression can be applied to correlate the acoustic impedance to the CBL attenuation (Figure 7.2). For the linear fit, the coefficient of determination is $R^2 = 0.967$.

Bond Index For a good cementation, the CBL attenuation of the signal amplitude is high, for a bad cementation, the attenuation is low. A quantitative measure for the cement bonding is the Bond Index (BI), calculated from the attenuation rate of the CBL signal (Smolen, 1996):

$$BI = \frac{\text{Attenuation rate in zone of interest (dB/ft)}}{\text{Attenuation rate in well cemented zone (dB/ft)}} \tag{7.7}$$

The attenuation rate can be calculated as (Pardue et al., 1963; Jutten and Morriss, 1990):

$$att = \frac{20}{d} \log_{10}\left(\frac{A}{A_{FP}}\right) \tag{7.8}$$

Table 7.4.: Compressive strength and acoustic properties for different slurry compositions (Jutten et al., 1989). Compressive strength σ_c, compressional-wave velocity u_p, acoustic impedance Z, CBL attenuation and shear bond strength σ_s after 6 days is listed for different slurry densities.

Density (kg/m^3)	σ_c (MPa)	u_p (m/s)	Z (10^6 (kg/(m^{2}s)))	CBL Attenuation (%)	σ_s (MPa)
1890	29	3463	6.55	102	10.3
1890	27.6	3390	6.41	97.4	9
1890	41.4	3454	6.53	99.6	8.6
1900	34.8	3445	6.55	98.8	9
1940	32.4	3300	6.40	94.5	9
1440	1.7	1944	2.80	41.1	0.7
1260	2.4	2500	3.15	54.3	
1440	16.5	3000	4.32	65.2	3.8
1340	4.8	2500	3.35	59.2	1.4
1890	29.6	3250	6.10	86.8	3
1820	25.8	3260	5.93	85.8	8.6
1890	33.8	3225	6.09	91.7	8.6
1890	34.1	3300	6.24	96.7	9
1890	30.3	3250	6.14	84.1	12.4
2160	19.5	3009	6.50	102.6	6.9
2280	46.2	3570	8.14	115.6	11
1200	6.2	2300	2.75	42.4	

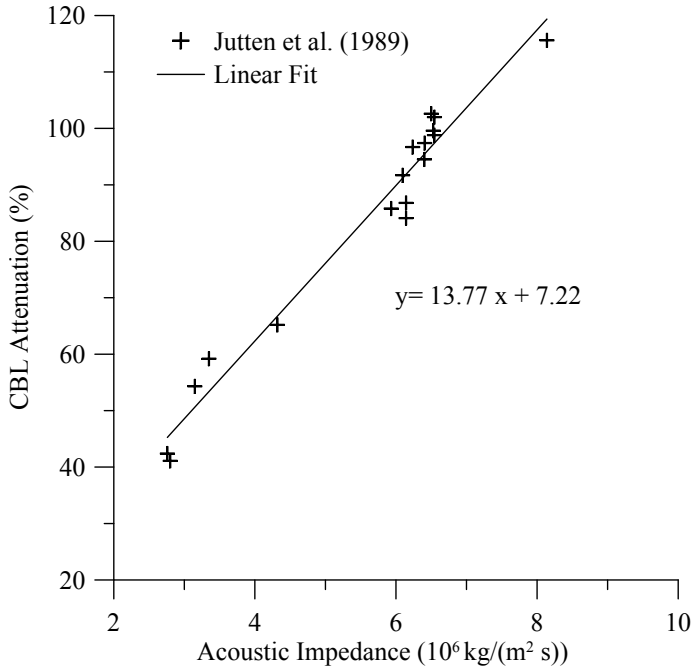

Figure 7.2.: CBL attenuation vs. acoustic impedance. Linear fit of data from Jutten et al. (1989).

with *att* being the attenuation rate (dB/ft) for a given transmitter-receiver distance d, A and A_{FP} is the actual signal amplitude at the receiver and the amplitude for a free pipe signal, respectively.

A $BI = 1$ is considered as a perfect bond between casing and cement with a 100 % cement coverage of the pipe. For a lower BI, the pipe is not fully covered. The annulus, however, might still be hydraulically sealed. A reasonable assurance criteria for an isolation between different lithologic units is assumed to be $BI = 0.8$ (Smolen, 1996).

In order to calculate the BI for well HE-53, the free pipe amplitude A_{FP} and the amplitude in a well cemented zone have to be known. The free pipe amplitude could be determined from the first CBL log. Within the uppermost 50 m the 3 ft amplitude was at maximum at A_{FP} =52 mV. Unfortunately, the second CBL measurement within the anchor casing was made before the cement was fully hydrated. The CBL amplitude for a "well cemented" zone can therefore not be determined. The minimum CBL amplitude recorded for the second CBL measurement has been defined to be "well cemented". The minimum measured amplitude was 4.1 mV.

7.1.4. Compressive and Tensile Strength

An important parameter to characterize the mechanical behaviour of cement is the strength. During setting, the cement gains compressive σ_c and tensile strength σ_t. For cements, the compressive strength is assumed to be ten times the tensile strength (Thiercelin, 2006):

$$\frac{\sigma_c}{\sigma_t} \approx 10 \tag{7.9}$$

Jutten et al. (1989) published a data set correlating different physical properties, like the compressional-wave velocity u_p, the compressive strength σ_c and the CBL attenuation of different slurry compositions and densities. Values are measured after 6 days of setting at room conditions (Table 7.4). For this dataset, an exponential relation between the compressive strength σ_c and the compressional velocity u_p at room temperature and pressure can be fitted (Figure 7.3):

$$u_p = 440.30\ ln(\sigma_c) + 1800.66 \tag{7.10}$$

The coefficient of determination for this fit is 0.92 for 17 data points. CBL attenuation reaches about 80 % of its final value after 24 h of hydration, whereas the compressional wave velocity reaches its final value after about 3 days of hydration (Jutten et al., 1989). Therefore, this relation is meaningful for curing times grater than three days.

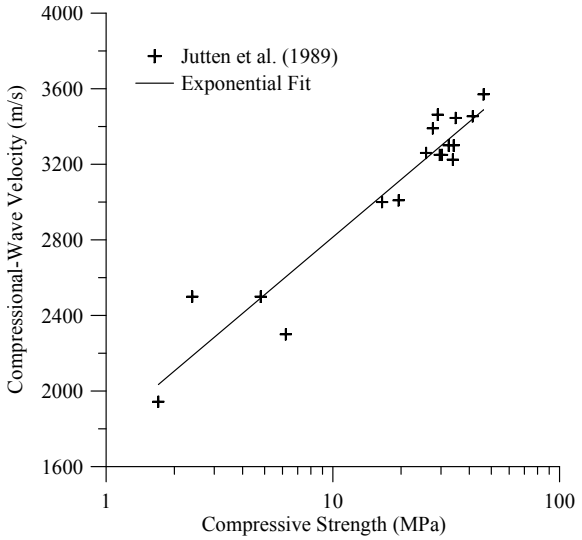

Figure 7.3.: Compressional wave velocity vs. compressive strength for cements. Exponential fit of data from Jutten et al. (1989)

7.1.5. Hydration Kinetics

In the past two decades, several investigators modelled the hydration and microstructure development of concrete. The models attempt to simulate hydration kinetics and microstructure formation on the elementary level of cement particles, taking into account chemical, physical and mechanical characteristics of cement hydration (for further details see Lin and Meyer, 2009, and references therein).

Within this study, a hydration kinetics model formulated based on the thermodynamics of multiphase porous media (Ulm and Coussy, 1995; Lin and Meyer, 2009) has been applied. The model described here is based on the formulation of Lin (2006); Lin and Meyer (2009) and takes into account curing temperature and applied hydrostatic pressure, which is important for wellbore simulations. The influence of different parameters on the cement hydration will be explained in detail and combined to a formulation of cement hydration under wellbore conditions.

7.1.5.1. Influence of Chemical Composition

The chemical composition of cement is the most important parameter influencing the cement hydration (Lin and Meyer, 2009). For this study, the Bogue calculation is used to describe the chemical composition of the cement (Bogue, 1929). When cement hydrates, it forms different clinker phases. The four main clinker phases are listed in Table 7.5 together with information about the reaction kinetics relative to each other. As the different constituents have different reaction rates, it is difficult to describe the kinetics in detail. A single overall degree of hydration α_{DOH}, however, is widely used to describe the kinetics of cement hydration (Lin and Meyer, 2009,

Table 7.5.: Clinker phases forming during the hydration of cement. Information about the relative kinetics of the reaction are given (Bogue, 1929; Lin and Meyer, 2009).

Clinker Phase	Compound	Kinetics
C_3S	$(CaO)_3 \cdot SiO_2$	fastest
C_2S	$(CaO)_2 \cdot SiO_2$	fast
C_3A	$(CaO)_3 \cdot Al_2O_3$	slow
CaAF	$(CaO)_3 \cdot Al_2O_3 \cdot Fe_2O_3$	slowest

and references therein).

Heat of Hydration

For each constituent of the cement, a unique heat of hydration can be determined. Therefore, the ultimate heat released $Q_{hyd,u}$ during the hydration process is the sum of the heat released by its components and can be approximated by (Roth and Chall, 1928; Thorvaldson et al., 1930; Lerch and Bogue, 1934; Schindler and Folliard, 2005):

$$\begin{aligned} Q_{hyd,u} =& 500\ w_{C_3S} + 260\ w_{C_2S} + 866\ w_{C_3A} + 420\ w_{C_4AF} + 624\ w_{SO_3} \\ &+ 1168\ w_{Free\,CaO} + 850\ w_{MgO} \end{aligned} \tag{7.11}$$

where w_i is the mass fractions of the different constituents i (see Table 7.2). For the Portland cement used in Iceland, the ultimate heat of hydration is therefore $Q_{hyd,u} \approx$ 490 J/g). The degree of hydration α_{DOH} is related to the maximum heat of hydration via:

$$\alpha_{DOH}(t) \approx \frac{Q_{hyd}(t)}{Q_{hyd,u}} \tag{7.12}$$

where $Q_{hyd}(t)$ (J/g) is the heat released at a specific time t during the hydration reaction (van Breugel, 1991).

7.1.5.2. Influence of Water/Cement Ratio

Another important factor influencing the hydration kinetics is the water/cement ratio (w/c). The w/c determines the availability of water for the hydration reaction. For a complete hydration $\alpha_{DOH} = 1.0$ of the cement, a theoretical value w/c =0.4 is sufficient given enough time to reach full hydration (Lin and Meyer, 2009), although more water is needed in reality (Jensen, 1995). The ultimate degree of hydration $\alpha_{DOH,u}$, however, is limited by the formation of hydration products, sealing the reactive surface of unhydrated portions of cement particles. A hyperbolic function can be used to describe the relation between ultimate degree of hydration and w/c. Mills (1966) derived the an equation for $\alpha_{DOH,u}$ which does not consider effects of

cement fineness and curing temperature (Lin and Meyer, 2009):

$$\alpha_{DOH,u} = \frac{1.031 \cdot w/c}{0.194 + w/c} \leq 1.0 \tag{7.13}$$

7.1.5.3. Influence of Cement Fineness

The fineness of cement has been observed to have an influence on the hydration rate as well as on the ultimate degree of hydration (Bentz et al., 1999; Bentz and Haecker, 1999). In general, the finer the cement, the higher $\alpha_{DOH,u}$ and the hydration rate $\dot{\alpha}_{DOH}$. At low w/c, the influence of the fineness on the $\alpha_{DOH,u}$ becomes less significant (Bentz and Haecker, 1999). As the w/c for Icelandic wellbore cement is relatively high (Chapter 3), the influence of the cement fineness has to be considered. Beside the fineness, the particle size distribution has a significant impact on the ultimate degree of hydration (Lin and Meyer, 2009, and references therein).

7.1.5.4. Influence of Curing Temperature

Lin and Meyer (2009) describe the influence of temperature on the hydration of cement to be twofold. First, the reaction rate $\dot{\alpha}_{DOH}$ increases with increasing temperature (e.g. Lerch and Ford, 1948) and second, the density of hydration products increases with increasing temperature as well (Bentur et al., 1979). This decreases the availability of water for unreacted anhydrous cement beneath a layer of hydration products. The ultimate degree of hydration at elevated temperature may therefore be lower (Lin and Meyer, 2009, and references therein). For the influence of temperature T (K) on the volume ratio of hydration products and reacted cement χ, van Breugel (1991) proposed an empirical formula (Lin and Meyer, 2009):

$$\begin{aligned} \chi(T) &= \frac{\text{Volume of Hydration Products at } T}{\text{Volume of Reacted Cement at } T} \\ &= \chi(293) \exp^{-28 \cdot 10^{-6}(\widetilde{T}-293)^2} \end{aligned} \tag{7.14}$$

where $\widetilde{T} = T/T_{aux}$ with an auxiliary constant T_{aux} =1 K and $\chi(293) \approx 2.2$ (van Breugel, 1991).

The hydration kinetics of cement are often described using the concept of an apparent activation energy E_a. As described in Section 7.1.5.1, the hydration kinetics are based on the reaction of different chemical compounds. The activation energy determined for the hydration of cement is therefore phenomenological and will be referred to as apparent (Lin and Meyer, 2009). Many authors relate E_a to temperature (e.g. van Breugel, 1991; Xiong and van Breugel, 2001). For the model proposed by Lin and Meyer (2009), however, chemical composition and fineness of cement are the only parameters influencing the apparent activation energy, as proposed by Schindler (2004).

7.1.5.5. Influence of Applied Pressure

Only very few authors investigated the influence of pressure on the hydration of cement. From the experiments conducted, however, it has been found that the hydration rate increases with increasing applied pressure (Bresson et al., 2002; Zhou and Beaudoin, 2003).

7.1.5.6. Mechanisms and Thermo-Chemical Concept of Cement Hydration

According to Lin and Meyer (2009), the mechanisms of cement hydration are understood on the basis of many experimental studies. Three main stages can be distinguished during the hydration of cement; early, middle and late (Jennings et al., 1981; van Breugel, 1991):

1. Early stage (several hours duration)
   a) Pre-induction period: rapid chemical dissolution
   b) Dormant Stage
2. Middle Stage ($24 - 48$ h)
   a) Ion transport from and to the surfaces of anhydrous cement particles. Layer of hydration products is gradually increasing.
3. Late Stage (very long time)
   a) Reaction is diffusion controlled. Free water permeates through the hydration products around the anhydrous cement particles, allowing further hydration reactions.

Within the first two stages, phase boundary mechanisms are dominant, whereas diffusion-controlled mechanisms dominate the last stage (van Breugel, 1991; Lin and Meyer, 2009).

Lin and Meyer (2009) assume that the phase boundary mechanisms can be regarded as a special case of the diffusion-controlled reaction with a very thin layer of hydration products around the anhydrous cement particles. All hydration reactions can therefore be unified to be diffusion controlled.

To quantify the reaction kinetics, changing with the growth of the layer of hydration products, the dimensionless chemical affinity of the cement hydration $\widetilde{A}_\alpha$ can be expressed as (Lin and Meyer, 2009):

$$\widetilde{A}_\alpha = \frac{\widetilde{\dot{\alpha}}_{DOH}}{\widetilde{\eta}_\alpha} \exp^{\frac{E_a}{RT}} \tag{7.15}$$

where $\widetilde{\dot{\alpha}}_{DOH} = \dot{\alpha}_{DOH}/\alpha_{aux}$ is the dimensionless reaction rate with the auxilliary constant α_{aux} =1 1/h, $\widetilde{\eta}_\alpha$ can be regarded as the dimensionless permeability of the

layer of hydration products, T is the absolute temperature and R is the universal gas constant. The hydration rate $\dot{\alpha}_{DOH}$ can therefore be rewritten as (Lin and Meyer, 2009):

$$\dot{\alpha}_{DOH} = \alpha_{aux} \widetilde{A}_{\alpha} \widetilde{\eta}_{\alpha} \exp^{\left(-\frac{E_a}{RT}\right)} \tag{7.16}$$

and provides the "ideal framework for modelling the hydration kinetics of cement" (Lin and Meyer, 2009). Normalizing Equation 7.16 gives (Lin and Meyer, 2009):

$$\dot{\alpha}_{DOH} = \alpha_{aux} \widetilde{A}_{\alpha} \widetilde{\eta}_{\alpha} \exp^{\left(-\frac{E_a}{RT}\right)} \exp^{\left(\frac{E_a}{RT_c}\right)} \tag{7.17}$$

which is important to transfer experimentally derived material properties (E_a) at constant room temperature (T_c =293 K) to different temperatures.

7.1.5.7. Effect of Additives

Additives have different effects on the hydration of cement. These can be grouped into several categories (Nelson et al., 1990):

1. Accelerators: reduction of setting time
2. Retarders: increase setting time
3. Extenders: lower cement density
4. Weighting agents: increase cement density
5. Dispersants: reduce viscosity
6. Fluid loss control agents: control loss of aqueous phase to formation
7. Loss circulation agents: control loss of slurry to formation
8. Specialty agents: miscellaneous

The additives used for Icelandic cements can be categorized as extenders (Silica, Bentonite, Perlite, see Table 7.1) (Nelson et al., 1990) and will not be considered for the hydration kinetics.

7.2. Hydration Model

7.2.1. Model Formulation

For modelling the hydration kinetics, the ultimate degree of hydration $\alpha_{DOH,u}$ has to be determined (Lin and Meyer, 2009). As stated above, the ultimate degree of hydration depends on several parameters like B fineness, temperature and the w/c ratio.

Lin and Meyer (2009) proposed a relation between the ultimate degree of hydration, the B fineness and the w/c of the paste. The ultimate degree of hydration at 293 K can be calculated by the empirical relation:

$$\alpha_{DOH,u}^{293} = \frac{\frac{1.0}{9.33\left(\frac{\widetilde{B}}{100}\right)^{-2.83}+0.38} \cdot w/c}{\frac{\widetilde{B}-220}{147.78+1.656(\widetilde{B}-220)} + w/c} \leq 1.0 \tag{7.18}$$

where $\widetilde{B} = B/B_{aux}$ with an auxiliary constant B_{aux}=1 m^2/kg for which a value below 270 m^2/kg for the B fineness is neglected and fixed to a value of 270 m^2/kg. The influence of temperature is expressed by an exponential function (Lin and Meyer, 2009):

$$\alpha_{DOH,u} = \alpha_{DOH,u}^{293} \exp^{-0.00003(\widetilde{T}-293)^2 \cdot \mathrm{SGN}(\widetilde{T}-293)} \tag{7.19}$$

where

$$\mathrm{SGN}(\widetilde{T}-293) = \begin{cases} 1, & T \geq 293 \text{ K} \\ -1, & T < 293 \text{ K} \end{cases} \tag{7.20}$$

The ultimate degree of hydration is limited by the available water for the hydration. The theoretical limit is given by the sum of chemically bound water (about 0.25) and the gel water ratio (about 0.15) (van Breugel, 1991):

$$\alpha_{DOH,u} \leq \frac{w/c}{0.4} \tag{7.21}$$

The dimensionless chemical affinity can be expressed as (Lin and Meyer, 2009):

$$\widetilde{A}_\alpha = \Omega \left(\frac{-0.0767 w_{C_4AF} + 0.0184}{\Omega \alpha_{DOH,u}} + \alpha_{DOH} \right) (\alpha_{DOH,u} - \alpha_{DOH}) \cdot s(\alpha_{DOH}, p) \tag{7.22}$$

where w_{C_4AF} the Bogue mass fraction of C_4AF, Ω is a function of the chemical composition and $s(\alpha_{DOH}, p)$ a function representing the pressure influence p (Lin and Meyer, 2009):

$$\Omega = 0.56 \left(w_{\mathrm{C_3S}}\right)^{-0.206} \left(w_{\mathrm{C_2S}}\right)^{-0.128} \left(w_{\mathrm{C_3A}}\right)^{-0.161} \tag{7.23}$$

$$s(\alpha_{DOH}, p) = \exp^{0.02\left(\frac{p}{p^a}-1\right)^{0.07}\left[\frac{\alpha_{DOH}}{\alpha_{DOH,u}} - 1.5\left(\frac{\alpha_{DOH}}{\alpha_{DOH,u}}\right)^2 + 0.4\right]} \tag{7.24}$$

where $w_{\mathrm{C_3S}}$, $w_{\mathrm{C_2S}}$ and $w_{\mathrm{C_3A}}$ are the Bogue mass fractions of C_3S, C_2S and C_3A, respectively, and the superscript a denotes atmospheric conditions.

The dimensionless permeability $\widetilde{\eta}_\alpha$ is given by (Lin and Meyer, 2009):

$$\widetilde{\eta}_\alpha = \exp^{-c_{hyd}\alpha_{DOH}} \tag{7.25}$$

with an empirical constant c_{hyd}:

$$c_{hyd} = c_{hyd,0} \cdot \left[1 + (1 - \alpha_{DOH})^2 + \ln\left(\frac{350}{\widetilde{B}}\right)\right] \cdot \left(\frac{\chi(293)}{\chi(T)}\right)^{10\alpha_{DOH}^4} \tag{7.26}$$

where $c_{hyd,0}$ is a material constant:

$$c_{hyd,0} = 10.945 \cdot w_{C_3S} + 11.25 \cdot w_{C_2S} - 4.10 \cdot w_{C_3A} - 0.892 \tag{7.27}$$

In order to calculate the apparent activation energy E_a from the chemical composition, the formula derived by Schindler (2004) has been used :

$$E_a = E_{a,aux} \cdot \left(w_{C_3S}\right)^{0.30} \cdot \left(w_{C_4AF}\right)^{0.25} \cdot \left(\widetilde{B}\right)^{0.35} \tag{7.28}$$

where $E_{a,aux}$=22100 J is an auxiliary constant. Lin and Meyer (2009) calibrated this model using various datasets.

7.2.2. Model Implementation

In order to calculate the hydration of cement slurry, an algorithm has been implemented in Python (van Rossum, 1995) based on the hydration model described in the previous Section 7.2.1. A simplified flowchart of this algorithm can be found in Appendix H, Figure H.3).

1. Calculate the ultimate heat released during hydration $Q_{hyd,u}$ (Equation 7.11).
2. Calculate the ultimate degree of hydration $\alpha_{DOH,u}$ (Equations 7.18 to 7.21).
3. Calculate the apparent activation energy E_a (Equation 7.28).
4. Get initial degree of hydration $\alpha_{DOH}(t)$ at $t = t_0$.
5. Adjust the degree of hydration $\alpha_{DOH}(t)$ for time t.
   a) Calculate the chemical affinity $\widetilde{A}_\alpha(t)$ at time t (Equations 7.22 to 7.24).
   b) Calculate the initial permeability $\widetilde{\eta}_\alpha(t)$ at time t (Equations 7.25 to 7.27).
   c) Calculate the initial reaction rate $\dot{\alpha}_{DOH}(t)$ at time t (Equation 7.17).
6. Calculate the released heat $Q_{hyd}(t)$ (Equation 7.12).
7. Calculate the specific heat capacity $c_p(t)$ (Equation 7.3).
8. Adjust temperature based on the specific heat capacity $c_p(t)$ and $Q_{hyd}(t)$.
9. Restart at 5 for the next time step $t = t+\Delta t$ until ultimate hydration $\alpha_{DOH,u}(t)$ at $t = t_u$.

In order to verify the implemented algorithm, the calculated degree of hydration has been compared to literature data given in Lin and Meyer (2009).

Cement Properties
For every time step, the degree of hydration α_{DOH} can be used to calculate the compressional-wave velocity u_p according to Equation 7.5. Together with the density, the acoustic impedance Z can be determined (Equation 7.6). For times longer than 3 days, u_p and Z can be related to the compressive strength and the CBL attenuation rate, respectively (Jutten et al., 1989).

7.3. Annular Temperature Model

During the hydration of cement, latent heat of hydration is released, causing a temperature increase within the cemented annulus. The temperature, measured at the cable is influenced by the exact location of the cable within the annulus as well as the w/c of the cement and the thermal properties of the materials in contact with the cement. In order to model the temperature increase during the hydration of the cement, a one dimensional conductive radial symmetric finite-difference temperature model has been developed (Chapter 6) and combined with a theoretical hydration model (Section 7.2.2).

7.3.1. Model Formulation

To model the temperature increase during hydration of cement within the annulus, specific changes to the finite-difference model have to be applied. First, inner sources have to be added, taking into account the released heat of hydration, and second, the initial as well as the boundary conditions have to be specified for the specific scenario. After modelling the temperature evolution at the position of the DTS cable, modelled and measured temperatures have been compared. In order minimize the variance between modelled and measured temperatures, the density of the slurry has been adjusted.

Inner Sources As described in Section 7.1.5.1, heat is released during the hydration of cement. The heat released during each step has been calculated based on the model described in Section 7.2.2.

Initial conditions DTS temperature data from the first hour of logging has been used as initial formation temperature. During drilling operations the well was cooled and wellbore temperatures at beginning of logging were almost isothermal at $7 - 8\,^{\circ}\mathrm{C}$ (Figure 7.4). As only a short time period has been modelled, static wellbore temperatures have been neglected.

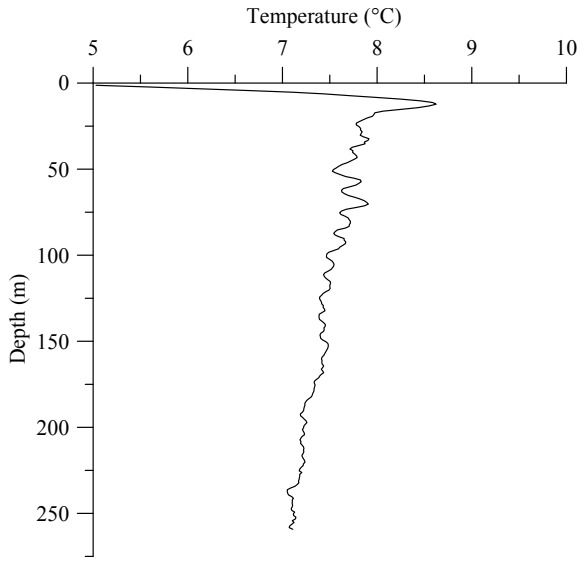

Figure 7.4.: First DTS temperature log acquired shortly after casing installation (5 m moving average). Temperature data has been averaged over 25 min.

In order to determine the onset of hydration, the slope of the measured DTS temperature data for 1 h before and 1 h after each data point has been calculated. The onset of hydration has been defined to be the location of the maximum difference between both slopes, i.e. the onset of the temperature increase between $13 - 14$ h_{DTS}. In certain depth intervals, the temperature increase during hydration is quite small. To decrease the error, all depth intervals have been manually revised and, if necessary, the time interval for searching for the onset has been adjusted based on time vs. temperature plots. The algorithm, however, led to satisfying results except for the interval $3 - 6$ m, where the begin of hydration has been delayed. Figure 7.5 shows an example for a depth of 163 m, where the onset of hydration is clearly visible at about 13.5 h_{DTS} at 10.5 °C.

As soon as the cement comes in contact with water, heat is released due to the rapid dissolution of cement in water (pre-induction period, Section 7.1.5.6). Hence, the pumped slurry is slightly warmer than the ambient temperature, which was determined by the pumping of water without cement during drilling activities. The initial temperature for the cement and the fluid column within the well has been defined to be equal to the DTS temperature at the onset of hydration. As the time between pumping of the cement and the onset of hydration is less than 10 h_{DTS} the influence on the formation temperature has been neglected.

The temperature profile at the onset of hydration is shown in Figure 7.6(a). Together with the formation temperature shown in Figure 7.5, the initial temperature conditions in radial direction can be determined. For the depth 163 m Figure 7.6(b) shows the radial temperature profile used as initial condition for the hydration

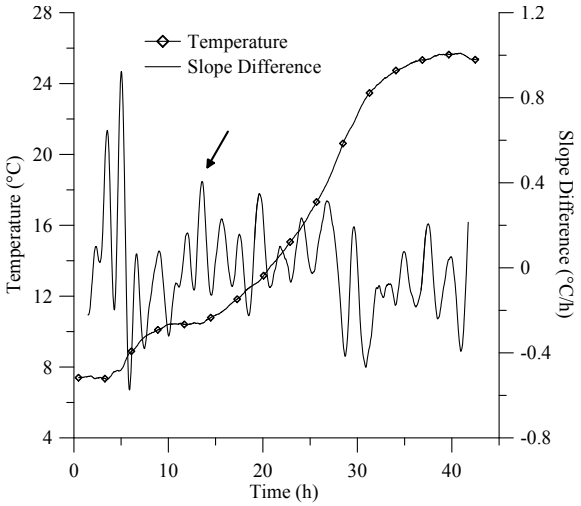

Figure 7.5.: Onset of cement hydration in 163 m. The arrow indicates the onset of hydration determined on the basis on the difference in calculated slopes prior and after each data point. Temperature data is displayed for a 1 h moving average.

model.

Thermal Properties of the Formation In order to assure homogeneous cement properties and thus a proper determination of the apparent formation thermal properties from Figure 5.7 (Chapter 5), a depth interval of a relatively homogeneous CBL amplitude and a homogeneous heat loss has been chosen. Another criteria was that the depth interval was below the water table within the casing during the cementation, i.e. the cement did not experience a large temperature variation during hydration, the calliper profile is smooth and drilling was relatively simple (see Appendix A).

For the depth interval $110 - 130$ m, an average porosity of $\phi = 0.59$ has been determind (Chapter 5). This porosity corresponds to a specific heat capacity of 1957 J/(kg K) and a density of 1802 kg/m^3. The determined thermal conductivity within this depth interval is 0.81 W/(m K). These values have been used for the simulation.

A complete list of initial conditions for a representative depth interval is given in Appendix F.

Wellbore Temperature From Section 5.2.3.1 it is known, that measured wellbore temperatures are close to the measured DTS temperatures within the annulus. The energy transfer between the casing and the annulus can be explained by convection (Chapter 5). The convective heat transfer coefficient ψ_{conv} has been determined based on the temperature difference between casing and wellbore fluid (Equation

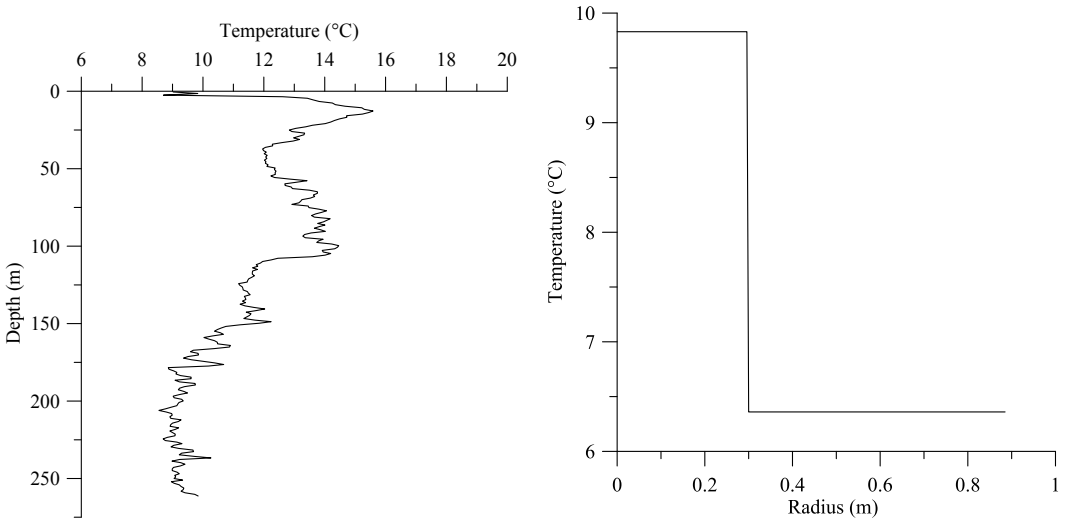

(a) Temperature profile at beginning of rapid hydration.

(b) Radial temperature profile in 163 m.

Figure 7.6.: (a) Initial temperature profile at the onset of rapid hydration (1 h temporal average; middle stage, Section 7.1.5.6). (b) Initial temperature conditions for the hydration model in 163 m. Wellfluid, anchor casing and hydrating cement is at higher temperature than the formation. The temperature step indicates the cement-formation interface for this depth interval.

5.22). The transferred energy $Q_{conv,f}$ to the fluid has been calculated for each step Δt and a surface area $A = \pi r_{csp,p}^{ID} L$ of the production casing of length L according to (Cengel, 2002):

$$Q_{conv,f} = \psi_{conv} A (T_{csg} - T_f) \Delta t \tag{7.29}$$

where T_f and $T_{csg,1}$ is the wellbore fluid temperature and the casing temperature of the first node (boundary node), respectively. A perfect mixture and therefore a homogeneous temperature is assumed for the fluid. The change in T_f between two iterations $j-1$ and j has been calculated according to:

$$T_f^j = T_f^{j-1} + \frac{Q_{conv,f}}{V_f \rho_f c_{p,f}} \tag{7.30}$$

where V_f is the fluid volume in each depth interval and ρ_f and $c_{p,f}$ are the density and specific heat capacity of the wellbore fluid. In order to account for the changing casing temperature, the change in temperature has been calculated according to:

$$\begin{aligned} T_{csg,1}^j &= T_{csg,1}^{j-1} + \frac{Q_{conv,f}}{2 V_{csg,1} \rho_{csg} c_{p,csg}} \\ T_{csg,2}^j &= T_{csg,2}^{j-1} + \frac{Q_{conv,f}}{2 V_{csg,2} \rho_{csg} c_{p,csg}} \end{aligned} \tag{7.31}$$

where $T_{csg,1}$ and $T_{csg,2}$ is the temperature of the first and second node of the casing and $V_{csg,1}$ and $V_{csg,2}$ are the volumes that belong to each node and ρ_{csg} $c_{p,csg}$ is the density and heat capacity of the casing material, respectively. In order to keep the energy change at the first node small enough for the calculation, i.e. to keep the temperature changes small in each calculation step, half of the energy is transferred from the first node and half from the second node.

During hydration, the wellbore has been filled with cold water to allow for CBL logging. For the uppermost about 107 m, the thermal capacity and density changes together with the temperature of the fluid. In order to account for this change, the fluid has been exchanged after about 29.5 h_{DTS} after beginning of logging with water of 4 °C. The temperature of the fluid has been determined on the temperature vs. time plot of the uppermost depth interval (Figure 7.7).

For the time the casing was filled with air, the transferred energy has been calculated according to:

$$Q_{conv,f}^{air} = (T_{csg,1} - T_f) V_f \rho_f^{air} c_{p,f}^{air} \tag{7.32}$$

where it is assumed that the air is heated instantaneously to the inital temperature of the casing. Due to the exchange of energy, the casing temperature change has been calculated according to Equation 7.31. An error is introduced by the fact that first the air is heated to the temperature of the casing and then the temperature of the casing changes due to the transferred energy. For small time steps, the error is small due to the low density and specific heat capacity of the air.

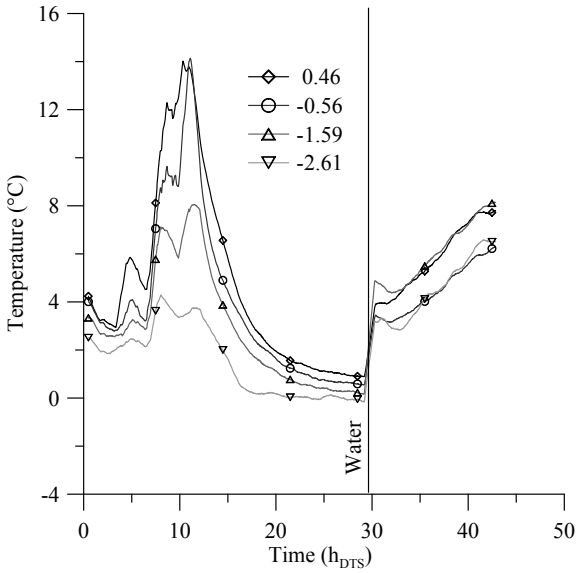

Figure 7.7.: Temperature vs. time for different depths (1 h moving average). The onset of hydration cannot be seen in this depth interval. Therefore, the temperature influence due to the hydration of cement is assumed to be very small. The injection of water at about 29.5 h_{DTS} is clearly visible. Fluid injection temperature is about 4 °C.

7.3.2. Model Implementation

The following algorithm has been applied to calculate the transient temperature conditions within the annulus during hydration of the cement. The initial temperature condition $T^0(r_n)$ is given for all nodes, the initial degree of hydration $\alpha^0_{DOH}(r_n)$ is given for the inner nodes in the cement. A simplified flowchart of this program can be found in Appendix H.

1. For a given cement, a given initial temperature $T^0(r_n)$ and degree of hydration $\alpha^0_{DOH}(r_n)$, calculate the change in the degree of hydration $\alpha^1_{DOH}(r_n)$ for a time step Δt. Within every time step, individual nodes are treated as being insulated.

2. Calculate the released heat based on the change in α_{DOH}.

3. Calculate the increase in temperature within the cement $T^{*,0}(r_n)$.

4. Calculate the change in temperature of the first two casing nodes according to Equations 7.29 to 7.32.

5. Solve Equation 6.1 to calculate the temperature change $T^1(r_n)$ due to conduction at every node.

6. Use $T^1(r_n)$ and $\alpha^1_{DOH}(r_n)$ as input parameters and start at 1.

For every modelled temperature evolution, the variance between measured and simulated temperatures has been calculated:

$$\varsigma = \frac{1}{J}\sum_{j=1}^{J}(T^j_{sim}(r_{DTS}) - T^j_{meas})^2 \tag{7.33}$$

where $T^j_{sim}(r_{DTS})$ and T^j_{meas} is simulated and measured temperature at the cable (r_{DTS}) at time $j\Delta t$, respectively. Δt is the length of an individual simulated time step and $J\Delta t$ is the total simulated time, i.e. J is the number of simulated time steps.

In order to minimize the variance, temperature models have been calculated with different slurry densities. The following algorithm has been implemented to calculate the minimum variance (for a flowchart, see Appendix H).

1. Calculate the temperature evolution for an initial slurry density (see above).

2. Calculate the variance between modelled and measured temperature evolutions.

3. Decrease the slurry density by 100 kg/m^3.

4. Iterate Steps 1 to 3 until the variance increases.

5. Increase the slurry density by 100 kg/m^3.

6. Iterate Steps 1, 2 and 5 until the variance increases.

7. Reduce the change in slurry density by an order of magnitude (10 kg/m^3) and restart at 1 until the variance increases.

8. Reduce the change in slurry density by an order of magnitude (1 kg/m^3) and restart at 1 until the variance increases.

The smallest error in variance between measured and simulated temperature evolutions gives the best fit for the slurry density.

For depth intervals above the water table within the casing in 107 m, the wellbore fluid changed at about 29.5 h_{DTS} as previously mentioned. For this depth range, the variance has been calculated for the first 30 h_{DTS} only, as complex fluid mixing phenomena like forced convection would have to be considered during the filling activities.

7.3.3. Model Validation

For every simulated temperature evolution, the variance between measured and simulated temperature evolutions has been calculated. Figure 7.8(a) shows a comparison between measured and simulated temperature evolutions after 15 iterations. At the beginning of the middle stage, simulated temperatures are slightly higher, afterwards, slightly lower than measured temperatures. Whether the peak of the temperature evolution has been reached for the measured temperature evolution is not known.

Figure 7.8(b) shows the evolution of the variance for successive iterations to match simulated and measured temperatures. The variance was reduced by the variation of the slurry density.

Figures 7.8(c) and 7.8(d) shows the calculation for a depth interval above the water table. The general trend of higher temperatures for the simulated temperature at the beginning and lower values at the end of the middle stage are similar, except that the offset between peak temperatures is higher. Furthermore, the temperature decrease due to filling the casing with cold water could only be reproduced qualitatively. Absolute differences are as high as 10 °C between measured and simulated temperatures. The trend of decreasing temperatures, however, as well as the peak temperature evolution at about $35 - 40$ h could be reproduced.

Due to the large differences in absolute temperatures, the calculated variance is quite high, compared to simulations below the water table. A comparison between variance values above and below the water table is therefore very difficult. A comparison between different values above the water table, however, is possible. The same applies to temperature simulations below the water table.

In order to see whether the simulated wellbore fluid temperature can reproduce conventionally measured fluid temperature, Figure 7.9 shows a comparison between both profiles at three different times during the cementation. Temperatures below the water table can be very well reproduced. As convective heat transfer between different depth intervals is neglected, the simulated temperature profile is not as smooth as the conventionally logged profile.

For the first log, the difference is 2.2 ± 0.3 °C, whereas it is 1.2 ± 1.0 °C and 2.5 ± 1.4 °C for the later logs. Depth with borehole breakouts can be reproduced with elevated temperatures. Here the difference is even smaller between simulated and measured temperatures. For the first log at $18 : 33$ h_{DTS}, the temperature above 107 m is much higher than measured wellbore fluid temperatures. Below, measured and simulated temperatures fit well. At $28 : 45$ h_{DTS}, shortly before filling the casing, measured temperatures are as well much lower than simulated temperatures above the water table. Temperatures differ by up to 29 °C. After filling the casing with water, modelled and measured temperatures correspond to each other within 5 °C, except for larger excursions of about 15 °C in $70 - 100$ m depth.

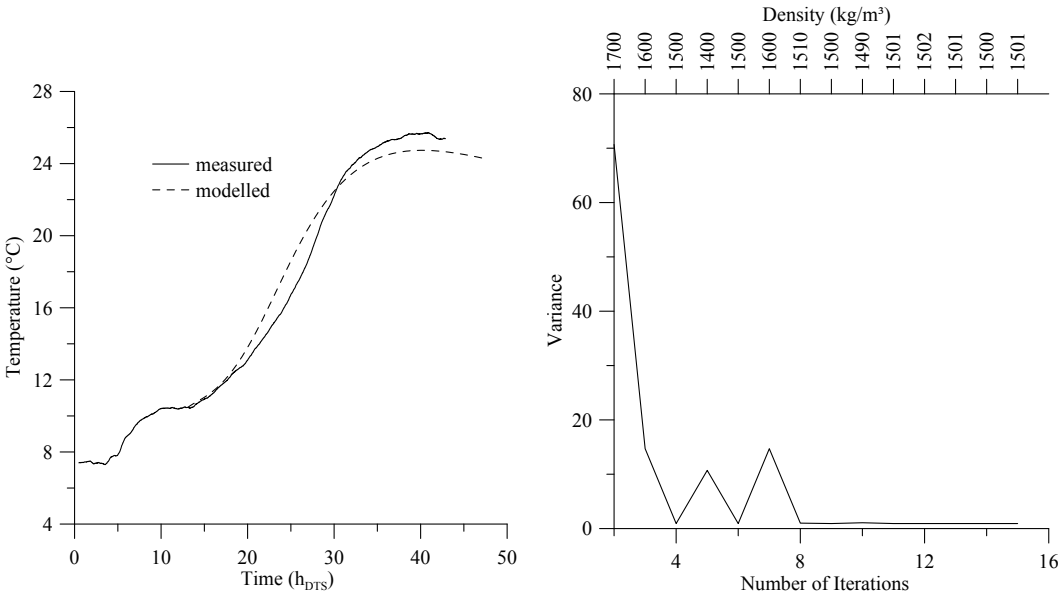

(a) 163 m temperature comparison.

(b) 163 m variance.

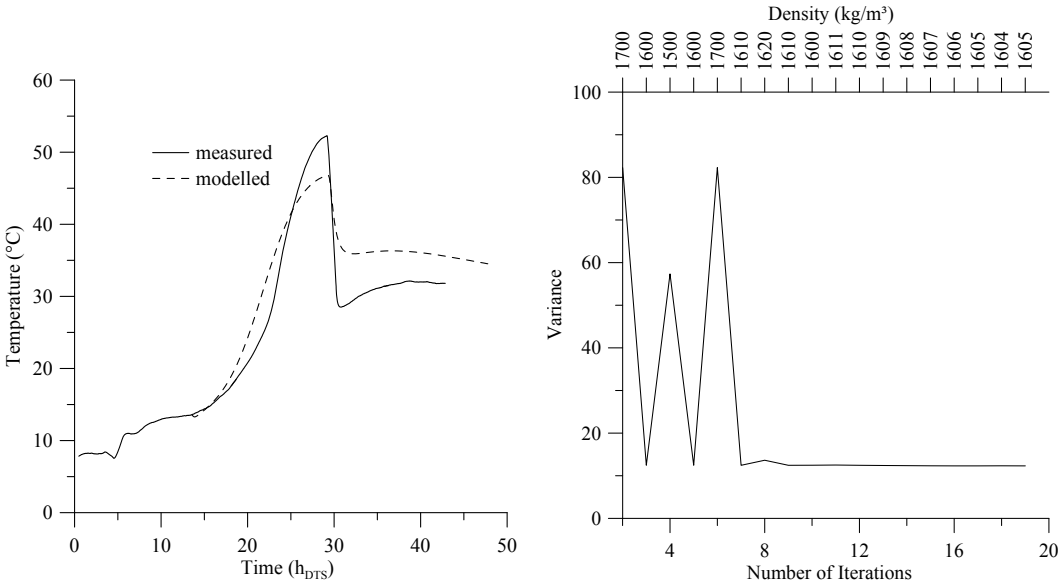

(c) 81 m temperature comparison.

(d) 81 m variance.

Figure 7.8.: Comparison between measured and simulated temperature evolutions for different slurry densities during the iteration procedure below the water table (a) and above the water table (c). The onset of hydration was at 13.12 h_{DTS} for the depth interval in 163 m (a) and 13.56 h_{DTS} for the depth interval in 81 m (c). (b), (d) Variance between measured and simulated temperature evolutions for different slurry densities during the iteration procedure.

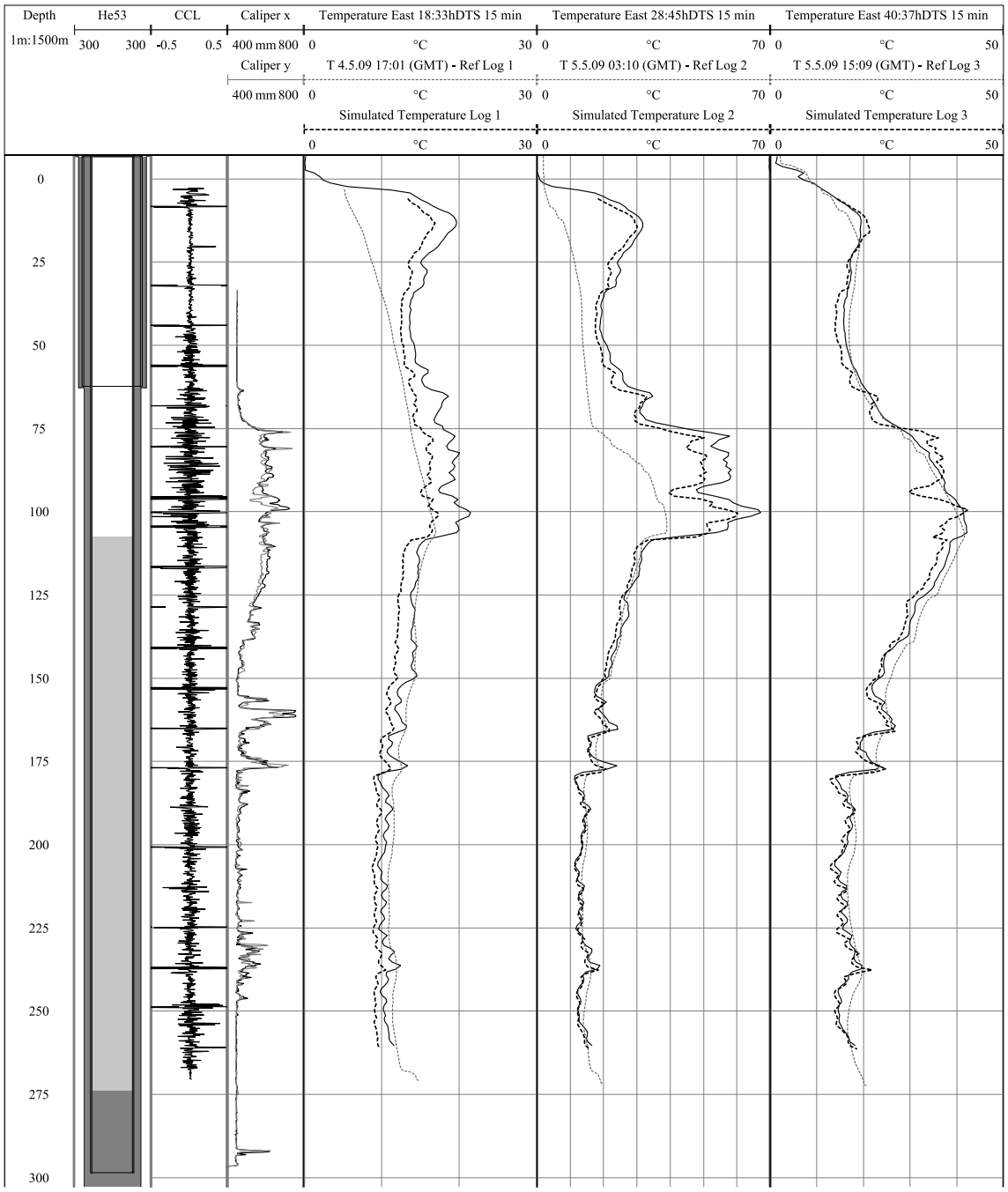

Figure 7.9.: Comparison of measured DTS temperatures behind casing and conventional wellbore fluid temperature data with simulated wellbore fluid temperature profiles during cement hydration. An engineering log is given together with calliper data. The water table during the first two measurements is indicated in the engineering log. Wellbore information and conventional logging data used with kind permission of Reykjavik Energy.

7.4. Discussions

In Iceland, CBL measurements are used to evaluate the cement quality shortly after cementing a casing. First measurements can be done 24 h after the cement job, as acoustic attenuation reaches about 80 % of its final value after this time interval. With CBL data, only bonded cement can be evaluated. Using the temperature evolution within the annulus during the hydration of cement, additional information on the cement properties can be deduced. If the cement composition is known, the hydration as well as thermal and mechanical properties can be simulated.

The correlation between CBL data and compressional wave velocities u_p is meaningful only after three days of hydration (Jutten et al., 1989). Therefore, no correlation between CBL data from Iceland and the u_p from the degree of hydration was made. A more detailed calculation accounting for the density and acoustic properties of wellbore fluid and casing, however, could be used to calculate a theoretical CBL attenuation from the simulated cement properties for times smaller than three days.

The thermal conductivity used for the modelling was at the lower end of calculated values, although within the error limit, determined in the Chapter 5, for almost all depth intervals. This can have several reasons. Measured thermal parameters might be wrong due to the reasons discussed in Chapter 5, like e.g. decentralization. Another reason might be that cement has been lost to the formation during the cement job. This cement hydrates within the formation, releasing heat and thus reducing the temperature difference between annulus and formation.

Figure 7.8 shows the capability of the algorithm to reproduce the measured temperature evolution. Despite all uncertainties regarding the actual hydration kinetics, the overall shape of the temperature release due to hydration can be reproduced and the variance between measured and simulated data could be reduced by the proposed algorithm. The determined density lies within a reasonable range. (see Chapter 8 for further details).

From Figure 7.9, it can be seen, that the modelled and measured temperatures fit quite well. Taking into account that measured DTS temperatures are, on average, 1.3 °C too low (Chapter 3), the error between simulated and measured wellbore fluid temperatures reduces to ≈ 1 °C. As convective heat transport between different depth intervals is not considered in the simulation, local variations in simulated temperatures are much higher than in the measured log.

Above the water table, measured and modelled temperatures have a greater error than below. The conventional log does not give proper results in air, as the thermal capacity of the temperature probe is large and the heat transfer between temperature probe and air is small. Furthermore, the energy needed to change the temperature of air in a meter of anchor casing is only 94 J/K. Considering the amount of thermal energy in the system to be about 20 MJ (see Chapter 6), this effect is negligible.

8. Structural Wellbore Integrity Monitoring

8.1. Cement Job Evaluation - Volumetric Balance

During pumping of the cement, Portland cement and additives are mixed with water directly prior to injection into the well. Due to rapid dissolution reactions (early stage of hydration, Chapter 7), the temperature of the injected slurry is slightly higher than the well temperature, which was cooled during drilling activities. Differences between well temperature and injected slurry temperature can be used to determine the position of slurry within the annulus. Together with the information about the calliper diameter, the amount of cement that has been lost to the formation can be estimated.

A major loss zone has been detected in a depth of about 293 m during the drilling process. In order to cement the anchor casing, a two stage cementation has been performed. First, a stinger cementation has been used to cement the shoe of the casing. Simultaneously, water has been injected through the annulus to keep a flow path open to the formation. Second, cement has been pumped through the annulus in 10 steps until the top of cement within the annulus stabilized at the surface.

8.1.1. Observation

As described in Chapter 7, heat of hydration is released during the setting of cement. Temperature data from the cementation process, especially the pumping of cement ($0 - 10$ h_{DTS}, Table 8.1) can be used to estimate the amount of cement being emplaced during the different cement jobs (Figure 8.1). Prior to the first cement job, cold water has been circulated within the well. The temperature, therefore, has been homogeneous at $7 - 8$ °C.

During the injection of cement through the stinger, cold water from deeper parts of the well was pushed upwards within the annulus up to a depth of 150 m. The cement head has been detected in a depth of 210 m. During second stage cement injection through the annulus, the top of cement from the first stage cementation gradually sank down. From calliper data it is known that cold water filled an annular volume of 6.0 m^3 ($150 - 210$ m). Below 210 m, a volume of maximum 9.2 m^3 has

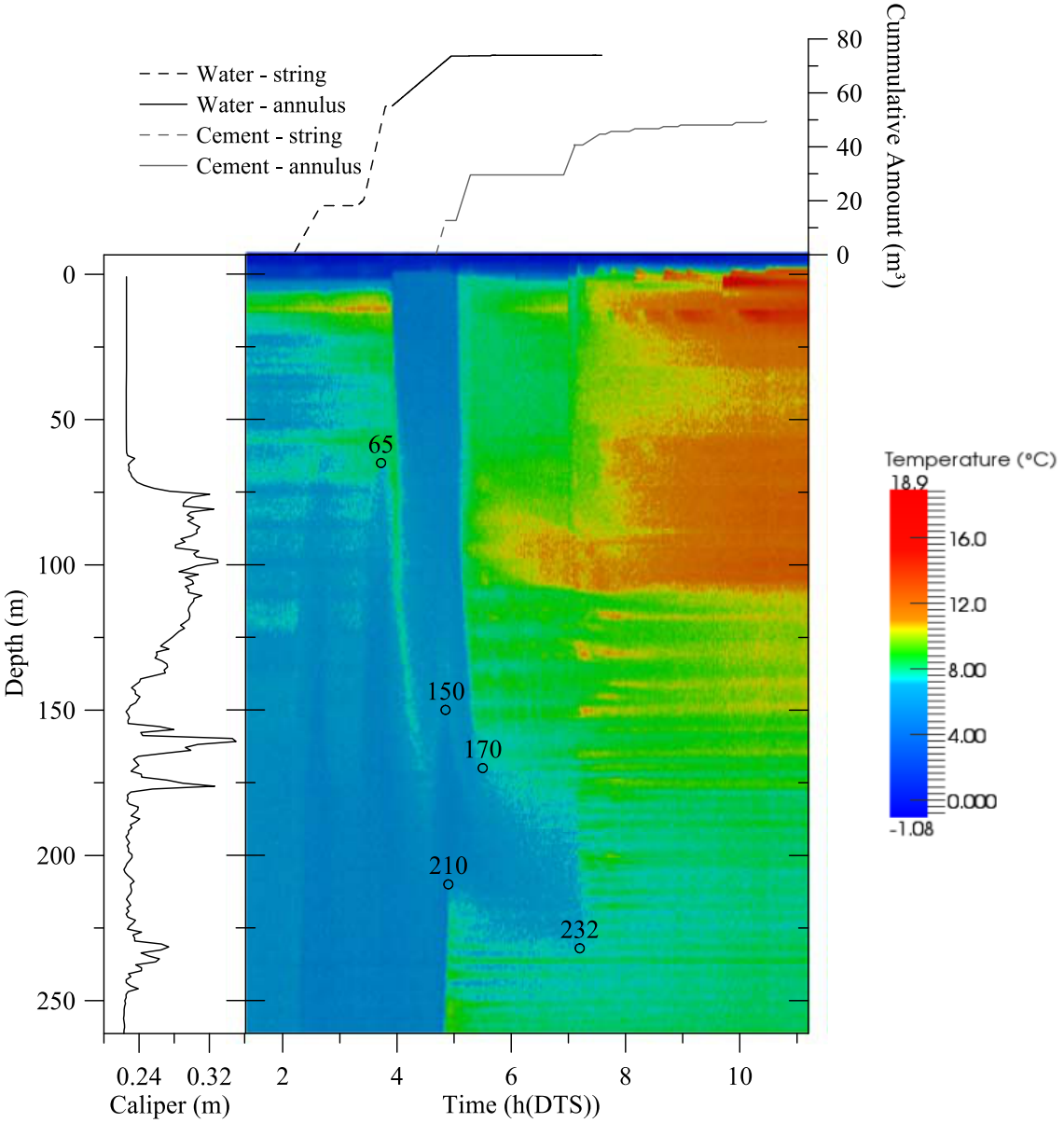

Figure 8.1.: Temperature evolution during beginning of cementation in comparison to the cummulative volume of pumped water and cement as well as the calliper radius. The type of emplacement (through string or through annulus) is indicated. Individual depth points are indicated. Further details are given in the text (calliper and cement data courtesy of Reykjavik Energy).

Table 8.1.: List of cement jobs for the anchor casing of HE-53. After the first stage cementation through the stinger (a: attached to the float collar; na: not attached to the float collar), the casing has been cemented through the kill line from the surface. The injected volumes are listed together with the cement density ρ and the start of the injection. Total injected fluid and cement volumes are given with the average cement density $\bar{\rho}$.

Cementation	Volume (m^3)	Density (g/cm^3)	Start (h_{DTS})	Circulation
	18.2		2.18	fluid in casing (na)
	36.9		3.30	fluid in annulus (a)
	18.6		3.9	fluid through annulus
1	12.7	1.67	4.68	stinger cementation (a)
2	16.9	1.69	5.03	cement through annulus
3	11.1	1.72	6.92	cement through annulus
4	4.0	1.73	7.25	cement through annulus
5	1.0	1.73	7.65	cement through annulus
6	1.0	1.73	8.07	cement through annulus
7	0.8	1.73	8.58	cement through annulus
8	0.6	1.73	8.92	cement through annulus
9	0.9	1.74	9.87	cement through annulus
10	0.5	1.74	10.42	cement through annulus
11	0.3	1.74	11.58	cement through annulus
Total Fluid	73.7			
Total Cement	49.8	$\bar{\rho} = 1.699$		

been filled with cement (Table 8.2). As only 6.0 m^3 of colder water have been pushed upwards during the stinger cementation and a total cement volume of 12.7 m^3 has been pumped through the stinger, at least 6.7 m^3 of water has been lost to the formation in the lower part of the well, below 150 m. Assuming the volume below the casing shoe and the casing between shoe and float collar is completely filled with cement, a total volume of 3.4 m^3 of cement has been lost to the formation during the first stage cementing job.

Within the first 2.5 h after the stinger cementation, the cement head sank down to 232 m, associated with a loss of another 1.8 m^3 (annular volume within the depth interval $210 - 232$ m). A further sinking of the cement head could not be determined based on the temperature data from the pumping period.

For the second stage cementation through the annulus, cement could reach the entire annulus down to a depth of 170 m. 16.9 m^3 of cement have been injected into an annular volume of 20.7 m^3. In order to cover the entire depth interval, the cement has been diluted with 3.9 m^3 of water. During the following 2 h, cement from the second cementation gradually sank down by about 20 m, increasing its dilution. Only cement from the third cementation reached the remaining depth interval $190 - 232$ m. During further cementations, additional cement has been lost to the formation (Table 8.1). Assuming that cement is filling the entire annular space after the cementation process (33.4 m^3), at least 16.4 m^3 of cement were lost to the formation (total volume of cement: 49.8 m^3, see Table 8.1). From the pumping period, however, it cannot be determined in which and how many depth intervals cement has been lost.

Table 8.2.: List of activities and cement quantities lost during different well operations. Different fluids have been circulated within the casing or within the annulus. In case the fluid has been pumped through the string, the annular flow is upwards (up). Otherwise, when pumped through the kill line, downwards (down). Depth range is taken from temperature profiles. Available volumes and injected volumes were compared to calculate loss to the formation.

Time (h_{DTS})	Fluid	Job (#)	Circulation	Flow	Depth Range (m)	Av. Vol. (m^3)	Inj. Vol. (m^3)	Loss (m^3)	Remarks
2:11-2:40	Fluid		Casing	up	? - 274.4		18.2	?	not determined
3:19-3:54	Fluid		Annulus	up	65 - 302.8	28.5	36.9	8.4	0.5 h; average 4.7 l/s
3:54-5:02	Cement	1	Annulus	up	210 - 302.8	9.2	12.7	3.4	loss below 210 m
	Fluid		Annulus	up	150 - 210	6.0	12.7	6.7	12.7 m^3 cement inj., only 6 m^3 fluid lifted
5:02-6:55	Cement	1	Annulus	down	210 - 232	1.8		1.8	lost below 232 m
	Cement	2	Annulus	down	6.7 - 170	20.7	16.9	-3.9	diluted
6:55-7:15	Cement	3	Annulus	down			11.1	?	
7:15-End	Cement	4 - 12	Annulus	down			9.0	?	

8.1.2. Discussions

From the temperature data acquired during the first 10 h_{DTS} of temperature logging (first field campaign), a volumetric balance could be calculated for the different cement injections. A gradually sinking of cement from the first stage cementation has been observed. From the lowering of the top of cement the amount of cement lost to the formation can be calculated. Most probably, the cement has been lost within the loss zone in about 293 m, known from the drilling process. For the second cementation, only a small amount could pass the narrow section of the well in about 150 m depth. Between cement job two and three, little cement sank down through the narrow section. During the third cementation, cement could reach the entire annulus from the bottom of the installation to the surface. Below 150 m, lower temperatures were observed. Lower temperatures indicate a dilution of the cement.

From low temperatures it can be deduced that only diluted cement has been emplaced between the narrow section of the well in about 150 m and above the cement head from the first cementation in about 230 m depth. Therefore, cement has been lost in the depth interval $\approx 62 - 155$ m, below the surface casing. The depth interval $-6.7 - 230$ m has an annular volume of 25.8 m^3, whereas 36.8 m^3 of cement have been injected through the annulus. Assuming that the top of cement from the stinger cementation is stationary, the difference has been most probably lost to the formation above the narrow section of the well. From the drilling reports it is known that the drilling has been delayed in 125 m, 143 m, 154 and 159 m due to several reasons. The well collapsed and the bit got stuck two times. Furthermore, cement plugs had to be placed to seal total drilling fluid loss zones (see Appendix A for details on the drilling progress). A cement loss within this weak depth interval is probable, although it has been cemented several times. The ascent of colder fluid during the first cementation only up to 150 m can be explained by a loss in about 150 m, as well.

A loss zone in about 150 m depth has been identified by the thermal properties in Figure 5.7 (Chapter 5), as well. Although a large amount of cement has been lost in this depth interval, the determined thermal conductivity is very high, indicating either a convective heat transfer within the formation or very little cement in this depth. In the light of the results from the pumping period, the highly variable thermal conductivity values measured below the narrow calliper interval can be explained. For the calculation of the cement-formation interface temperature, a fully cemented annulus has been assumed. Low density values, i.e. a small temperature increase during the hydration, indicates a very diluted cement which might be inhomogeneously distributed around the perimeter of the well, as indicated by high CBL amplitudes in e.g. 175 m depth (Figure 5.4). The calculated interface temperature is therefore too low, as the insulating cement is partly missing. The calculated formation thermal properties, therefore, do not represent real formation properties.

8.2. Cement Job Evaluation - Density Profile

From Section 8.1 it is known that neither cement is evenly distributed within the annulus nor is its density constant. Therefore, the thermal properties, calculated in Chapter 5 do not correspond to the real thermal properties of the formation. Furthermore, it is known that several m^3 of cement have been lost to the formation. Hydrating cement within the formation generates heat and reduces the heat transfer between annulus and formation. Therefore, the previously determined profile of thermal properties is not applied to calculate the cement-density profile.

Figure 8.2 shows a comparison of measured and simulated temperatures for different porosities of basalt at 20 °C. The higher the porosity, however, the better the fit. A higher porosity results in a decreased thermal conductivity of the formation. The temperature increase, therefore, does not consume as much energy as if more energy can be transferred at high thermal conductivities. This results in a lower simulated density (0 % porosity: 1779 kg/m^3; 100 % porosity: 1627 kg/m^3).

In order to simulate a reasonable density profile, the thermal properties of the formation are taken from the interval $110 - 130$ m and set constant for the entire profile (see Section 7.3 for further details). Neglecting variations in the formation thermal properties, however, leads to an overestimation of the simulated slurry density variation. The effect of the slurry variation, however, is assumed to be the dominant one, as variations in the formation thermal conductivity for basalt formations is generally low ($1.5 - 2$ W/(m K), e.g. Oxburgh and Agrell, 1982; Pálmason et al., 1985; Flóvenz and Saemundsson, 1993; Ouali, 2009).

Based on the algorithm developed in Chapter 7, a density versus depth plot has been simulated on the basis of temperature data from the eastern cable branch. Figure 8.3 shows the resulting density profile. In case the hydrating cement is in contact with the surface casing, thermal properties of the cement behind the surface casing were determined based on the pumped density according to the discussion in Section 7.1.

8.2.1. Observation

Three depth intervals can be assigned in the density plot. The uppermost interval $0 - 75$ m shows quite variable densities with high density values at top, gradually reduced values in the middle and higher values in the bottom part, again. The same tendency can be observed for the variance.

In the middle interval from 75 m to 155 m depth, a homogeneous density has been simulated to give the best results for the comparison between simulated and measured temperatures. A slight increase in density has been observed for the bottom part of this interval ($130 - 155$ m). The variance within this interval can be divided into an upper and lower interval, indicating simulations above and below the

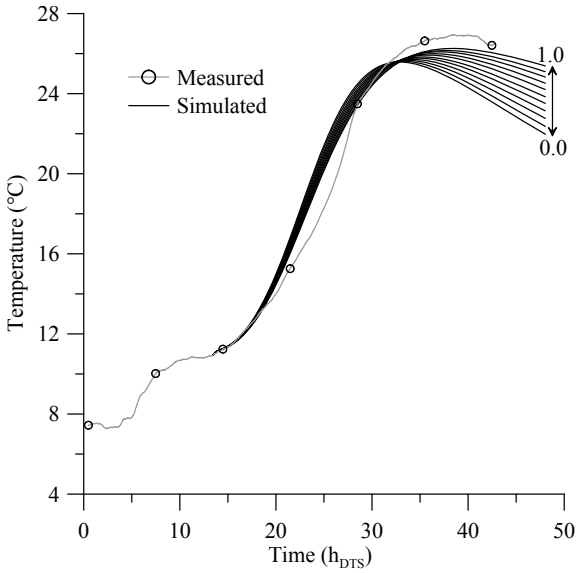

Figure 8.2.: Comparison of measured and simulated temperature evolution during hydration (best fit). The simulated temperature evolution for different basalt porosities is displayed together with the measured temperature evolution for a depth of 164 m. Porosities are varied between 0.0 and 1.0.

water table. Within both intervals, the variance between measured and simulated temperatures has a similar magnitude. A clear trend to increasing or decreasing variance magnitudes was not observed.

Within the bottom interval, below 155 m depth, a lower simulated density was observed to predominate. Comparing the simulated density with the calliper information shows that lower densities correspond to depths of larger borehole diameter. Within the lower part of such breakouts, the density increases again. At the very bottom of the profile below 255 m, where a very smooth calliper diameter predominates, the density increases, again.

8.2.2. Discussions

During the different cementations, cement with an average density of 1699 kg/m^3 has been pumped into the well (Table 8.1). Despite the uncertainties regarding the thermal parameters of the formation, the hydration kinetics of the cement as well as the fluid exchange within the uppermost 107 m of the well, the simulated density corresponds to the pumped density within the middle interval of the well. Here, due to borehole breakouts, a large borehole diameter predominate. Cement has been emplaced through the annulus within this depth interval (Section 8.1). The increase in density within the lower part of the well might be explained by a sedimentation effect of solids within the slurry.

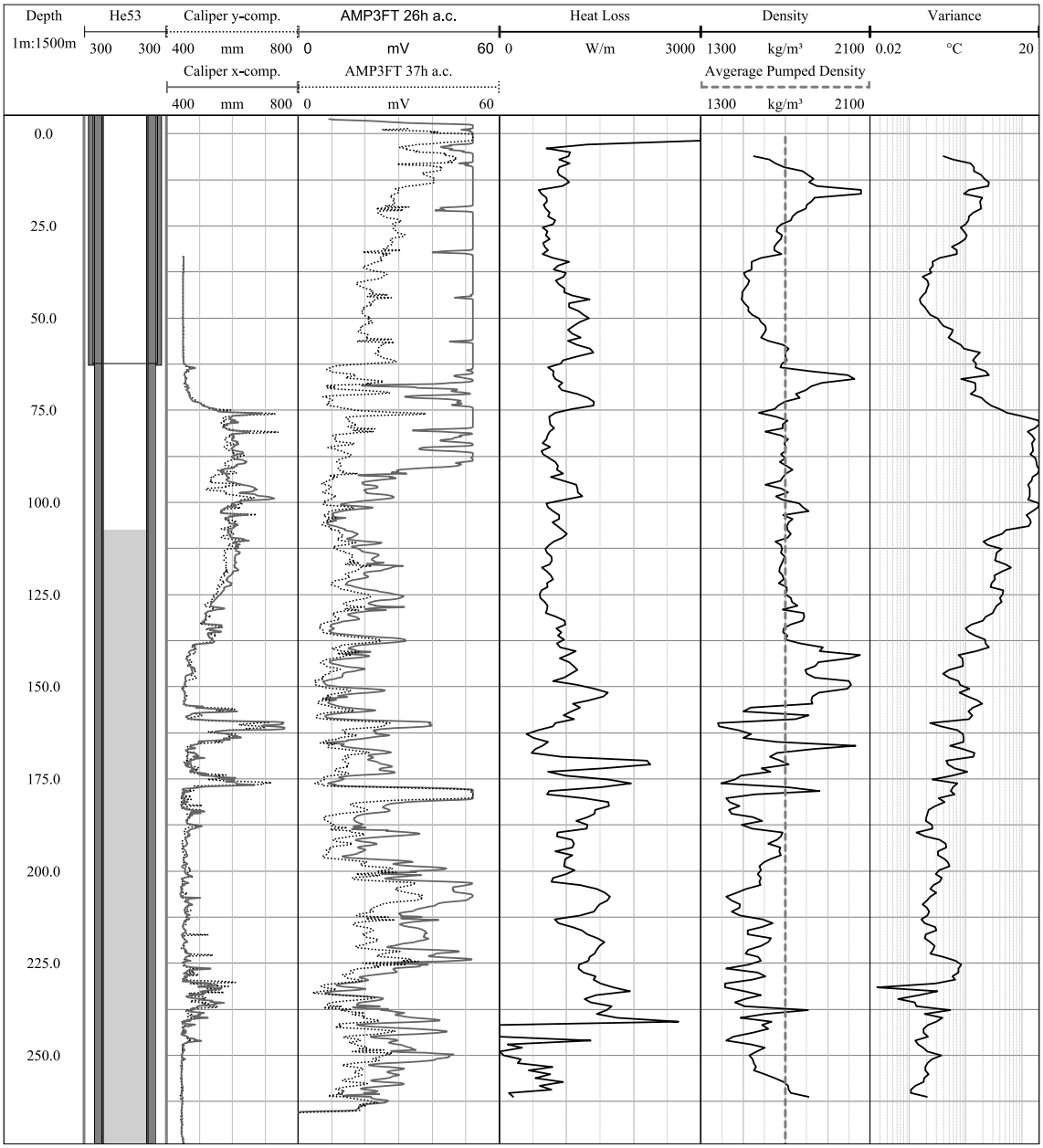

Figure 8.3.: Simulated cement density of the cement behind the anchor casing for the eastern cable branch in comparison to the average pumped density. The density is displayed together with CBL data, calliper data as well as heat loss values. Variance data between measured and simulated temperatures is shown in logarithmic scale. Well information used with kind permission of Reykjavik Energy.

Below the narrow section of the well in about 150 m depth, less cement could be emplaced. This interval has been predominantly cemented through the annulus as well (Section 8.1). Although cement was injected through the string, this cement sank down in the course of the following cementations. Only diluted cement from top reached to this interval. The cement, furthermore, did not fill large breakouts, as the simulated density is much lower, here. Increasing simulated densities at the bottom of large breakouts can be explained by sedimentation effects, again. Flow of cement along preferred channels down into the well might be the reason for this. The increase in simulated density at the very bottom of this interval can be regarded as the depth to which cement from the first stage cementation sank down during successive cement injections through the annulus.

The interpretation of the results from the upper interval, down to about 75 m, is ambivalent. On the one hand, a sedimentation effect in the lower part between the anchor and surface casing might be the reason for an increase in the simulated density here. The increase in the upper part might be explained by cement with an increasing simulated density that has been successively used to fill up the annulus (Table 8.1). On the other hand, the same trend in simulated density variations can be observed for the variance. High values at top and bottom of the interval, lower values in the middle.

From temperature measurements before the flow testing period it is known that static temperatures within this interval are much higher than the initial temperature of the formation used in this simulation (Chapter 3). Especially the position of the maxima in about 15 m and 65 m depth, as well as the minima in static formation temperature in about 40 m depth correspond to the observed trend in simulated densities. An influence of the static formation temperature on the simulates temperature is probable, although the well has been cooled down during drilling.

Beside the erroneous assumption on the formation temperature, the measured DTS temperature is influenced by successive cementations of small amounts of cement. The onset of hydration for the cements pumped during successive cementations is different. Therefore, the measured temperature increase is a superposition of hydration reactions of cements of different age. An estimate on the actual density within this interval is difficult to determine.

From the simulated density profile, the amount of solids and cement can be calculated for each depth interval. For the depth interval below the DTS cable, the pumped density for the first stage cementation has been assumed. For the uppermost 10 m, where the density has not been simulated, the nominal density of the last cementation has been assumed. Together with the information about the available annular volume, an amount of 13.3 m^3 of solids has been calculated from the simulated density profile to be emplaced within the annulus. From Table 8.1 it is known that 21.2 m^3 of solids have been injected. For an average slurry density of 1699 kg/m^3, this results in a loss of 18.5 m^3 of slurry to the formation. The difference between available annular volume and pumped cement volume was 16.4 m^3.

From the comparison of both values, an average dilution of $\frac{18.5-16.4}{16.4} \approx 13$ % can be deduced for the remaining cement within the annulus.

8.3. Structural Integrity Evaluation -Fracture Evolution Within Annulus

8.3.1. Observation

During the onset of hot fluid production, the wellhead temperature increased continuously (Figure 3.12). Although the wellbore fluid temperature was increasing, the DTS temperature measured within the annulus behind the anchor casing, decreased locally. Successively, decreasing temperatures were observed in adjacent depth intervals (Figure 8.4).

Within the depth interval $69 - 74$ m (Figure 8.4(a)), the temperature decrease was observed locally and simultaneously at about 75 h_{DTS} in three different depth intervals for the eastern cable branch, whereas the effect was greatest in the middle interval in 72 m depth. A little effect was even seen in the fourth interval in 70 m. Here, the effect was only observed on the eastern side of the casing. On the western side, the decrease was not observed, but significantly lower temperatures were measured in 72 m and 73 m (Figure 8.4(b)). Furthermore, the change in slope between the steep increase during the beginning of hot fluid production and the constant difference to the wellhead temperature was more gradual for the western branch than for the eastern branch.

Within the depth interval $62 - 54$ m, the temperature anomaly migrated upwards along the annulus. For the first time, it has been observed at the location of the bottom of the surface casing. Afterwards, it migrated upwards between the anchor and surface casing.

The beginning of the anomaly in different depth intervals has been determined visually. Furthermore, the end of the anomaly and the absolute temperature difference between beginning and end of the temperature decrease has been determined visually at different depth intervals. The resulting migration velocity, determined between the time of beginning between different depth intervals, between the end of the temperature decrease between different intervals as well as the time between start and end in individual depth intervals is in displayed in Figure 8.5(a). Data is displayed for both branches of the cable on different sides of the casing.

Due to plugging and unplugging activities of the surface excess length during OTDR attenuation measurements, temperature data is skewed at different times (Chapter 3). Therefore, the determination of the exact beginning and end of an anomaly is obscured and an error in time and temperature determination of the anomaly is introduced. For the visual determination, an uncertainty in temperature

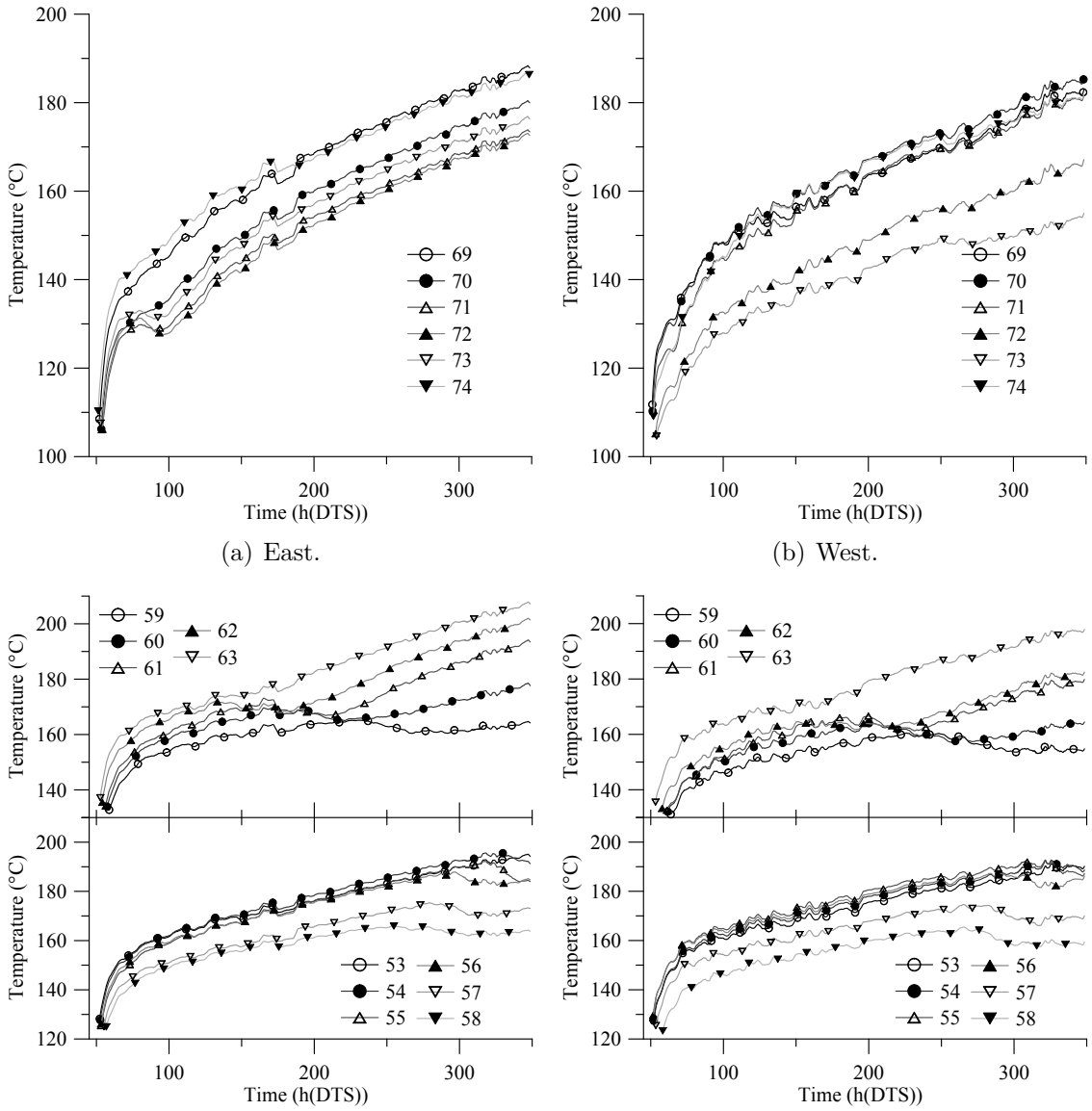

(a) East. (b) West.

(c) East. (d) West.

Figure 8.4.: DTS temperature data for individual depth intervals. Locally decreasing temperatures could be observed in adjacent depth intervals. The temperature anomaly was observed below the surface casing (a,b; > 62 m) as well as within the annulus between anchor and surface casing (c,d; < 62 m). Displayed is a 3 h running average.

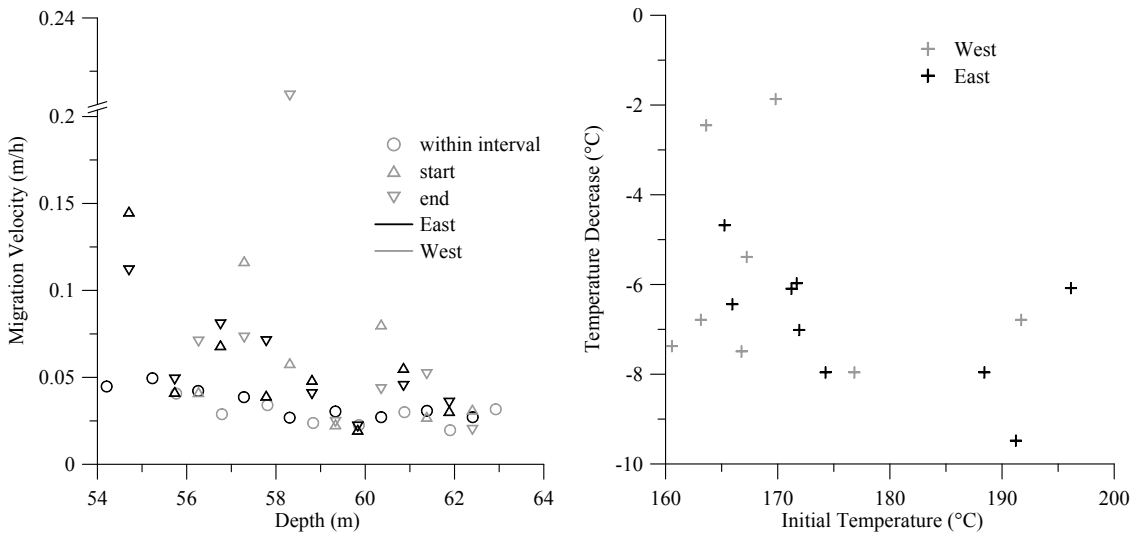

(a) Migration velocity.

(b) Magnitude of anomaly.

Figure 8.5.: Analysis of the observed temperature anomaly. The migration velocity for both cable branches (a) as well as the absolute temperature decrease was determined visually from Figure 8.4. Together with the migration velocity, the absolute temperature decrease has been calculated and plotted against the initial temperature at the beginning of the anomaly in every depth interval (b).

of about ±2 °C and ±3 h in time has been estimated.

The migration velocity of the temperature decrease as well as the absolute amplitude of the temperature decrease is similar for both cable branches. The anomaly migrated with a velocity of $2.5 - 10$ cm/h with a slight increasing velocity at lower depths. Furthermore, the temperature decrease seems to be larger with increasing temperature at the beginning of the anomaly (Figure 8.5(b)). The correlation, however, is very small. For a linear regression, the coefficient of determination R^2 is 0.03 and 0.29 for western and eastern cable branch, respectively. The initial temperature is lower with increasing distance between cable and casing (Figure 8.6(a)) and the magnitude of the temperature decrease seems to be higher with increasing distance to the casing (Figure 8.6(b)). As the onset of the anomaly is observed in different depths at different times and the wellbore fluid temperature is constantly increasing, the trends seen in Figure 8.6 are superimposed by the increasing well temperature. The time derivative for different depths, i.e. the rate of the temperature change, however, seems to increase with increasing distance to the casing (Figure 8.7).

Another aspect of the temperature anomaly is displayed in Figure 8.8. Two different depth intervals with a similar thermal behaviour before the onset of the anomaly

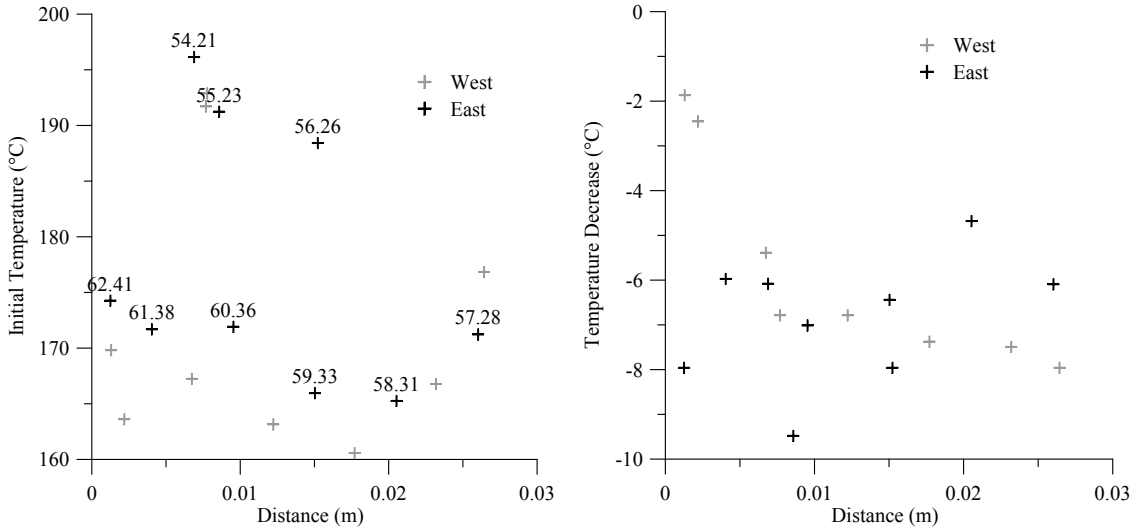

(a) Initial temperature vs. distance.

(b) Temperature decrease vs. distance.

Figure 8.6.: Temperature versus distance cable-casing for the onset of the temperature anomaly (a). Temperature decrease versus cable-casing distance (b). Higher temperatures and a lower temperature decrease can be observed close to the casing.

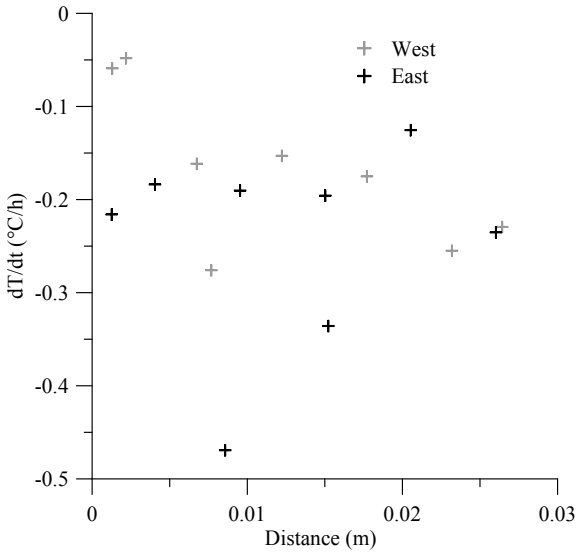

Figure 8.7.: Rate of temperature change versus distance cable-casing.

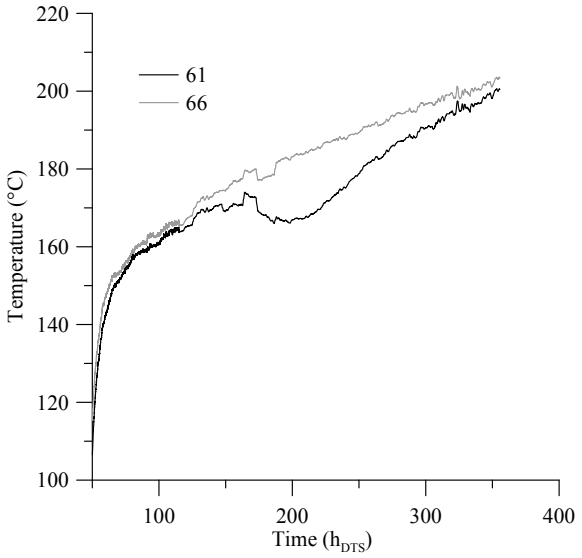

Figure 8.8.: Comparison of depth intervals with and without the temperature anomaly. A 1 h moving average is displayed.

have been chosen. A temperature decrease was observed in one but not the other depth interval. Although the temperature decrease was observed only for a limited time interval of approximately 20 h, the temperature after the temperature decrease was still influenced, so that absolute temperatures were much lower than in the depth-interval where no anomaly was observed.

Within the depth interval $62 - 54$ m, an influence on the measured temperatures after the anomaly could be observed for at least 200 h, in case there was a sufficiently long measurement time after the onset of the temperature anomaly. After that time, the temperature trend was similar to the trend observed in depth intervals without any anomaly. A slight difference, however, has been observed comparing the depth interval 66 m and 61 m. At the end of the measurement at about 350 h_{DTS}, the temperature difference between both depth intervals was similar to the difference before the anomaly (≈ 2 °C), the temperature increase for the interval in 61 m was still steeper than for the interval in 66 m.

8.3.2. Hypothesis

The hypothesis to explain the temperature anomaly migrating along the DTS cable is a fracture evolution in the cement sheath of the anchor casing (Figure 8.9). Due to the large temperature increase at the beginning of the flow test, the internal pressure (casing on cement) increases. Stress within the cement sheath is released by creation of tangential (sub-vertical) fractures. The process of fracture evolution within the cement due to a large internal pressures or temperature increase is well

known (e.g. Goodwin, 1992).

Cement is a low permeable, porous medium, saturated with liquid. Producing hot geothermal fluid, the temperature of the cement increases and the fluid pressure increases until it starts to evaporate. Due to the low permeability of cement and as cement and fluid are trapped between two casings above 62 m, the vapour cannot escape. As a result, the fluid is at boiling point pressure within the entire annulus, but at decreasing temperature in radial direction; i.e. higher temperature and pressure close to the casing, lower temperature and pressure further away in the cement.

The matrix permeability of wellbore cement is usually lower than 0.1 mD (Economides, 1990). Together with the third cementation of the anchor casing, however, polypropylene (PP) fibres have been injected into the annulus. From the DTS temperature observation it is known, that the third cementation had an effect on the temperature profile along the entire length of the cable down to at least 232 m. Therefore, cement from this cementation is present within the annulus in all depths (Section 8.1). As these PP fibres melt at temperatures above 157 °C(315 °F) (FORTA Corporation, 2011), permeability might be increased (Kalifa et al., 2001; Noumowe, 2005) within parts of the cemented annulus. Furthermore, the permeability of the cement itself increases with increasing temperature (e.g. Patchen, 1960; Eilers and Root, 1976).

The water table within the formation is at 118 m. Gas permeabilities measured for Icelandic rock types range from 10^{-3} mD to 10^{5} mD (Sigurdsson et al., 2000). As the lithology is quite heterogeneous within the uppermost 300 m, high permeable layers are ambient and the pressure within the formation above the water table is therefore assumed to be similar to the ambient pressure at the surface.

Initially, the pore fluid within the cement is pressurized, as stated above. When the cement is fractured, the pores are connected to a fluid pathway and the liquid can evaporate, consuming latent heat of evaporation and drying out the cement. For a migrating fracture front within the annulus, the cement dries out in successive depth intervals. Elevated temperatures and drying of the cement changes its thermal properties as well as its density (e.g. Ickes et al., 1940; Harmathy, 1970; Marshall, 1972; Khan, 2002).

The vapour produced during the evaporation flows through the previously formed fractures and is released to the formation. As the formation is at ambient pressure, the consumed latent heat of evaporation can thus be calculated by the difference between the enthalpy at boiling point pressure at initial temperature and at 100 °C, which is the boiling point temperature at ambient pressure.

A fracture starts to evolve at the location of a weak spot and travels from there onwards. At the bottom of a casing, thermal gradients within the cement are greatest, as the diameter of the well decreases abruptly. Temperature gradients, together with different materials in contact, allow for the evolution of fractures close to the end of a casing. From here fractures can migrate upwards between the surface casing

and the anchor casing. As the cement is trapped between two casings, the vapour pressure is released to the formation below the end of the surface casing. Therefore, the actual location of fracture evolution is cooled by consumption of latent heat and deeper intervals are cooled by the flowing vapour, which is initially at 100 °C after flashing to ambient pressure.

From the temperature measurements it is known that the anomaly is located on opposite sites of the casing at equal times with a similar magnitude. Therefore, the fracture propagation is either located at only two positions, the positions of the cable branches, or it is more or less evenly distributed around the casing between the anchor casing and the surface casing.

Below the surface casing, a difference in the temperature anomaly between both sides can be observed. On the western side, the temperature increase during the onset of flow testing is slower than on the eastern side. On the eastern side, a localised temperature increase has been observed in three neighbouring depth intervals simultaneously. Fracturing the cement below the anchor casing, the vapour pressure can be released to the formation simultaneously in all depth intervals. Furthermore, the temperature increase after the anomaly is faster below the surface casing than between surface and anchor casing. On the western side, the slow increase can be explained by a gradual evaporation of pore fluid without rapid fracture evolution.

Generally, a large temperature decrease has been observed when the initial temperature was high. Initially high temperatures result in a high vapour pressure within the fluid and therefore a high enthalpy difference when flashing the fluid to atmosphere via a fracture network.

The slightly higher temperatures increase in 61 m than in 66 m after the anomaly might reflect a decreased thermal conductivity of the dry cement in comparison to a cemented interval without drying.

8.3.3. Simulation

In order to test the hypothesis of a fracture propagation, the temperature decrease due to evaporation has been simulated. For the simulation, only evaporation has been considered as a means to change the annular temperature. The flow of liquid or vapour that will occur when the cement fractures and the pore-fluid evaporates has been neglected.

The temperature evolution within the annulus has been modelled using the annular temperature model developed in Chapter 6. Therefore, the initial and boundary conditions have been changed. The process of evaporation has been introduced as an energy sink within the cement.

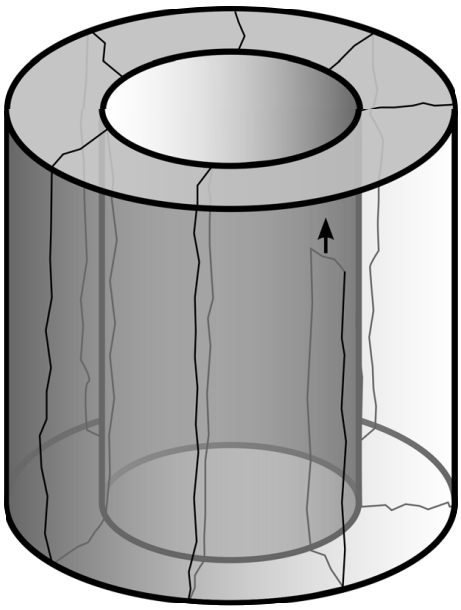

Figure 8.9.: Concept of fracture evolution within the cemented annuls. Fractures are evenly distributed around the perimeter. The fracture network is very dense to allow for all pore fluid to evaporate.

8.3.3.1. Geometry

The migrating temperature anomaly has been observed between the anchor and the surface casing. In order to model the temperature evolution within the annulus, a seven layer radial symmetric model has been calculated. The material and thickness of the different layers, together with the thermal properties, is given in Table 8.3. The step width between different nodes was 0.004 m. The *OD* of the simulated anchor casing was 0.328 m.

8.3.3.2. Initial Conditions

For the simulation of the temperature increase due to the production of hot geothermal fluid, a temperature of 10 °C has been set as initial formation temperature.

8.3.3.3. Boundary Conditions

For the formation, the static formation temperature has been set constant (Dirichlet boundary condition). For the inner boundary, the contact between wellbore fluid and casing, a constant temperature has been set as well. To better approximate the changing well temperature over time, the interface temperature at different times has been simulated using the result of a linear regression of the wellhead

Table 8.3.: List of different materials to simulate temperature anomaly. The materials are given with their thickness, density ρ, thermal conductivity λ and specific heat capacity c_p. For the thermal properties see Chapter 5. The *ID* of the production casing has been set to 0.216 m

Layer	Material	Thickness (m)	ρ (kg/m^3)	λ (W/m K)	c_p (J/kg K)
1	Casing	0.012	7800	50	450
2	Cement	0.032	1690	1	1000
3	Casing	0.012	7800	50	450
4	Cement	0.052	1690	1	1000
5	Casing	0.012	7800	50	450
6	Cement	0.032	1690	1	1000
7	Formation	≈25.5	3000	2	1040

temperature during the late period of DTS logging ($200 - 350$ h$_{DTS}$, Figure 3.8). The temperature evolution has been modelled as:

$$T_0 = 0.1120\ t + 201.34 \tag{8.1}$$

where T_0 is the temperature of the first node and t is the time after beginning of flow testing.

8.3.3.4. Inner Sources

At a certain point in time, as seen in Figure 8.4, the temperature anomaly starts in different depth intervals. In order to model the temperature decrease due to evaporation of pore fluid in a single depth interval, the consumption of latent heat of evaporation has been calculated based on the available amount of pore fluid and the enthalpy difference between liquid and vapour at the inital temperature. Pore fluid can evaporate as long as the temperature of the liquid and the cement is above 100 °C, assuming the liquid is flashed to the atmosphere.

The pores within the cement are very small. For a class G oilwell cement at $w/c = 0.44$ the pore size has been determined to be predominantly below 0.1 μm (Ghabezloo et al., 2008). Therefore, the surface area between fluid and cement is large and an instantaneous evaporation can be assumed.

In order to calculate the amount of energy, needed to change the temperature of the annulus by one degree, the volume V_n within each node has been multiplied with the density of the slurry ρ_{sl} as well as the specific heat capacity $c_{p,sl}$, calculated in Chapter 7. The thermal energy $Q_{th,n}$ at each node n, available to evaporate the pore fluid at time step j is then:

$$Q^j_{th,n} = V_n \rho_{sl} c_{p,sl} \Delta T^j_n \tag{8.2}$$

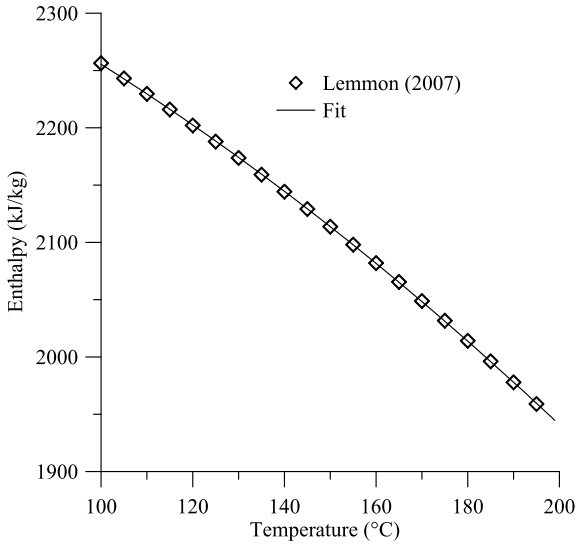

Figure 8.10.: Enthalpy of water versus temperature in the range $100 - 200$ °C fitted with a polynomial function of second order. Data from Lemmon et al. (2007).

where $\Delta T_n^j = T_n^j - 100$ is the temperature above 100 °C at node n.

In order to calculated the latent heat of evaporation for different temperatures $h_{evap}(T)$ (KJ/kg), the enthalpy difference between liquid and vapour state at boiling point pressure at different temperatures in the range of $100 - 200$ °C has been fitted to a second order polynomial function (Figure 8.10, Lemmon et al. (2007)):

$$h_{evap}(T) = 2445.37 - 1.28\ T - 0.00623\ T^2 \tag{8.3}$$

where the coefficient of determination for the first and second degree is $R^2 = 0.9974$ and $R^2 = 0.99998$, respectively.

For every time step, the amount of water that can be evaporated at the initial temperature is calculated. Therefore, for a given temperature T, the amount of thermal energy in the system and the amount of energy needed to evaporate the entire pore fluid is compared. The total energy needed for the phase transition Q_{evap} within each node n is calculated according to:

$$Q_{evap,n}(T) = h_{evap}(T) m_{f,n} \tag{8.4}$$

where $m_{f,n}$ is the liquid water mass within each node. The mass is calculated according to:

$$m_{f,n} = V_n \phi \rho_f \tag{8.5}$$

where V_n the volume of the node, ϕ the cement porosity and ρ_f the fluid density. For simplicity, $\rho = 1000$ kg/m^3 has been used.

In case $Q^j_{th,n} > Q_{evap,n}$ all fluid can be evaporated in a single time step. The temperature decrease within the annulus is determined by $Q_{evap,n}$. In case $Q_{th,n} < Q_{evap,n}$, the temperature of the annulus is reduced to 100 °C, which is the lower temperature limit for evaporation. The amount of water that is evaporated in a single time step j is calculated according to:

$$m^j_{f,evap,n} = \frac{Q^j_{th,n}}{Q_{evap,n}} V_n \phi * \rho_f \tag{8.6}$$

In the next time step, the temperature of the system increases due to conductive heat transfer. In subsequent iterations, the entire fluid evaporates.

The porosity of the cement used in HE-53 has been measured at two samples cured under atmospheric conditions, in the GFZ laboratory. In order to prepare the cement samples, 90 g cement has been mixed with 47.87 g deionized water to have a slurry density of 1684 kg/m^3, similar to the pumped density in HE-53. The samples have been cured for 6 month at room temperature. The porosity has been determined by the comparison of wet and dry weight. The samples have been dried for 35 days at 60 °C in a vacuum oven. Afterwards, the samples have been saturated with deionized water. The porosity has been determined to be 39 and 41 % for the different samples, respectively. An average value of 40 % has been used for the simulation.

For a full hydration of cement, a theoretical water-cement ratio of $w/c = 0.4$ is required (Lin and Meyer, 2009). As water has been used in excess for the cementations in HE-53 ($w/c = 0.65 - 0.75$), residual water is trapped within the pores of the cement.

As seen in Figure 8.5, the propagation of the anomaly along the annulus is steady. The migration of the evaporation front is therefore continuous. As DTS temperatures are averaged over an interval of 1 m, the evaporation front, travelling along the annulus, is influencing an increasing section of an individual DTS interval with time. For the simulation a very distinct evaporation front has been assumed. In order to simulate the propagation of the evaporation front using the one-dimensional, radial symmetric, conductive temperature simulator developed in Chapter 6, a running average has been calculated for the simulated temperature of a single depth interval. The temperatures have been averaged over a period of 20 h, representing the time, the anomaly takes to move along one DTS temperature interval ($\frac{20\text{ h}}{1\text{ m}} = 5$ cm/h).

8.3.4. Results

8.3.4.1. Simulated Temperature Anomaly

Figure 8.11(a) shows a simulated temperature anomaly for a constant wellbore fluid temperature of 220 °C. The time difference between individual time steps Δt for this simulation has been set to 400 s. Here, the temperature anomaly has been set to start at 200 h after beginning of production.

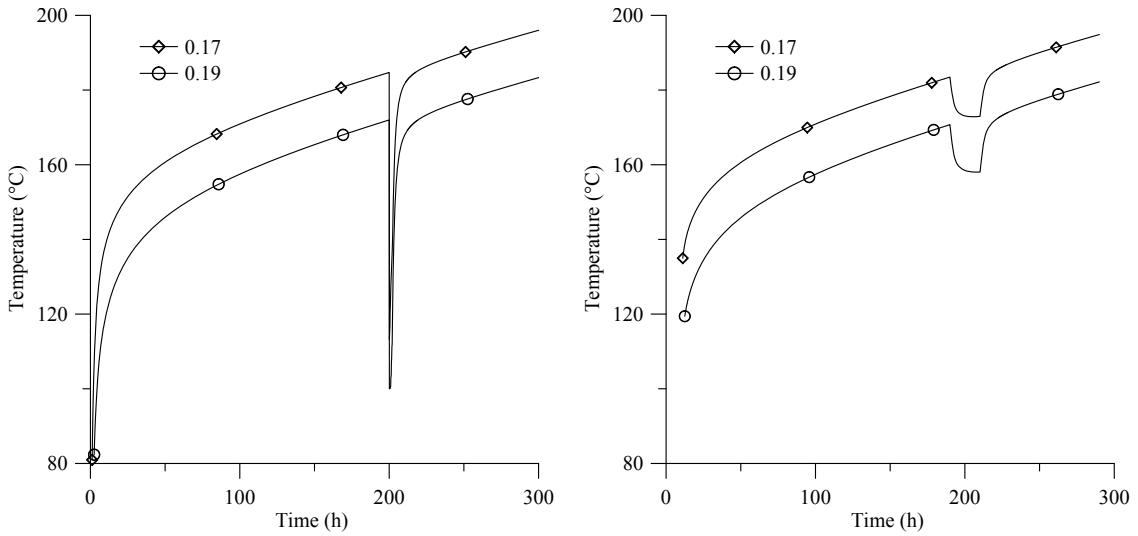

(a) Temperature in individual depth. (b) Averaged DTS temperature.

Figure 8.11.: (a) Simulated temperature evolution within annulus with temperature anomaly. The temperature for two radii (m) is displayed. The cable-casing distance is 0.006 m and 0.026 m, respectively. (b) The temperature anomaly is averaged over 20 h resembling the DTS temperature interval.

The temperature, measured by the DTS system is an average over a 1 m interval. As stated above, the anomaly takes ≈ 20 h to travel along a 1 m interval. The resulting temperature decrease calculated using a 20 h running average is about 10 °C for the location close to the casing and 13 °C further away in the cement (Figure 8.11(b)).

8.3.4.2. Simulated vs. Measured Temperature Anomaly

For a variable wellbore fluid temperature, Figure 8.12 shows a comparison between the anomaly in a depth interval of about 55 m depth. Overall, measured and simulated temperatures correspond to each other except for the very beginning of flow testing, as the input temperature for the model is slightly different to true wellhead temperature. Furthermore, a 20 h running average is displayed for the simulated temperature.

The simulated and measured anomalies have the same magnitude but not a similar shape. The time between maximum and minimum temperature at the beginning and end of the anomaly is similar. The measured temperature decrease is more or less linear, whereas the simulated temperature decrease is rapid at the beginning and very slow at the end of the period of decreasing temperatures. Furthermore, the temperature increase at the end of the anomaly for the simulated temperature

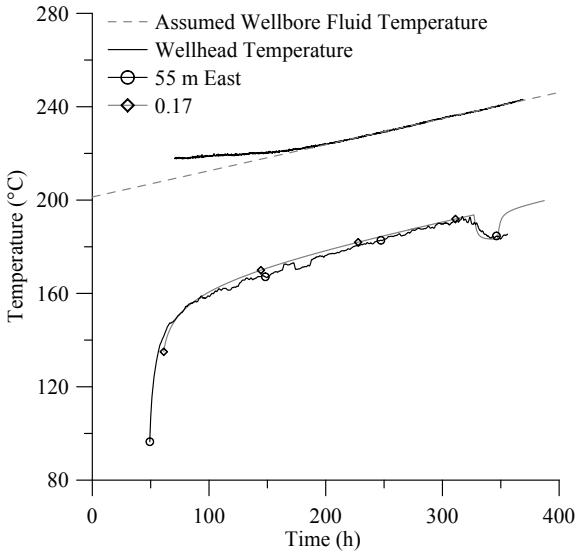

Figure 8.12.: Comparison of measured and simulated anomaly for the eastern cable branch in a depth of 55 m. The calculated cable-casing distance in this depth is ≈ 0 mm, simulated data is shown for a distance of 6 mm. DTS temperature data is averaged over a period of 1 h. Wellhead temperatures as well as the linear fit used to calculated the wellbore fluid temperatures is shown as well.

is far more rapid than observed by the DTS temperatures.

The initial temperature for the temperature decrease correlates to the cable casing distance similarly for the measured and modelled temperature evolution, if corrected for the linear temperature increase measured at the wellhead (Figure 8.13(a)). The magnitude of the temperature decrease increases with increasing distance cable-casing for the measured as well as the simulated temperatures (Figure 8.13(b)). The trend of an increasing magnitude of the anomaly with increasing initial temperature, on the contrary, could not be reproduced (Figure 8.13(c)), whereas the rate of the temperature change increases with increasing distance cable-casing for both, simulated as well as measured temperatures (Figure 8.13(d)). The rate of change for the simulated temperature anomaly has been determined between local maximum and minimum temperatures shortly before the anomaly and at the end of the anomaly, respectively. The calculated rate does not represent the strong decrease in temperatures at the beginning of the simulated anomaly.

8.3.5. Discussions

Within this section, a thermal anomaly, observed within the annulus, has been related to a fracture evolution and a subsequent evaporation of pore fluid within the

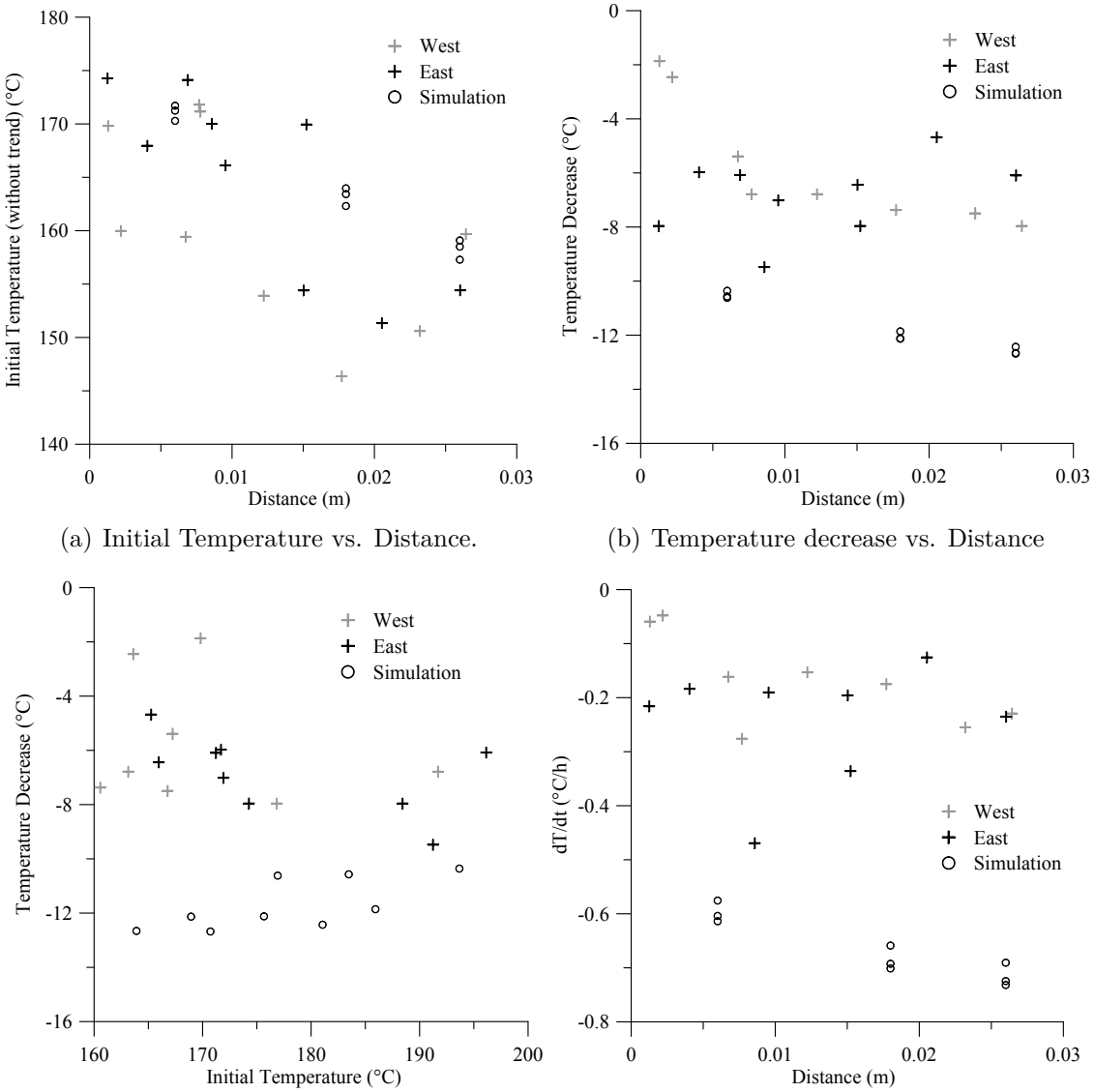

(a) Initial Temperature vs. Distance.

(b) Temperature decrease vs. Distance

(c) Magnitude of Temperature Change

(d) Rate of Temperature Change

Figure 8.13.: (a) Measured initial temperature at the beginning of the anomaly, corrected for the linear increase in temperature over time, in comparison to corrected simulated initial temperatures. (b) Comparison of the measured and simulated temperature decrease. (c) Magnitude of the temperature decrease for simulated and measured temperatures for different initial temperatures. (d) Rate of temperature change versus distance cable-casing for measured and simulated temperature anomaly; simulated temperatures are displayed for an assumed anomaly at 200, 250 and 337 h_{DTS}.

cement sheath of the second casing. Results of a numerical simulation support this hypothesis, as the general properties of the anomaly could be very well reproduced, except for the comparison of the temperature decrease for different initial temperatures. The difference between the opposing trends for the measured and simulated temperature decrease, however, is very small. Taking into account the error in determining the measured temperature for e.g. different plugging and unplugging activities ΔT =4.6 °C, the observed trend for the measured temperature might be skewed (Section 3.2.2).

The error in T_{DTS} affects all trends observed in Figure 8.13. Another error affecting the measured temperatures is the uncertainty in the depth determination. As absolute depths for different data points have been estimated with an accuracy of ±0.5 m, depth information between the eastern and western cable branch might differ by $2 \cdot 0.5 = 1$ m (Chapter 3). Despite differences in the absolute numbers between measured and simulated properties of the anomaly, however, a good agreement can be observed.

It has been observed that the temperature decrease is related to the initial temperature before the anomaly and therefore to the cable-casing distance. This could be qualitatively reproduced by the simple simulation (Figure 8.11).The temperature increase after the anomaly, however, was much quicker for the simulated anomaly.

Provided the hypothesis of a fractured annulus is valid, the difference between measured and simulated temperature evolutions can be explained by several factors. Only conductive heat transfer in radial direction is implemented in the annular temperature simulator. Therefore, any advective flow of cold vapour from neighbouring depth intervals is neglected. The slow temperature increase at the end of the anomaly for the measured DTS temperatures can be explained by such an advective vapour flow along the previously formed fractures.

As the fractures migrate along the annulus, the length of the flow path increases and the vapour temperature increases successively. Therefore, the influence on measured temperatures in deeper depth intervals mitigates over time. Another aspect to be considered is the exchange of liquid pore fluid by vapour. Vapour has a significantly lower thermal conductivity. Hence, the temperature gradient in radial direction within the cement is steeper. For a fracture migrating at the interface anchor-casing-cement, the temperature within the cement might be lower due a thermal contact resistance introduced by such a vapour filled annulus. The exchange of liquid by vapour, however, is a rapid process compared to the slow changes in DTS temperature. Furthermore, it has been observed that the final temperatures after the anomaly increased more rapidly compared to depth intervals with similar pre-anomaly thermal properties. Therefore, the flow of colder vapour might be the dominant effect and a contact resistance can be neglected.

For the simulation, a temperature decrease down to 100 °C has been assumed. If the pressure within the fractures is higher than the atmospheric pressure, however, the boiling point temperature is higher and the cooling is slower, as the fluid

cannot be cooled down to 100 °C. Higher pressures can be caused by a very low permeable formation. The evaporation within the cemented annulus might lead to a pressure increase at the cement-formation interface. Furthermore, if only a very limited number of fractures is present in the annulus, the evaporation is limited by the permeability of the cement, reducing the rate of evaporation and therefore the temperature decrease.

Another aspect supporting the fracture theory is the temperature anomaly observed below the surface casing (Figure 8.4). A rapid temperature decrease is observed for one side (East), whereas a gradual temperature increase is observed for the second side (West). Bad cement and gradual evaporation of pore fluid is reasonable on one side (West), whereas evaporation on the second side starts only after a fracturing process (East).

Beside the evaporation of pore fluid, however, the dehydration of cement phases is a possible heat sink. During heating of cement, several temperatures, associated with endothermic reactions can be assigned. In the low temperature range, below 200 °C where the temperature anomaly has been observed, data from differential scanning calorimetry measurements indicate dehydration reactions of individual mineral phases as well as ion exchange reactions in selected minerals (e.g. Bhatty, 1991; Sha et al., 1999; Morsy et al., 2010). Such reactions have been identified at temperatures above 100 °C for ordinary Portland cement, where dehydration reactions contribute much more to the energy consumption than ion exchange reactions. The kinetic of mineral dehydration reactions might be another possibility to slow down the temperature decrease and delay the temperature increase after the anomaly passed individual depth intervals.

The porosity of the cement samples has been determined after heating the samples for over a month. Therefore, bound water has been evaporated as well and the porosity is probably overestimated. The amount of evaporable water, however, can be estimated by comparing the dry with the saturated weight.

A rapid temperature decrease, as observed within the cemented annulus cannot be explained by a dehydration reaction alone. After the initial rapid temperature increase, the temperature increase in individual depth intervals is very slow. Dehydration reactions, as well as the evaporation of pore fluid, would lead to a constant temperature, as soon as the temperature required for the process is reached. Such a process can explain the slow temperature increase below the surface casing on the western side. The temperature decrease on the opposite side can only be explained if the system (hydrated cement - pore fluid) can suddenly release its vapour pressure.

Different phenomena than dehydration of pores and mineral phases alone, like ion exchange reactions mentioned above, are not very likely to be the reason for the observed temperature anomaly. For such reactions, the anomaly would be solely temperature dependent, as well. Anomalies would have to be observed in more than one depth at a single time, as different depth are at a similar temperature. Furthermore, the temperature should stay constant until all material reacted. The

observed decrease in temperature can therefore not be explained. The difference between the observations on opposite sides below the surface casing (Figure 8.4) cannot be explained by ion exchange reactions, as the processes on both sides should be similar.

Apart from the consumption of latent heat of evaporation, an increased thermal energy transfer between well and formation can decrease the temperatures, locally. A sudden increase in heat loss cannot be explained by conduction alone, considering that no mineral transitions occurred, as discussed above. Therefore, advective energy transfer has to be considered. As the water table within the formation is at 118 m, any kind of fluid flow, starting at different times in different depth intervals within the formation, cannot explain the observed thermal anomaly. Furthermore, a fluid flow on a single side of the casing only, like necessary for the difference in the observed temperature anomaly below the surface casing is not very likely.

Assuming a fractured annulus, a density driven convection within the fractures is reasonable. As the width of the fractures is very small, individual convection cells could be limited to a small vertical extend. Due to the fact that the temperature anomaly below the surface casing has been observed on one side but not the other, however, it is very unlikely that convection is the reason for the temperature decrease. A convective fluid transport between a permeable formation and the casing cannot be established. All liquid would evaporate as soon as there is a pathway to the formation. The same applies for the depth intervals between anchor and surface casing. If the fractured cement is open to the formation, the liquid would evaporate. A convective heat transfer can therefore be neglected.

The preceding discussion assumes similar cement properties in different depth intervals, where the temperature anomaly has been observed. The results from the density profile indicate a slight reduction of the density with decreasing depth, i.e. an increased w/c and therefore changing mechanical properties. The results, however, are biased as the variance between measured and simulated temperatures is quite high. An influence of cementations during the drilling activities in about 150 m depth on the formation in 70 m depth has been neglected (Appendix A).

The different phenomena described above depend on the evolution of a fracture network within the cemented annulus. Otherwise, a temperature decrease cannot be sufficiently explained. The hypothesis of a fracture propagation and a subsequent evaporation of pore fluid and dehydration reactions of mineral phases proved to be capable of explaining the observed temperature anomaly.

It remains to be mentioned that elevated thermal conductivity values determined in Chapter 5 (Figure 5.7) in about 70 m depth and above the bottom of the surface casing might be partly attributed to the observed thermal anomaly. After the anomaly, the measured DTS temperature within the annulus was significantly lower. Hence, the calculated cement-formation-interface temperature was significantly colder, leading to an overestimation of the formation thermal conductivity.

9. Summary

Within this study, a novel fibre optic cable has been developed and tested under field conditions in a high temperature geothermal well in Hellisheiði, Iceland. As the sensing element, a polyimide fibre with an additional carbon coating has been used. The cable has been installed permanently behind the anchor casing of well HE-53 to 261.3 m depth and the temperature evolution during cementing and flow testing of the well was monitored.

Damages of the cable, observed after the installation, are attributed to the properties of the young and brittle igneous rock formations and individual operational details during running of the casing. Despite the damages, temperature measurements could be performed during the cementation of the anchor casing, the onset of a flow test as well as after the flow test.

During the onset of the flow test, maximum temperatures of up to 230 °C were measured. After the end of the two-week logging campaign, wellhead temperatures reached more than 280 °C, which exceeded the maximum temperatures expected for this well. As the cable was damaged during the installation, flushing the cable continuously with argon was not possible. Therefore the concentration of harmful substances like hydrogen produced within the cable at elevated temperatures could not be reduced. Consequently, the temperature profile during the third field campaign after the end of the flow test was significantly affected by the degradation of the optical fibre.

Using DTS temperature data acquired during the onset of the flow test, the heat loss to the formation in individual depth could be measured. The measured heat loss has been used to determine the porosity of the formation. With a simple relation between porosity, thermal conductivity, specific heat capacity and density the thermal properties of the formation can be calculated. Thus, thermal conductivity, specific heat capacity and thermal diffusivity has been calculated for individual depth intervals. Thereby, depth intervals with unexpectedly large thermal conductivities were identified.

The information of the formation thermal properties has been used to implement a one dimensional finite-difference model to calculate conductive heat transfer to the formation. Together with a theoretical hydration model for the cement, the temperature evolution within the annulus has been simulated and compared to the measured temperature evolution during the cementation of the anchor casing. To fit measured and simulated temperatures, the slurry density used for the simulation has been varied. Performing a simulation for every depth interval, a density-depth

profile of the cement could be calculated to evaluate the cementation in individual depth intervals.

Temperature data from the flow test revealed a thermal anomaly within the cemented annulus behind the anchor casing. Although the wellhead temperature was constantly increasing, the temperature within the annulus decreased, locally. The effect of decreasing temperatures could be successfully related to a migrating fracture network within the cemented annulus and a resulting drying of the cement. It was therefore possible to on-line monitor a thermal process behind the second casing that can be related to a process influencing the structural integrity of the subsurface installation. Issues like zonal isolation and a change in thermal and mechanical properties of the cement within the annulus are affected.

10. Conclusions

10.1. Fibre Degradation

The laboratory measurements prior to the installation in Iceland helped to select and evaluate the operating limit for the high temperature optical fibres as well as the fibre optic cable. For high temperature applications metal and polymer coated fibres can be used. From the tested fibres, however, polyimide coated fibres were best suited for the application in a wellbore cable in Iceland. It is known that the polyimide coating degrades at temperatures close to 300 °C, if applied for a long time. The degradation rate increases with increasing temperatures. For fibres heated in inert atmosphere, however, the observed degradation was greatly reduced.

After selecting and characterising the optical fibre, a fibre optic cable has been manufactured and tested. At elevated temperatures, hydrogen was released within the cable, which has an effect on the long time performance of the fibre. Therefore, it is recommended to flush a fibre optic cable with inert atmosphere, when measuring under high temperature conditions. A flushing rate of 50 ml/min at room conditions proved to be successful in reducing the hydrogen concentration within the cable without affecting the measured DTS temperatures.

10.2. Installation

Although the cable has been cut during the installation, a temperature profile could be acquired down to 261.3 m. Flushing the cable with inert atmosphere, however, was not possible. Therefore, a severe degradation as observed after flow testing for a period of 3 month and temperatures close to 300 °C. As the cable has been damaged during rapid temperature changes at the onset of the flow test as well, an improved protection for the cable is necessary for an installation on the outside of a casing within brittle formations like in Iceland.

10.3. Thermal Properties of the Formation

DTS measurements on the outside of the casing proved to have the potential to online monitor the heat loss to the formation. Heat loss values could be used to determine the formation thermal properties like thermal conductivity, specific heat capacity

and thermal diffusivity. A better constrain on the properties of the components used for the subsurface installation has to be achieved in order to reduce the error estimate of the calculation (thermal properties of the cement/casing as well as geometrical parameters like the location of the cable, centralization,...). If the properties of the formation are known, heat loss values can be used to estimate the quality of the cementation and the properties of the cement. Furthermore, changes in the thermal parameters of the cement can be detected.

10.4. Cementation

Together with a theoretical hydration model for the cement, DTS temperature data from the first field campaign could successfully be used to estimate a reasonable density of the cement behind the anchor casing. Using a proper model for the elastic property evolution within the hydrating cement, acoustic properties of the cement could be estimated. A theoretical CBL log could be calculated. The simple correlation between acoustic properties of the cement and CBL attenuation given in Jutten et al. (1989), however, is only reasonable for hydration times greater than three days. As conventional CBL data was only available for smaller times, a theoretical CBL log has not been calculated within this study. Having the a conventional CBL log for greater times than three days, differences between a theoretical and a measured log might be used to detect microannuli behind the casing and give a better estimate on the zonal isolation of the cement sheath than with acoustic tools alone. For the field data from Iceland, a more detailed calculation, accounting for the density and acoustic properties of wellbore fluid and casing, could be applied to calculate a theoretical CBL attenuation from the simulated cement properties.

10.5. Structural Wellbore Integrity Monitoring

Using data from the flow testing period, a thermal anomaly behind the second casing could be related to a process influencing the integrity of the cemented annulus. A fracturing process within the cement has been identified as the most reasonable explanation for the observed thermal anomaly. A migration of the fracture evolution could be online monitored over several meters along the annulus. The fracture evolution indicates a change in mechanical properties of the cemented annulus as well as a loss of zonal isolation. Possible pathways for fluid migration along the annulus might be produced. In order to prevent the loss of zonal isolation, the information about this process might be used to perform counteractions like changing the production pressure or temperature. Furthermore, information on such a fracturing process and the according depth information could be used to optimize cost intensive remedial actions within the well.

The structural wellbore integrity is essential for a safe and sustainable utilization of the subsurface reservoir. In order to minimize the environmental impact of wellbore fluid production activities as well as maximize the return on investment on completing and operating a well, processes that might influence the integrity have to be carefully monitored. Installing a permanent distributed temperature monitoring system is capable of identifying such processes in different depth intervals and can help the wellbore operator to take mitigating measures maintaining the wellbore integrity.

A. Drilling Progress HE-53

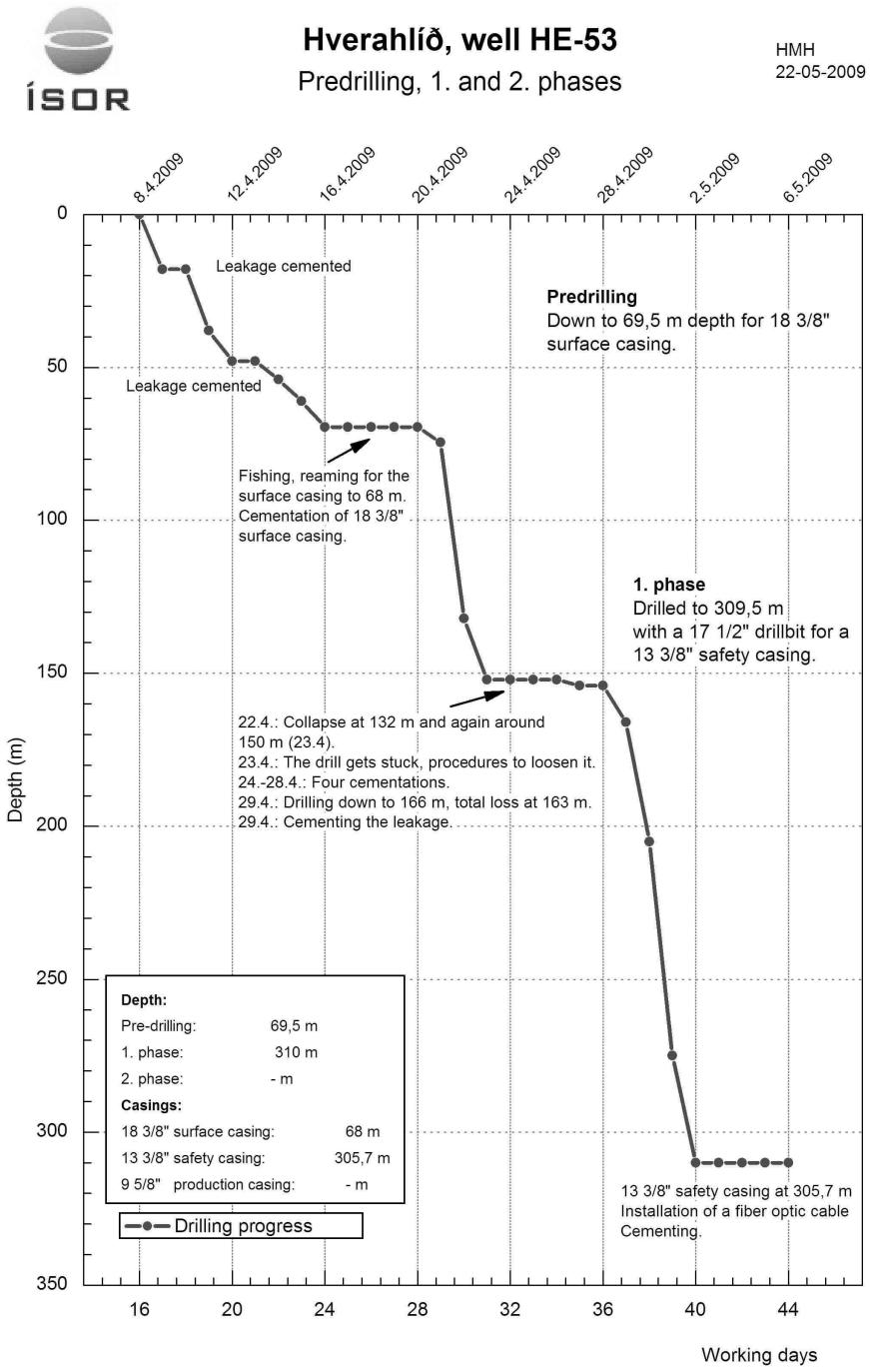

Figure A.1.: Drilling progress. Courtesy of Reykjavik Energy.

B. Lithology HE-53

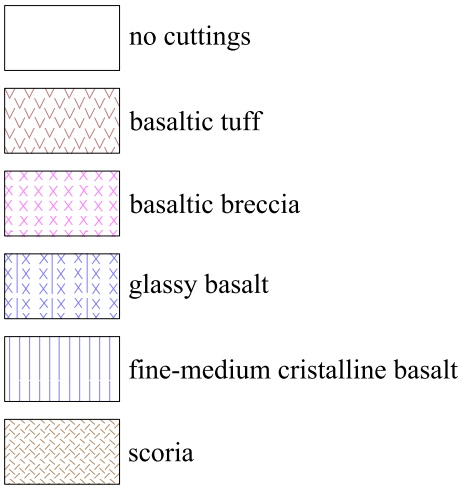

Figure B.1.: Lithology.

C. Installation

Table C.1.: List of different activities in well HE-53 prior and during the cementation of the anchor casing. DTS logging time is given as reference. Data has been provided by ISOR.

Date	Time (CET)	Activity	DTS Time (hh:mm)
03.05.09	03:16	Temperature / CCL	
03.05.09	04:25	Calliper	
04.05.09	00:25	Begin DTS Logging	00:00
04.05.09	05:06	Begin Cementation	04:41
04.05.09	18:58	Temperature / CCL	18:33
05.05.09	05:10	Temperature / CCL	28:45
05.05.09	06:37	CBL	30:12
05.05.09	16:47	Temperature / CCL	40:22
05.05.09	18:18	CBL	41:53
05.05.09	22:30	End DTS Measurement	46:05

Table C.2.: Depth correlation of different well logs during cementation. Reference: CCL-Log from 3.5.2009, 18:58. Data has been provided by ISOR.

Date	Time	Log	Shift (m)	Remarks
03.05.09	15:16	Temperature / CCL	0	No correlation possible
03.05.09	04:25	Calliper	0.5	Breakouts to CBL
04.05.09	18:58	Temperature / CCL	0	Reference
05.05.09	05:10	Temperature / CCL	0.2	CCL to reference
05.05.09	06:37	CBL	1.4	Travel Time to CCL
05.05.09	16:47	Temperature / CCL	0	CCL to reference
05.05.09	18:18	CBL	0.7	Travel Time to CCL
		DTS (eastern cable branch)	0	Depth of Installation from CCL
		DTS (western cable branch)	0	Correlated to eastern branch

Table C.3.: Depth of installation interpreted from three different Casing Collar Locator (CCL) logs (see Table C.1).

Casing	Top of Joint (m below surface)	Installed Centralizer	Remark
1	-0.13 ± 0.02	0	two Datapoints
2	8.23 ± 0.01	1	
3	20.36 ± 0.12	0	
4	32.01 ± 0.13	1	
5	43.98 ± 0.09	0	
6	56.09 ± 0.12	1	
7	68.18 ± 0.11	1	
8	80.27 ± 0.10	1	
9	92.46 ± 0.11	1	
10	104.46 ± 0.12	1	
11	116.61 ± 0.13	1	
12	128.57 ± 0.11	1	
13	140.68 ± 0.09	1	
14	152.92 ± 0.06	1	
15	164.99 ± 0.05	1	
16	176.80 ± 0.08	1	
17	188.51 ± 0.07	1	
18	200.65 ± 0.05	1	
19	212.77 ± 0.10	1	
20	224.85 ± 0.08	1	
21	237.00 ± 0.09	1	
22	248.81 ± 0.07	1	
23	260.78 ± 0.15	2	modified centralizer

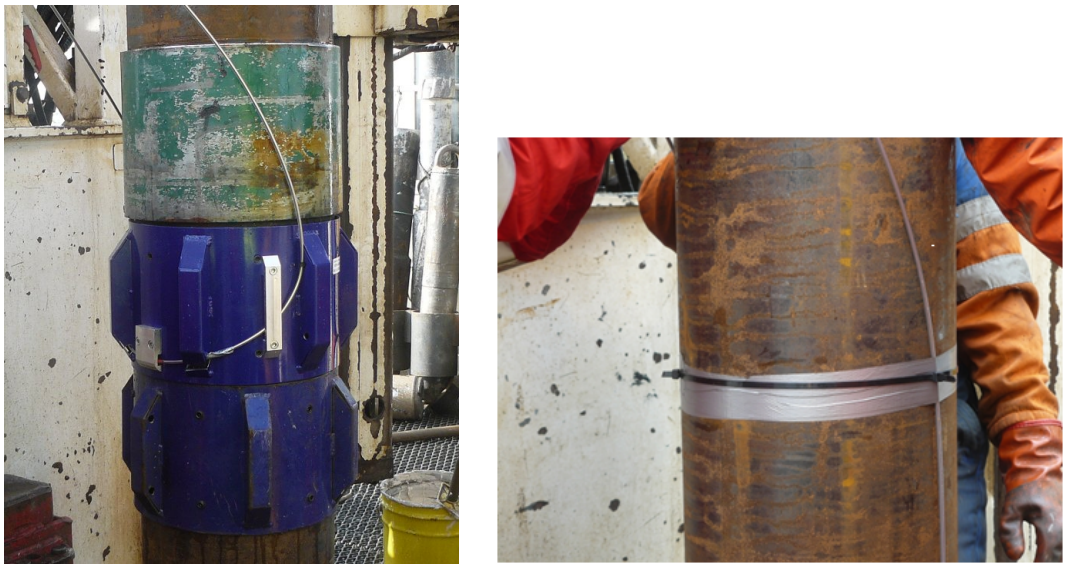

(a) Turnaround. (b) In between two joints.

Figure C.1.: Installation of the DTS sensor cable. (a) Turnaround of the cable. (b) Fastening the cable to the casing in between two joints using tape and ties.

D. DTS Data Points

Data Point	Depth (m) (below surface)	Depth (m) (below platform)	Distance (m)
1	-1.15	5.55	
2	-0.12	6.58	
3	0.9	7.6	0.0000
4	1.93	8.63	0.0000
5	2.95	9.65	0.0000
6	3.98	10.68	0.0005
7	5	11.7	0.0023
8	6.03	12.73	0.0047
9	7.05	13.75	0.0072
10	8.08	14.78	0.0083
11	9.1	15.8	0.0185
12	10.13	16.83	0.0223
13	11.15	17.85	0.0168
14	12.18	18.88	0.0113
15	13.2	19.9	0.0059
16	14.23	20.93	0.0019
17	15.25	21.95	0.0016
18	16.28	22.98	0.0033
19	17.3	24	0.0050
20	18.33	25.03	0.0066
21	19.35	26.05	0.0083
22	20.38	27.08	0.0049
23	21.4	28.1	0.0000
24	22.43	29.13	0.0000
25	23.45	30.15	0.0000
26	24.48	31.18	0.0000
27	25.5	32.2	0.0000
28	26.53	33.23	0.0007
29	27.55	34.25	0.0023
30	28.58	35.28	0.0041
31	29.6	36.3	0.0059
32	30.63	37.33	0.0076
33	31.65	38.35	0.0079
34	32.68	39.38	0.0257
35	33.7	40.4	0.0233
36	34.73	41.43	0.0177
37	35.75	42.45	0.0121
38	36.78	43.48	0.0066
39	37.8	44.5	0.0021

40	38.83	45.53	0.0014
41	39.85	46.55	0.0031
42	40.88	47.58	0.0048
43	41.9	48.6	0.0065
44	42.93	49.63	0.0082
45	43.96	50.66	0.0053
46	44.98	51.68	0.0000
47	46.01	52.71	0.0000
48	47.03	53.73	0.0000
49	48.06	54.76	0.0000
50	49.08	55.78	0.0000
51	50.11	56.81	0.0005
52	51.13	57.83	0.0018
53	52.16	58.86	0.0035
54	53.18	59.88	0.0052
55	54.21	60.91	0.0069
56	55.23	61.93	0.0086
57	56.26	62.96	0.0152
58	57.28	63.98	0.0260
59	58.31	65.01	0.0205
60	59.33	66.03	0.0150
61	60.36	67.06	0.0095
62	61.38	68.08	0.0040
63	62.41	69.11	0.0013
64	63.43	70.13	0.0021
65	64.46	71.16	0.0038
66	65.48	72.18	0.0055
67	66.51	73.21	0.0072
68	67.53	74.23	0.0089
69	68.56	75.26	0.0190
70	69.58	76.28	0.0249
71	70.61	77.31	0.0194
72	71.63	78.33	0.0139
73	72.66	79.36	0.0084
74	73.68	80.38	0.0029
75	74.71	81.41	0.0009
76	75.73	82.43	0.0025
77	76.76	83.46	0.0042
78	77.78	84.48	0.0059
79	78.81	85.51	0.0076
80	79.83	86.53	0.0086
81	80.86	87.56	0.0236
82	81.88	88.58	0.0238
83	82.91	89.61	0.0184
84	83.93	90.63	0.0129
85	84.96	91.66	0.0075
86	85.98	92.68	0.0024
87	87.01	93.71	0.0011
88	88.04	94.74	0.0027
89	89.06	95.76	0.0044
90	90.09	96.79	0.0061

91	91.11	97.81	0.0078
92	92.14	98.84	0.0077
93	93.16	99.86	0.0265
94	94.19	100.89	0.0231
95	95.21	101.91	0.0176
96	96.24	102.94	0.0120
97	97.26	103.96	0.0065
98	98.29	104.99	0.0021
99	99.31	106.01	0.0014
100	100.34	107.04	0.0031
101	101.36	108.06	0.0048
102	102.39	109.09	0.0065
103	103.41	110.11	0.0083
104	104.44	111.14	0.0114
105	105.46	112.16	0.0270
106	106.49	113.19	0.0216
107	107.51	114.21	0.0161
108	108.54	115.24	0.0107
109	109.56	116.26	0.0052
110	110.59	117.29	0.0016
111	111.61	118.31	0.0018
112	112.64	119.34	0.0035
113	113.66	120.36	0.0051
114	114.69	121.39	0.0068
115	115.71	122.41	0.0085
116	116.74	123.44	0.0143
117	117.76	124.46	0.0262
118	118.79	125.49	0.0206
119	119.81	126.51	0.0151
120	120.84	127.54	0.0095
121	121.86	128.56	0.0039
122	122.89	129.59	0.0012
123	123.91	130.61	0.0022
124	124.94	131.64	0.0039
125	125.96	132.66	0.0056
126	126.99	133.69	0.0074
127	128.01	134.71	0.0091
128	129.04	135.74	0.0207
129	130.07	136.77	0.0244
130	131.09	137.79	0.0189
131	132.12	138.82	0.0134
132	133.14	139.84	0.0079
133	134.17	140.87	0.0026
134	135.19	141.89	0.0009
135	136.22	142.92	0.0026
136	137.24	143.94	0.0043
137	138.27	144.97	0.0060
138	139.29	145.99	0.0077
139	140.32	147.02	0.0081
140	141.34	148.04	0.0254
141	142.37	149.07	0.0235

142	143.39	150.09	0.0181
143	144.42	151.12	0.0126
144	145.44	152.14	0.0072
145	146.47	153.17	0.0023
146	147.49	154.19	0.0011
147	148.52	155.22	0.0028
148	149.54	156.24	0.0045
149	150.57	157.27	0.0062
150	151.59	158.29	0.0078
151	152.62	159.32	0.0075
152	153.64	160.34	0.0270
153	154.67	161.37	0.0230
154	155.69	162.39	0.0175
155	156.72	163.42	0.0120
156	157.74	164.44	0.0065
157	158.77	165.47	0.0021
158	159.79	166.49	0.0014
159	160.82	167.52	0.0031
160	161.84	168.54	0.0048
161	162.87	169.57	0.0065
162	163.89	170.59	0.0082
163	164.92	171.62	0.0103
164	165.94	172.64	0.0272
165	166.97	173.67	0.0216
166	167.99	174.69	0.0159
167	169.02	175.72	0.0103
168	170.04	176.74	0.0047
169	171.07	177.77	0.0015
170	172.09	178.79	0.0020
171	173.12	179.82	0.0038
172	174.15	180.85	0.0055
173	175.17	181.87	0.0072
174	176.2	182.9	0.0090
175	177.22	183.92	0.0197
176	178.25	184.95	0.0245
177	179.27	185.97	0.0188
178	180.3	187	0.0131
179	181.32	188.02	0.0074
180	182.35	189.05	0.0024
181	183.37	190.07	0.0012
182	184.4	191.1	0.0030
183	185.42	192.12	0.0047
184	186.45	193.15	0.0065
185	187.47	194.17	0.0082
186	188.5	195.2	0.0116
187	189.52	196.22	0.0270
188	190.55	197.25	0.0215
189	191.57	198.27	0.0160
190	192.6	199.3	0.0106
191	193.62	200.32	0.0051
192	194.65	201.35	0.0016

193	195.67	202.37	0.0018
194	196.7	203.4	0.0035
195	197.72	204.42	0.0052
196	198.75	205.45	0.0069
197	199.77	206.47	0.0085
198	200.8	207.5	0.0147
199	201.82	208.52	0.0262
200	202.85	209.55	0.0207
201	203.87	210.57	0.0152
202	204.9	211.6	0.0097
203	205.92	212.62	0.0042
204	206.95	213.65	0.0013
205	207.97	214.67	0.0021
206	209	215.7	0.0038
207	210.02	216.72	0.0055
208	211.05	217.75	0.0072
209	212.07	218.77	0.0088
210	213.1	219.8	0.0181
211	214.12	220.82	0.0252
212	215.15	221.85	0.0197
213	216.17	222.87	0.0142
214	217.2	223.9	0.0086
215	218.23	224.93	0.0031
216	219.25	225.95	0.0009
217	220.28	226.98	0.0024
218	221.3	228	0.0041
219	222.33	229.03	0.0058
220	223.35	230.05	0.0075
221	224.38	231.08	0.0089
222	225.4	232.1	0.0227
223	226.43	233.13	0.0240
224	227.45	234.15	0.0185
225	228.48	235.18	0.0130
226	229.5	236.2	0.0076
227	230.53	237.23	0.0025
228	231.55	238.25	0.0010
229	232.58	239.28	0.0027
230	233.6	240.3	0.0044
231	234.63	241.33	0.0061
232	235.65	242.35	0.0078
233	236.68	243.38	0.0077
234	237.7	244.4	0.0264
235	238.73	245.43	0.0230
236	239.75	246.45	0.0173
237	240.78	247.48	0.0117
238	241.8	248.5	0.0061
239	242.83	249.53	0.0019
240	243.85	250.55	0.0016
241	244.88	251.58	0.0033
242	245.9	252.6	0.0051
243	246.93	253.63	0.0068

244	247.95	254.65	0.0086
245	248.98	255.68	0.0152
246	250	256.7	0.0259
247	251.03	257.73	0.0204
248	252.05	258.75	0.0148
249	253.08	259.78	0.0093
250	254.1	260.8	0.0037
251	255.13	261.83	0.0011
252	256.15	262.85	0.0023
253	257.18	263.88	0.0040
254	258.2	264.9	0.0057
255	259.23	265.93	0.0074
256	260.25	266.95	0.0091
257	261.28	267.98	0.0211

Table D.1.: Depth to DTS data points together with the distance between cable and casing, averaged over a one meter interval, for the eastern cable branch.

E. Wavetek Measurements

File #	Branch	Wavelength (nm)	Date	Time (CET)	Time (h_{DTS})
11	West	850	7/28/2009	0:20	
12	East	850	7/28/2009	0:20	
13	West	850	7/28/2009	15:49	-0.88
14	West	1300	7/28/2009	15:52	-0.83
15	East	1300	7/28/2009	15:53	-0.82
16	East	850	7/28/2009	15:55	-0.78
17	West	850	7/29/2009	23:25	30.72
18	West	1300	7/29/2009	23:27	30.75
19	East	1300	7/29/2009	23:30	30.80
20	East	850	7/29/2009	23:32	30.83
21	West	850	7/30/2009	11:10	42.47
22	West	1300	7/30/2009	11:13	42.52
23	East	1300	7/30/2009	11:15	42.55
24	East	850	7/30/2009	11:17	42.58
25	West	850	7/30/2009	16:49	48.12
26	West	1300	7/30/2009	16:52	48.17
27	East	1300	7/30/2009	16:54	48.20
28	East	850	7/30/2009	16:56	48.23
29	West	850	7/30/2009	19:48	51.10
30	West	1300	7/30/2009	19:50	51.13
31	East	1300	7/30/2009	19:52	51.17
32	East	850	7/30/2009	19:54	51.20
33	West	850	7/31/2009	11:49	67.12
34	West	1300	7/31/2009	11:51	67.15
35	East	1300	7/31/2009	11:55	67.22
36	East	850	7/31/2009	11:58	67.27
37	West	850	7/31/2009	21:02	76.33
38	West	1300	7/31/2009	21:04	76.37
39	East	1300	7/31/2009	21:08	76.43
40	East	850	7/31/2009	21:11	76.48
41	West	850	7/31/2009	23:44	79.03
42	West	1300	7/31/2009	23:47	79.08
43	East	1300	7/31/2009	23:50	79.13
44	East	850	7/31/2009	23:51	79.15
45	West	850	8/1/2009	11:57	91.25
46	West	1300	8/1/2009	11:59	91.28
47	East	1300	8/1/2009	12:01	91.32
48	East	850	8/1/2009	12:04	91.37
49	West	850	8/1/2009	16:36	95.90

50	West	1300	8/1/2009	16:38	95.93
51	East	1300	8/1/2009	16:40	95.97
52	East	850	8/1/2009	16:52	96.17
53	West	850	8/1/2009	22:11	101.48
54	West	1300	8/1/2009	22:14	101.53
55	East	1300	8/1/2009	22:16	101.57
56	East	850	8/1/2009	22:18	101.60
57	West	850	8/2/2009	12:01	115.32
58	West	1300	8/2/2009	12:03	115.35
59	East	1300	8/2/2009	12:05	115.38
60	East	850	8/2/2009	12:07	115.42
61	West	850	8/2/2009	22:20	125.63
62	West	1300	8/2/2009	22:23	125.68
63	East	1300	8/2/2009	22:25	125.72
64	East	850	8/2/2009	22:27	125.75
65	West	850	8/3/2009	12:47	140.08
66	West	1300	8/3/2009	12:49	140.12
67	East	1300	8/3/2009	12:51	140.15
68	East	850	8/3/2009	12:56	140.23
69	West	850	8/3/2009	20:47	148.08
70	West	1300	8/3/2009	20:29	147.78
71	East	1300	8/3/2009	20:32	147.83
72	East	850	8/3/2009	20:34	147.87
73	West	850	8/4/2009	12:18	163.60
74	West	1300	8/4/2009	12:20	163.63
75	East	1300	8/4/2009	12:22	163.67
76	East	850	8/4/2009	12:24	163.70
77	West	850	8/4/2009	22:13	173.52
78	West	1300	8/4/2009	22:15	173.55
79	East	1300	8/4/2009	22:17	173.58
80	East	850	8/4/2009	22:19	173.62
81	West	850	8/5/2009	11:52	187.17
82	West	1300	8/5/2009	11:54	187.20
83	East	1300	8/5/2009	12:05	187.38
84	East	850	8/5/2009	12:07	187.42
85	East	850	8/5/2009	12:10	187.47
86	East	1300	8/5/2009	12:12	187.50
87	West	1300	8/5/2009	22:12	197.50
88	West	850	8/5/2009	22:14	197.53
89	East	850	8/5/2009	22:17	197.58
90	East	1300	8/5/2009	22:19	197.62
91	West	1300	8/6/2009	12:11	211.48
92	West	850	8/6/2009	12:15	211.55
93	East	850	8/6/2009	12:17	211.58
94	East	1300	8/6/2009	12:18	211.60
95	West	1300	8/6/2009	22:42	222.00
96	West	850	8/6/2009	22:44	222.03
97	East	850	8/6/2009	22:49	222.12
98	East	1300	8/6/2009	22:51	222.15
99	West	1300	8/7/2009	11:56	235.23
100	West	850	8/7/2009	11:58	235.27

101	East	850	8/7/2009	12:00	235.30
102	East	1300	8/7/2009	12:02	235.33
103	West	1300	8/7/2009	23:03	246.35
104	West	850	8/7/2009	23:07	246.42
105	East	850	8/7/2009	23:11	246.48
106	East	1300	8/7/2009	23:14	246.53
107	West	1300	8/8/2009	13:18	260.60
108	West	850	8/8/2009	13:21	260.65
109	East	850	8/8/2009	13:25	260.72
110	East	1300	8/8/2009	13:27	260.75
111	West	1300	8/8/2009	20:22	267.67
112	West	850	8/8/2009	20:24	267.70
113	East	850	8/8/2009	20:27	267.75
114	East	1300	8/8/2009	20:31	267.82
115	West	1300	8/9/2009	12:22	283.67
116	West	850	8/9/2009	12:25	283.72
117	East	850	8/9/2009	12:28	283.77
118	East	1300	8/9/2009	12:30	283.80
119	West	1300	8/9/2009	20:16	291.57
120	West	850	8/9/2009	20:18	291.60
121	East	850	8/9/2009	20:20	291.63
122	East	1300	8/9/2009	20:22	291.67
123	West	1300	8/10/2009	11:57	307.25
124	West	850	8/10/2009	11:59	307.28
125	East	850	8/10/2009	12:02	307.33
126	East	1300	8/10/2009	12:04	307.37
127	West	1300	8/10/2009	20:35	315.88
128	West	850	8/10/2009	20:38	315.93
129	East	850	8/10/2009	20:42	316.00
130	East	1300	8/10/2009	20:45	316.05
131	West	1300	8/11/2009	13:04	332.37
132	West	850	8/11/2009	13:06	332.40
133	East	850	8/11/2009	13:11	332.48
134	East	1300	8/11/2009	13:13	332.52
135	West	1300	8/11/2009	18:41	337.98
136	West	850	8/11/2009	18:46	338.07
137	East	850	8/11/2009	18:49	338.12
138	East	1300	8/11/2009	18:51	338.15
139	West	1300	8/12/2009	12:54	356.20
140	West	850	8/12/2009	12:56	356.23
141	East	850	8/12/2009	12:58	356.27
142	East	1300	8/12/2009	13:00	356.30

Table E.1.: List of OTDR measurements.

F. Input Parameters for Hydration Calculation

Table F.1.: Exemplary input parameters for annular temperature simulation. The parameters can be categorised in different components, e.g. rock parameters, number of nodes, calculation time, etc..

Parameter	Value	Unit
Wellbore Fluid		
ID casing	0.32	m
Specific heat capacity	4187	J/(kg K)
Thermal conductivity	0.58	W/(m K)
Density	1000	kg/(m^3)
Casing		
Number of casings	1	–
Thickness	0.012	m
Specific heat capacity	450	J/(kg K)
Thermal conductivity	50	W/(m K)
Density	7800	kg/(m^3)
Cement		
Thickness	0.124	m
Specific heat capacity	1000	J/(kg K)
Thermal conductivity	1	W/(m K)
Density	1690	kg/(m^3)
Formation		
Thickness	1	m
Specific heat capacity	1957	J/(kg K)
Thermal conductivity	0.82	W/(m K)
Density	1802	kg/m^3
Time		
Calculated time	125000	s
Sampling rate	1000	s
Sampling for writing to file	10	–
Nodes		
Number of nodes per meter	250	1/m
Hydration Parameters		
Number of casing to cement	1	–
Depth in well	118	m
File Handling		
Input file with cement specification	cement.ini	–
Name for output file	cement.dat	–

Table F.2.: Exemplary input parameters for hydration calculation. The parameters can be categorised in different components, e.g. cement compositon, thermal parameters, etc..

Parameter	Value	Unit
Chemical compositionof Portland cement		
w_{C_3S}	0.52	–
w_{C_2S}	0.2	–
w_{C_3A}	0.075	–
w_{C_4AF}	0.115	–
w_{SO_3}	0.033	–
w_{CaO}	0.015	–
w_{MgO}	0.031	–
Blaine Fineness	460	kg/m^2
Volume fraction		
$\phi_{PortlandCement}$	0.596821	–
$\phi_{SilicaFlour}$	0.274763	–
$\phi_{Perlite}$	0.104017	–
$\phi_{Bentonite}$	0.015297	–
$\phi_{Retarder}$	0.009102	–
Density		
$\rho_{PortlandCement}$	3050	kg/m^3
$\rho_{Silicaflour}$	2650	kg/m^3
$\rho_{Perlite}$	350	kg/m^3
$\rho_{Bentonite}$	2380	kg/m^3
$\rho_{Retarder}$	1000	kg/m^3
ρ_{Water}	1000	kg/m^3
Thermal properties		
$c_{p,PortlandCement}$	750	J/(kg K)
$c_{p,SilicaFlour}$	773	J/(kg K)
$c_{p,Perlite}$	387	J/(kg K)
$c_{p,Bentonite}$	1120	J/(kg K)
$c_{p,Retarder}$	4180	J/(kg K)
$c_{p,Water}$	4180	J/(kg K)
$\lambda_{PortlandCement}$	1.55	W/(m K)
$\lambda_{SilicaFlour}$	7.69	W/(m K)
$\lambda_{Perlite}$	0.38	W/(m K)
$\lambda_{Bentonite}$	0.7267	W/(m K)
$\lambda_{Retarder}$	0.604	W/(m K)
λ_{Water}	0.604	W/(m K)
Slurry properties		
ρ_{Slurry}	1700	kg/m^3
w/c	0	–
$\alpha_{DOH,ini}$	0.000001	–

G. Moody Diagram

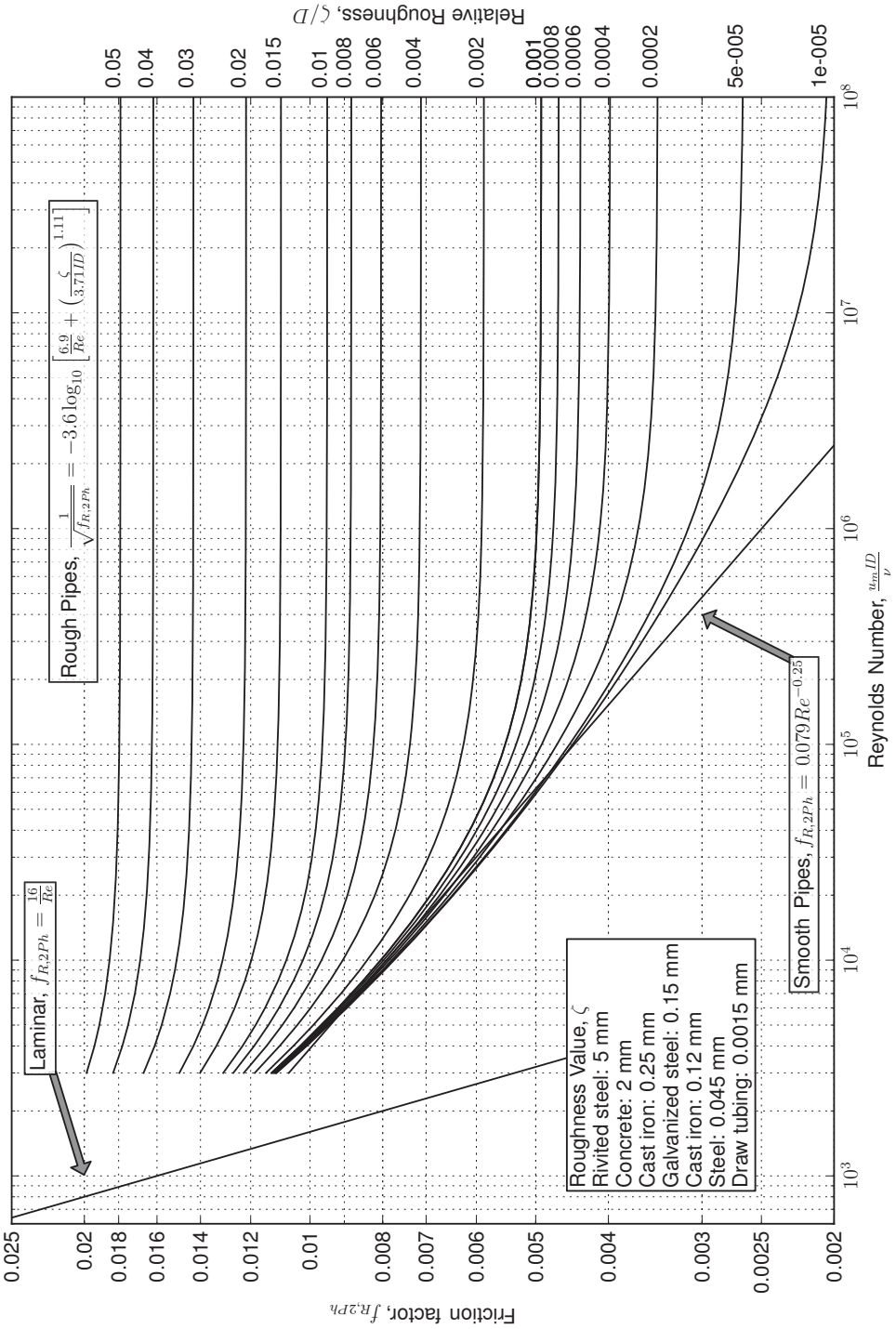

Figure G.1.: Moody diagram (Moody, 1944); displayed for the $f_{R,2Ph} = 16/Re$ convention. The $f_{R,2Ph} = 64/Re$ convention has been used for the calculations. A Python script to generate this plot has been provided by Grant Ingram (modified after Ingram, 2011).

H. Flow Charts

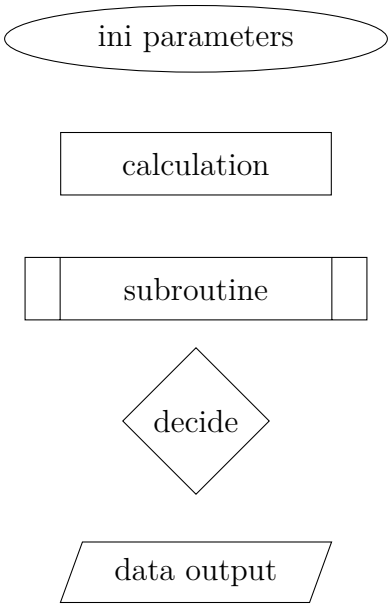

Figure H.1.: Flowchart symbols modified from ECMA (1966)

H.1. Wellbore Simulator

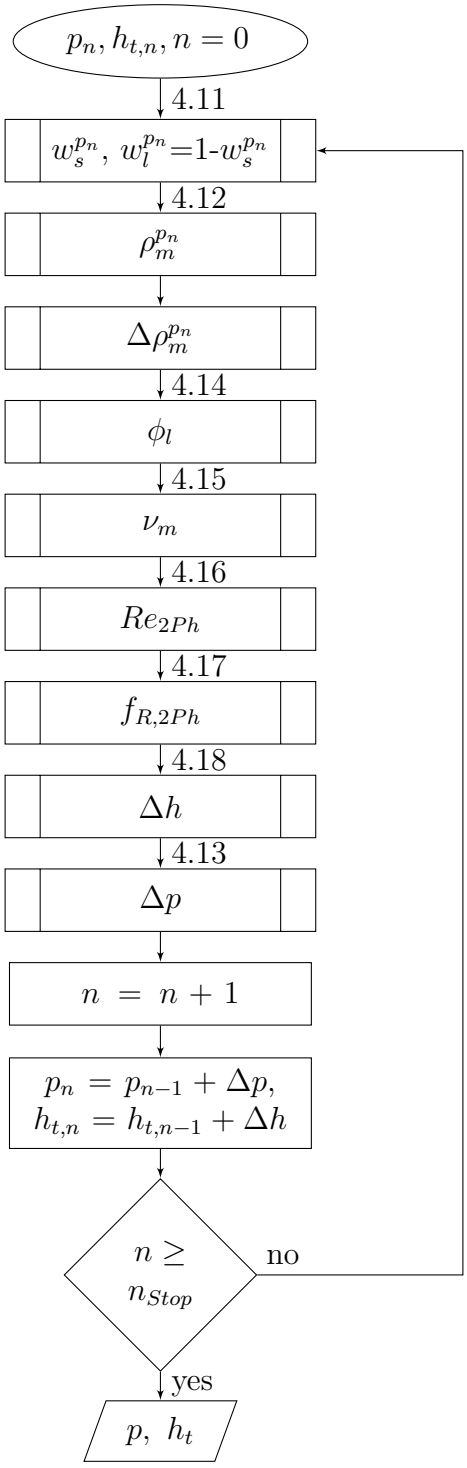

Figure H.2.: Simplified flowchart of the wellbore simulator. The equations used to calculate individual quantities are indicated. The maximum depth to calculate is $n_{Stop}z_h$.

H.2. Cement Hydration

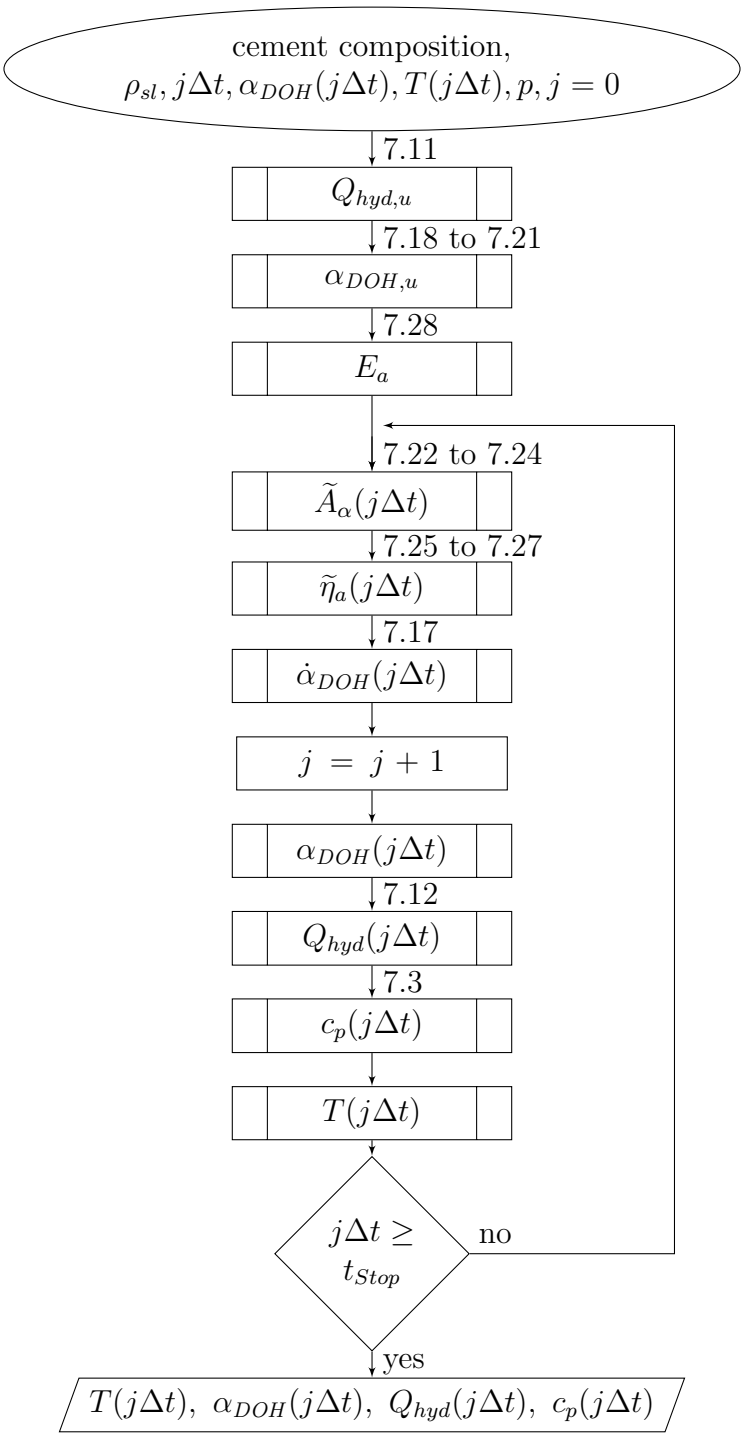

Figure H.3.: Simplified flowchart for cement hydration model. The equations used to calculate individual quantities are indicated. t_{Stop} is the maximum time to simulate.

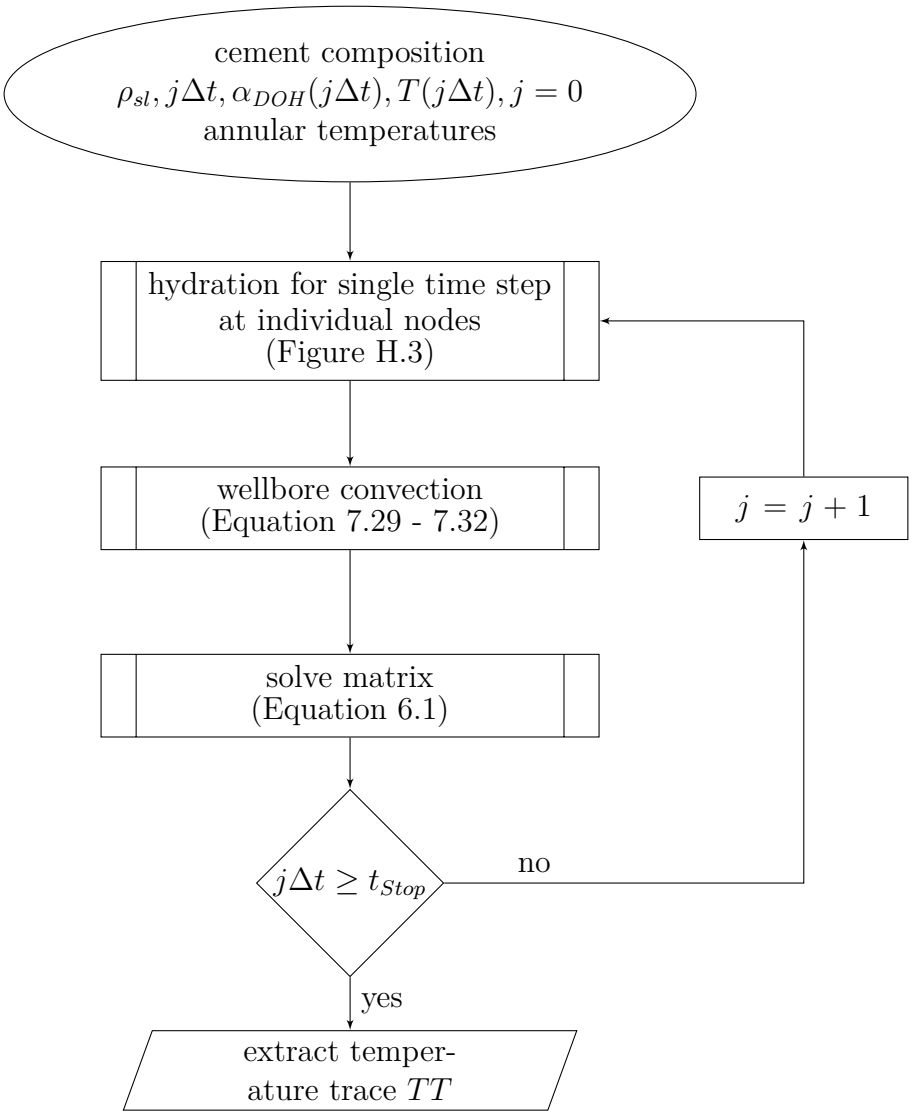

Figure H.4.: Simplified flowchart for the annular temperature increase during cement hydration. The equations used to calculate individual quantities are indicated. Flow chart is displayed for constant time-steps Δt. t_{Stop} is the maximum time to be modelled.

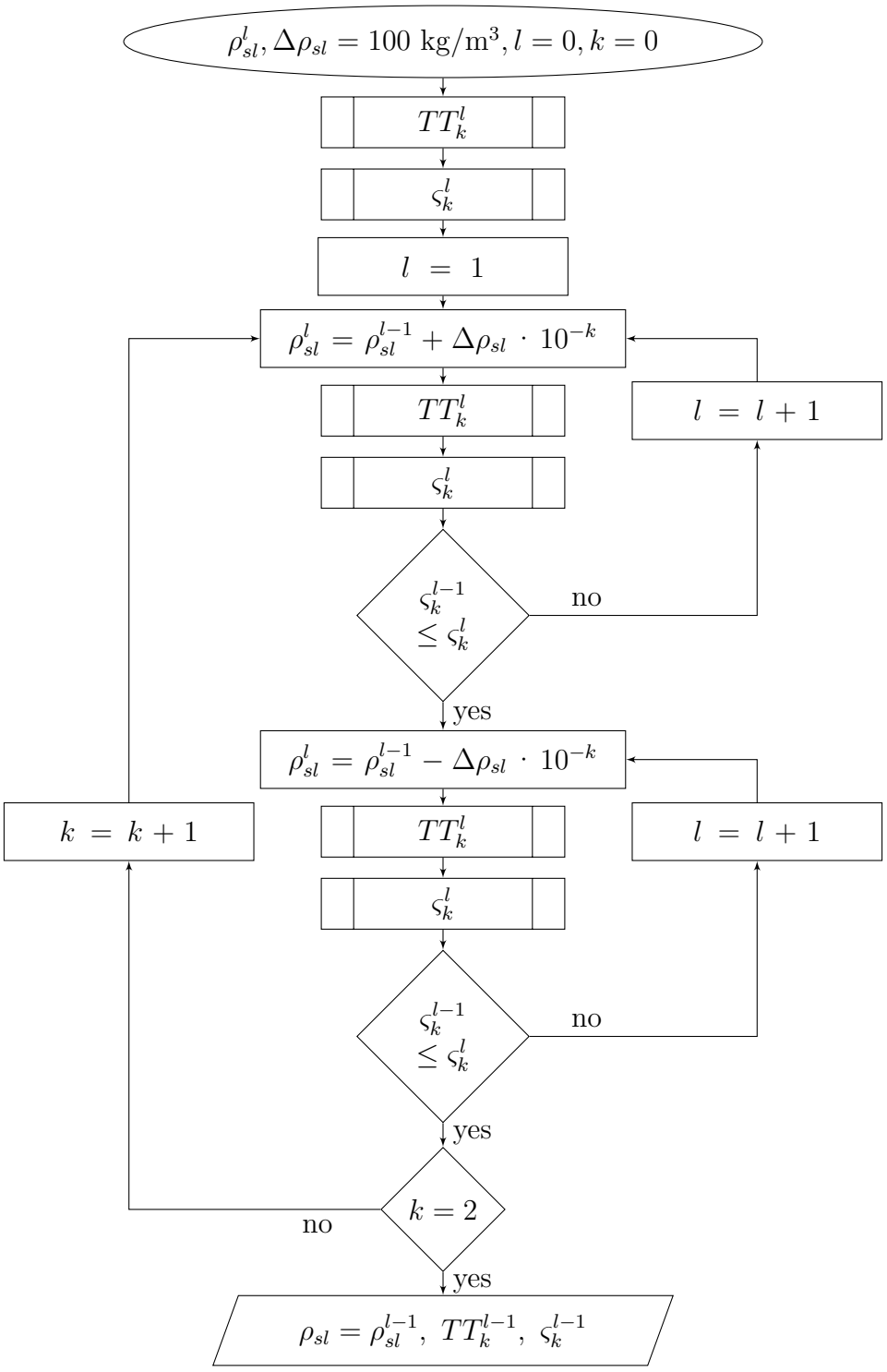

Figure H.5.: Simplified flowchart to iterate best fit for slurry density with an accuracy of 1 kg/m^3. ς is the variance between measured and simulated temperature traces (TT) (Equation 7.33). l and k are control variables.

I. DTS Calibration

I.1. Theory

Every fibre has to be calibrated to the DTS system. The manual provided by Sensa (Sensa, 2004) suggests an iterative heating and cooling process to calibrate fibres. As an iterative heating and cooling procedure over a large temperature range, as desired within this study, is very time consuming, a simple linear regression over multiple temperature points has been applied.

The DTS temperature is calculated using ratio of the backscattered photons at the Stokes and Anti-Stokes wavelength. Actual temperatures can be determined by the linear relation (Al-Asimi et al., 2002):

$$\frac{1}{T_{DTS}(z)} = \frac{1}{T_{rc}} - \frac{1}{S_{DTS}} \left(\ln \left(\frac{I_{ast}(z)}{I_{st}(z)} \right) - \ln \left(\frac{I_{ast}(rc)}{I_{st}(rc)} \right) \right) \tag{I.1}$$

where T_{DTS} is the measured DTS temperature (K) at distance z along the fibre. T_{RC} and S_{DTS} are the reference coil temperature (K) and the slope value (K) for the DTS temperature calculation. $I_{ast}(z)$ and $I_{st}(z)$ are the intensities of the Anti-Stokes and the Stokes signal at point z, respectively, and rc refers to the reference coil.

I.2. Calibration Procedure

During the calibration procedure, T_{rc} and S_{DTS} have to be determined. For an initial guess of $T_{rc,ini}$ and $S_{DTS,ini}$, initial DTS temperatures $T_{DTS,ini}$ can be monitored at different temperature conditions. Using Equation I.1, the following *ln*-relation can be deduced:

$$\ln \left(\frac{I_{ast}(z)}{I_{st}(z)} \right) - \ln \left(\frac{I_{ast}(rc)}{I_{st}(rc)} \right) = - \left(\frac{1}{T_{DTS,ini}(z)} - \frac{1}{T_{rc,ini}} \right) S_{DTS,ini} \tag{I.2}$$

Comparing DTS temperature readings T_{DTS} to a reference temperature measurement T_{ref}, a simple linear regression can be applied to calculate a new T_{rc} and S_{DTS}

Table I.1.: Calibration temperatures.

$T_{DTS,ini}$ °C	T_{ref} °C	$T_{rc,ini}$ °C	$S_{DTS,ini}$ °C
56.60	49.66	40.00	500.00
118.19	99.48	40.00	500.00
182.43	149.26	40.00	500.00
248.87	198.98	40.00	500.00
317.93	248.94	40.00	500.00
360.33	279.15	40.00	500.00

value.

$$
\begin{aligned}
y &= ax + b \qquad \text{(I.3)}\\
\text{with } y &= \frac{1}{T_{DTS}(z)}\\
a &= -\frac{1}{S_{DTS}}\\
b &= \frac{1}{T_{rc}}\\
x &= \ln\left(\frac{I_{ast}(z)}{I_{st}(z)}\right) - \ln\left(\frac{I_{ast}(rc)}{I_{st}(rc)}\right)
\end{aligned}
$$

I.3. Calibration of Wellbore Cable for HE-53

The calibration of the DTS sensor cable up to 280 °C has been performed in an oven with forced air circulation (UFE 600, Memmert). As reference temperature sensor, a thermometry bridge (ASL-F300 with a PT-25) has been used. The inner stainless steel loose tube containing the optical fibre has been placed between two aluminium plates to increase the temperature stability. Three successive heating tests have been performed and the resulting DTS temperatures have been compared to the reference temperatures.

Table I.1 lists the measured DTS temperatures together with the reference temperature. From the linear regression, T_{rc} and S_{DTS} values have been determined to be 34.99 °C and 565.03 °C.

During temperature calibration in the lab, a non-linear relation between actual and measured DTS temperatures was observed when measured over a wide temperature range of more than 150 °C. In order to account for this non-linear response of the DTS unit, a fourth order polynomial function $f(T_{DTS})$ (Equation I.4) has been fitted to the calibration data and used to correct measured temperature data

(a) (b)

Figure I.1.: Experimental Set-up for the calibration of the fibre optic cable. The inner stainless steel loose tube, containing the optical fibre, has been placed in the centre of an oven. For temperature stabilization, it has been placed between two aluminium plates. The coil with the larger diameter contains the calibration fibre. At the tip of the orange cables, PT-100 sensors have been placed to ensure the temperature stability between the plates. As reference, a PT-25 has been used (placed in the centre of the coil).

Table I.2.: Parameters for polynomial fitting of DTS temperature data.

Parameter	Value	R^2
a_0	$1.21 * 10^{0}$	0.00
a_1	$-1.62 * 10^{-2}$	0.05
a_2	$2.43 * 10^{-5}$	0.84
a_3	$-2.84 * 10^{-7}$	0.92
a_4	$1.59 * 10^{-9}$	0.92

(Figure I.3).

$$f(T_{DTS}) = \sum_{k=0}^{4} a_k T_{DTS}^k \tag{I.4}$$

The fitted parameters are listed in Table I.2. In order to correct for the non-linear response of the system, the following equation has been applied to calculate corrected DTS temperature data:

$$T_{DTS}^{corr} = T_{DTS} + f(T_{DTS}) \tag{I.5}$$

From Figure I.3 it can be seen that a residual error of less than ΔT_{DTS}^{corr} =0.5 °C was observed below 240 °C, which is the temperature range measured during the flow test.

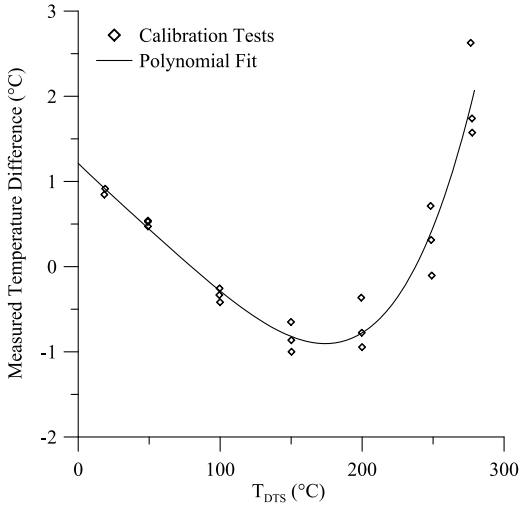

Figure I.2.: Polynomial correction for the measures DTS data. The difference $T_{ref} - T_{DTS}$ is displayed. Correction based on three heating cycles measured in the lab prior to the installation.

J. Publication in Measurement Science and Technology

Temperature dependent characterization of optical fibres for distributed temperature sensing in hot geothermal wells

Thomas Reinsch and Jan Henninges

Helmholtz Centre Potsdam, GFZ - German Research Centre for Geosciences, Telegrafenberg, 14473 Potsdam, Germany

E-mail: Thomas.Reinsch@gfz-potsdam.de

Abstract. This study was performed in order to select a proper fibre for the application of a distributed temperature sensing system within a hot geothermal well in Iceland. Commercially available high temperature graded index fibres have been tested under in-situ temperature conditions. Experiments have been performed with four different polyimide coated fibres, a fibre with an aluminum coating and a fibre with a gold coating. To select a fibre, the relationship between attenuation, temperature, and time has been analyzed together with SEM micrographs. On the basis of these experiments, polyimide fibres have been chosen for utilisation. Further tests in ambient and inert atmosphere have been conducted with two polyimide coated fibres to set an operating temperature limit for these fibres. SEM micrographs, together with coating colour changes have been used to characterize the high temperature performance of the fibres.
A novel cable design has been developed, a deployment strategy has been worked out and a suitable well for deployment has been selected.

PACS numbers: 42.81.Cn, 93.85.Fg

In press: *Meas. Sci. Technol.*

Keywords: distributed temperature sensing (DTS), optical time domain reflectometry (OTDR), geothermal well, optical fibre, coating material, attenuation, degradation

1. Introduction

Temperature is a key parameter to understanding fundamental processes within a wellbore. Transient temperatures help characterize geothermal reservoirs and design a strategy for the use of a geothermal field and a sustainable production of energy.
In the past two decades, distributed temperature sensing (DTS) based on Raman Scattering has increasingly been used for wellbore applications [1, 2, 3]. Quasi-continuous temperature profiles can be measured in boreholes by using an optical fibre as sensing element. Since no electronics have to be lowered downhole, DTS is especially suited for high temperature applications.
Measuring at high temperatures becomes increasingly important with accessing unconventional oil and gas resources or geothermal reservoirs. For the oil and gas industry, maximum well temperatures can be as high as 340°C [4]. In conventional hot geothermal wells, e.g. in high-enthalpy areas in Iceland, temperatures up to 350-380°C can be reached [5]. In order to increase the energy output from a single geothermal well by an order of magnitude, current research activities aim at producing geothermal fluids with temperatures up to 550-600°C from depths of about 4-5 km [6, 7].
In hydrogen rich environments, optical properties of fibres degrade rapidly due to hydrogen ingression and hydroxyl formation [4, 8, 9]. Hydrogen ingression and subsequent hydroxyl formation causes strong absorption peaks at relevant wavelengths [10, 11, 4]. Increasing differential attenuation between the Stokes and Anti-Stokes band skews temperature measurements over time [9]. Furthermore, the ingression of hydrogen can lead to a total transmission loss for the optical fibre. To reduce the ingression of hydrogen and the subsequent formation of hydroxyl within the interstices of the silica, hermetic carbon coatings have been used as a hydrogen diffusion barrier. Hydrogen diffusion through carbon coatings, however, can be detected at temperatures above 100°C [12]. Recently, pure silica core fibres have been shown to be well suited for application in hydrogen rich environments [13].
Using conventional DTS units, the influence of hydrogen on the measured temperatures can be reduced using an experimental set-up where both ends of the fibre can be accessed. Averaging measurements from both ends alleviates the problem of skewed temperature measurements. Another means to mitigate the effect of hydrogen onto measured temperatures is the dual laser principle where measurements from two different incident wavelengths are used [14, 15]. If only one end of the fibre can be accessed, the dual laser principle can be used to account for wavelength dependent changes along the attenuation profile.
For high temperature applications (< 300°C), polyimide coated fibres are widely used in wellbore applications. Higher temperatures can be measured with metal coated fibres, but it is well known that these fibres have high attenuation values at low temperatures [16]. A further drawback of aluminum coated fibres is additional hydroxyl absorption that can be observed at temperatures of 400°C [17].
This work has been performed within the framework of the HiTI Project (**Hi**gh

Temperature **I**nstruments for geophysical reservoir characterization and exploitation) in order to test the applicability of fibre optic temperature measurements at temperatures above 300°C within a hot geothermal well. HiTI aims to provide geophysical and geochemical sensors and methods for the evaluation of deep geothermal wells up to supercritical conditions of water. Up to now, DTS measurements in geothermal wells are documented up to temperatures of 275°C for a duration of a few hours [18].
In order to select a proper fibre for deployment, different commercially available graded index fibres have been tested at temperatures up to 400°C within a three zone tube furnace under laboratory conditions.
Optical attenuation levels have to remain sufficiently low to allow for fibre optic measurements in wellbore applications. Most available DTS systems have an optical budget of ≈ 20 dB. Different fibre optic measurement techniques, however, have an even smaller budget. With wells being several kilometers deep, attenuation characteristics have to be rather favorable. Four polyimide coated fibres as well as two metal coated fibres have been tested with focus on additional loss levels of the Stokes signal of a 1064 nm laser. Among the polyimide fibres, a fibre with an additional hermetic carbon coating has been tested. Although the ingression of hydrogen, is likely to occur, as the coating material and the ambient atmosphere might act as sources of hydrogen, this study is focused on microbending losses during temperature cycling experiments. The contribution of hydrogen and hydroxyl to the additional loss level, is assumed to be negligible compared to microbending losses due to thermal stress applied to the fibres.
After selecting a fibre, further experiments have been conducted to set an operating limit, an important parameter for the selection of a proper well for deployment.

2. Experiments

Two different sets of experiments have been conducted. First, temperature cycling experiments have been used to select a fibre for deployment. Second, the selected fibres have been heated in ambient air and inert atmosphere at temperatures of 250°C, 300°C and 350°C for a period of approximately 200 h. SEM micrographs have been used to characterize the performance of the fibres at high temperatures. An attempt was made to use colour changes to estimate the state of degradation and therewith additional loss characteristics of the optical fibre.
All tests have been performed with 50/125 μm graded index multimode fibres.

2.1. Attenuation changes during temperature cycling

In order to characterize the different fibres, samples of the fibres have been heated in ambient air within a Carbolite® three zone tube furnace (TZF) (Figure 1(a)). The samples were rolled and fitted into the tube with a minimum bending diameter of 4.5 cm. A thin sheet of rock wool has been used to separate the fibres from the ceramic

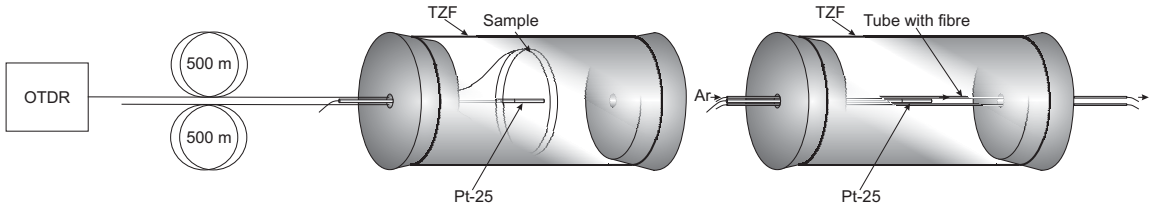

(a) Attenuation measurements.

(b) Heating the fibres in ambient air and inert atmosphere.

Figure 1. (a) Experimental set up for the attenuation measurements. Fibres were spliced to a 500 m launch cable (Section 2.1). (b) Experimental set up for heating the fibres in ambient air and inert atmosphere. Small tubes were heated within the TZF and argon was flushed continuously through one of the tubes during heating (Section 2.2). A Pt-25 was used as reference temperature sensor.

Table 1. List of tested fibres with respective coating diameters. The maximum operating temperature range (manufacturer specification), the maximum temperature during heating and cooling periods as well as the number of heating and cooling cycles and the total testing time is listed for each fibre. Sample 4 has an additional carbon layer to reduce hydrogen ingression.

Sample	Coating (Diameter (μm))	T.-Range (°C)	Max.-T. (°C)	Cycles	Time (h)
1	Polyimide (145)	-90 - 385	385	3	190
2	Polyimide (145)	-90 - 385	385	3	190
3	Polyimide (155)	-65 - 300	300	1	130
4	Polyimide/Carbon (155)	-65 - 300	300	1	130
5	Aluminum (155)	-269 - 400	400	4	180
6	Gold (155)	-269 - 700	400	4	180

wall of the TZF. All samples were spliced to a 500 m launch cable. Attenuation data was calculated from the backscattered Stokes signal of a 1064 nm laser. Data has been acquired using a DTS-800 system from Sensa.

Table 1 lists test conditions for different fibres that have been tested within the first set of experiments. Sample lengths have been 20 m for all fibres except the gold fibre (10 m). Temperature cycling has been used to simulate conditions for a wellbore cable that will be subjected to repeated temperature changes, e.g. during logging or well testing operations. To simulate downhole temperature conditions, temperatures were increased for samples 1 to 6 until the maximum testing temperature was reached. Afterwards, the fibres were cooled down to temperatures below 100°C. Subsequently, fibres 1, 2, 5 and 6 were heated and cooled, again, with a very brief high temperature period for the last cycle.

2.2. Heating in inert atmosphere and air

Polyimide fibres were selected for deployment, on the basis of these experiments. To test the performance of a fibre with an additional carbon layer beneath the coating, and to compare it to a fibre with an ordinary polyimide coating, samples 1 and 4 have been selected for further testing. Samples of 1 m length were heated at constant temperatures of 250°C for 190 h, 300°C for 269 h and 350°C for 216 h, to set an operating limit for these fibres. A sample of each fibre was heated in ambient air and a second one was heated in an argon atmosphere (Figure 1(b)). Each sample was placed in a stainless steel loose tube with an outer diameter of 2 mm and a wall thickness of 0.2 mm. The tubes were placed in the centre of the TZF and one of the tubes was continuously flushed with Argon 5.0.

The effect of argon flow on temperature readings along the fibre is negligible. In order to test this, a 20 m section of a several hundred meter long fibre optic cable was placed in an oven. The temperature difference between inside and outside the oven was 100°C. Flushing the cable with argon did not change measured DTS temperatures along the fibre.

SEM micrographs and coating colour changes have been analysed to estimate the state of degradation. In order to quantify colour changes, high resolution digital photographs have been taken using a Nikon D3 camera. The samples have been illuminated using an Osram Dulux L 18W/12 Lumilux Deluxe Daylight lamp (5400K).

3. Results

3.1. Attenuation changes during temperature cycling

In Figure 2, additional loss versus temperature is shown for the polyimide fibres (samples 1-4). For sample 2, three complete cycles could be measured, whereas only one could be measured for sample 1 due to an early fibre break (Figure 2(a)). During the first heating period, attenuation levels stayed rather constant, except for a greater variation around 275°C. Here, temperature was held constant for a period of 60 h. During the period of constant temperature at 375°C, attenuation increased irreversibly. During cooling attenuation levels increased reversibly, as attenuation values decreased during subsequent heating. This behavior was observed for all of the three heating and cooling cycles. Reversible attenuation changes occur during heating and cooling; irreversible attenuation changes occur during the 375°C periods. The slope of the reversible attenuation changes increased in subsequent temperature cycles.

Samples 3 and 4 were tested up to 300°C (Figure 2(b)). Only one temperature cycle was performed. The fibre samples were held at elevated temperature for more than 120 h. Attenuation values remained constant for sample 3 and decreased at this temperature for sample 4 (Figure 3(a)). During cooling, attenuation values rose for both fibres (Figure 2(b)). The slope of this increase was ten times lower than the slope observed for fibres 1 and 2. Taking the fibres out of the TZF, the fibre rolls remained in an oval shape and

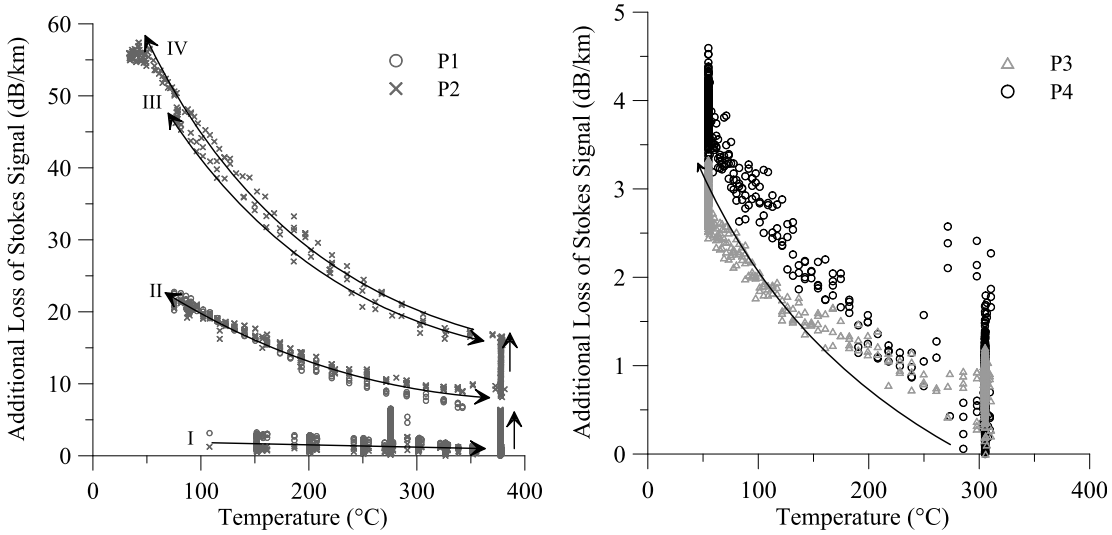

(a) Samples 1 and 2.

(b) Samples 3 and 4.

Figure 2. Additional loss vs. temperature for fibre samples 1 - 4. Arrows indicate the evolution in time. Individual heating and cooling cycles are labeled with Roman numbers. Fibre sample 1 broke at the beginning of the second cycle (a). For samples 3 and 4, a single temperatur cycle is displayed (b). Data acquisition started at the end of the heating phase. Note the different scales on the abscissa.

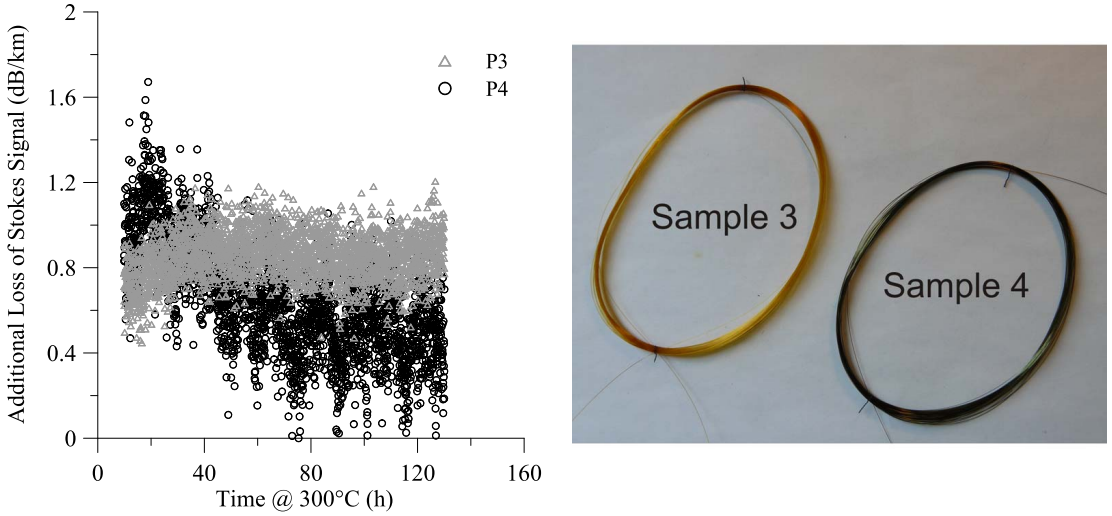

(a) Loss at 300°C.

(b) Samples 3 and 4 after heating.

Figure 3. (a) Additional loss vs. time at 300°C for fibre samples 3 and 4. Attenuation values slowly decrease for sample 4. (b) Picture of fibres after heating.

got stuck to each other (Figure 3(b)).

As examples for metal coatings, results for samples 5 and 6 are shown in Figure 4. The plots show basically two regions. Low temperature region 2 has high attenuation values, high temperature region 1 has low attenuation values. During temperature cycling, elevated attenuation values decreased at approximately 300°C during the

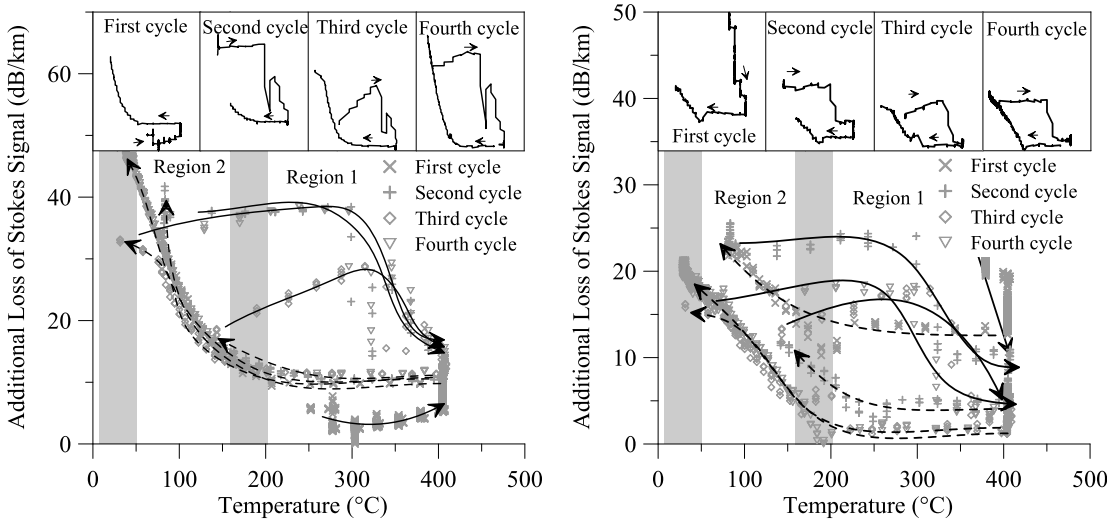

(a) Aluminum. (b) Gold.

Figure 4. Additional loss vs. temperature for fibre sample 5 (a) and 6 (b). Arrows indicate the evolution in time. Individual heating and cooling cycles are displayed separately on top.

heating periods. During cooling, attenuation stayed constant until a temperature of approximately 200°C (Transition Region 1 - Region 2) was reached. Further cooling led to an increase in attenuation values (Region 2). This increase was reversible, and attenuation values decreased during the next heating period, again. Generally, a decrease in attenuation was observed for every heating period. Nevertheless, this decrease was observed at a higher temperature compared to the increase during cooling periods.

The overall temperature-attenuation behavior is similar for both fibres. Initial attenuation was low for the aluminum fibre, however, whereas it was high for the gold fibre. Lowest attenuation levels for the gold fibre were measured after the third heating period. Absolute additional loss values are approximately doubled for the aluminum in comparison to the gold coated fibre.

3.2. Heating in inert atmosphere and air

Figure 5 shows SEM micrographs of fibre samples 1 and 4 heated at different temperatures in ambient air and argon atmosphere. SEM micrographs of the fibres clearly show an increase in size and frequency of surface depressions with temperature. Furthermore, depressions increase both in size and frequency in ambient air, compared to fibres heated in argon atmosphere. The depressions were not evenly distributed along the fibre. Sample 4 developed fewer and smaller depressions compared to sample 1.

3.2.1. Colour Changes Due to degradation, the cladding was partly exposed for samples heated at 350°C. For each fibre, three representative areas where the coating

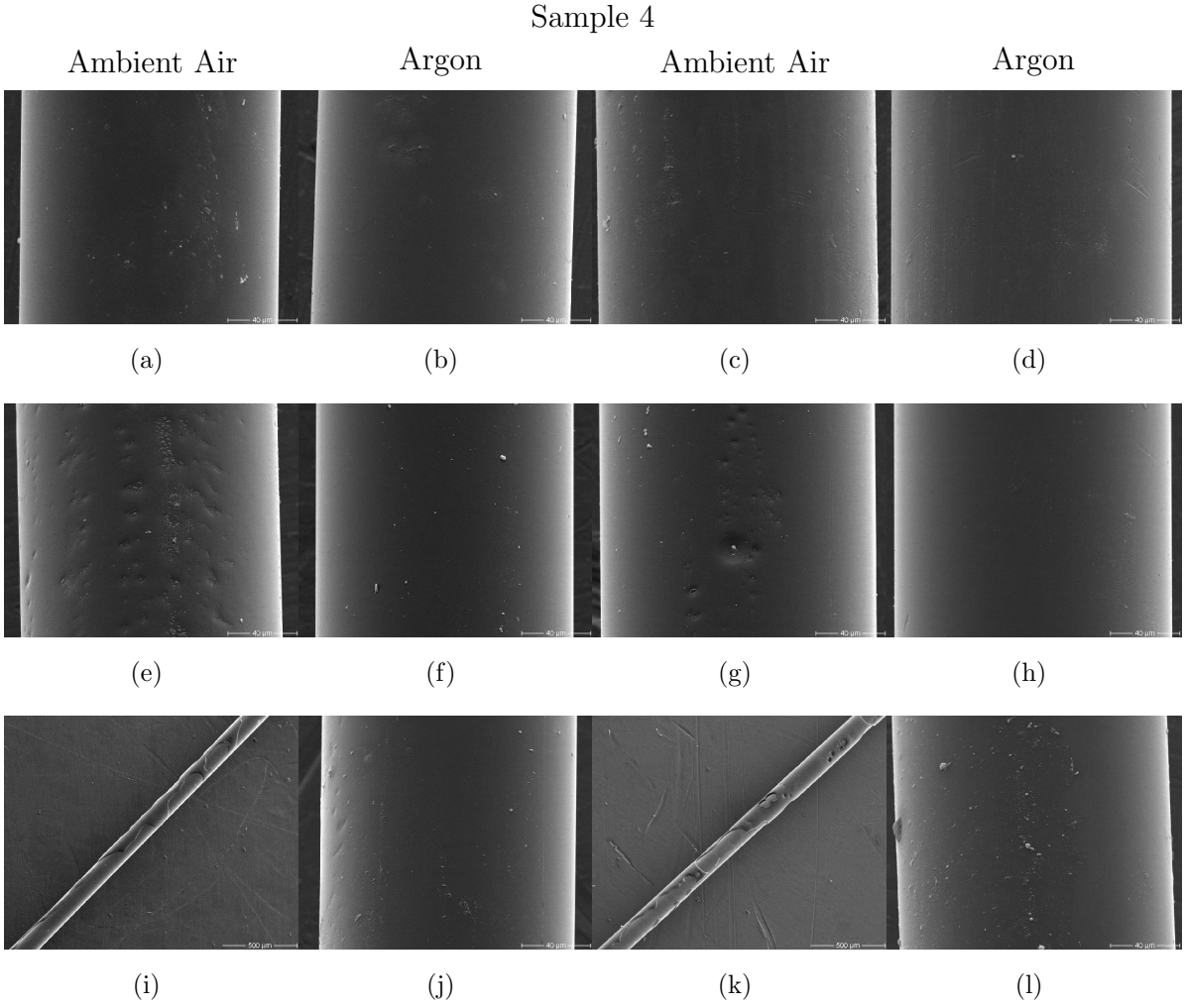

Figure 5. SEM micrographs from fibres 1 and 4. Samples were heated at constant temperature. The scale bar in the lower right corner indicates 40 μm for all pictures except (i) and (k) where it is 500 μm. (a)-(d): 250°C, 190 h; (e)-(h): 300°C, 269 h; (i)-(l): 350°C, 216 h.

was still covering the cladding have been used to determine a sRGB value for the coating colour. These values have been converted to the CIE 1976 L*a*b* colour space [19] using a CIE 1931 - 2° standard colorimetric observer. The L* axis represents colours from black to white, a* represents green to red and b* blue to yellow. Averages and standard deviations of the colours has been calculated for each fibre from the recorded digital photographs. The colour difference along a single axis has been calculated as the norm $\Delta L^* = |L^* - L^*_R|$, $\Delta a^* = |a^* - a^*_R|$ and $\Delta b^* = |b^* - b^*_R|$, respectively. The subscript R denotes the reference sample. Total colour differences ΔE^*_{ab} have been calculated as the Euclidean distance within the L*a*b* space according to equation 1.

$$\Delta E^*_{ab} = \sqrt{(\Delta L^*)^2 + (\Delta a^*)^2 + (\Delta b^*)^2} \quad (1)$$

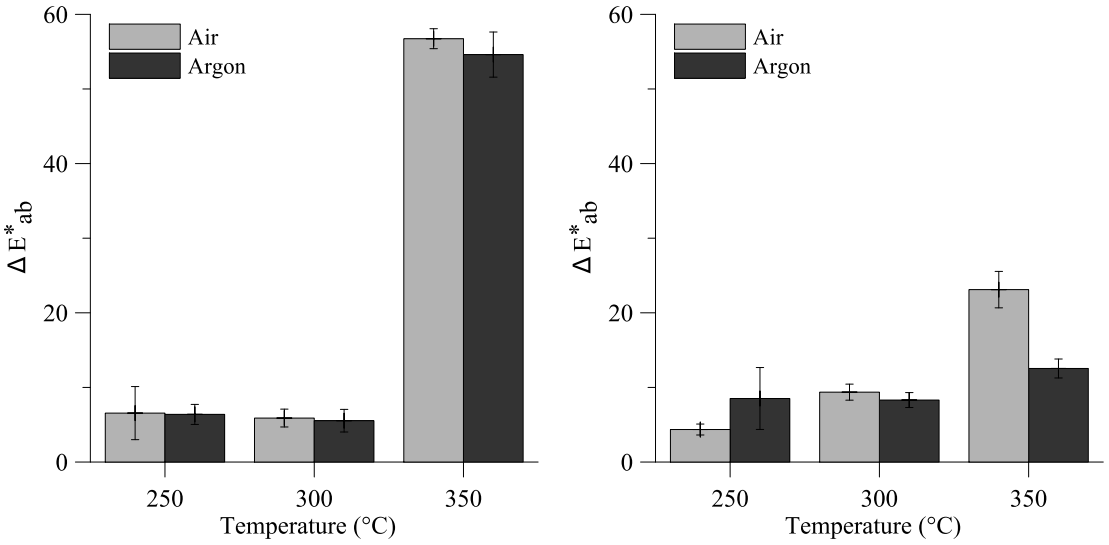

(a) P1. (b) P4.

Figure 6. Colour change ΔE^*_{ab} for sample 1 and 4. Non heated fibre samples have been used as reference.

The calculations are based on colorimetry and the results are therefore illuminant-dependent. In order to compare absolute values of colour differences, measurement conditions have to be identical.

Colour changes were observed for all fibres that have been heated (Figure 6). Different fibres show different colour changes with temperature and atmosphere. The colour remains similar, however, for the samples heated at 250°C and 300°C. ΔE^*_{ab} values stay below 10 compared to the reference fibre. At 350°C colour changes considerably for all fibres and ΔE^*_{ab} increases to more than 10.

Initially, polyimide fibres have a light yellow colour. The additional carbon layer beneath the polyimide coating of sample 4 causes a dark, greenish appearance of this fibre. After heating, the colour appearance did not change for sample 4 as much as for the light yellow sample 1 without the carbon layer. The difference at 350°C in comparison to the colour changes at 300°C is large for fibre sample 1, whereas it appears to be small for sample 4.

4. Discussion

4.1. Attenuation changes during temperature cycling

Polyimide coated fibres At elevated temperatures, additional loss for samples 1 and 2 shows an irreversible increase in attenuation levels (Figure 2(a)). This is in good agreement with the fact that polyimide coatings suffer from curing, thermal, thermoxidative and moisture induced degradation at elevated temperatures [20, 21]. Degradation rates increase with increasing temperature. The material looses plasticity and stress onto the silica structure of core and cladding increase irreversibly. Hence, microbending loss

increases attenuation levels [4].
During cooling periods, attenuation changes reversibly. After initial heating at elevated temperatures, a more rigid coating and different coefficients of thermal expansion (CTE) cause an increase of stress onto the silica during cooling. Depending on the chemical composition, the CTE for polyimide (e.g. $34 * 10^{-6}/K$ (30-400°C) [22]) is roughly one to two orders of magnitude larger than the CTE of silica ($0.5 * 10^{-6}/K$ [23]). This effect is reversible, and stress is released during subsequent heating cycles. The slope of the reversible attenuation changes during subsequent temperature cycles increases with reduced elasticity of the coating material.
Due to considerably increased degradation rates at temperatures above 300°C, attenuation values increase irreversibly for samples 1 and 2. At constant temperatures around 300°C, attenuation stays constant for sample 3, and decreases for sample 4 (Figure 3(a)). Although the oval shape of the fibre roll and the adherence indicate a degradation of the coating material (Figure 3(b)), irreversible attenuation changes have not been observed at this temperature. Attenuation changes during cooling indicate a rigidification of the polyimide coating at 300°C.

Metal-coated fibres Metal-coated fibres show high loss values at temperatures below 200°C (Region 2, Figure 4) and low attenuation at temperatures above 200°C (Region 1). Accelerated plastic deformation of the metal at temperatures above 200°C and annealing of microbends reduce the attenuation levels in region 1. Plastic deformation is caused by recrystallization processes within the metal and leads to a reduction of residual stresses within the coating. In region 2, slow plastic deformation processes and different coefficients of thermal expansion between silica and metal cause a significant increase in attenuation [16]. The transition between Region 1 and 2 was determined to start below 200°C during cooling. This is in good agreement with results shown in [16] for the aluminum coating, whereas it is about 50°C higher for the gold coating.
The reduction of additional loss during heating was observed to be at a higher temperature as the loss increase during cooling. Since it was not possible to actively cool down the TZF, temperature decrease during cooling took much longer than temperature increase during heating. Thus, the decrease in attenuation during heating was delayed and the transition would have most probably occurred at similar temperatures compared to the cooling phase.
An increase of more than 20 dB/km was observed for the tested wavelength in region 1. Absolute additional loss values are almost doubled for aluminum in comparison to gold coated fibres. This is in good agreement with the CTE difference of the materials (Gold: $14.9 * 10^{-6}/K$, Aluminum: $26.4 * 10^{-6}/K$ (0-400°C) [24]). As the coating diameter is similar for both fibres, absolute additional loss values are mainly influenced by the CTE. The higher the CTE, the more microbending occurs and attenuation increases. Different initial attenuation values might be explained by a different mechanical and thermal stress history, different drawing techniques and different elastic properties of gold in

comparison to aluminum.
The small bending diameter of 4.5 cm increased microbending effects and absolute loss values are certainly larger than values acquired for fibres heated with a larger bending diameter. Furthermore, the small length of the samples adds an error to the absolute loss values. The general tendency, however, should be similar.

4.2. Heating in inert atmosphere and air

The SEM micrographs show large differences for fibres heated in ambient air and argon atmosphere (Figure 5). Fibres heated in argon atmosphere show less signs of degradation as the fibre samples heated in ambient air. Thermooxidative and moisture induced degradation are unlikely to occur due to the low oxygen and moisture content within the flushed tubes. Thermal degradation and curing reactions remain as the most relevant degradation mechanisms (see Section 4.1).
Morphological and colour changes were observed to increase with temperature for all samples. This is in good agreement with increasing degradation rates at elevated temperatures [20, 21].
Heated in argon atmosphere, sample 4 shows fewer and smaller depressions on the surface after the 350°C period. Differences in the chemical composition and thickness of the polyimide material might cause this phenomenon. Depressions, however, were not evenly distributed. Either a larger volume would need to be analyzed or themogravimetric measurements would need to be done in order to quantify differences in the volume change and differences in weight due to heating.

4.2.1. Colour Changes Observing colour changes is a quick and inexpensive means to approximate the state of degradation of the polyimide coating material. For fibres heated at temperatures up to 300°C, an irreversible increase in attenuation levels has not been observed (Section 3.1) and colour changes remain below $\Delta E^*_{ab} \approx 10$ (Figure 6). For fibre samples heated at temperatures up to 350°C, colour changes of $\Delta E^*_{ab} > 10$ have been observed. Attenuation measurements for samples 1 and 2 heated up to 375°C for a much shorter period of time, show an irreversible increase in loss characteristics. The increase of ΔE^*_{ab} seems to correlate with the transition of reversible to irreversible attenuation changes. A more detailed analysis including simultaneous measurements of additional loss and colour changes would need to be done to define appropriate threshold values for every fibre.
The additional carbon layer of sample 4 adds difficulty to this simple approach. For sample 1, the colour of the fibre is only determined by the colour of the polyimide material. For sample 4, the colour appears darker due to the underlying black carbon layer. As stated earlier, the polyimide layer degrades at elevated temperature. Eventually, it exposes the underlying cladding in the case of sample 1 or the underlying carbon coating for sample 4. If it comes into contact with air at elevated temperatures,

the carbon coating degrades as well. Loss of the black carbon coating significantly increases calculated colour changes for sample 4. Since only areas of the samples, where the polyimide coating covers the fibre, have been considered, this effect should be negligible.

5. Conclusion and Outlook

For high temperature applications, the selection of a proper fibre is essential for a successful and long-lasting installation of the sensing cable. Therefore, different fibres have been tested in order to select a suitable fibre for the deployment in the harsh environment of a geothermal well.

One of the limitations for measuring temperatures over distances of several kilometers is the optical budget of the surface readout unit. For most units available today, this budget is about 20-25 dB. For fibres having high attenuation values, the optical budget limits the deployable length. Attenuation values higher than a few dB/km are not tolerated for wellbore applications with sensor lengths of several kilometers. Due to the high attenuation values at low temperatures, the tested metal coated fibres cannot be used for DTS in wellbore applications. Thus, polyimide fibres have been chosen despite their limited operating temperature range in comparison with metal coated fibres. To test the performance of a carbon coated fibre that reduces the hydrogen ingression within the hostile environment of a geothermal well, tests with sample 4 and reference sample 1 have been conducted. To keep attenuation at moderate levels, degradation of the coating material has to be minimized.

Further testing has been done in order to select an operating limit for the selected polyimide fibres. If a polyimide fibre is heated in inert atmosphere, degradation of the coating material, especially thermooxidative and moisture induced degradation, can be greatly reduced. Although 350°C is close to the glass transition temperature of polyimide, utilization at these temperatures might be possible for an extended period of time. Sample 4, in particular, might be suitable for a deployment at temperatures close to 350°C.

The results for ΔE^*_{ab} show that colour changes might be used to indicate irreversible attenuation changes at temperatures above 300°C. An appropriate threshold value, however, would need to be determined for every fibre.

Based on these results, a wellbore cable has been designed, fibre 4 has been incorporated and first measurements under in-situ conditions within a geothermal well in Iceland have been performed. Results of long term monitoring will be analyzed with regard to reversible and irreversible attenuation changes. If the optical properties degrade such that loss characteristic do not allow for DTS measurements but the additional loss is reversible, DTS measurements will be possible as soon as the temperature rises, again. If the loss is irreversible, the fibre is lost for further DTS measurements.

Acknowledgments

This work was performed within the framework of the HITI project (http://www.hiti-fp6.eu/) and funded by the European Commission in the 6th Framework Programme, Proposal/Contract no.: 019913. The authors would like to thank Jörg Schrötter and Christian Cunow for their support during design and performance of the fibre tests as well as the two anonymous reviewers for editing and reviewing the manuscript.

References

[1] E Hurtig, S Grosswig, M Jobmann, K Kühn, and P Marschall. Fiber-optic temperature measurements in shallow boreholes: experimental application for fluid logging. *Geothermics*, 23(4):355–364, 1994.

[2] A Förster, J Schrötter, D F Merriam, and D D Blackwell. Application of optical-fiber temperature logging—an example in a sedimentary environment. *Geophysics*, 62(4):1107–1113, 1997.

[3] J Henninges, E Huenges, and H Burkhardt. In situ thermal conductivity of gas-hydrate-bearing sediments of the Mallik 5L-38 well. *Journal of Geophysical Research (Solid Earth)*, 110:B11206, November 2005.

[4] G R Williams, G Brown, W Hawthorne, A H Hartog, and P C Waite. Distributed temperature sensing (DTS) to characterize the performance of producing oil wells. In A Wang and E Udd, editors, *Industrial Sensing Systems*, volume 4202, pages 39–54. SPIE, 2000.

[5] S Arnórsson. Geothermal systems in Iceland: Structure and conceptual models–I. High-temperature areas. *Geothermics*, 24(5-6):561–602, 1995.

[6] A Albertsson, J Ö Bjarnason, T Gunnarsson, C Ballazus, and K Ingason. Part III: Fluid handling and evaluation. In G Ó Fridleifsson, editor, *Iceland Deep Drilling Project, Feasibility Report, Orkustofnun Report OS-2003-2007*, pages 1–33. Orkustofnun, 2003.

[7] G Ó Fridleifsson and W A Elders. The Iceland Deep Drilling Project: A search for deep unconventional geothermal resources. *Geothermics*, 34(3):269–285, 2005.

[8] C Smithpeter, R Norman, J Krumhansl, D Benoit, and S Thompson. Evaluation of a distributed fiber-optic temperature sensor for logging wellbore temperature at the Beowawe and Dixie Valley geothermal fields. In *Twenty-Fourth Workshop on Geothermal Reservoir Engineering*, Stanford, California, January 1999. Stanford University.

[9] R Norman, J Weiss, and J Krumhansl. Development of fibre optic cables for permanent geothermal wellbore deployment. In *Twenty-Sixth Workshop on Geothermal Reservoir Engineering*, Stanford, California, January 2001. Stanford University.

[10] J Stone and G E Walrafen. Overtone vibrations of OH groups in fused silica optical fibers. *The Journal of Chemical Physics*, 76(4):1712–1722, 1982.

[11] O Humbach, H Fabian, U Grzesik, U Haken, and W Heitmann. Analysis of OH absorption bands in synthetic silica. *Journal of Non-Crystalline Solids*, 203:19 – 26, 1996.

[12] P J Lemaire and E A Lindholm. Hermetic optical fibers: Carbon-coated fibers. In A M and T F Morse, editors, *Specialty Optical Fibers Handbook*, pages 453–490. Academic Press, 2007.

[13] J Kaura and J Sierra. High temperature fibers provide continuous DTS data in a harsh SAGD environment. *World Oil Magazine*, June 2008.

[14] C Lee. Self-calibrating technique enables long-distance temperature sensing. *Laser Focus World*, 43(8):101–108, 2007.

[15] K Suh and C Lee. Auto-correction method for differential attenuation in a fiber-optic distributed-temperature sensor. *Optical Letters*, 33(16):1845–1847, 2008.

[16] V A Bogatyrev and S Semjonov. Metal-coated fibers. In A Méndez and T F Morse, editors, *Specialty Optical Fibers Handbook*, pages 491–512. Academic Press, 2007.

[17] V Voloshin, I Vorob'ev, G Ivanov, V Isaev, A Kolosovskii, S Popov, and Yu Chamorovskii. Effect of

metal coating on the optical losses in heated optical fibers. *Technical Physics Letters*, 35(4):365–367, April 2009.

[18] N Ikeda. Fracture reservoir characterization by fiber-optic distributed temperature log. In *Twenty-Eighth Workshop on Geothermal Reservoir Engineering*, Stanford, California, January 2003. Stanford University.

[19] E C Carter, Y Ohno, M R Pointer, A R Robertson, R Sève, J D Schanda, and K Witt, editors. *Colorimetry; CIE 15-2004*. CIE International Commission on Illumination, 3 edition, 2004.

[20] J A Cella. Degradation and stability of polyimides. In M K Ghosh and K L Mittal, editors, *Polyimides: Fundamentals and Applications*, pages 343–366. Marcel Dekker, Inc., 1996.

[21] A A Stolov, D A Simoff, and J Li. Thermal stability of specialty optical fibers. *Journal of Lightwave Technology*, 26(20):3443–3451, 2008.

[22] DuPont. Summary of properties for Kapton® polyimide films. Technical report, 2008. `http://www2.dupont.com/Kapton/en_US/assets/downloads/pdf/summaryofprop.pdf`.

[23] R Roy, D K Agrawal, and H A McKinstry. Very low thermal expansion coefficient materials. *Annual Review of Materials Science*, 19(1):59–81, 1989.

[24] F C Nix and D MacNair. The thermal expansion of pure metals : Copper, gold, aluminum, nickel, and iron. *Physical Review*, 60:597–605, 1941.

Statement of Provenance

References

Al-Asimi, M., G. Butler, G. Brown, A. Hartog, T. Clancy, C. Cosad, J. Fitzgerald, J. Navarro, A. Gabb, J. Ingham, S. Kimminau, J. Smith, and K. Stephenson (2002). Advances in Well and Reservoir Surveillance. *Oilfield Review 14*(4), 14–35. Oilfield Review.

Albertsson, A., J. O. Bjarnason, T. Gunnarsson, C. Ballazus, and K. Ingason (2003). Part III: Fluid Handling and Evaluation. In G. O. Fridleifsson (Ed.), *Iceland Deep Drilling Project, Feaibility Report*, pp. 33. Orkustofnun Report OS-2003-007.

Ambastha, A. and J. Gudmundsson (1986). Pressure profiles in two-phase geothermal wells: Comparison of field data and model calculations. In *Proceedings, Eleventh Workshop on Geothennal Reservoir Engineering*.

Anderson, E., Z. Bai, C. Bischof, S. Blackford, J. Demmel, J. Dongarra, J. Du Croz, A. Greenbaum, S. Hammarling, A. McKenney, and D. Sorensen (1999). *LAPACK Users' Guide* (3 ed.). Philadelphia, PA: Society for Industrial and Applied Mathematics.

Arnórsson, S. (1995). Geothermal systems in Iceland; structure and conceptual models; I, High-temperature areas. *Geothermics 24*, 561–602.

Arnórsson, S. and E. Gunnlaugsson (1985). New gas geothermometers for geothermal exploration—calibration and application. *Geochimica et Cosmochimica Acta 49*(6), 1307 – 1325.

Ascher, D., P. F. Dubois, K. Hinsen, J. Hugunin, and T. Oliphant (1999). *Numerical Python* (UCRL-MA-128569 ed.). Livermore, CA: Lawrence Livermore National Laboratory.

Baehr, H. and K. Stephan (2008). *Wärme- und Stoffübertragung* (6 ed.). Springer.

Bartoli, A. (1890). Sul calore specifico, fino ad altissima temperatura, delle lave dell' etna e di altri vulcani. *Bulletino mensile della Accademia gioenia di scienze naturali in Catania 15*, 11–14. in Italian.

Bentur, A., R. L. Berger, J. H. Kung, N. B. Milestone, and J. F. Young (1979). Structural properties of calcium silicate pastes: Ii, effect of curing temperature. *Journal of the American Ceramic Society 62*(7-8), 362–366.

Bentz, D. P. (2007). Transient plane source measurements of the thermal properties. *Materials and Structures 40*, 1073–1080.

Bentz, D. P., E. Garboczi, C. Haecker, and O. M. Jensen (1999). Effects of cement particle size distribution on performance properties of portland cement-based materials. *Cement and Concrete Research 29*(10), 1663–1671.

Bentz, D. P. and C. J. Haecker (1999). Argument for using coarse cements in high-performance concretes. *Cement and Concrete Research 29*, 615–618.

Berryman, J. G. (1995). Mixture theories for rock properties. In T. J. Ahrens (Ed.), *Rock Physics & Phase Relations A Handbook of Physical Constants*, AGU Reference Shelf 3, pp. 205–228. American Geophysical Union.

Bhatty, J. I. (1991). A review of the application of thermal analysis to cement-admixture systems. *Thermochimica Acta 189*(2), 313 – 350.

Bignall, G. (2010, 25-29 April). Hotter and deeper: New zealand's research programme to harness its deep geothermal resources. In *Proceedings World Geothermal Congress 2010*, Bali, Indonesia.

Björnsson, A., K. Saemundsson, P. Einarsson, E. Tryggvason, and K. Grönvold (1977). Current rifting episode in north Iceland. *Nature 266*(5600), 318–323.

Bogatyrev, V. A. and S. Semjonov (2007). Metal-coated fibers. In A. Méndez and T. F. Morse (Eds.), *Specialty Optical Fibers Handbook*, Chapter 15, pp. 491–512. Academic Press.

Bogue, R. H. (1929). Calculation of the compounds in portland cement. *Industrial & Engineering Chemistry Analytical Edition 1*(4), 192–197.

Breddam, K., M. D. Kurz, and M. Storey (2000). Mapping out the conduit of the Iceland mantle plume with helium isotopes. *Earth and Planetary Science Letters 176*, 45–55.

Bresson, B., F. Meducin, H. Zanni, and C. Noik (2002). Hydration of tricalcium silicate (C3S) at high temperature and high pressure. *Journal of Materials Science 37*, 5355–5365. 10.1023/A:1021093528888.

Buck, J. A. (2004). *Fundamentals of Optical Fibers*. Wiley Series in Pure and Applied Optics. John Wiley & Sons, Inc.

Carslaw, H. S. and J. Jaeger (1959). *Conduction of Heat in Solids* (2 ed.). Oxford Univ Press.

Carter, E., Y. Ohno, M. Pointer, A. Robertson, R. Sève, J. Schanda, and K. Witt (2004). Colorimetry. Technical Report CIE 15:2004, International Commission on Illumination.

Cella, J. A. (1996). Degradation and stability of polyimides. In M. K. Ghosh and K. L. Mittal (Eds.), *Polyimides: fundamentals and applications*, pp. 343–366. Marcel Dekker, Inc.

Cengel, Y. A. (2002). *Heat Transfer: A Practical Approach* (2 ed.). McGraw-Hill Publishing Co.

Clauser, C. and E. Huenges (1995). Thermal conductivity of rocks and minerals. In T. J. Ahrens (Ed.), *Rock Physics and Phase Relations: A Handbook of Physical Constants*, pp. 105–126. Washington: American Geophysical Union.

Crank, J. (1975). *The Mathematics of Diffusion* (2 ed.). Oxford: Clarendon Press.

Danielsen, P. E. (2010, 25-29 April). Servicing geothermal wells during completion and follow-up monitoring. In *Proceedings World Geothermal Congress 2010*, Bali, Indonesia.

Diersch, H.-J. G. (2009). *Reference Manual for FEFLOW®*. DHI-WASY GmbH.

Dowdle, W. and W. Cobb (1975). Static formation temperature from well logs - an empirical method. *Journal of Petroleum Technology 27*(11), 1326–1330.

Dreike, P., D. Fleetwood, D. King, D. Sprauer, and T. Zipperian (1994, Dec). An overview of high-temperature electronic device technologies and potential applications. *IEEE Transactions on Components, Packaging, and Manufacturing Technology, Part A 17*(4), 594–609.

Driesner, T. and C. A. Heinrich (2007, October). The system H2O-NaCl. Part I: Correlation formulae for phase relations in temperature-pressure-composition space from 0 to 1000 °C, 0 to 5000 bar, and 0 to 1 XNaCl. *Geochimica et Cosmochimica Acta 71*(20), 4880–4901.

ECMA (1966, September). *Standard ECMA-4 Flow Charts* (2 ed.). European Computer Manufacturers Association.

Economides, M. J. (1990). Implications of cementing on well performance. In E. B. Nelson (Ed.), *Well Cementing* (1 ed.)., Chapter 1, pp. 1–01–1–06. Schlumberger Educational Services.

Eilers, L. and R. Root (1976). huimbach. In *SPE California Regional Meeting, 7-9 April 1976, Long Beach, California*. Society of Petroleum Engineers.

Eppelbaum, L. V. and I. M. Kutasov (2006). Determination of formation temperatures from temperature logs in deep boreholes: comparison of three methods. *Journal of Geophysics and Engineering 3*(4), 348–355.

Europerl (2011). Cryogenic-Europerl - Data Sheet. http://www.europerl.com/fileadmin/downloads/Europerl/Allgemein/Andere_Sprachen/Cryogenic_Europerl_englisch___1.4.pdf (22.02.2012).

Flandre, D., S. Adriaensen, A. Akheyar, A. Crahay, L. Demeûs, P. Delatte, V. Dessard, B. Iniguez, A. Nève, B. Katschmarskyj, P. Loumaye, J. Laconte, I. Martinez, G. Picun, E. Rauly, C. Renaux, D. Spôte, M. Zitout, M. Dehan, B. Parvais, P. Simon, D. Vanhoenacker, and J. P. Raskin (2001). Fully depleted soi cmos technology for heterogeneous micropower, high-temperature or rf microsystems. *Solid-State Electronics 45*(4), 541 – 549.

Flóvenz, O. G. and K. Saemundsson (1993). Heat flow and geothermal processes in Iceland. *Tectonophysics 225*, 123–138.

Förster, A., J. Schrötter, D. F. Merriam, and D. D. Blackwell (1997). Application of optical-fiber temperature logging—an example in a sedimentary environment. *Geophysics 62*(4), 1107–1113.

FORTA Corporation (2011). FORTA Super-Sweep. http://www.norteks.ru/en/product/forta/super_sweep/ (22.02.2012).

Fourier, J. (1822). *Théorie analytique de la chaleur*. Chez Firmin Didot, père et fils.

Franzson, H., S. T. Gudlaugsson, and G. O. Fridleifsson (2001). Petrophysical properties of icelandic rocks. In *Proceedings of the 6th Nordic Symposium on Petrophysics*.

Franzson, H., B. R. Kristjánsson, G. Gunnarsson, G. Björnsson, A. Hjartarson, B. Steingrímsson, E. Gunnlaugsson, and G. Gíslason (2005, 24-29 April). The Hengill-Hellisheiði geothermal field. Development of a conceptual geothermal model. In *Proceedings World Geothermal Congress 2005*, Antalya, Turkey.

Freifeld, B. M., S. Finsterle, T. C. Onstott, P. Toole, and L. M. Pratt (2008, July). Ground surface temperature reconstructions: Using in situ estimates for thermal conductivity acquired with a fiber-optic distributed thermal perturbation sensor. *Geophysical Research Letters 35*(14), L14309.

Fridleifsson, G. O. and W. A. Elders (2005). The Iceland Deep Drilling Project: a search for deep unconventional geothermal resources. *Geothermics 34*, 269–285.

Fujii, K., M. Yasuda, B. Cho, T. Ikegami, H. Sugiyama, Y. Imasato, S. R. Dallimore, and J. F. Wright (2008, July 6-10). Development of a monitoring system for the jogmec/nrcan/aurora mallik gas hydrate production test program. In *Proceedings of the 6th International Conference on Gas Hydrates (ICGH 2008)*, Vancouver, British Columbia, Canada.

Gautsch, W. and W. F. Cahill (1972). Exponential integral and related functions. In M. Abramowitz and I. A. Stegun (Eds.), *Handbook of Mathematical Functions with Formulas, Graphs, and Mathematical Tables* (9 ed.)., Chapter 5, pp. 227–252. Dover Publications Inc.

Geckeis, O., W. Nolden, J. Henninges, M. Zimmer, and T. Reinsch (2011, February). Verfahren zum Betreiben eines Bohrlochkabels und Bohrlochkabel. German Patent DE102008026082B8.

Ghabezloo, S., J. Sulem, S. Guédon, F. Martineau, and J. Saint-Marc (2008). Poromechanical behaviour of hardened cement paste under isotropic loading. *Cement and Concrete Research 38*, 1424–1437.

Ghabezloo, S., J. Sulem, and J. Saint-Marc (2009). The effect of undrained heating on a fluid-saturated hardened cement paste. *Cement and Concrete Research 39*, 54–64.

Günzel, U. and H. Wilhelm (2000). Estimation of the in-situ thermal resistance of a borehole using the distributed temperature sensing (DTS) technique and the temperature recovery method (TRM). *Geothermics 29*(6), 689–700.

Goodwin, K. (1992). Guidelines for ultrasonic cement-sheath evaluation. *SPE Production Engineering 7*(3), 280–284.

Goodwin, K. and R. Crook (1992, December). Cement sheath stress failure. *SPE Drilling Engineering 7*(4), 291–296.

Goranson, R. W. (1942). Heat capacity; heat of fusion. In F. Birch, J. F. Schairer, and H. C. Spicer (Eds.), *Handbook of Physical Constants*, Volume 36 of *Special Papers*, pp. 223–242. Geological Society of Ameica.

Grant, M. A., I. G. Donaldson, and P. F. Bixley (1982). *Geothermal Reservoir Engineering*. Energy Science and Engineering: Resources, Technology, Management. New York: Academic Press.

Grattan, K. T. V. and B. T. Meggitt (1995). *Optical Fiber Sensor Technology*. London: Chapman & Hall.

Guyod, H. (1946). Temperature well logging - part 5 wells not in thermal equilibrium - part b fluid intrusions. *Oil Weekly*, 40–44.

Haaland, S. E. (1983). Simple and explicit formulas for the friction factor in turbulent pipe flow. *Journal of Fluids Engineering 105*(1), 89.

Hadgu, T., R. W. Zimmerman, and G. S. Bodvarsson (1994). Theoretical studies of flowrates from slimholes and production-size geothermawl ells. In *Proceedings, Nineteenth Workshop on Geothermal Reservoir Engineering*.

Hagedorn, A. R. and K. E. Brown (1965). Experimental study of pressure gradients occurring during continuous two-phase flow in small-diameter vertical conduits. *Journal of Petroleum Technology 17*(4), 475–484.

Hahne, E. (2006). *VDI Wärmeatlas* (10 ed.)., Chapter Zweidimensionale Wärmeleitung, pp. Ea4–Ea12. Springer.

Harmathy, T. Z. (1970). Thermal properties of concrete at elevated temperatures. *Journal of Materials 5*(1), 47–74.

Hartog, A. (1983). A distributed temperature sensor based on liquid-core optical fibers. *Journal of Lightwave Technology 1*(3), 498–509.

Hasan, A. and C. Kabir (2010). Modeling two-phase fluid and heat flows in geothermal wells. *Journal of Petroleum Science and Engineering 71*(1-2), 77 – 86.

Hashin, Z. and S. Shtrickman (1962). A variational approach to the theory of the effective magnetic permeability of multiphase materials. *Journal of Applied Physics 33*, 3125–3133.

Helgadóttir, H. M., S. O. Snaebjörnsdóttir, S. Níelsson, S. H. Gunnarsdóttir, T. Matthíasdóttir, B. S. Hardarson, G. M. Einarsson, and H. Franzson (2010, 25-29 April). Geology and hydrothermal alteration in the reservoir of the hellisheiði high temperature system, sw-iceland. In *Proceedings World Geothermal Congress 2010*, Bali, Indonesia.

Hemingway, B. S. (1987). Quartz: Heat capacities from 340 to 1000 K and revised values for the thermodynamic properties. *American Mineralogist 72*, 273–279.

Henninges, J. (2005). *Thermal Properties of Gas-Hydrate-Bearing Sediments and Effects of Phase Transitions on the Transport of Heat Deduced from Temperature Logging at Mallik, NWT, Canada*. Ph. D. thesis, Technical University Berlin.

Henninges, J., E. Huenges, and H. Burkhardt (2005, November). In situ thermal conductivity of gas-hydrate-bearing sediments of the Mallik 5L-38 well. *Journal of Geophysical Research (Solid Earth) 110*, B11206.

Henninges, J., B. Prevedel, and M. Loizzo (2008). Echtzeit-Beobachtung von Bohrlochzementationen und Sondenbehandlungen mit ortsverteilten Temperaturmessungen. In *DGMK/ÖGEW-Frühjahrstagung, Celle*.

Horai, K.-i. and G. Simmons (1969). Thermal conductivity of rock-forming minerals. *Earth and Planetary Science Letters 6*(5), 359 – 368.

Humbach, O., H. Fabian, U. Grzesik, U. Haken, and W. Heitmann (1996). Analysis of oh absorption bands in synthetic silica. *Journal of Non-Crystalline Solids 203*, 19 – 26.

Hurtig, E., S. Grosswig, M. Jobmann, K. Kuhn, and P. Marschall (1994). Fiber-optic temperature measurements in shallow boreholes: experimental application for fluid logging. *Geothermics 23*(4), 355–364.

Iceland Cement Ltd. (2007). Portlandsement - Technical Data Sheet. http://www.sement.is/resources/Files/pdf/TDS-Portlandsement2007.pdf.

Ickes, H. L., J. C. Page, and S. O. Harper (1940). Boulder canyon project report, final reports, thermal properties of concrete. Technical report, United States Departement of the Interior - Bureau of Reclamation. Bulletin No. 1, Part VII Cement and Concrete Investigations.

Ikushima, A. J., T. Fujiwara, and K. Saito (2000). Silica glass: A material for photonics. *Journal of Applied Physics 88*(3), 1201–1213.

Ingram, G. (2011). Moody.py. online. http://www.dur.ac.uk/g.l.ingram/download/moody.py (5. May 2011).

Jaaskelainen, M. (2010). Temperature monitoring of geothermal energy wells. In J. L. Santos, B. Culshaw, J. M. López-Higuera, and W. N. MacPherson (Eds.), *Proceedings SPIE 7653*, Volume 7653, pp. 765303. SPIE.

Jakobsson, S. P. (1972). Chemistry and distribution pattern of recent basaltic rocks in iceland. *Lithos 5*(4), 365 – 386.

James, R. (1962). Steam-water critical flow through pipes. *Proceedings of the Institution of Mechanical Engineers 176*, 741–748.

James, R. (1970). Factors controlling borehole performance. *Geothermics 2*(Part 2), 1502 – 1515. Proceedings of the United Nations symposium on the development and utilization of geothermal resources.

Jennings, H. M., B. J. Dalgleish, and P. L. Pratt (1981). Morphological development of hydrating tricalcium silicate as examined by electron microscopy techniques. *Journal of the American Ceramic Society 64*(10), 567–572.

Jensen, O. M. (1995). Thermodynamic limitation of self-desiccation. *Cement and Concrete Research 25*(1), 157 – 164.

Johnson, D., R. Sugianto, P. Mock, and C. Jones (2004). Identification of steam-breakthrough intervals with DTS technology. *SPE Production & Facilities 19*, 41–48.

Jutten, J., D. Guillot, and P. Parcevaux (1989). Relationship between cement slurry composition, mechanical properties, and cement-bond-log output. *SPE Production Engineering 4*(1), 75–82.

Jutten, J. and S. L. Morriss (1990). Cement job evaluation. In E. B. Nelson (Ed.), *Well Cementing* (1 ed.)., Chapter 16, pp. 16–01–16–44. Schlumberger Educational Services.

Kalifa, P., G. Chéné, and C. Gallé (2001). High-temperature behaviour of hpc with polypropylene fibres: From spalling to microstructure. *Cement and Concrete Research 31*(10), 1487 – 1499.

Kaura, J. and J. Sierra (2008). High-temperature fibers provide continuous DTS data in a harsh SAGD environment. *World Oil and Gas Journal 229*(6), 47–53.

Khan, M. (2002). Factors affecting the thermal properties of concrete and applicability of its prediction models. *Building and Environment 37*(6), 607 – 614. Retrofitting of Office Buildings: Papers from the Research Project Office.

Köckritz, V. (1979). *Wärmeübertragungs- und Strömungsvorgänge bei der Förderung und Speicherung von gasförmigen Medien.* Ph. D. thesis, TU Bergakademie Freiberg.

Kulin, G. and P. R. Compton (1975). A guide to methods and standards for the measurement of water flow.

Kutasov, I. (2007). Dimensionless temperatures at the wall of an infinitely long, variable-rate, cylindrical heat source. *Geothermics 36*(3), 223 – 229.

Kutasov, I. M. and M. Kagan (2003, April). Cylindrical probe with a constant temperature–determination of the formation thermal conductivity and contact thermal resistance. *Geothermics 32*(2), 187–193.

Lee, C. E. (2007). Self-calibrating technique enables long-distance temperature sensing. *LaserFocusWorld 43*(8).

Lemaire, P. J. and E. A. Lindholm (2007). Hermetic optical fibers: Carbon-coated fibers. In A. Méndez and T. F. Morse (Eds.), *Specialty Optical Fibers Handbook*, Chapter 14, pp. 453–490. Academic Press.

Lemmon, E. W., M. L. Huber, and M. O. McLinden (2007). *NIST Standard Reference Database 23: Reference Fluid Thermodynamic and Transport Properties-REFPROP, Version 8.0*. Gaithersburg: National Institute of Standards and Technology.

Lerch, W. and R. H. Bogue (1934, May). Heat of hydration of portland cement pastes. *Journal of Research of the National Bureau of Standards 12*(RP 684), 645–664.

Lerch, W. and C. L. Ford (1948). Long-time study of cement performance in concrete. *Journal of the American Concrete Institute 44*(8), 745–795.

Lin, F. (2006). *Modeling of Hydration Kinetics and Shrinkage of Portland Cement Paste*. Ph. D. thesis, Columbia University.

Lin, F. and C. Meyer (2009). Hydration kinetics modeling of portland cement considering the effects of curing temperature and applied pressure. *Cement and Concrete Research 39*(4), 255 – 265.

Lingle, Jr., R., D. W. Peckham, A. McCurdy, and J. Kim (2007). Light-guiding fundamentals and fiber design. In A. Méndez and T. F. Morse (Eds.), *Specialty Optical Fibers Handbook*, Chapter 2, pp. 19–68. Academic Press.

Marcuse, D. (1976, September). Microbending losses of single-mode, step-index and multimode, parabolic-index fibers. *The Bell System Technical Journal 55*(7), 937–955.

Marshall, A. (1972). The thermal properties of concrete. *Building Science 7*(3), 167 – 174.

Massiot, C., R. Ásmundsson, and P. Pezard (2010, 25-29 April). Achievements and ongoing progress of the european hiti project: High temperature instruments for supercritical geothermal reservoir characterization and exploitation. In *Proceedings World Geothermal Congress 2010*, Bali, Indonesia.

Mendieta, E. P. (1991). Production characteristics of the momotombo geothermal field, nicaragua. Technical report, UNU Geothermal Training Programme.

Mills, R. H. (1966). Factors influencing cessation of hydration in water cured cement pastes. Technical Report 90, Highway Research Board, Washington DC, USA.

Moody, L. F. (1944). Friction factors for pipe flow. *Transactions of the ASME 66*(8), 671–684.

Morsy, M. S., S. H. Alsayed, and M. Aqel (2010). Effect of elevated temperature on mechanical properties and microstructure of silica flour concrete. *International Journal of Civil & Environmental Engineering 10*(1), 1–6.

Nelson, E. B. (1986). Improved cement slurry design for thermal EOR wells. *Oil and Gas Journal 84*(48), 39–44.

Nelson, E. B., J.-F. Baret, and M. Michaux (1990). Cement additives and mechanisms of action. In E. B. Nelson (Ed.), *Well Cementing* (1 ed.)., Chapter 3, pp. 3–01–3–37. Schlumberger Educational Services.

Níelsson, S. and H. Franzson (2010, 25-29 April). Geology and hydrothermal alteration of the Hverahlid HT-system, SW-Iceland. In *Proceedings World Geothermal Congress 2010*, Bali, Indonesia.

Normann, R., J. Weiss, and J. Krumhansl (2001, January). Development of Fibre Optic Cables for Permanent Geothermal Wellbore Deployment. In *Twenty-Sixth Workshop on Geothermal Reservoir Engineering*, Stanford, California. Stanford University.

Noumowe, A. (2005). Mechanical properties and microstructure of high strength concrete containing polypropylene fibres exposed to temperatures up to 200 °C. *Cement and Concrete Research 35*(11), 2192 – 2198.

Nowak, T. (1953). The estimation of water injection profiles from temperature surveys. *Petroleum Transactions, AIME 198*, 203–212.

Odler, I. (2004). Hydration, setting and hardening of portland cement. In P. C. Hewlett (Ed.), *Lea's Chemistry of Cement and Concrete* (4 ed.)., Chapter 6, pp. 241–297. Elsevier Science & Technology Books.

Oldham, K., J. Myland, and J. Spanier (2009). *An Atlas of Functions with Equator, the Atlas Function Calculator* (2 ed.)., Chapter The Exponential Integrals Ei(x) and Ein(x), pp. 375–383. Springer.

Ouali, S. (2009). Thermal conductivity in relation to porosity and geological stratigraphy. Technical Report 23, United Nations University - Geothermal Training Programme.

Oxburgh, E. R. and S. O. Agrell (1982, August). Thermal conductivity and temperature structure of the Reydarfjordur borehole. *Journal of Geophysical Research 87*, 6423–6428.

Pálmason, G., G. V. Johnsen, H. Torfason, K. Saemundsson, K. Ragnars, G. I. Haraldsson, and G. K. Halldórsson (1985). Mat á jardvarma Íslands [Evaluation of geothermal resources in Iceland]. Technical Report OS-85076/JHD-10, Orkustofnun, Reykjavík, Iceland. in Icelandic.

Pardue, G. H., R. L. Morris, L. H. Gollwitzer, and J. H. Moran (1963). Cement bond log-a study of cement and casing variables. In *Proceedings 37th Annual Fall Meeting of SPE*.

Patchen, F. (1960). Reaction and properties of silica-portland cement mixtures cured at elevated temperatures. *Petroleum Transactions, AIME 219*, 281–287.

Pimenov, V., G. Brown, V. Tertychnyi, A. Shandrygi, and Y. Popov (2005). Injectivity profiling in horizontal wells via distributed temperature monitoring. In *SPE Annual Technical Conference and Exhibition, 9-12 October 2005, Dallas, Texas*.

Pirow, R. and I. Buchen (2004). The dichotomous oxyregulatory behaviour of the planktonic crustacean daphnia magna. *The Journal of Experimental Biology 207*, 683–696.

Poole, H. H. (1914). V. on the thermal conductivity and specific heat of granite and basalt at high temperatures. *Philosophical Magazine Series 6 27*(157), 58–83.

Press, W. H., S. A. Teokolsky, W. T. Vetterling, and B. P. Flannery (1992). *Numerical Recepies in Fortran 77 The Art of Scientific Computing* (2 ed.). Cambridge University Press.

Prevedel, B., L. Wohlgemuth, J. Henninges, K. Krüger, B. Norden, A. Förster, and the CO2SINK Drilling Group (2008, July). The CO2SINK boreholes for geological storage testing. *Scientific Drilling 6*(6), 32–37.

Ramey Jr., H. (1962). Wellbore heat transmission. *Journal of Petroleum Technology 14*(4), 427–435.

Ramey Jr., H. (1978). Hand computer program for james' lip pressure steam flow rate. *Geothermal Resources Council Transactions 2*, 555–557.

Reinsch, T. (2008). Prospects and limitations of a distributed temperature measuring system for the deployment in hot geothermal wells. Master's thesis, University of Cologne.

Reinsch, T. and J. Henninges (2010). Temperature-dependent characterization of optical fibres for distributed temperature sensing in hot geothermal wells. *Measurement Science and Technology 21*(9), 094022.

Rist, D. (1996). *Dynamik realer Gase*. Springer.

Roberts-Austen, W. C. and A. W. Rücker (1891). Xliv. on the specific heat of basalt. *Philosophical Magazine Series 5 32*(197), 353–355.

Robertson, E. and D. Peck (1974). Thermal conductivity of vesicular basalt from hawaii. *Journal of Geophysical Research 79*(32), 4875–4888.

Roth, W. A. and P. Chall (1928). Die thermische verfolgung einiger metallurgisch wichtiger reaktionen in einem bei höherer temperatur arbeitenden calorimeter. *Zeitschrift für Elektrochemie und angewandte physikalische Chemie 34*(4), 185–199.

Saadat, A., S. Frick, S. Kranz, and S. Regenspurg (2010). Energetic use of EGS reservoirs. In E. Huenges (Ed.), *Geothermal Energy System - Exploration, Development, and Utilization*, Chapter 6, pp. 303–372. John Wiley & Sons, Ltd.

Saemundsson, K. (1995). Hengill, geological map (bedrock) 1:50000. Orkustofnun, Hitaveita Reykjavíkur and Landmaelingar Íslands.

Sarian, S. and A. Gibson (2005, May). Wireline evaluation technology in hpht wells. In *SPE High Pressure/High Temperature Sour Well Design Applied Technology Workshop*, The Woodlands, Texas. SPE.

Schindler, A. K. (2004). Effect of temperature on hydration of cementitious materials. *ACI Materials Journal 3*, 72–81.

Schindler, A. K. and K. J. Folliard (2005, January). Heat of hydration models for cementitious materials. *Materials Journal 102*(1), 24–33.

Sensa (2004). *DTS 800 Installation & Maintenance* (8 ed.). Schlumberger Limited.

Sha, W., E. A. O'Neill, and Z. Guo (1999). Differential scanning calorimetry study of ordinary portland cement. *Cement and Concrete Research 29*(9), 1487 – 1489.

Sigfusson, B. and I. Gunnarsson (2011, January 31 - February 2). Scaling prevention experiments in the hellisheiði power plant, iceland. In *Proceedings, Thirty-Sixth Workshop on Geothermal Reservoir Engineering*, Stanford University, Stanford, California. SGP-TR-191.

Sigurdsson, O., A. Gudmundsson, G. O. Fridleifsson, H. Franzson, S. T. Guðlaugsson, and V. Stefánsson (2000, May-June). Database on igneous rock properties in icelandic geothermal systems. status and unexpected results. In *Proceedings World Geothermal Congress 2000*, Kyushu - Tohoku, Japan, pp. 3021–3026.

Sigvaldason, G. E. (1969). Chemistry of basalts from the icelandic rift zone. *Contributions to Mineralogy and Petrology 20*, 357–370. 10.1007/BF00373304.

Sims, R., R. Schock, A. Adegbululgbe, J. Fenhann, I. Konstantinaviciute, W. Moomaw, H. Nimir, B. Schlamadinger, J. Torres-Martínez, C. Turner, Y. Uchiyama, S. Vuori, N. Wamukonya, and X. Zhang (2007). Energy supply. In B. Metz, O. R. Davidson, P. R. Bosch, R. Dave, and L. A. Meyer (Eds.), *Climate Change 2007: Mitigation. Contribution of Working Group III to the Fourth Assessment Report of the Intergovernmental Panel on Climate Change*, pp. 251–322. Cambridge, United Kingdom and New York, NY, USA: Cambridge University Press.

Smithpeter, C., R. Normann, J. Krumhansl, D. Benoit, and S. Thompson (1999, January). Evaluation of a distributed fiber-optic temperature sensor for logging wellbore temperature at the beowawe and dixie valley geothermal fields. In *Twenty-Fourth Workshop on Geothermal Reservoir Engineering*, Stanford, California. Stanford University.

Smolen, J. J. (1996). *Cased Hole and Production Log Interpretation*. PennWell Books.

Southon, J. N. A. (2005, April). Geothermal well design, construction and failures. In *Proceedings World Geothermal Congress 2005*, Antalya - Turkey.

Stefánsson, V. and B. Steingrímsson (1980). Geothermal logging I - an introduction to techniques and interpretation. Technical Report OS80017/JHD09, Orkustofnun.

Stolov, A. A., D. A. Simoff, and J. Li (2008). Thermal stability of specialty optical fibers. *Journal of Lightwave Technology 26*(20), 3443–3451.

Stone, J. and G. E. Walrafen (1982). Overtone vibrations of oh groups in fused silica optical fibers. *The Journal of Chemical Physics 76*(4), 1712–1722.

Suh, K. and C. Lee (2008). Auto-correction method for differential attenuation in a fiber-optic distributed-temperature sensor. *Optical Letters 33*(16), 1845–1847.

Suman, Jr., G. O. and R. C. Ellis (1977). *World oil's - Cementing Handbook*. Gulf Professional Publishing.

Thiercelin, M. (2006). Mechanical properties of well cements. In E. B. Nelson and D. Guillot (Eds.), *Well Cementing* (2 ed.)., Chapter 8, pp. 269–288. Schlumberger.

Thiercelin, M., B. Dargaud, J. Baret, and W. Rodriquez (1998). Cement design based on cement mechanical response. *SPE Drilling & Completion 13*(4), 266–273.

Thordarson, T. and G. Larsen (2007). Volcanism in Iceland in historical time: Volcano types, eruption styles and eruptive history. *Journal of Geodynamics 43*, 118–152.

Thorhallsson, S. (2003, September). Geothermal well operation and maintenance. IGC2003 - Short Course.

Thorhallsson, S. (2008). Geothermal drilling and well pumps. In *Workshop for Decision Makers on Direct Heating Use of Geothermal Resources in Asia*. UNU-GTP.

Thorvaldson, T., W. G. Brown, and C. R. Peaker (1930). Studies on the thermochemistry of the compounds occurring in the system cao-al2o3-sio2. iii. the heat of hydration of calcium oxide. *Journal of the American Chemical Society 52*(3), 910–915.

Thyagarajan, K. and A. Ghatak (2007). *Fiber Optic Essentials*. Wiley & Sons.

Ulm, F. J. and O. Coussy (1995). Modeling of thermochemomechanical couplings of concrete at early ages. *Journal of Engineering Mechanics 121*(7), 785–795.

van Breugel, K. (1980, April). Artificial cooling of hardening concrete. Research Report - Concrete Structures 5-80-9, Delft University of Technology.

van Breugel, K. (1991). *Simulation of Hydration and Formation of Structure in Hardening Cement-Based Materials*. Ph. D. thesis, Delft University of Technology.

van Rossum, G. (1995). Python tutorial. Report CS-R9526, Centrum Wiskunde & Informatica, Amsterdam.

Walker, S. (1986, aug). Rapid modeling and estimation of total spectral loss in optical fibers. *Journal of Lightwave Technology 4*(8), 1125 – 1131.

Wang, W., G. Kosakowski, and O. Kolditz (2009). A parallel finite element scheme for thermo-hydro-mechanical (thm) coupled problems in porous media. *Computers & Geosciences 35*(8), 1631 – 1641.

Watanabe, N., W. Wang, C. McDermott, T. Taniguchi, and O. Kolditz (2010). Uncertainty analysis of thermo-hydro-mechanical coupled processes in heterogeneous porous media. *Computational Mechanics 45*, 263–280. 10.1007/s00466-009-0445-9.

Willhite, G. (1967). Over-all heat transfer coefficients in steam and hot water injection wells. *Journal of Petroleum Technology 19*(5), 607–615.

Williams, G. R., G. Brown, W. Hawthorne, A. H. Hartog, and P. C. Waite (2000). Distributed temperature sensing (DTS) to characterize the performance of producing oil wells. In A. Wang and E. Udd (Eds.), *Proceedings of SPIE*, Volume 4202, pp. 39–54. SPIE.

Wyo-Ben, Inc. (2011). Grout-well. http://www.wyoben.com/psgroups/drilling/water/productwell.html (22.02.2012).

Xiong, X. and K. van Breugel (2001). Isothermal calorimetry study of blended cements and its application in numerical simulations. *Heron 46*, 151–159.

Zhou, Q. and J. Beaudoin (2003). Effect of applied hydrostatic stress on the hydration of Portland cement and C3S. *Advances in Cement Research 15*, 9–16.

Zhou, Z., J. He, M. Huang, J. He, and G. Chen (2010). Casing pipe damage detection with optical fiber sensors: A case study in oilwell constructions. *Advances in Civil Engineering 2010*, 9.

Acknowledgements

I am grateful to Kurt M. Reinicke, Professor at the Technical University Clausthal, and Catalin Teodoriu for sharing their knowledge about wellbore integrity and supervising this work. Furthermore, I would like to thank Jan Henninges for his support and the fruitful discussions during this PhD work as well as Ernst Huenges, Professor at the Technical University Berlin and head of the section Reservoirtechnologies at the Helmholtz Centre Potsdam, GFZ German Research Centre for Geosciences, for making this work possible.

At the Helmholtz Centre Potsdam, GFZ German Research Centre for Geosciences, I am indebted to my colleagues for the open discussions on the different topics related to geothermal energy provision and reservoir engineering as well as for reviewing parts of this work. Especially, I would like to extend my gratitude to Jörg Schrötter, Mathias Poser and Christian Cunow for their help in planning and performing the measurements within the lab and in Iceland.

The field campaigns would not have been possible without the help of Ragnar Ásmundsson and the staff of ÍSOR (Iceland GeoSurvey) who coordinated the field work and supported this work with unconventional solutions for problems arising on site in Iceland. Furthermore, I am grateful to Reykjavik Energy for providing a well for installation as well as the staff of Mannvit and Iceland Drilling for the support during installation and measurements.

I would like to thank Matteo Loizzo for the discussions about cement hydration and wellbore integrity. For his very descriptive explanations of Icelandic geothermal well engineering and all topics related to it as well as the discussions on my measurement data, I am grateful to Sverrir Thorhallsson.

Without the support of my wife, family and friends, however, this work would not have been possible.

This study was performed within the framework of the HITI project (http://www.hiti-fp6.eu/) and funded by the European Commission in the 6th Framework Programme, Proposal/Contract no.: 019913, as well as the GeoEn-Phase 2 project (http://www.geoen.de/) and funded by the Federal Ministry of Education and Research (BMBF, 03G0767A).